X-460-70-401
PREPRINT

THRUSTER EXHAUST EFFECTS UPON SPACECRAFT

OCTOBER 1970

GSFC
GODDARD SPACE FLIGHT CENTER
GREENBELT, MARYLAND

X-460-70-401

THRUSTER EXHAUST EFFECTS UPON SPACECRAFT

Warren C. Lyon
Hittman Associates, Inc.,
Columbia, Maryland 21043*

October 1970

*This work was performed under the technical direction of R. Bartlett, D. Fordyce, and R. Hunter of GSFC. It was supported by Contracts NAS 5-9479 and NAS 5-11826

Goddard Space Flight Center
Greenbelt, Maryland

PRECEDING PAGE BLANK NOT FILMED

CONTENTS

CONTENTS (continued)

APPENDICES

THRUSTER EXHAUST EFFECTS UPON SPACECRAFT

Warren C. Lyon
Hittman Associates, Inc., Columbia, Maryland 21043

Abstract

A study has been conducted of the effect of thruster exhaust effluent upon spacecraft. Small thrusters (micropounds to several millipounds) utilizing cesium, Teflon, ammonia, and hydrazine as fuel have been considered. A brief summary of mercury thruster effects reported by others is included. We found few problems with ammonia and hydrazine. The major potential interactions are the effect upon the environment density and exhaust from these thrusters can coat radiators which operate at 70°K. Cesium and mercury will coat surfaces, particularly radiators which operate in the vicinity of 100°K. Charge exchange effects are quite important in predicting some of these effects. Contaminants in the exhaust beam can be particularly important because these components do not evaporate once condensed upon surfaces. The Teflon thruster can coat any surface placed in the vicinity of the exhaust beam. This coating will be quite inert, and would require high temperatures for its removal. It would consist, in part, of the basic Teflon polymer. A preliminary study of potential cesium thruster – Polaris star tracker interactions indicates that reflected sunlight will be a problem. Similar behavior may occur with other thruster exhausts. Further work is indicated in many areas.

THRUSTER EXHAUST EFFECTS UPON SPACECRAFT

1. BACKGROUND

Interactions between rocket and thruster exhaust products, other contaminants, and spacecraft components have been reported in numerous references. Many of the observed effects were not anticipated. For example, deposits were formed on the outside of the astronaut's viewing windows during the first two Gemini flights (Refs. 1 and 2). Particulate contamination was first reported by astronauts Glenn and Scott and has been observed in many manned flights as well as being recorded by TV from the Pegasus 2 spacecraft (Ref. 3). The Nimbus II and III HRIR (High Resolution Infrared Radiometer) detector cell temperature control was unsatisfactory (Refs. 4 and 5), probably due to contaminant recondensation phenomena (Ref. 6). The Gemini S-010 and S-012 micrometeorite experiments revealed a number of contaminants, including deposited material, surfaces pitted by thruster debris, corrosion from chemical reactions, and gouging by cohesive particles (Ref. 7). Clearly, space in the vicinity of a spacecraft provides an environment that is far from the vacuum many times assumed by the designer. Anything that contributes to the environment is of immediate concern.

Spacecraft are becoming more sophisticated. The Nimbus HRIR detector cell was to operate between -70 and -80°C (design point was -75°C) (Ref. 4). The initial values were close to the design point, but over a few hundred orbits, the temperature rose to greater than -65°C (Refs. 4, 8, 9). This almost tripled instrument noise to signal ratios. Now we are considering temperatures of 100°K for an ATS experiment (Ref. 10) and of 70°K on SMS (Ref. 11). If we have difficulty at -75°C, the need to carefully investigate behavior at -200°C is obvious. (A 30°C change in temperature at 100°K can change contaminant evaporation rate by 10^6 (Ref. 12).)

On board thrusters are a potential major source of spacecraft contamination. Their exhaust characteristics must be carefully investigated if problems are to be recognized prior to flight. Many studies of exhaust plume shapes, heating rates, and pressures have been reported, but most were intended for application to large motors. A number of Apollo oriented studies have covered exhaust behavior of intermediate range motors. The small thruster (<one pound thrust) literature provides, with a few exceptions, reports limited to thruster performance, design features, etc. Consideration of small thruster exhaust effects is the topic of few investigations. Most of the available data are concerned with mercury ion thrusters, which we will briefly review. Cesium, Teflon, ammonia, and hydrazine are covered in the remainder of this report.

The text of this report was, with minor changes, presented at the AIAA 8th Electric Propulsion Conference (paper number 70-1143) and has been submitted to the Journal of Spacecraft and Rockets. The detailed investigations and substantiating data are presented in Appendices. These contain all of the information originally contained in the Hittman Associates reports covering the studies.

2. ION THRUSTERS

2.1 Exhaust Plume

2.1.1 Description. Exhaust from an ion thruster consists of collimated ions and uncollimated ions and neutral atoms. The collimated ions, which constitute most of the

exhaust, are high energy ions primarily contained within an envelope defined by a relatively small semi-angle. These ions, referred to as Group 1 ions, do not interact with a spacecraft unless something is placed directly in the beam. All other ions are secondary ions produced by charge exchange reactions between neutral atoms and the Group 1 ions. Those produced within the thruster accelerating structure which escape the thruster, referred to as Group 2 ions, travel in approximately straight lines with the origin at the thruster exhaust. Those which are generated in the primary beam external to the thruster, termed Group 4, travel roughly perpendicular to the beam. (Group 3 ions are those which are produced within the thruster with insufficient energy to escape. Since they do not escape, they are of no concern here.) The un-ionized portion of the exhaust drifts outward from the thruster at approximately thermal energy. This behavior is shown schematically in Figure 1.

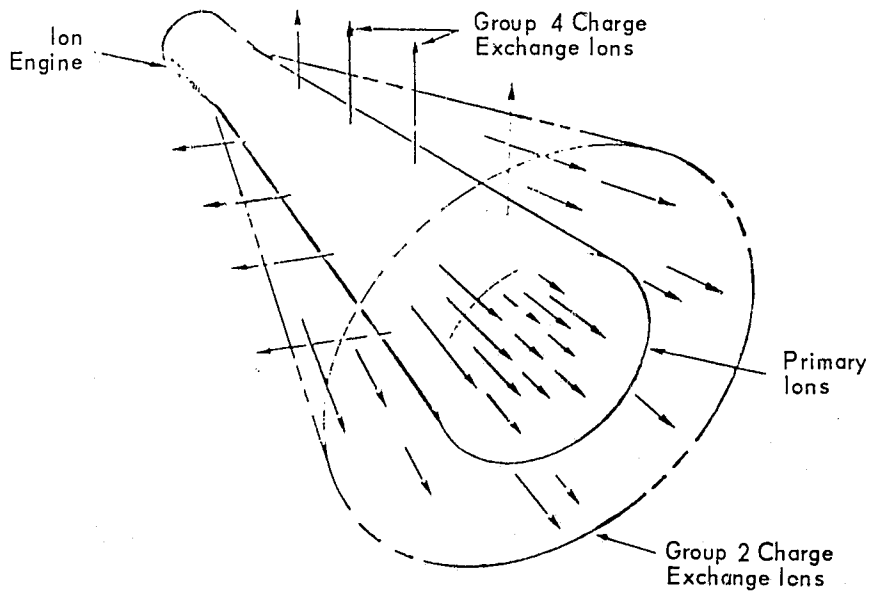

Figure 1. Ion Distribution Schematic

2.1.2 Neutral Atom Distribution. The neutral atom distribution; for $r > a$, is approximately (Ref. 13).

$$\Gamma(r, \theta) = \frac{\Gamma_0 \frac{a^2}{r^2} \cos\theta}{\left[1 + \frac{2a^2}{r^2}\cos\theta + \frac{a^4}{r^4}\right]^{1/2}} \qquad (1)$$

where Γ is the particle current density in the direction of the radius vector; r is the distance from the center of the ion engine exhaust plane to the position of interest; θ is the angle between r and the normal to the engine exhaust plane; Γ_0 is the particle current density at the ion engine exhaust plane; and a is the radius of the ion engine exhaust opening.

2.1.3 Group 4 Ions. The charge exchange ion production rate is

$$N = Q \Delta L A n n_0 \qquad (2)$$

where N is the ion production rate, charge exchange ions produced per unit time in the volume (A Δ L); Q is the charge exchange cross section; Δ L is an increment of length; A is the cross sectional area; n is the number of ions arriving at the volume per unit time per unit area; and n_0 is the neutral atom density. The cross sectional area of the exhaust plume at the engine is $\pi D^2/4$ where D is the engine exhaust diameter. Taking Δ L in Eq. (2) to be unity and considering only the central portion of the beam ($\theta = 0$ in Eq. (1)) gives the number of charge exchange ions produced per unit length (See Appendix I)

$$N(r) = \frac{\pi Q D^2 n n_0'}{\left(4\left[16\frac{r^4}{D^4} + 8\frac{r^2}{D^2} + 1\right]^{1/2}\right)} \tag{3}$$

where n_0' is the neutral atom density at the exhaust plane

$$n_0' = \mu_0' (\pi m/8 k T)^{1/2} \tag{4}$$

where μ_0' is the rate per unit area at which neutral atoms leave the engine exhaust plane. Experiments (Ref. 14) have shown the electric field in ion exhaust beams to be primarily radial. Therefore, the charge exchange ions will move radially. The arrival rate per unit area at a distance x perpendicular to the exhaust plume centerline is

$$N(r, x) = N(r)/2\pi x \tag{5}$$

Hence

$$N(r, x) = \frac{Q D^2 n \mu_0' (\pi m/8 k T)^{1/2}}{8x\left[16\left(\frac{r}{D}\right)^4 + 8\left(\frac{r}{D}\right)^2 + 1\right]^{1/2}} \tag{6}$$

2.1.4. Group 2 Ions. Preliminary estimates can be based upon behavior of an equivalent thruster. Staggs (Ref. 15) presents the following scaling relations for electron bombardment thrusters:*

Propellant Change

$$\frac{N_1}{N_2} = \frac{Q_1}{Q_2}\left(\frac{m_2}{m_1}\right)^{1/2} \tag{7}$$

Temperature

$$\frac{N_1}{N_2} = \sqrt{\frac{T_2}{T_1}} \tag{8}$$

Accelerator Voltage

$$\frac{N_1}{N_2} = \left(\frac{E_1}{E_2}\right)^3 \tag{9}$$

*These relationships are derived in Appendix I.

Propellant Utilization Efficiency

$$\frac{N_1}{N_2} = \frac{1 - \eta_1}{\eta_1} \frac{\eta_2}{1 - \eta_2} \tag{10}$$

where m is the propellant mass, T the temperature; E the accelerator voltage; and η the efficiency.

Another approach, based upon somewhat different data, is to ratio Eq. (2)*

$$N_1 / N_2 = (Q\,An'\,n_0')_1 / (Q\,An'\,n_0')_2 \tag{11}$$

where the ΔL's are taken as the same for each thruster. The efficiency is given by

$$\eta = n'/(n' + \mu_0') \tag{12}$$

Next note that the current is

$$J = n'\,A \tag{13}$$

Combining Eqs. (4) and (11) through (13) yields

$$\frac{N_1}{N_2} = \frac{\eta_1\,(1 - \eta)_1\,(m_1\,T_2)^{1/2}\,(J_1)^2\,A_2\,Q_1}{\eta_2\,(1 - \eta)_2\,(m_2\,T_1)^{1/2}\,(J_2)^2\,A_1\,Q_2} \tag{14}$$

2.1.5 Typical Characteristics. The Group 1 primary ion beam principally is contained within a 15 to 20° semi-angle (Refs. 13, 14, 16, 17). The propellant utilization efficiency is 80 to 90% for mercury E. B. thrusters, (Refs. 13, 15, 18, 19, 20, 21, 22) about 99% for cesium contact engines, (Refs. 13, 23, 24) and about 80 to 93% for cesium E. B. thrusters (Ref. 25). The neutral efflux normally is assumed to correspond to a thermal velocity of about 1400°K for the cesium contact thruster and in the vicinity of 500°K for the E.B. thrusters. Recent information indicates that neutral atom temperatures for the latter may be in the vicinity of 1000°K (Ref. 26). If this preliminary information is correct, the neutral atom velocities are higher than commonly assumed, and neutral density therefore is lower. (Our calculations have been based on the older 500°K values.)

Typical primary velocities are about 30000 m/sec and current densities of E. B. thrusters range from about one to four m a/cm^2. Short life Cs contact thruster densities are about 10 to 20 m a/cm^2 (at the exit plane) (Ref. 13).

2.1.6 Contaminants. Most studies neglect the effect of material other than propellant in the exhaust plume. This may, in some instances, not be correct. For example, Hall (Ref. 13) points out that mercury E. B. engines typically produce a molybdenum flux of about 2×10^{14} atoms/cm^2 sec due to electrode sputtering. Richley (Ref. 27), in a preliminary document, reports on experiments and calculations showing that sputtered accelerator grid material was deposited on a solar cell cover plate. The cells were located well away from the primary ion beam. Staskus (Refs. 28, 29) has found similar effects with the SERT II spacecraft (molybdenum deposits with a mercury thruster). The effect probably

*Based upon a suggestion by an Associate Editor of the Journal of Spacecraft and Rockets.

does not occur or is minimal with cesium thrusters since they operate at low voltage and utilize different grid materials (Ref. 30).

2.2 Plume Effects

2.2.1 Surface Accumulation. A preliminary determination of propellant accumulation may be based upon a balance between condensation rate and evaporation rate, with the additional assumption that the surface behaves as though it were composed of pure propellant. Further, the condensation rate can be computed from the arrival rate multiplied by a condensation coefficient. The latter is the ratio between the rate at which the molecules condense on a surface and the rate at which they intersect the surface. Dushman (Ref. 31) quotes two investigators who determined the coefficient as equal to one; one for metal atoms condensing on metal surfaces and the other for high boiling point organic liquids. Hall (Ref. 13) also quotes two investigators (Refs. 32, 33) which state that metallic vapors have a unity sticking coefficient. This means the arrival rate may be treated as the condensation rate for cesium and mercury. Basic thermodynamic considerations relating the number of atoms which cross an area, pressure, and mean velocity lead immediately to a mathematical representation of the accumulation rate (See Appendix II)

$$\frac{dN}{dt} = \Gamma_a - \frac{P}{\sqrt{2\pi m k T}} \qquad (15)$$

where dN/dt is the rate of change of the number of atoms per unit area of surface, Γ_a is the atom arrival rate, P is the pressure, m the atom mass, k the Boltzmann constant, and T the temperature. It is useful to assume the accumulation rate equal to zero so that the resulting equation represents equal accumulation and evaporation rates. Then the theoretical predictions may be compared to computed arrival rates to see if propellant buildup is possible. Hall (Refs. 13, 17) has plotted this behavior to define the accumulation and non-accumulation regions as a function of temperature. We have extrapolated his mercury line and recomputed the cesium line using Nottingham's (Ref. 34) and Hatsopoulos' (Ref 35) vapor pressure data. The results are shown in Figure 2. We have terminated the plots at a rate of 10^6 since anything lower than this will be beyond concern. In effect, anything which sticks to a surface at a temperature beyond the range of the graph will remain on the surface. Conversely, anything which arrives at a rate less than this will take so long to accumulate (roughly one mono-layer per 10,000 days) that it will not be of concern.

Reynolds (Refs. 16, 20) and Hall (Refs. 13, 17) have published the results of studies of mercury thrusters upon typical spacecraft surfaces. They found that impingement rates were high enough under some conditions that condensation could be a problem. Specifically, they found perturbations in solar-panel characteristics close to the spacecraft due to the change in optical behavior. Hall warned that such metals as gold and solder could cause trouble and that insulator resistivity and electrode gaps could be degraded. Reynolds warned that even surfaces not in the line-of-sight of the initial propellant trajectories could still receive impingement through reflection or reevaporation from surfaces in the direct line-of-sight of the thruster exhaust.

We have studied this problem specifically for a radiator designed to operate at 100°K (Ref. 10). (Details are presented in Appendix III.) A schematic of the thruster-radiator orientation is shown in Figure 3. The thruster was assumed to have an un-ionized flow rate of 10^{-7} pounds per second of cesium (Ref. 36). In our geometry, the direct neutral flux upon the lower 300°K surface was 2.3×10^{12} atoms/cm^{2}sec. At this temperature, cesium does not accumulate. The re-evaporated atoms become distributed on the 200°K surfaces as well as being lost in space. No cesium arrives directly on the 100°K cold patch since it cannot "see" a 300°K surface.

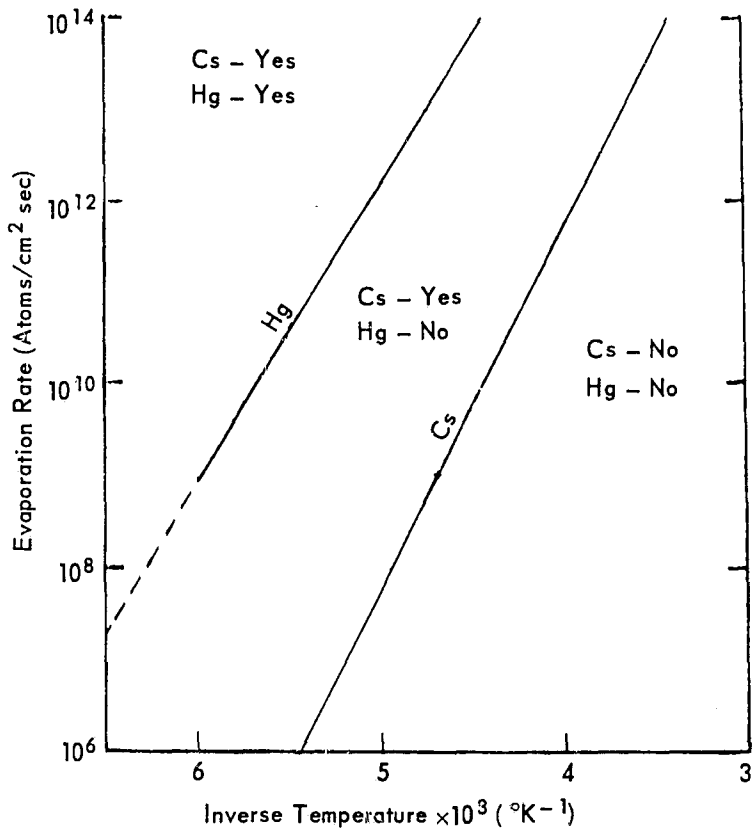

Figure 2. Evaporation Rate Behavior

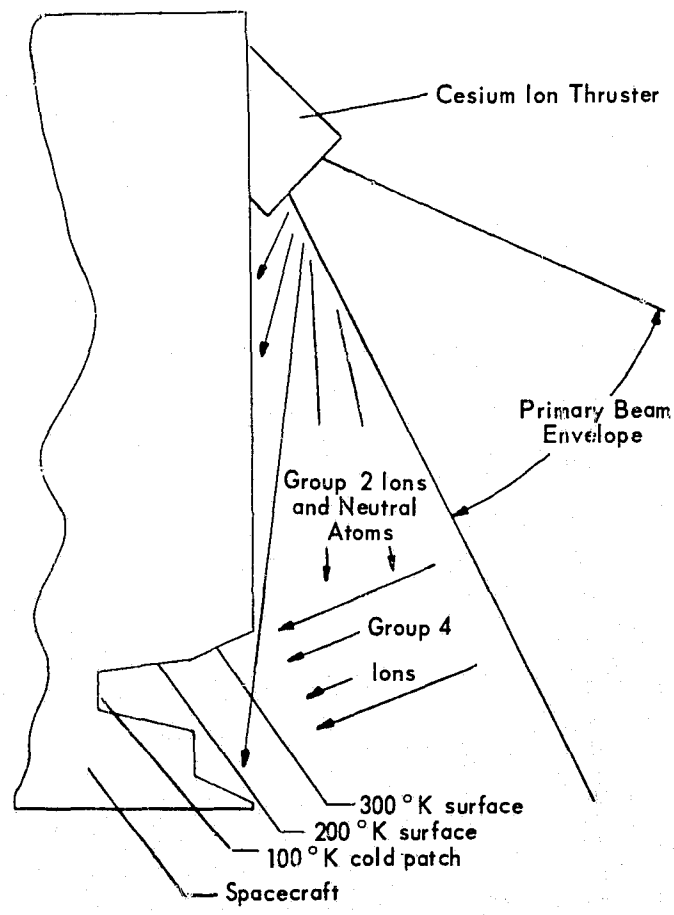

Figure 3. Approximate Spacecraft – Thruster Configuration Showing Low Temperature Radiator

The evaporation rate for a surface at 200°K is 7.1×10^7 atoms/cm^2 sec. Hence, the accumulation rate is roughly the arrival rate. One monolayer will accumulate on the upper 200°K surface in a little less than one hour and on the other 200°K surfaces in about five hours. In a few days a 200°K surface will behave as though it were composed of cesium. Since the cold patch "sees" only space and the 200°K surfaces, the evaporation rate from these surfaces determines the rate at which cesium arrives at the cold patch. (Evaporation is nil at 100°K.) The cold patch accumulation rate is about 5×10^7 atom/cm^2-sec or one monolayer each 2400 hours. The cold patch accumulation rate is not serious for radiator lifetimes of a few thousand hours. A preliminary check of the 200°K wall accumulation effect shows the relative emissivity and absorptivity of cesium and of aluminum to be similar. As a rough guess, cesium accumulation within the radiator is not serious. We did not investigate the specular behavior of uncoated and coated aluminum, and this could introduce trouble. A better approach would be to eliminate the neutral cesium completely. This can easily be done with the studied geometry by either recessing the thruster, providing a small shield, or extending the radiator beyond the plane of the thruster exhaust. All three approaches block the direct view of the thruster exhaust opening from the radiator, thus eliminating a direct path.

Since there are no indirect paths other than interaction of the exhaust beam with the environment (an area which should be investigated), one might presume that with the modified configuration cesium would not be a problem. Normally, this is a good assumption; but in this case it is not (Ref. 37). Figure 3 clearly indicates that the Group 4 ions have a direct path to the cold patch. The ion flux can be computed from Eq. (6), (See Appendix I), which gives the behavior indicated in Figure 4 for the assumed thruster characteristics. The resulting Group 4 flux at the cold patch is about 2.2×10^{10} ions/cm^2 sec which corresponds to about one monolayer in five hours. One hundred monolayers will accumulate in roughly 20 days, causing a fatal deterioration in radiator characteristics. Clearly, this cannot be tolerated.

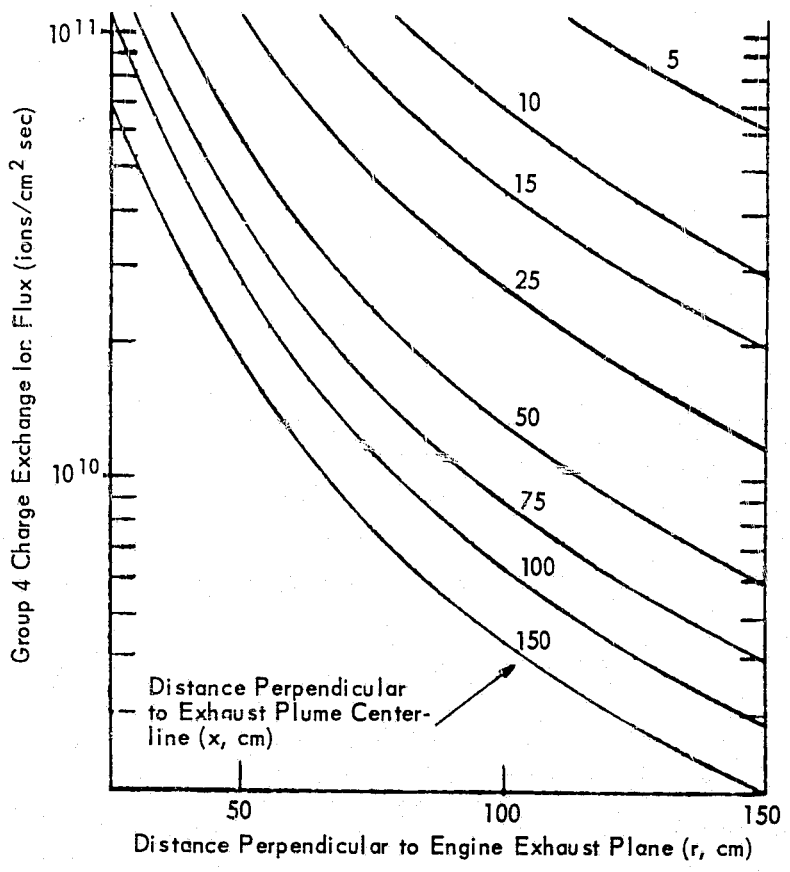

Figure 4. Group 4 Ion Flux

Staggs (Ref. 15) indicated the energy of the Group 4 ions was less than roughly 50 volts. Sellen (Ref. 14) indicated that the potential across the beam was 7 to 8 volts and beam potentials relative to the ion source are less than 10 volts. Consequently, if the spacecraft is biased positively with respect to the beam to the order of 20 to 50 volts, the Group 4 ions will not have sufficient energy to reach the spacecraft. Such biasing may be accomplished by biasing the thruster neutralizer. This will eliminate the Group 4 problem.

2.2.2 Plume Sunlight and Absorption Behavior. Since an ion thruster ejects mass in the vicinity of a spacecraft, there may be concern that observations of faint light sources could be seriously perturbed. We have investigated this effect in studying interaction of a cesium thruster with a Polaris star tracker. Surprisingly (because of the tenuous nature of the thruster exhaust), there may be a problem. The preliminary analysis, presented in Appendices IV-VI, shows that sufficient sunlight may be scattered by the exhaust plume that the tracker would be affected. If this occurs with cesium, it also may occur with mercury (which we have not investigated).

For purposes of the study, the Polaris star tracker sensor was assumed to follow the spectral response curve shown in Figure 5 (Ref. 39). The principal series for cesium is shown in Table 1 (Ref. 40). With the exception of the first two lines, there are a number of lines which correspond to the sensor response range. (This is only a summary table. The sharp, diffuse, and fundamental series also have lines within the sensor response range. Further, Moore (Ref. 41) lists 73 transitions involving the ground state (See Appendix V). For the time being, we will work only with the sharpest lines of the principal series.) The first line for cesium II (singly ionized cesium) occurs at 930 Å (Ref. 41). This indicates that cesium ions are transparent to photon energy in the range of interest. Therefore, the analysis may be limited to neutral cesium atoms.

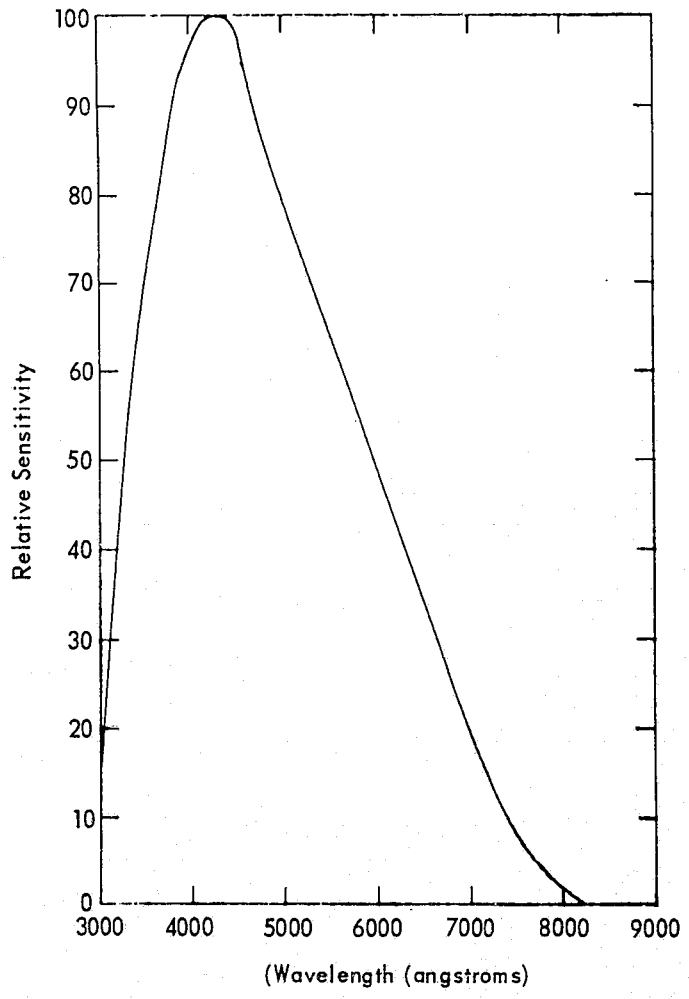

Figure 5. Spectral Response Curve S-20

Table 1
The Principal Series of Cs (Ref. 40)

Wavelength (Angstrom)	Energy level, ev from Ground State
8943.46	1.386
8521.12	1.455
4593.16	2.699
4555.26	2.721
3888.65	3.188
3876.39	3.198
3617.41	3.427
3611.52	3.433
3480.13	3.562
3476.88	3.566
3184.2	3.893

The radiative decay coefficients indicate that excited state lifetimes are in the microsecond range (Ref. 42). Therefore, we assumed all atoms would be in the ground state and the analysis could be simplified since the various excited levels could be neglected (for the preliminary treatment). Consistent with this assumption is the assumption that if a ground state atom absorbs a photon and becomes excited, it will immediately decay, re-emitting one or more photons. We assumed it would decay to the ground state, thus re-emitting a photon of the same length that it absorbed. This assumption is open to considerable question and will introduce error into the analysis. Finally we assumed an optically thin gas. This means sunlight intensity within the plume is a constant and any photons emitted by excited atoms will not be absorbed. (The assumption is not good adjacent to the exhaust opening; but becomes acceptable a meter or two away.)

If atoms of level n' are exposed to photons of frequency ν (nn') at an intensity I_ν(nn'), the number of upward transitions per unit volume per unit time is (Ref. 43)

$$N'_\nu = N_{n'} I_{\nu(nn')} B_{n'n} \tag{16}$$

where $N_{n'}$ is the number of n' level atoms per unit volume and $B_{n'n}$ is an absorption coefficient. This is related to the Einstein coefficient of spontaneous emission, $A_{nn'}$, by

$$\frac{\tilde{\omega}_n}{\tilde{\omega}_{n'}} A_{nn'} = B_{n'n} \frac{2h\nu^3}{c^2} \tag{17}$$

Here $\tilde{\omega}_n$ is the statistical weight of level n, h the Planck constant, ν the frequency, and c the speed of light. If the inner quantum number is J,

$$\tilde{\omega}_n = 2J + 1 \tag{18}$$

One may show that the Einstein A value is related to the f value by

$$A_{nn'} = \frac{8\pi^2 e^2 \nu^2}{mc^3} \frac{\tilde{\omega}_{n'}}{\tilde{\omega}_n} f_{nn'} \tag{19}$$

where e is the electron charge and m its mass. Combining this and noting the basic relation between frequency and wavelength, λ , gives

$$N'_{\nu} = N'_{n} I_{\nu\,(nn')} \frac{4\pi^2 e^2 \lambda}{hmc^2} f_{nn'} \tag{20}$$

This equation, coupled with the geometric considerations, makes it possible to compute plume absorption effects since f values are available in the literature (References 44 and 45 data are reproduced in Appendix V). Since we have assumed immediate decay from excited states, it also provides re-emission rates.

In actuality, Eq. (20) is a distribution function. To obtain true numbers we must consider wavelengths between λ and $\lambda + \Delta\lambda$. This is most easily done by introducing the line width, defined as the range of wavelengths over which a photon will interact in the vicinity of a line. This has been the topic of many investigators (Refs. 46-49). One of the simplest equations is Richtmyer's (Ref. 47)

$$\Delta = \lambda^2 / 2\pi c \tau \tag{21}$$

where τ is the mean life of the level and the transition involves the ground state. Since $\tau = 1/A_{nn'}$, immediately

$$\Delta = \frac{4\pi e^2}{mc^2} \frac{2j' + 1}{2j + 1} f_{nn'} \tag{22}$$

To complete the treatment, we consider the geometry of the spacecraft shown in Figure 6. The geometrical relationships for the spacecraft, the thruster exhaust plume, and Polaris tracker are illustrated in Figure 7 (see also Appendix IV). The neutral atom distribution is known from Eq. (1). Therefore, if we "look" outward from the center of the Polaris tracker opening we can, with the known geometry, compute the atom density along the line of sight. Immediately, the probability of photon absorption from the sun's light may be computed for any incremental volume along the line of sight. This absorption creates an excited state atom, which then (according to our assumption) immediately decays. If the re-emitted photon has equal probability of being emitted in any direction, the number of photons scattered into the tracker instantaneous field of view may be calculated from the known scattering position and the instantaneous field of view geometry. There results, as shown in Appendix VI

$$I = \int_{y'=0}^{\infty} \int_{x'=\tan\alpha'_1}^{y'\tan\alpha'_2} \int_{z'=y'\tan\beta'_1}^{y'\tan\beta'_2} \frac{A_{\ell}\, y'\, P_a\, I_0\, dx'\, dy'\, dz'}{4\pi (x'^2 + y'^2 + z'^2)^{3/2}} \tag{23}$$

where I is the intensity of the scattered photons which enter the tracker lens within the field of view, y' is the northerly direction determined from the tracker lens, α and β describe the range of the instantaneous field of view, A_{ℓ} is the lens area, P_a is the probability of absorption (as a function of position), and I_0 is the sunlight intensity at the wavelength of interest. The probability of absorption can be determined from Eqs. (20 and 22) with consideration to the geometry and resulting atom density. Using the solar flux data of Figure 8 (Ref. 50), we can compute the energy entering the tracker for each of the principal series lines. Finally, taking into account the relative response of the sensor, neglecting the effect of the lens system (which introduces a small error), (Figure 5) and adding the response for each of the lines, we obtain the total response of the sensor to the scattered sunlight. The same response curve can be combined with the

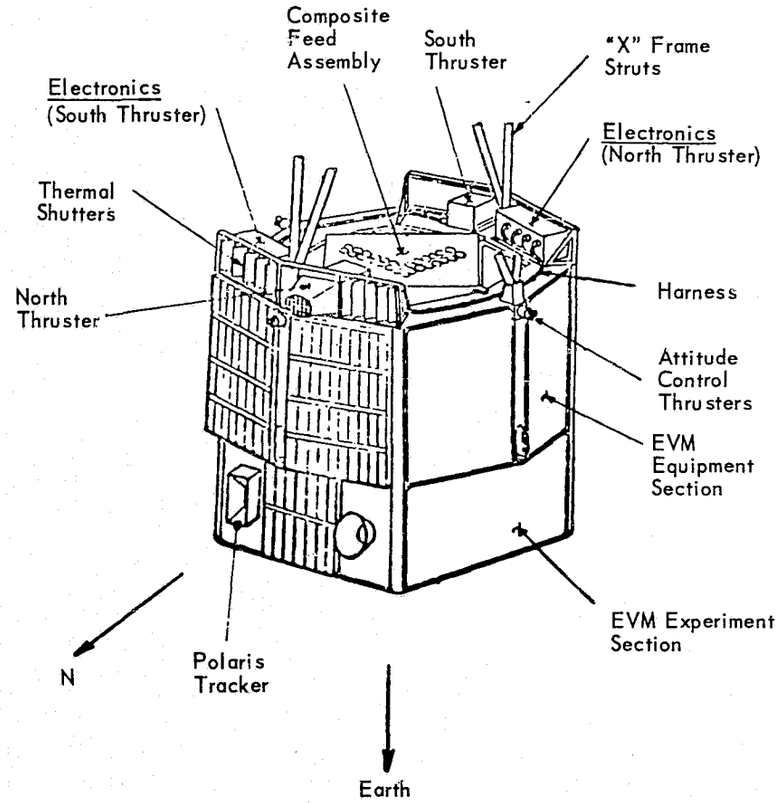

Figure 6. Assumed ATS-F and -G Configuration

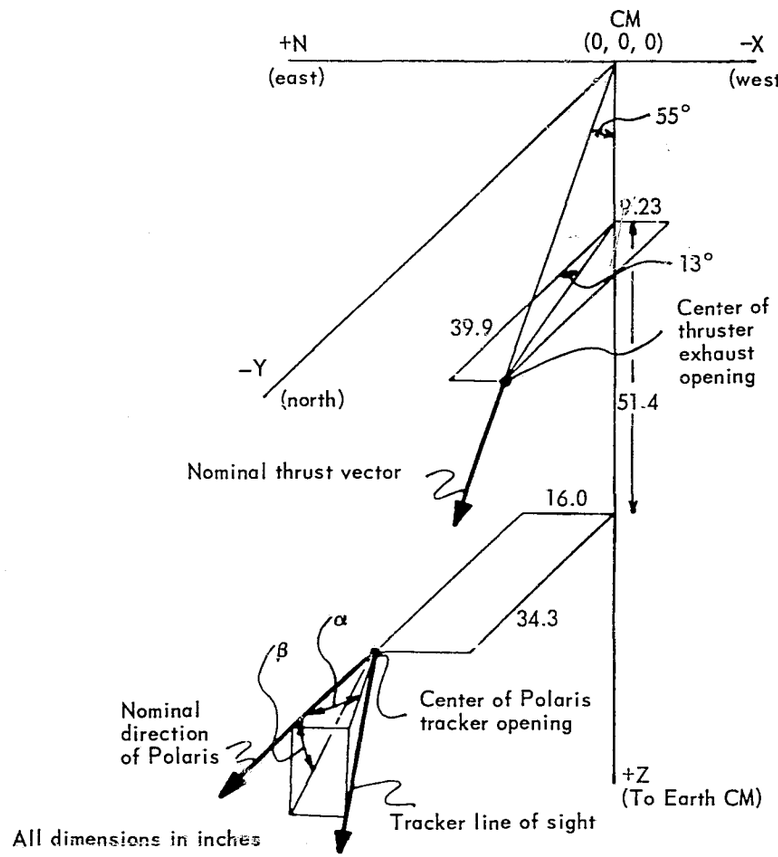

Figure 7. Tracker – Thruster Geometry

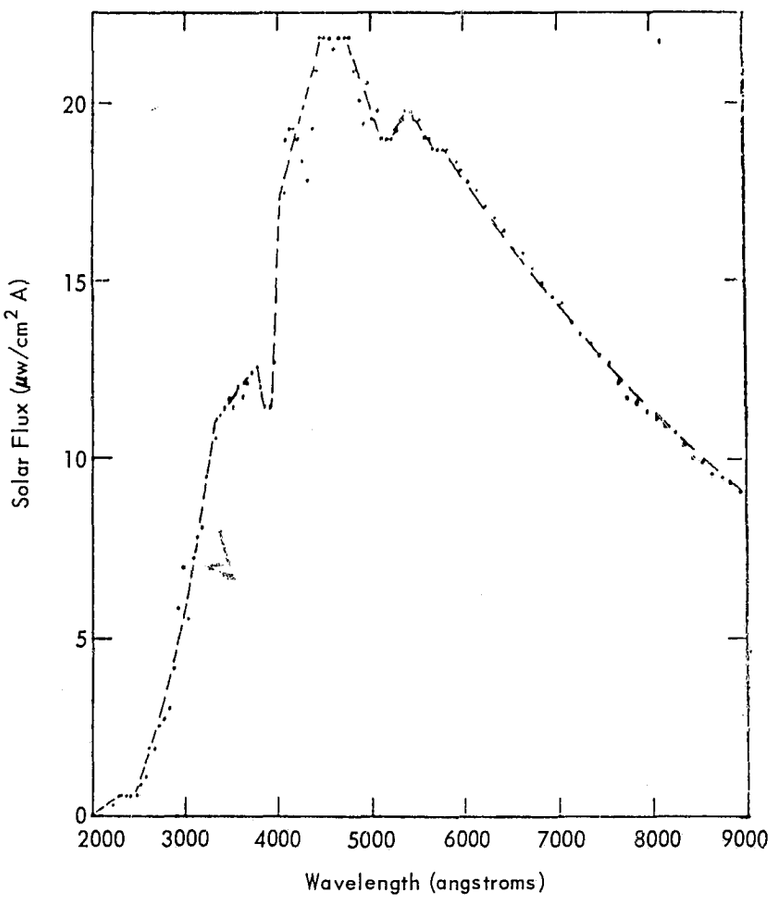

Figure 8. Solar Spectral Irradiance

Polaris spectral energy data presented in Figure 9 (Ref. 51) to obtain the relative tracker response to Polaris. There results the behavior shown in Table 2. Immediately, we see the energy reflected from the plume to be larger than the energy received from Polaris. The preliminary analysis indicates that a problem may exist. Also note the line widths. These are so small that the amount of Polaris energy absorbed by the plume will be completely negligible in comparison to the total.

We conclude that plume absorption of starlight is no problem, but plume scattering of sunlight into the star tracker field of view may be a problem.

2.2.3 Contaminant Effects. The major contaminant effect appears to be due to materials from the engine rather than any contaminant originally contained within the propellant. Staskus (Refs. 28, 29) has reported on the SERT II spacecraft experience. In this spacecraft, solar cells were located 60° from the beam centerline at a distance of 30° from the exhaust opening. Cells maintained at 55 to 60°C showed only molybdenum deposits. Those at -40°C gave similar indications. However, the molybdenum accumulation was so rapid it may have completely covered up mercury accumulation. In about 8 to 12 hours of thruster operation, the solar cell output had dropped 50%. Within 2 days, the telemetry was almost off scale in the zero voltage direction.

Richley (Ref. 27) has reported similar contaminant experience in the laboratory and has treated the problem analytically. He points out that the contaminant will readily adsorb and not re-evaporate, which, of course, compounds the problem. He reported a 50% degradation in cell output in 12 hours with cells in the range of 0 to 25°C where no mercury accumulation was expected. He estimated the coating thickness at 10 to 30 monolayers

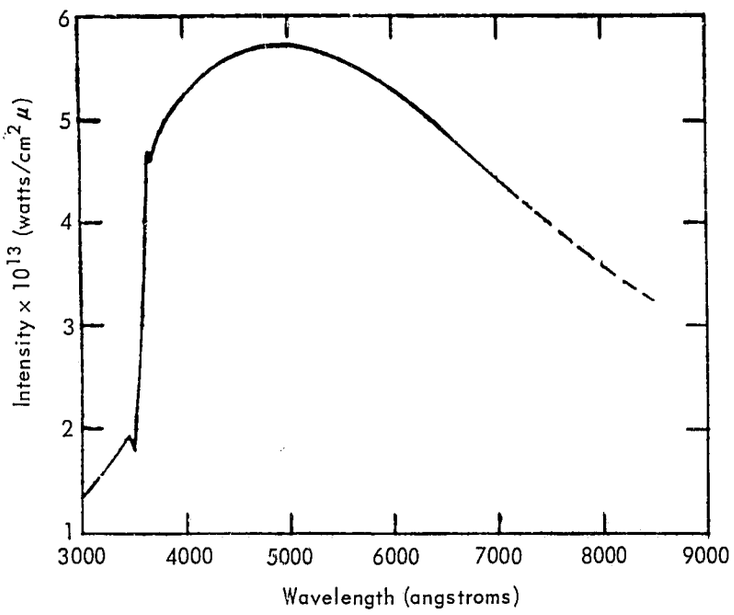

Figure 9. Polaris Spectral Energy Distribution.

Table 2
Polaris Tracker – Cs Thruster Interaction Results

Cs Atom Level	λ, cm	f	Line Width, cm	Sensor Relative Response
6 $P_{1/2}$	0.8943	0.394	1.400×10^{-12}	0
6 $P_{3/2}$	0.8521	0.814	1.445×10^{-12}	0
7 $P_{1/2}$	0.4593	0.284×10^{-2}	1.009×10^{-14}	2.75×10^{-6}
7 $P_{3/2}$	0.4555	0.174×10^{-1}	3.09×10^{-14}	1.60×10^{-5}
8 $P_{1/2}$	0.3888	0.317×10^{-3}	1.127×10^{-15}	1.09×10^{-7}
8 $P_{3/2}$	0.3876	0.349×10^{-2}	6.20×10^{-15}	1.19×10^{-6}
9 $P_{1/2}$	0.3618	0.725×10^{-4}	2.58×10^{-16}	1.92×10^{-8}
9 $P_{3/2}$	0.3612	0.125×10^{-2}	2.22×10^{-15}	3.15×10^{-7}
10 $P_{1/2}$	0.3481	0.289×10^{-4}	1.027×10^{-16}	5.96×10^{-9}
10 $P_{3/2}$	0.3478	0.620×10^{-3}	1.101×10^{-15}	1.28×10^{-7}
11 $P_{1/2}$	0.3401	0.124×10^{-4}	4.40×10^{-17}	2.19×10^{-9}
11 $P_{3/2}$	0.3399	0.356×10^{-3}	6.32×10^{-16}	6.25×10^{-8}
12 $P_{1/2}$	0.3350	0.620×10^{-5}	2.20×10^{-17}	9.74×10^{-9}
12 $P_{3/2}$	0.3348	0.208×10^{-3}	3.70×10^{-16}	3.26×10^{-8}
			Total	2.01×10^{-5}

Note: Polaris energy gives a relative response of 1.31×10^{-5}

and, from a spectrographic analysis, qualitatively identified iron, chromium, nickel, silicon, molybdenum, copper, tin, lead, and traces of potassium and zinc; all materials which he stated to be identifiable with thruster components (for example, a stainless steel accelerator grid).

Clearly, contamination may be serious for some thruster-spacecraft component situations.

2.2.4 Erosion Effects. Erosion effects have been the subject of several experiments (see, for example, Ref. 52). The strong effect of the primary beam has long been known. However, the effects of Group 2 ions normally are neglected. This may be a mistake.

Hall (Ref. 13) gives the erosion rate equation

$$\frac{dx}{dt} = -\frac{\Gamma S}{n} \tag{24}$$

where dx/dt is the rate of change of target thickness with respect to time, Γ is the bombarding ion flux density, S is the sputtering yield, target atoms/ion, and n the target number density, atoms/cm^3. Daley's (Ref. 53) data show that the sputtering yield is about one atom per incident cesium ion for an energy of 600 electron volts. For a primary flux at the engine exhaust of 1.816×10^{16} ions/cm^2 sec, an erosion rate of 3×10^{-7} cm/sec (one cm/thousand hours) results due to the primary beam.

A very preliminary estimate of the Group 2 effect for a cesium thruster may be obtained by ratioing from Staggs (Ref. 15) mercury thruster data. The following are applicable

Item	Hg	Cs
η	0.80	0.80
T, °K	500	533
J, ions/sec	1.54×10^{18}	8.28×10^{17}
Q, cm^2 (Refs. 54-57)	6×10^{-15}	2.43×10^{-14}
Molecular Weight	201	132.9
Exhaust diameter, cm	15	7.62

Equation (14) immediately gives*

$$N_{Cs} = 3.5\, N_{Hg} \tag{25}$$

The point where the engine is closest to the spacecraft represents a separation distance of 13.3 cm at a 90-degree angle with the exhaust plume. Reference 15 shows the same Group 2 flux as at a 52-degree angle. Taking this value (the real value will approach zero at 90 degrees), we obtain a Group 2 cesium ion flux of about 10^{12} ions/cm^2-sec. If we further assume the same erosion rate as caused by Group 1 ions, the Group 2 ions erode about 4×10^{-5} cm/1000 hrs. This is a very small amount and should not be a problem for a solid surface, but may be significant for a surface such as aluminized Mylar. A more detailed investigation would be indicated if such a surface were located close to the thruster.

*See end of Section III.4 for an error discussion. The possible error appears high.

2.2.5 Other Effects. Hunter (Ref. 58) reported no detectable EMI on the ATS-IV satellite. An experiment on the SERT II is designed to study the RFI problem.

Hall (Ref. 13) points out that H-film and Teflon FEP are affected by cesium. He also identifies potential problems with gold and soft solder with both cesium and mercury. Thermal control surfaces also may be susceptable. Finally, Hall points out that insulator resistivity and electrode gaps may be degraded by exposure to propellants.

3. TEFLON THRUSTERS

3.1 Background

A Number of Teflon thrusters have been studied in the past several years and four are in use on the LES-6 satellite (Ref. 59). (Guman (Ref. 60) reported in 1968 that more than one hundred different thrusters had been placed on test.) Despite this experience, we found no studies of the effects of Teflon thruster exhaust upon spacecraft. Further, upon initiating such a study we found that behavior of the exhaust from a Teflon thruster is not understood. Nevertheless, sufficient experimental "feel" exists that postulated characteristics may be obtained.

Two basic types of "Teflon" thrusters have been reported. One utilizes solid Teflon (Refs. 59-63) and the other a so called liquid Teflon (Ref. 54). The latter is a perfluorocarbon wax consisting of a polymer built up from a basic 2C-3F-Cl structure (Ref. 65). The exhaust from the two appears similar, but outgassing can be expected from the wax-like polymer because of its higher vapor pressure.* Our study (Ref. 11) concentrated on the solid Teflon propellant.

Teflon thruster principles appear straightforward although the details are not understood. Operation is initiated by charging a storage capacitor to its operating voltage. This voltage is impressed across an interelectrode spacing located adjacent to the surface of the end of a Teflon fuel rod. An igniter plug is fired, which initiates a micro-discharge in the interelectrode spacing. Apparently, a small portion of Teflon is depolymerized and promptly vaporized. A portion of this ablated portion is ionized and accelerated within the interelectrode gap due to the voltage difference impressed by the capacitor. This causes further depolymerization and ionization until a micro-discharge results which closes the circuit and allows the capacitor to discharge. The main discharge depolymerizes a surface layer of Teflon which is ionized and ejected through the thruster nozzle by the electrical effects. Virtually all of the thrust comes from the ions. Only a small portion is associated with the neutral components. Efficiency is relatively low since only a small fraction of the effluent is ionized.

Experimental measurement shows that the entire process requires only a few microseconds (Ref. 59). The ionized constituents are ejected at about 35,000 m/sec and the neutral effluent comes off at roughly 3,000 m/sec (Ref. 61).

Four Teflon thrusters have been in operation on the LES-6 satellite since October 15, 1968 (Ref. 59). There has been no recognizable interference with the telemetry communications or solar panels on the satellite after roughly 18 months of operation (Ref. 66). These thrusters are located so that the nozzle protrudes slightly from the curved surface of a cylindrical spacecraft. There are no objects which can see the opening of the exhaust nozzle (Ref. 59).

*The oil has a 5 μ vapor pressure at 140°F. The waxes have vapor pressures in the 1/10 to 1/100 μ range (Ref. 65). A mixture of oils and waxes that has been outgassed to remove lighter elements may have a lower vapor pressure.

3.2 Plume Characteristics

3.2.1 Plume Observations. Limited observations of the exhaust plume have been performed with a calibrated RCA-1-P42 phototube (Ref. 59). This tube, positioned to look directly along the thrust axis into the thruster nozzle, showed a peak light intensity at 1.45μ sec after discharge initiation. Light was observed for 10μ sec. With the detector at right angles to the plume centerline, a signal could not be obtained for distances of more than 4 or 5 inches downstream of the exhaust opening. Guman (Ref. 66) suspects, because of this and other observations, that most chemical and ionic reactions and recombinations occur very close to the thruster.

Spectroscopic analyses of LES-6 type thruster exhaust plumes have shown neutral carbon and fluorine atoms as well as singly, doubly, and triply ionized atoms of these species (Ref. 67). Iron also has been identified, probably originating from the stainless steel electrodes or the spark plugs. The amounts are small since erosion has not been a problem. Unidentified molecular species also were observed. (The data were obtained at a position close to the exhaust opening (Ref. 68).) Since a highly reactive environment exists at the exhaust opening, but there is no evidence of chemical reaction several feet away (see below and Appendix VII) we probably can conclude the reactive species recombine within a few inches of the exhaust opening and few or no reactions occur within the exhaust further out. (Observations of the charge distribution present further confirmation.)

3.2.2 Charge Observations. Vondra (Ref. 67) has provided preliminary data that show the ion distribution is Gaussian with a 1/e value at ±13°. On a spherical surface located a constant distance from the Teflon face, 90% of the charge is contained within an included cone angle of 36° (18° half angle). If the total charge collected is integrated over the entire plume, we find that 9 to 10% of the exhaust is ionized. The remainder in neutral (Ref. 67).

From roughly 10 cm out, the charge behaves as an inverse distance squared relationship. This indicates no recombinations. Charge still behaves in this manner at a 20 to 30 inch distance (Ref. 68). Deviations occur closer than 10 centimeters, indicating that recombination processes are occurring. Vondra has plotted voltage data from 10 centimeters to about 80 centimeters on a log plot (Ref. 61). These data follow a straight line which behaves with the cube of distance, behavior which should occur if no recombinations take place.

3.2.3 Deposit Observations. Virtually every extended test of a Teflon thruster has resulted in observable deposit formation. Mirrors located in the beam become coated with a translucent deposit, the end of vacuum chambers used for engine testing become coated, and deposits are observed in bell jars. No chemical reactions with surfaces or erosion have been found (Refs. 66, 69-74). An object in the beam will shade any region downstream (Refs. 60, 71). A slight diffraction pattern also is evident. The coating changes color and some of the deposit will flake off a mirror when it is left in air for a half hour. Apparently a reaction is taking place which complicates deposit analysis. Analysis of deposits indicates material which could have come from Teflon, as well as showing various constituents which could have come from diffusion pump oil or other test chamber materials (Refs. 73, 75-77).

Material distribution within the plume is basically unknown (Ref. 70). The maximum turning angle probably is less than 90°. Vondra (Ref. 72) feels the total included angle for most of the materials is 20°. LaRocca estimates that 98-99% of all condensable material is within a 15° semi-angle. (He cautions that this is very approximate.) (Ref. 71). Apparently, any object placed close to the beam centerline will become coated with a Teflon-like polymer material with incorporated contaminants if any are in the vicinity of the exhaust beam.

3.2.4 Theoretical Understanding. Since we know little of the composition and distribution, theoretical understanding of beam characteristics is poor to nil. Charge distribution and characteristics have been estimated and we can postulate condensable behavior from test experience. Deposit analysis indicates a repolymerization reaction. We may use Teflons known characteristics to postulate what is taking place. (See Refs. 78-82). Apparently, the reaction is one of depolymerization of the Teflon followed by partial decomposition of the monomer with partial ionization. The radicals, atoms, and ions then recombine within a few inches of the exhaust opening. Whether the monomer recombines significantly prior to leaving the vicinity of the thruster has not been investigated. We do know that surfaces will serve as a catalyst. Probably, some monomer remains uncombined after the beam has become frozen (in a rarified atmosphere).

Teflon impurities should not cause a problem. Virgin Teflon is extremely pure and for practical purposes the quantity of impurities cannot be determined. (It is beyond the sensitivity range of most tests (Ref. 83)). However, scrap Teflon commonly is saved for reuse. This, despite all precautions, becomes contaminated. Only virgin Teflon should be used for this application.

3.3 Spacecraft Effects

Most of the neutral and charged material is concentrated within a 20° semi-angle of the beam centerline. The beam is highly reactive close to the thruster exhaust nozzle and appears to become less so as one increases distance. Consequently, anything placed very close to the exhaust nozzle and close to the centerline will react strongly. Anything placed in the vicinity of the beam further out will become coated. Probably, a cone of about 40 or 50° semi-angle should be used as an exclusion zone for spacecraft components. It would be desirable to avoid a cone of 90° semi-angle. Further, anything placed within the recommended exclusion zone could bounce material back to other spacecraft components. These "bounces" probably would be specular or semi-specular since anything that stuck long enough to give diffuse behavior probably would remain on the surface.

There is a visible light plume which extends outward a few centimeters from the Teflon surface and has a lifetime of only microseconds per pulse. Any light sensor which saw this plume could be temporarily disturbed. The material in the plume probably would provide sufficient absorption that sensitive instruments such as star trackers would be perturbed, as we found for the cesium ion thruster. Tests have been conducted to determine RFI behavior (Ref. 59). These included bell jar tests, as well as pre-launch tests with the LES-6 flight system. No problems were found, although there were indications that changing the thruster exhaust cone would change the amount of interference. No problems have been found with the LES-6 flight.

A preliminary analysis for indirect effects which could return exhaust to the spacecraft uncovered no problems. Apparently, the ions leave the thruster prior to appearance of neutrals external to the thruster. This eliminates charge exchange as a potential return mechanism. (Were the process reversed, there might be a serious problem.) Similarly, elastic collisions between the two species (ions and low speed neutrals) appear to be eliminated. The overall beam appears to be neutral, and generation of a net charge would appear not to be a problem. The ionic and electron velocities emitted from the thruster exhaust may be different, but since the process requires only a few microseconds, the charge effect, if any, would be short lived. There remains the possibility of collisions between exhaust and environment atoms or molecules. This would appear to be slight, but was not investigated. For most spacecraft experiments, it should be no problem. Experiments which depend upon an exceedingly clean environment, such as radiators which are to operate at cryogenic temperatures, may experience a long term change by such an effect.

4. HYDRAZINE THRUSTERS

4.1 Operation Principles

4.1.1 Thruster. In principle, hydrazine thruster operation is straightforward. Cold hydrazine, under pressure, is forced through an injector within the thruster into a catalyst bed. The hydrazine decomposes in the bed and is ejected to space through a nozzle. The catalyst normally is an alumina vehicle containing iridium (the active ingredient).

4.1.2 Chemical Reaction. Hydrazine injected into a cold catalyst bed (70°F) begins to decompose in 10 to 100 msec. The reaction is exothermic, causing rapid bed heating with increasing decomposition rate. Initially, the effluent may contain a small portion of hydrazine but after 0.1 sec no further hydrazine appears. The principle decomposition products are ammonia and nitrogen. A portion of these products undergo a endothermic reaction to form nitrogen and hydrogen. Once the three constituents leave the catalytic bed, the composition is chemically frozen.

Hydrazine decomposition has been studied by many investigators (Refs. 84-95). The basic reaction is

$$N_2 H_4 \longrightarrow 4/3\ (1 - x)\ N H_3 + 1/3\ (1 + 2x)\ N_2 + 2x\ H_2$$

where x = fraction of originally formed ammonia that is dissociated. Typically, the temperature at the exit of the catalytic bed is less than 1800°F (Ref. 85). Price (Ref. 92) has found the decomposition reaction to be transport process controlled with the following ammonia reaction rate limited. Consequently, the exhaust composition and temperature can be controlled by varying catalytic bed length and reactant residence time.

4.1.3 Exhaust Composition. Kesten (Refs. 93-95) has determined reactant concentrations as a function of position within the catalyst bed. Typically, in the steady state the exhaust will be composed of about 10-20% ammonia, 30% nitrogen, and 50-60% hydrogen (on a mole basis). The hydrazine has decomposed within the first 5 to 10% of the bed length. In a transient, the initial exhaust composition might be 40 to 50% ammonia and then, as steady state is approached, it approaches the lower value. The hydrazine appears only as a trace in the exhaust after one tenth second, and has assumed the steady state distribution within one third second.

The exhaust will contain contaminants from the hydrazine feed and from the catalyst bed. Normally, the major contaminant in the fuel is about 0.5% water (Ref. 96). Catalyst loss rate varies widely, and rates from 0.05% to 10% per minute have been reported. Reported particle sizes have ranged between 1 and 500 microns (Refs. 85, 97, 98). This loss also will perturb the ammonia dissociation rate and quantity (Ref. 98). The catalyst also can absorb significant quantities of gases. These will outgas when exposed to a vacuum and, for practical purposes, will be exhausted the first time the thruster is operated (Ref. 99).

4.2 Exhaust Properties

4.2.1 Nitrogen. Nitrogen is inert at ordinary temperatures and has a high vapor pressure (one atmosphere at -195.8°C). This will preclude condensation on spacecraft and its inertness should preclude chemical problems.

4.2.2 Hydrogen. Hydrogen has a vapor pressure even higher than that of nitrogen (one atmosphere at -252.5°C) and should not collect on spacecraft surfaces unless there is

a strong chemical or physical attraction. It is a strong reducing agent at elevated temperatures, but is inert at room temperature.

4.2.3 Ammonia. Ammonia is alkaline and is compatible with many organic and most inorganic materials. Most metals are no problem, and most plastics and elastomers resist attack to temperatures which approach the softening point. Boyd (Ref. 100) provides a detailed listing of compatibility data (see Appendices VIII and IX). Ammonia has a boiling point of 431.59°R and a melting point of 351.74°R (Ref. 101). Specific gravity is 0.6817. Its vapor pressure is shown in Figure 10. Most of the experimental data cover the range smaller than 6×10^{-3} $°K^{-1}$. We have only one point at a value of 0.01 (100°K) (Ref. 102) (a personal communication). We correlated the experimental data using the Clausius-Clapeyron equation (Ref. 103) with the assumptions that liquid or solid volume was small and that the ideal gas relationship could be used. The resulting equation was applied to the liquid and to the solid portion of the data. The slopes were cross-checked from the predicted behavior and the phase change heats and the resulting solid equation was extrapolated. The extrapolation agreed with the 100°K data point and no adjustments were necessary. (This might have been the way in which the data point was obtained in the first place. We have not followed it up.)

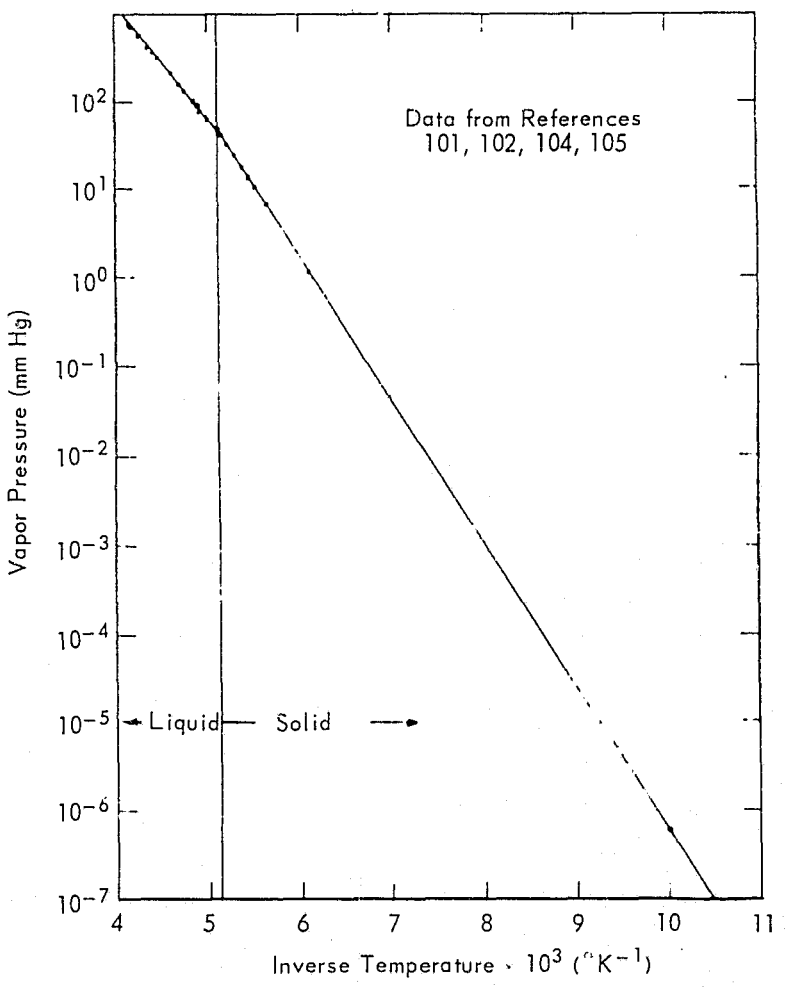

Figure 10. Ammonia Vapor Pressure

4.2.4 Hydrazine. Hydrazine is a clear oily liquid with an ammonia-like odor. It melts at 1.4°C, freezes at 0°C, and boils at 236°F (Refs. 100, 106).

Hydrazine compatibility data may be inconsistant. Some investigators report satisfactory behavior if a surface in contact with hydrazine is unaffected; others require that both the hydrazine and surface be unaffected. Most metallic materials are compatible with hydrazine, and many plastics and rubber are compatible at room temperature. (Refs. 96, 97, 100 provide additional data.)

Hydrazine normally is purchased according to military specifications (Ref. 107) but the reported impurities for propellant grade hydrazine show a better quality. Salvanski (Ref. 96) has reported 0.4-0.5% water, 0.7-0.9% ammonia plus amines, and small quantities of dissolved metals and particulate matter (mg/l).

Thin films of hydrazine absorb strongly in the 2.5 to 20 micron region. Reported transmittances range from almost 0 to about 80% in a reference sample and from 60 to 95% in a specification grade sample (Ref. 96). Little low temperature hydrazine vapor pressure data exist. We supplemented our hydrazine thruster literature study by looking at the Chemical Abstracts (1907-1969) and the Engineering Index. When we found no additional information we tried several research centers (Refs. 108-110) but found only one additional reference (Ref. 110). Good data exists for liquid hydrazine and we have estimated the vapor pressure of solid hydrazine by the same process as applied to ammonia. The data are shown in Figure 11.

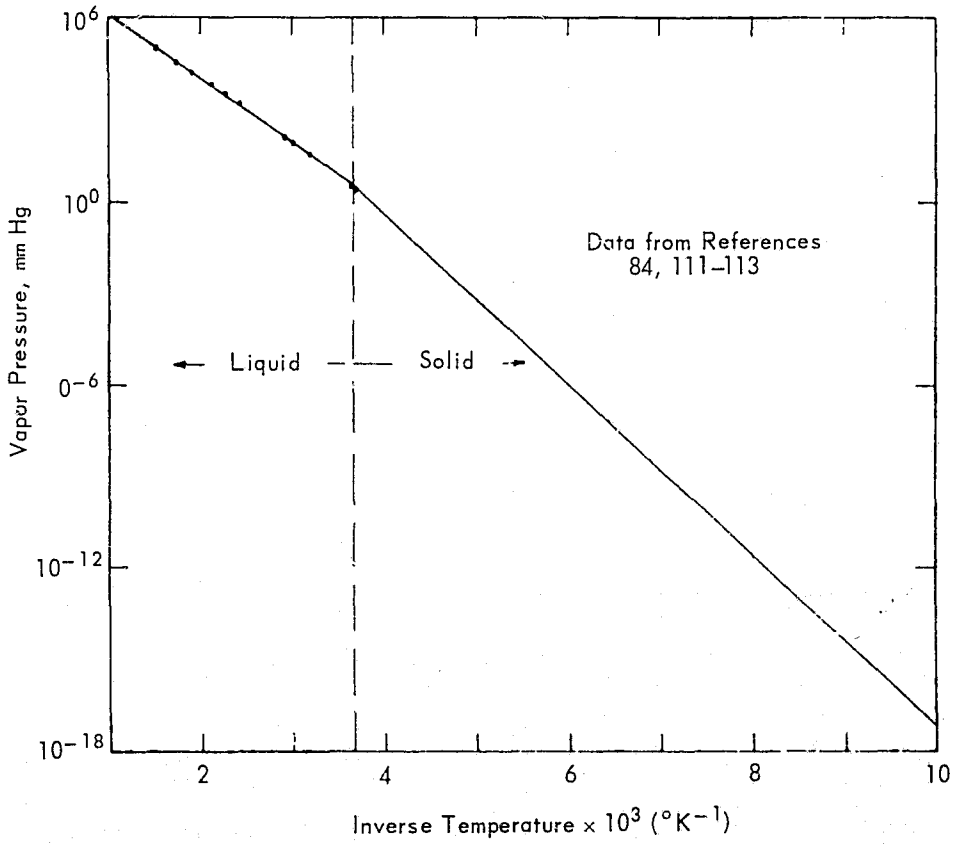

Figure 11. Hydrazine Vapor Pressure

4.3 Exhaust Effects

Plume impingement and shape calculations have been the subject of many investigations. References 114-122 are appropriate for estimating the exhaust plume. We used Refs. 115, 117, and 119. (The mathematical treatment is presented in Appendix VIII.) Typical thrusters with an exit semi-angle of 15° showed a limiting streamline angle of

91° (the Prandtl-Meyer value). Most of the exhaust from these thrusters is confined to one hemisphere. Only minor propellant fluxes will occur in the hemisphere behind the exhaust plane. The higher vapor pressures and chemical compatible data indicate that for most spacecraft surfaces, no problem will exist. Low temperature surfaces, such as 70-100°K cold patches used in instrumentation, may be susceptable. Hydrazine from a cold start-up could collect on these surfaces. Ammonia should be no problem on a 100°K surface, but could accumulate on a 70°K surface. In either event, heating the surface to 150 to 200°K would evaporate the contaminant. The only question remaining unanswered would be whether any chemical effects had occurred. Such effects should be investigated experimentally because of the extreme sensitivity of these instruments to changes in surface characteristics.

Placement of an object directly in the plume, aside from perturbing the thrust, probably would not be serious unless sensitive components could be involved. We found only one experiment for a hydrazine thruster. A 25 pound thrust engine with Shell 405 catalyst and 2 × 2 cm 10 ohm cm solar cells with 20 mil fused silica covers was tested. The cells were exposed to 200 firings of 200 msec duration each at locations five and nine feet downstream of the nozzle directly in the plume. Pre- and post-exposure electrical data showed no significant changes as a result of plume impingement. Optical examination of the cells uncovered no apparent mechanical damage. (Firings were spaced about 10 minutes apart and sample temperature increases were less than 100°K.) Scattering from the plume could affect other parts of the spacecraft. Certainly, the environmental density would be perturbed and low temperature radiators could be affected. Finally, the quantity of material exhausted from hydrazine thrusters is significantly greater than from ion thrusters. Since a star tracker perturbation appears to exist for ion thrusters, the perturbation probably would be greater for a hydrazine thruster.

5. AMMONIA THRUSTERS

5.1 Propellant Properties

Most of the properties of ammonia have been discussed in the previous section. There remains only the contamination in the original material. Flight certified ammonia contains < 33 ppm water < 2 ppm oil, and < 10 ppm salt (borax, silicon) (Ref. 102). Page (Ref. 125) reports that in the highest purity ammonia obtainable at a reasonable cost the impurities are 0.8 ppm oxygen and 0.7 ppm water. Hydrogen purity was reported as 99.9996%. Additional information is given in Appendix IX and Ref. 126. Contaminants probably will not be a problem (unless significant water is returned to low temperature radiators).

5.2 Exhaust Effects

No exhaust effects were found which would change any conclusions presented in the hydrazine thruster section. Additional studies were performed (Ref. 123) in an attempt to define other interaction effects, but none were found. (See Appendix IX.)

6. CONCLUSIONS

6.1 Study Conclusions

Few problems exist with ammonia and hydrazine thrusters. The major effects appear to be a small visibility perturbation in the plume and an effect upon environment density. (Interaction with environmental matter was not considered.) An ammonia thruster will perturb operation of a cold patch designed to maintain 70°K; 100°K should be no problem.

Hydrazine would condense on cold patches at both temperatures if sufficient material (of the order of monolayers) could be intercepted by the patch. Either hydrazine or ammonia could be removed by warming the cold patch to about 150 or 200°K.

A Teflon thruster will coat anything placed within its exhaust plume (roughly 45° semi-angle). The coating, being of a Teflon-like nature, will have a high vaporization and decomposition temperature. For practical purposes it cannot be removed by heating. Conceivably, anything placed within the plume could scatter Teflon monomer back toward the spacecraft, and other portions could receive a coating. The coating probably would be inert so that the only change would be of an optical nature. Unless located extremely close to the thruster nozzle, no chemical reactions would be expected. Minor perturbations in optical viewing from the satellite can be expected in the vicinity of the exhaust plume. Again, the potential exists for a significant perturbation of the environmental density and composition.

Mercury and cesium ion thrusters can cause coating of spacecraft surfaces if such surfaces are at low enough temperatures. The cold patches required by some spacecraft instruments may be particularly sensitive because of the directional nature of the plume charge exchange ions. Problems also appear to exist due to erosion of engine structure. A minor optical problem can exist. The flow from the thrusters is so rarefied that little absorption occurs. However, if sensitive star tracker equipment is on board, the scattering of energy from the sunlight may be great enough that the tracker operation is perturbed.

6.2 Other Cooler Problems

There is another effect which we have not evaluated in this study which could cause a non-reversible increase in cooler temperature. If a significant quantity of exhaust material interacts with material that is outgassing from the spacecraft, and returns some of this material to the cooler, it could be deposited. Such a deposit might not be removable by increasing cooler temperature. Whether the effect could be reversed or not would depend upon the material and its effect upon the cooler. If we look at the NIMBUS experience, we would have to be very pessimistic. Consensus appears to be that the increasing NIMBUS cooler temperature is due to collection of contaminant material. The NIMBUS cooler operates at a temperature in the vicinity of -70°C. The difference in outgassing rates and deposit rates between 70°C and 70°K can easily be a factor of 10^{10} or 10^{20}. This is an exceedingly large difference. We are very concerned about the ability to maintain a 70°K temperature in an environment composed of unknown materials and behavior. We strongly recommend that this effect be looked into further.

As one would expect, two approaches may be followed. Either one conducts further analyses, or one conducts experiments, or both. We will briefly comment on each approach.

To our knowledge, an analytical investigation of this behavior has never been conducted. Some analogous work has been performed, particularly in the nuclear field where the behavior of photons and neutrons is commonly traced. Diffusion, transport, and MONTE CARLO techniques all are successfully applied. However, all of these techniques depend upon a stationary interaction center with a moving "particle" that is under consideration. For such an investigation involving a spacecraft in space, one would have to consider both the interaction center and the particle as moving. The mathematical treatment and, in particular, the bookkeeping aspects could become very interesting. We do not know whether such an approach would be reasonable. There is another important aspect to an analytical treatment as well. To our knowledge, the various mechanisms which could return exhaust products or outgassing products have not been studied. Hence, one additionally would have to define the return mechanisms prior to setting up analyses.

Experimentally, many problems exist. Most space simulation chambers will not achieve vacuums even remotely resembling those which occur in space. Yet, it is precisely this very high vacuum which enables the phenomenon to occur which we are undertaking to study. A few chambers appear to exist which could achieve the required vacuums, at least under some application conditions. Not even concerning ourselves with scheduling problems, we then must pose the question of whether these chambers can simulate the behavior which must be studied. First, to investigate exhaust effects one must operate a thruster in the chamber. This generates a large amount of material which could easily completely destroy the chamber vacuum, thus negating the very environment essential to the study. Secondly, the return mechanisms appear to be totally absent in such a chamber. Such mechanisms include solar wind, and "far-removed" interactions between outgassing products and environmental particles. Before undertaking a laboratory based experimental program, these areas must be recognized.

This consideration leads us to the most accurate investigation, namely, a flight experiment. Here, we need not worry about the environment since it is there. We need only concentrate upon the design of a suitable experiment and the definition of just what it is we wish to determine.

Our overall conclusion is that further work is needed. When a thruster, as such, is not a direct problem on a long term basis, other materials very well may be. Thruster exhaust may be a mechanism for compounding the problem. Two approaches are, in our opinion, indicated. We feel that some work in the analytical direction and some work in the experimental direction both are needed. We do not recommend an extensive analytical investigation at this time. Instead, a first step should be taken in which feasibility of an analysis is investigated. This step should be taken with a very careful consideration given to the requirements of the approach and the mechanisms which are considered. It would be very easy to embark upon an analysis program which was so bogged down in computer requirements as to require several years of effort before any meaningful answers were obtained. The second approach, directed in the experiment direction, should be to see if meaningful measurements are possible using laboratory facilities and to embark upon the beginnings of a flight experiment. Eventually, this last item must be performed if we are to fully understand the effects which were first observed with NIMBUS, and which we fear will seriously perturb operation of low temperature coolers.

6.3 Star Tracker Interactions

The star tracker interaction study was limited to an approximate model and did not, for practical purposes, concern itself with star tracker characteristics. Some energy input data to the star tracker were computed. These data were not furnished as a function of variables such as sunlight angle, view direction, and thrust direction. The model which was used was very preliminary, and should be improved.

We are concerned that the calculated energy seen by the star tracker may not be accurate enough for purposes of star tracker response analysis. The basic data appear quite adequate, but the preliminary model, as mentioned, is weak if applied to a response analysis. We recommend an additional study which improves upon the model and provides more complete, more accurate data in a form which can be readily used to predict star tracker response.

6.4 Contaminant Effects

Most impurities in exhaust plumes appear to be of a form which do not evaporate rapidly. Mercury thrusters eject molybdenum, cesium thrusters aluminum, hydrazine

thrusters water, etc. The special circumstances of each when integrated into a spacecraft must be carefully considered. This has not been accomplished.

7. REFERENCES

1. Blome, James C., and Upton, Bruce E. "Gemini Window Contamination Due to Outgassing of Silicones" contained in The Effects of the Space Environment on Materials, Vol. 11, 11th National Symposium and Exhibit, SAMPE, St. Louis, Apr. 1967 (A67-29555).

2. Bonner, George P., et. al., "Postflight Optical Evaluation of the Right-Hand and Left-Hand Windows of Gemini Missions IV, V, VI, and VII," NASA TN D-4916 (N69-13232), Dec., 1968.

3. Grenda, R., Neste, S., and Soberman, R., "Contaminant Particle Trajectories Near A Spacecraft," COSPAR, Plenary Meeting, May 9-21, 1968 (A68-31916).

4. McNaney, Joseph J., Palmer, Bennie A., and Shapiro, Ralph, "Nimbus II Flight Evaluation and Engineering Report, Launch through Orbit 5275," NASA TN D-4881, Feb. 1969.

5. McNaney, J. J., "Nimbus III Monthly Flight Evaluation Report Number 3, 14 June to 13 July 1969 Orbits 800-1200," Document Number 69 SD 4338, General Electric, 8 Aug. 1969.

6. Frankel, Dr. Henry E., "Degradation of the Radiant Cooler of the Nimbus III High Resolution Infrared Radiometer (HRIR) – Report of the Committee," NASA-GSFC Memorandum, Oct. 21, 1969.

7. Hallgren, D. S., and Hemenway, C. L., "Direct Observation of Particulate and Impact Contamination of 'Optical' Surfaces In Space," COSPAR, Plenary Meeting, May 9-21, 1968 (A68-31919).

8. McNaney, J. J., "Nimbus IIIMonthly Flight Evaluation Report Number 1, 14 Apr. to 14 May 1969, Orbits 1 through 400" Document Number 69 SD 4295, General Electric, 10 June 1969.

9. McNaney, J. J., "Nimbus III Monthly Flight Evaluation Report Number 4, 13 July to 12 August 1969, Orbits 1200 to 1600," Document Number 69 SD 4350, 10 Sept. 1969.

10. "A Study of Cesium Exhaust from a Ion Engine and its Effect Upon Several Spacecraft Components," HIT-399, Hittman Associates, June 26, 1969.

11. Lyon, Warren C., "A Study of the Effects of Teflon Thruster Exhaust Upon a Spacecraft," HIT-443, Hittman Associates, Inc., April 1970.

12. Lyon, Warren C., "A Study of the Effects of Hydrazine Thruster Exhaust Upon a Spacecraft," HIT-454, Hittman Associates, Inc., June 1970.

13. Hall, David F., Newnam, Brian E., and Womack, James R., "Electrostatic Rocket Exhaust Effects on Solar-Electric Spacecraft Subsystems," Journal of Spacecraft and Rockets, Vol. 7, No. 3, Mar. 1970, pp. 305-312.

14. Sellen, J. M., Jr., Kemp, R. F., and Hieler, R. H., "Observations of Neutralized Ion Thrust Beams in the 25-Meter NASA Testing Chamber," NASA CR-53634, TRW, Apr. 1964.

15. Staggs, J. F., Gula, W. P., and Kerslake, W. R., "Distribution of Neutral Atoms and Charge-Exchange Ions Downstream of an Ion Thruster," Journal of Spacecraft and Rockets, Vol. 5, No. 2, Feb. 1968, pp. 159-164.

16. Reynolds, Thaine, and Richley, Edward A., "Propellant Condensation on Surfaces near an Electric Rocket Exhaust," Journal of Spacecraft and Rockets, Vol. 6, No. 10, Oct. 1969, pp. 1155-1161.

17. Hall, D. F., "Evaluation of Electric Propellant Beam Divergence and Effects on Spacecraft," 08965-6013-R0-00, TRW Systems, Sept. 1969.

18. Reader, P. D., "Durability Tests of Mercury Electron-Bombardment Ion Thruster," AIAA Paper 66-231, San Diego, Calif., 1966.

19. Kerslake, W. R., Byers, D. C., and Staggs, J. F., "SERT II: Mission and Experiments," Journal of Spacecraft and Rockets, Vol. 7, No. 1, Jan. 1970, pp. 4-6.

20. Reynolds, Thaine W., and Richley, Edward A, "Distribution of Neutral Propellant from Electric Thrusters Onto Spacecraft Components," NASA-TN D-5576, Dec. 1969.

21. Byers, David C., and Staggs, John F., "SERT II: Thruster System Ground Testing," Journal of Spacecraft and Rockets, Vol. 7, No. 1, Jan. 1970, pp. 7-14.

22. Bechtel, Robert T., "Performance and Control of a 30-cm-diam, Low-Impulse, Kaufman Thruster," Journal of Spacecraft and Rockets, Vol. 7, No. 1, Jan. 1970, pp. 21-25.

23. Hall, D. F., Cho, A. Y., and Shelton, H., "An Experimental Study of Porous Metal Ionizers," AIAA Paper 66-218, San Diego, Calif., 1966.

24. Staggs, John F., and Lathem, Walter C., "Experimental Performance of a Low-Thrust, Divergent-Flow, Contract – Ionization Electrostatic Thruster," Journal of Spacecraft and Rockets, Vol. 4, No. 5, May 1967, pp. 610-615.

25. Sohl, G., Reid, G. C., and Speiser, R. C., "Cesium Electron Bombardment Ion Engines," Journal of Spacecraft and Rockets, Vol. 3, No. 7, July 1966, pp. 1093-1098.

26. Miller, Nelson L., "A Survey and Evaluation of Research on the Discharge Chamber Plasma of Kaufman Thrusters," Journal of Spacecraft and Rockets, Vol. 7, No. 6, June 1970, pp. 641-649.

27. Richley, Edward A., and Reynolds, Thaine W., "Condensation On Spacecraft Surfaces Downstream Of A Kaufman Thruster," NASA TM X-52746, Jan. 2, 1970.

28. Staskus, J., and Burns, R., "Deposition of Ion Thruster Effluents on SERT II Spacecraft Surfaces," AIAA Paper, 8th Electric Propulsion Conference, Stanford, Calif., Aug. 31-Sept. 2, 1970.

29. Staskus, John V., Personal Communication, NASA Lewis, 216-433-4000, ext 743, July 16, 1970.

30. Bartlett, Robert, Personal Communication, NASA-GSFC, 301-982-6487, July 16, 1970.

31. Dushman, Saul, Scientific Foundations of Vacuum Technique, Second Edition (edited by J. M. Lafferty), John Wiley & Sons, 1962.

32. Langmuir, I., "The Condensation and Evaporation of Gas Molecules," Collected Works of Irving Langmuir, Vol. 9, edited by C. G. Suits, Pergamon Press, New York, 1961, pp. 69-74.

33. Langmuir, I., "The Evaporation, Condensation, and Reflection of Molecules and the Mechanism of Adsorption," Collected Works of Irving Langmuir, Vol. 9, edited by C. G. Suits, Pergamon Press, New York, 1961, pp. 43-46.

34. Nottingham, Wayne B. and Breitwieser, Roland, "Theoretical Background for Thermionic Conversion Including Space-Charge Theory, Schottky Theory, and the Isothermal Diode Sheath Theory," NASA TN D-3324, Mar. 1966.

35. Hatsopoulos, G. N., and E. P. Gyftopoulos, Thermionic Energy Conversion, Draft Copy of book prepared for the Atomic Energy Commission, Part 1, no date (Received 1968).

36. Hunter, R., Personal Communication, NASA-GSFC, Apr. 1969.

37. Lyon, W. C., "Comments on Propellant Condensation On Surfaces Near An Electric Rocket Exhaust," Journal of Spacecraft and Rockets, (to be published).

38. Lyon, Warren C., "A Study of the Effects of a Cesium Ion Thruster Upon a Polaris Star Tracker for ATS-F and G," HIT-452, Hittman Associates, Inc., May 1970.

39. Unknown RCA Reference, pp. 184-185.

40. Nottingham, Wayne B., Proceedings of the IEEE, Dec. 1963, pp. 1771-1772.

41. Moore, Charlotte, E., Atomic Energy Levels, Vol. III, NBS Circular 467, 1 May 1958.

42. Norcross, D. W., and Stone, P. M., "Recombination, Radiative Energy Loss, and Level Populations in Nonequilibrium Cesium Discharges," J. Quant. Spectrosc. Radiat. Transfer, Vol. 8, pp. 655-684.

43. Aller, Lawrence, "Atomic Line Strengths," Cp. 3, Part 7, Condon, E. V., and Odishaw, Hugh, (Editors), Handbook of Physics, Second Edition, McGraw-Hill, 1967, pp. 7-54 – 7-65.

44. Corliss, Charles H., and Bozman, William R., "Experimental Transition Probabilities for Spectral Lines of Seventy Elements," NBS Monograph 53, 20 July 1962.

45. Stone, Philip M., "Cesium Oscillator Strengths," Physical Review, Vol. 127, No. 4, 15 Aug. 1962, pp. 1151-1156.

46. Leighton, Robert B., Principles of Modern Physics, McGraw-Hill, 1959.

47. Richtmyer, F. K., Kinnard, E. H., Lauritsen, T., Introduction to Modern Physics, McGraw-Hill, 1955.

48. Gregory, Chris, "Resonance Broadening of Caesium," Physical Review, Vol. 61, 1 and 15 Apr., 1942, pp. 465-469.

49. Pollock, D. H., and Jensen, A. O., "Absorption of Resonance Radiation and Formation of Molecular Ions in Cesium Vapor," Journal of Applied Physics, Vol. 36, No. 10, Oct. 1955, pp. 3184-3192.

50. Johnson, F. S., "The Solar Constant," Journal Meteorology 11 (6), Dec. 1954, pp. 431-439.

51. Cleavinger, Richard L., Gutshall, Richard L., and Morgan, C. Allen, "Final Report for Polaris Star Tracker Breadboard Model," No Number, Ball Brothers Research Corp., 23 May 1967 – 1 Aug. 1968.

52. Etheridge, F. G., and Boudreaux, R. A., "Attitude-Control Rocket Exhaust Plume Effects on Spacecraft Functional Surfaces," Journal of Spacecraft and Rockets, Vol. 7, No. 1, Jan. 1970, pp. 44-48.

53. Daley, Howard L., and Perel, Julius, "Cesium Ion Sputtering of Aluminum, Copper, and Titanium, Paper 66-203 (A66-21445), AIAA 5th Electric Propulsion Conference, Mar. 7-9, 1966.

54. Marino, Lawrence, L., Smith, A. C. H., and Caplinger, E., "Charge Transfer Between Positive Cesium Ions and Cesium Atoms," Physical Review, Vol. 128, No. 5, Dec. 1, 1962, p. 2243.

55. Marino, Lawrence L., "Charge Transfer Between Alkali-Metal Ions and Cesium Atoms," Physical Review, Vol. 152, No. 1, Dec. 2, 1966, p. 46.

56. Perel, Julius, Bernon, Richard H., and Daley, Howard L., "Measurement of Cesium and Rubidium Charge-Transfer Cross Sections," Physical Review, Vol. 138, No. 4A, May 17, 1965, p. A937.

57. Zuccaro, David, "Measurement of the Charge Exchange Cross Section of Mercury," NASA CR-72398 (N68-30824), Hughes Research Laboratories, Apr. 1968.

58. Hunter, Robert E., Bartlett, Robert O., Worlock, Robert M., and James, Edmund L., "Cesium Contact Ion Microthruster Experiment Aboard Applications Technology Satellite (ATS) - IV," Journal of Spacecraft and Rockets, Vol. 6, No. 9, Sept. 1969, pp. 968-970.

59. Guman, William J. and Nathanson, David M., "Pulsed Plasma Microthruster Propulsion System for Synchronous Orbit Satellite," AIAA Paper No. 69-298, AIAA 7th Electric Propulsion Conference, Williamsburg, Virginia, Mar. 3-5, 1969.

60. Guman, William J., "Pulsed Plasma Technology In Microthrusters," AFAPL-TR-68-132, Fairchild-Hiller Corporation, Nov. 1968.

61. Vondra, Robert, Thomassen, Keith, and Solbes, Albert, "Analysis of Solid Teflon Pulsed Plasma Thruster," AIAA Paper No. 70-179, AIAA 8th Aerospace Sciences Meeting, New York, New York, Jan. 19-21, 1970.

62. Guman, William J. and Peko, Paul E., "Solid-Propellant Pulsed Plasma Microthruster Studies," Journal of Spacecraft and Rockets, Vol. 5, No. 6, June 1968, pp. 732-733.

63. Guman, William J., "Pulsed Plasma Technology in Microthrusters," AFAPL-TR-68-132, AD845757, Air Force Aero Propulsion Laboratory (Prepared by Fairchild-Hiller Corporation), Nov. 1968.

64. LaRocca, A. V., and Perkins, G. S., "Pulsed Plasma Microthruster Applications and Techniques," AIAA Paper No. 68-554, 4th Propulsion Joint Specialist Conference, Cleveland, Ohio, June 10-14, 1968.

65. Ehrenfield, Personal Communication, Halo-carbon Corp., Hackensack, New Jersey, 201-343-8703, March 4, 1970.

66. Guman, Dr. William J., Personal Communication, Fairchild-Hiller Corporation, Farmingdale, New York, Mar. 31 and Apr. 7, 1970.

67. Vondra, Dr. Robert, Personal Communication, Mar. 30, 1970.

68. Vondra, Dr. Robert, Personal Communication, MIT Lincoln Laboratories, Cambridge, Massachusetts, Apr. 7, 1970.

69. Lyon, Warren C., Personal Observations of Fairchild-Hiller test chamber, Mar. 31, 1970.

70. McClellan, Donald, Personal Communication, MIT Lincoln Laboratory, Cambridge, Massachusetts (Telephone No. 617-862-5500), Mar. 5, 1970.

71. LaRocca, Aldo V., Personal Communication, General Electric Company, Valley Forge, Pennsylvania (Telephone No. 823-2287), Mar. 4, 1970.

72. Vondra, Dr. Robert, Personal Communication, MIT Lincoln Laboratory, Cambridge, Massachusetts (Telephone No. 617-862-5500, ext. 7241), Mar. 5, 1970.

73. Murphy, Edward B., Personal Communication, MIT Lincoln Laboratory, Cambridge, Massachusetts (Telephone No. 617-862-5500, ext 5515 or 7745), Mar. 5, 1970.

74. Nathanson, David M., Personal Communication, MIT Lincoln Laboratory, Cambridge, Massachusetts (Telephone No. 617-862-5500, ext. 7241), Mar. 5, 1970.

75. Murphy, E. B., "Analysis of Char From Teflon Arc Thruster, "Materials and Processing Memo #4E, MIT Lincoln Laboratory, June 6, 1968.

76. Murphy, E. B., "RFI Teflon Vacuum Arc Thruster Vs. Ground Plain Antenna," MIT Lincoln Laboratory Memo, Aug. 5, 1968.

77. Murphy, Ed., "VAT Deposit-Fairchild-Hiller Sample (Memo #4G)," MIT Lincoln Laboratory Memo, May 1, 1969.

78. Rudner, Merritt Allen, Fluorocarbons, Reinhold, 1958.

79. Sperati, C. A., and Starkweather, H. W., Jr., "Fluorine-Containing Polymers. II. Polytetrafluoroethylene," Advances in Polymer Science, 1961, pp. 465-495.

80. Settlage, P. H., and Siegle, J. C., "Behavior of 'Teflon' Fluorocarbon Resins at Elevated Temperatures," Planetary and Space Science, 3, 1961, pp. 73-81.

81. Mathias, Eckart, and Miller, Glenn H., "The Decomposition of Polytetrafluoroethylene in a Glow Discharge," Journal of Physical Chemistry, Vol. 71, No. 8, July 1967, pp. 2671-2675.

82. Brandkamp, W., DeCecco, A., and Hanson, J. "Laser-Induced Teflon Char," Journal of Spacecraft and Rockets, Vol. 6, No. 9, Sept. 1969, pp. 1087-1088.

83. Bro, Dr. M. I., Personal Communication, E. I. duPont de Nemours & Co., Wilmington, Delaware (302-774-8364), Mar. 4, 1970.

84. Audrith, L. F., and Ogg, B. A., The Chemistry of Hydrazine, Wiley, 1951.

85. Price, T. W., and Evans, D. D., "The Status of Monopropellant Hydrazine Technology," Technical Report 32-1227, N68-16344, NASA-CR-92742, Jet Propulsion Laboratory, Feb. 15, 1968.

86. Eberstein, I. J., and Glassman, I., "Consideration of Hydrazine Decomposition," ARS Propellants, Combustion, and Liquid Rockets Conference, Columbus, Ohio, July 18-19, 1960. Contained in Liquid Rockets and Propellants, pp. 351-366.

87. Fresenius, W., and Karweil, J. "The Normal Oscillations and the Configuration of Hydrazine," Z. Physikal. Chem. Abt. B. Bd. 44, Heft I., pp. 5-12.

88. Lucien, Harold W., "Thermal Decomposition of Hydrazine," Journal of Chemical and Engineering Data, Vol. 6, No. 4, Oct. 1961, pp. 584-586.

89. Eberstein, Igor J., "The Gas Phase Decomposition of Hydrazine Propellants," Technical Report 708, Department of Aerospace and Mechanical Sciences, Princeton University, AD607334, 1964.

90. Stief, L. J., DeCarlo, V. J., and Mataloni, R. J., "Vacuum-Ultraviolet Photochemistry. VII Photolysis of Hydrazine at 1236 and 1470 A," The Journal of Chemical Physics, Vol. 46, No. 2, 15 Jan. 1967, pp. 592-598.

91. Schreib, R. R., Pugmire, T. K., and Chapin, S. G., "The Hybrid (Hydrazine) Resistojet," AIAA Paper 69-496, AIAA 5th Propulsion Joint Specialist Conference, June 9-13, 1960.

92. Price, T. W., "Hydrazine Monopropellant Provides 0.5-600 lb. Thrust," Space/Aeronautics, Oct. 1969, pp. 70-72.

93. Kesten, Arthur S., "Analytical Study of Catalytic Reactors for Hydrazine Decomposition," UACRL F910461-12, N68-10633, NASA-CR-89791, United Aircraft, May 1967.

94. Kesten, A. S., NASA-CR-80336, N67-12972, Oct. 1966.

95. Kesten, A. S., NASA-CR-92988, N68-16663, Jan. 1968.

96. Salvinski, R. J., "Investigation of the Formation and Behavior of Clogging Material in Earth and Space Storable Propellants," Interim Report, No. 08113-6016-R000, NASA-CR-191569 (X69-16132), TRW Systems, Oct. 1968.

97. Sutherland, George S., et. al., "Monopropellant Hydrazine Reaction Control Systems – A Five Year Status Report," obtained from AIAA under A68-33429.

98. "Spacecraft Attitude Control Gas Systems Analysis," NASA-CR-86661, N67-32369, Hughes, Apr. 1967.

99. Carlson, Ronald A., Blumenthal, Jack L., and Grassi, Robert J., "Space Environment Operation of Experimental Hydrazine Reactors," Rpt. No. 4715. 3.68-27, N69-12432, TRW Systems, July 1968.

100. Boyd, W. K., Berry, W. E., and White, E. L., "Compatibility of Materials with Rocket Propellants and Oxidizers," DMIC Memo 201, Jan. 29, 1965.

101. Weast, Robert C., and Selby, Samuel M., Handbook of Chemistry and Physics, 48th Edition, 1967.

102. Suddeth, D., Personal Communication, GSFC, Oct. 1, 1969.

103. Axworthy, A. E., et al, "Research On Hydrazine Decomposition," AD826121, AD830860 and AD842500, Rocketdyne, Jan. 1968, Apr. 1968, and Oct. 1968.

104. Knox, Bruce P., and Eberle, Henry R., "Propellant Performance Handbook, Vol. IV, Part A, Fluorine/Ammonia, "Bell Aerosystems, 8173-902008- Vol. 4, Part A, AD802908, June 1964.

105. Overstreet, Roy, and Giauque, W. F., "Ammonia. The Heat Capacity and Vapor Pressure of Solid and Liquid. Heat of Vaporization. The Entropy Values from Thermal and Spectroscopic Data," Journal of the American Chemical Society, Vol. 59, Feb. 1937, pp. 254-259.

106. Mellor, J. W., A Comprehensive Treatise on Inorganic and Theoretical Chemistry, Vol. VIII, Wiley, 1962.

107. "Military Specification, Propellant, Hydrazine," MIL-P-26536B, Mar. 13, 1964.

108. Wagman, Dr. Donald D., Personal Communication, Chemical Thermodynamics Data Group, NBS, Washington, D. C. 20234, 301-921-2773, June 8, 1970.

109. Williamson, Frank, Personal Communication, Cryogenic Data Center, NBS, Boulder, Colorado 80302, 303-447-1000, ext. 3797, June 8, 1970.

110. Shafer, Wade H., Personal Communications, Thermophysical Properties Research Center, West Lafayette, Indiana 47906, 317-463-1581, June 8 and 9, 1970.

111. Haws, Jimmy L., and Harden, Darrel G., "Thermodynamic Properties of Hydrazine," Journal of Spacecraft and Rockets, Vol. 2, No. 6, Nov.-Dec. 1965, pp. 972-974.

112. Washburn, Edward W., et al, International Critical Tables . . . . , Vol. III, McGraw-Hill, 1928.

113. Scott, D. W., Oliver, G. D., Gross, Margaret E., Hubbard, W. N., and Huffman, Hugh M., "Hydrazine: Heat Capacity, Heats of Formation and Vaporization, Vapor Pressure, Entropy, and Thermodynamic Functions," Journal of the American Chemical Society, Vol. 71, 1949, pp. 2293-7.

114. Grier, Norman T., "Back Flow From Jet Plumes in Vacuum," NASA-TN/D-4978 (N69-14385), Jan. 1969.

115. Sibulkin, M. and Gallaher, W. H., "Far-Field Approximation for a Nozzle Exhausting into a Vacuum," AIAA Journal, Vol. 1, No. 6, June 1963, pp. 1452-1453.

116. Mirles, H., and Mullen, J. F., "Expansion of Gas Clouds and Hypersonic Jets Bounded by a Vacuum" AIAA Journal, Vol. 1, No. 3, Mar. 1963, pp. 596-602.

117. Hill, Jacques A. F., and Draper, James Stark, "Analytical Approximation for the Flow from a Nozzle into a Vacuum," J. Spacecraft and Rockets, Vol. 3, No. 10, Oct. 1966, pp. 1552-1554.

118. Zucrow, M. J., Aircraft and Missile Propulsion, Vol. II, Wiley, 1964.

119. Brook, John W., "Far Field Approximation for a Nozzle Exhausting into a Vacuum," J. Spacecraft and Rockets, Vol. 6, No. 5, May 1969, pp. 626-628.

120. Shapiro, Ascher H., The Dynamics and Thermodynamics of Compressible Fluid Flow, Vol. 1, Ronald Press, 1953.

121. Draper, James Stark, and Hill, Jacques A., "Rarefaction in Underexpanded Flows," AIAA Journal, Vol. 7, No. 7, July 1969, pp. 1400-1401.

122. Grier, Norman T., "Back Flow of Jet Plumes in Vacuum," NASA TM X-52468, N68-29919, 6th International Symposium on Rarefied Gas Dynamics, Cambridge, Massachusetts, July 22-26, 1968.

123. Lyon, Warren C., "Study of the Effects of Ammonia Thruster Exhaust Products Upon ATS Spacecraft," HIT-422, Hittman Associates, Nov. 5, 1969.

124. Massie, Lowell D., and Martinkovic, Paul J., "Attitude Control Rocket Exhaust Plume Effects On Solar Cells," A69-35678, 7th Photovoltaic Specialists Conference, Pasadena, California, Nov. 19-21, 1968.

125. Page, Russell, Halback, Carl R., Ownby, Michael L., and Short, Robert A., "Life Test of Six High Temperature Resistojets," AIAA 7th Electric Propulsion Conference, Paper No. 69-294, Mar. 3-5, 1969.

126. Knox, Bruce P., and Eberle, Henry R., "Propellant Performance Handbook, Vol. IV, Part A, Fluorine/Ammonia," Bell Aerosystems, 8173-902008-Vol. 4, Part A, AD802908, June 1964.

PRECEDING PAGE BLANK NOT FILMED

APPENDIX I

ION ENGINE PLUME ATOM AND ION CHARACTERISTICS

1. EXHAUST SYMMETRY

Hall (Ref. I-1) reports that the exhaust plume of electrostatic thrusters is axially symmetric. As long as we have only primary particles, the exhaust will remain axially symmetric. (Collisons between uncollided particles to form primary particles will, on the average, not disturb the axial symmetry.) Introduction of a secondary or contaminent particle will destroy the symmetry. We conclude that uncollided and primary particles can be analyzed by a two dimensional model. Introduction of secondaries or contaminents will require a three-dimensional model unless primary-secondary or primary-contaminant interactions are negligible.

2. NEUTRAL ATOM DISTRIBUTION

White (Ref. I-2) requested that we assume a cosine distribution of neutral atoms in the primary engine exhaust as a starting point for this study. Hall has confirmed the validity of this request since he concluded that the neutral atom "distribution must be nearly that of an extended cosine source, particularly at distances in excess of one thruster diameter." The neutral atom angular distribution therefore is given by:*

$$\Gamma(r, \theta) = \frac{\Gamma_0 \frac{a^2}{r^2} \cos\theta}{\left[1 + \frac{2a^2}{r^2} \cos\theta + \frac{a^4}{r^4}\right]^{1/2}} \qquad (1)$$

where:

Γ = particle current density in the direction of the radius vector

r = distance from center of ion engine exhaust plane to the position of interest

θ = angle between r and the normal to the engine exhaust plane

Γ_0 = particle current density at the ion engine exhaust plane

a = radius of the ion engine exhaust opening

This configuration is shown in Figure I-1.

The solution of this equation is shown in Figure I-2.

*This equation should not be used for $r < a$

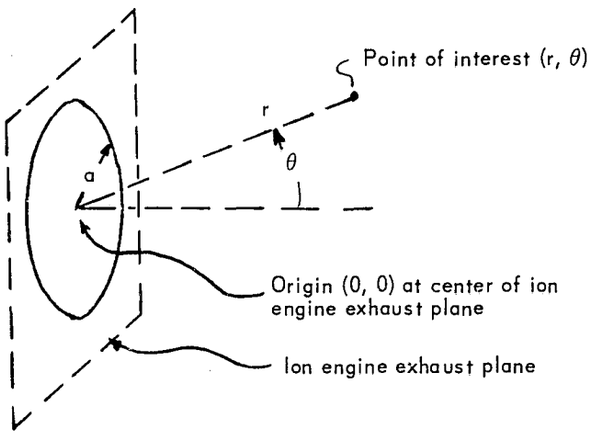

Figure I-1. Geometry Illustration.

3. IONIZED CESIUM DISTRIBUTION

3.1 General Characteristics

Collisions which generate charge exchange ions in the engine exhaust introduce low velocity charged particles which are accelerated due to the potential difference between the beam plasma and the surroundings. Staggs (Ref. I-3) has divided the charge exchange ions into four groups:

(1) Ions which remain in the primary beam (dispersion angle, θ, between 0° and 20°)

(2) Ions which are forced into a cone which surrounds the primary beam due to interactions within the engine acceleration structure ($20° < \theta < 90°$)

(3) Ions which return to the engine

(4) Ions which are accelerated normal to the beam boundary.

Determination of ion engine beam composition and particle trajectories requires not only study of interactions outside the engine but also consideration of internal engine behavior. Internal characteristics determine the initial behavior outside of the engine, and therefore affect the beam downstream of the engine. The region within the engine is shown in Figure I-3. This region is described by the equation:

$$\nabla^2 V = -\frac{\rho}{\epsilon_0} \tag{I-1}$$

where

V = potential (function of position)

ρ = space charge density (function of position)

ϵ_0 = permittivity of free space

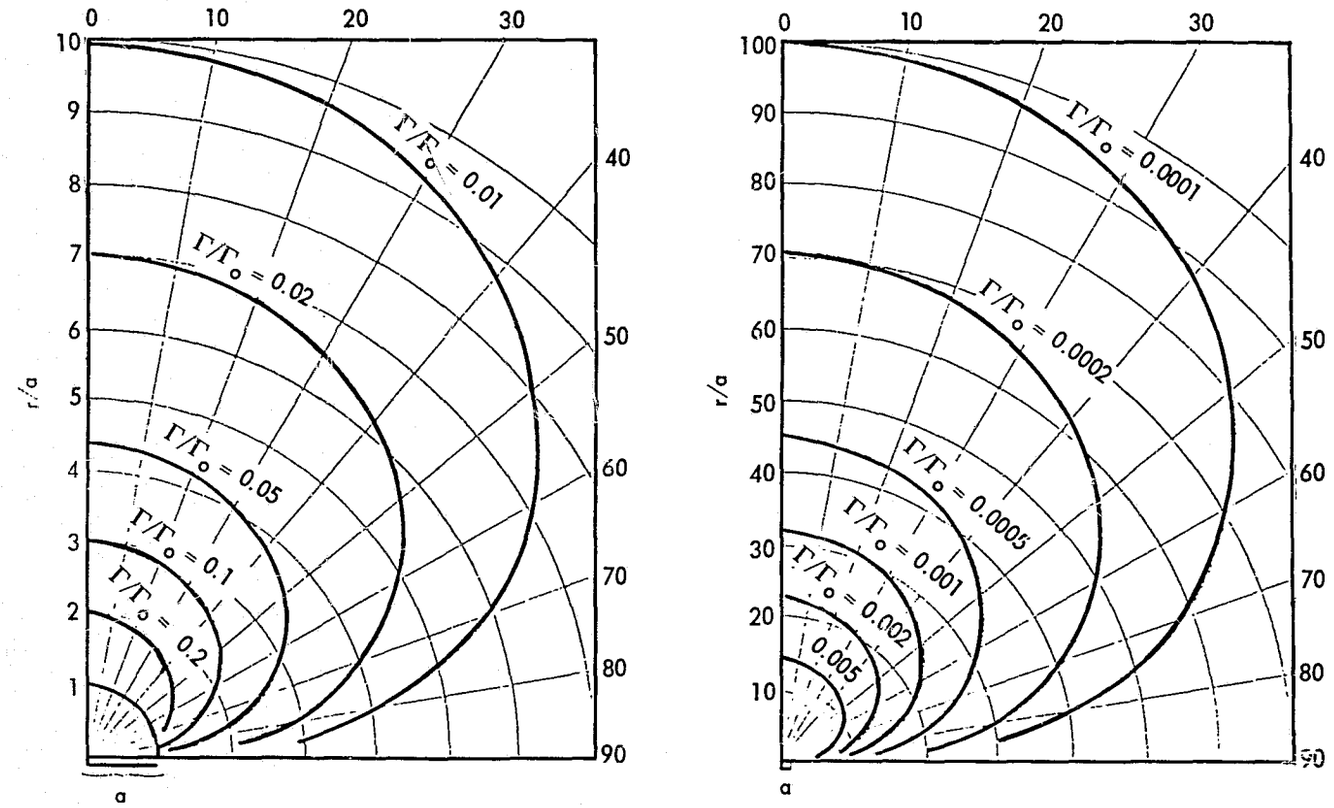

Figure I-2. Polar Plot of Lines of Constant Γ/Γ_0 as a Function of r/a (Ref. I-1).

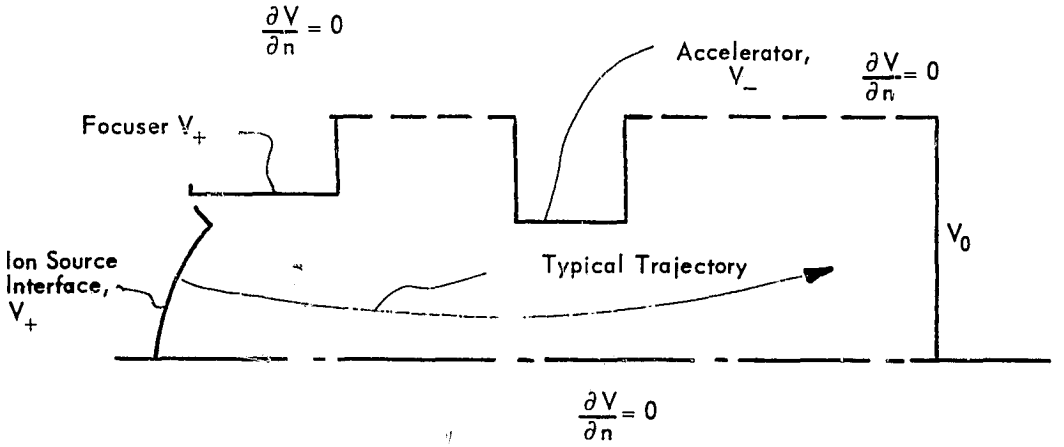

Figure I-3. Ion Extractor System Boundaries.

Solution of this equation with suitable boundary conditions will provide potential and current density distributions and ion trajectories; including the trajectory of charge-exchange ions formed in the exhaust beam. Unfortunately, solution of this equation in closed form has not been accomplished.

Staggs (Ref. I-4) has briefly described the overall approach for designing ion extractor systems for electrostatic thrusters. In principle, either digital computer, analog techniques, or combinations of the two may be employed. The first two are described in References I-5 through I-12 and the last is described by Staggs as possessing advantages over the first two. In any event, extensive calculational and/or analog facilities are required in addition to the effort needed to set up the analyses. Fortunately, we need not undertake as extensive an analysis as described in these references because of a generalized approach presented by Staggs (Ref. I-13).

There are three major constituents in the exhaust from an ion engine:

- high velocity ions
- low velocity (charge exchange) ions
- neutral atoms

For most applications the high velocity ions will not hit the spacecraft. We therefore will, for the time being, neglect the primary (high velocity) ions and will investigate behavior of the other ionic constituents.

Staggs (Refs. I-3 and I-13) presents several plots of distributions based upon a computer calculation of characteristics. One of these, reproduced in Figure I-4 shows the total Group 2 ions as a function of angle. The value between 45° and 90° is a guess because computation was terminated at 45°. Hall (Ref. I-1) has applied this distribution (as contained in Ref. I-13), which was calculated for a 15 cm Lewis E-B mercury engine, to a spacecraft interception problem. First, he defines the function shown in Fig. I-4 by F (θ) where θ is the dispersion angle and F (θ) is the ion flux (number per steradian per sec). Next, he notes that:

$$d\omega = \frac{dA_s}{r^2} \qquad \text{(I-2)}$$

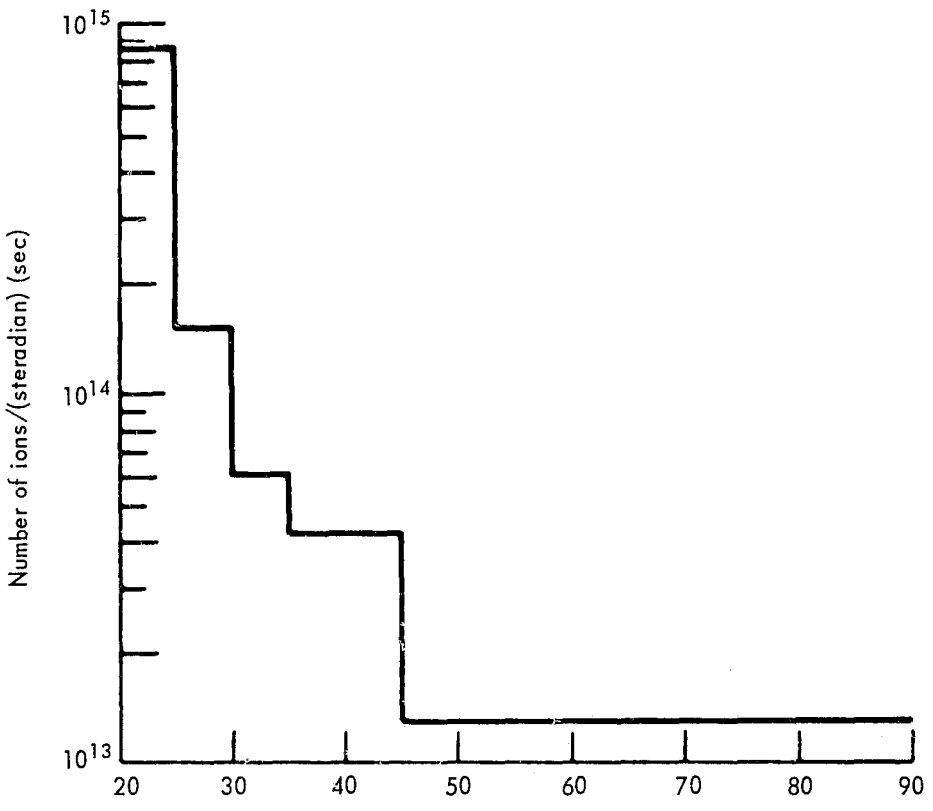

Figure I-4. Total Group 2 Charge-Exchange Ions Escaping Thrustor

where:

ω = solid angle

A_s = spherical surface area intercepting the ions

r = distance between ion beam and intercepting surface

Further:

$$\Gamma (r, \theta) = \frac{F (\theta)}{r^2} \qquad \text{(I-3)}$$

where:

Γ = ion flux, ions/cm^2 sec

Hall immediately arrives at the isoflux expression:

$$(r (\theta))_{\Gamma = \text{constant}} = \left[\frac{F (\theta)}{\Gamma (r, \theta)}\right]^{1/2} \qquad \text{(I-4)}$$

This function is used to determine the distance at which the flux is one ion/cm² sec, as shown in Fig. I-5. Hall further fitted several curves to these data to obtain an analytic function for F (θ). His recommended expression for the range $0 \leq \theta \leq 90°$ is:

$$F(\theta) = 10^{(16.17 - 0.017\,\theta - 0.0018\,\theta^2)} \text{ (ions/ster. sec)} \qquad \text{(I-5)}$$

(Group 2 ions do not exist for $\theta > 90°$ because of their origination point.) Finally, Hall presents the diagram shown in Fig. I-6 for the 15 cm NASA/Lewis mercury engine. This shows the Group 1, 2, and 4 ion fluxes.

3.2 Group 2 Ion Behavior

The Group 2 ion flux for the mercury engine analyzed by Staggs is about 10^9 to 10^{10} ions/cm² sec (see Fig. I-6). This flux exists near the engine between a solid angle of 20° and 90° of the thrust line (center of the exhaust beam). Near the engine, the neutral atom

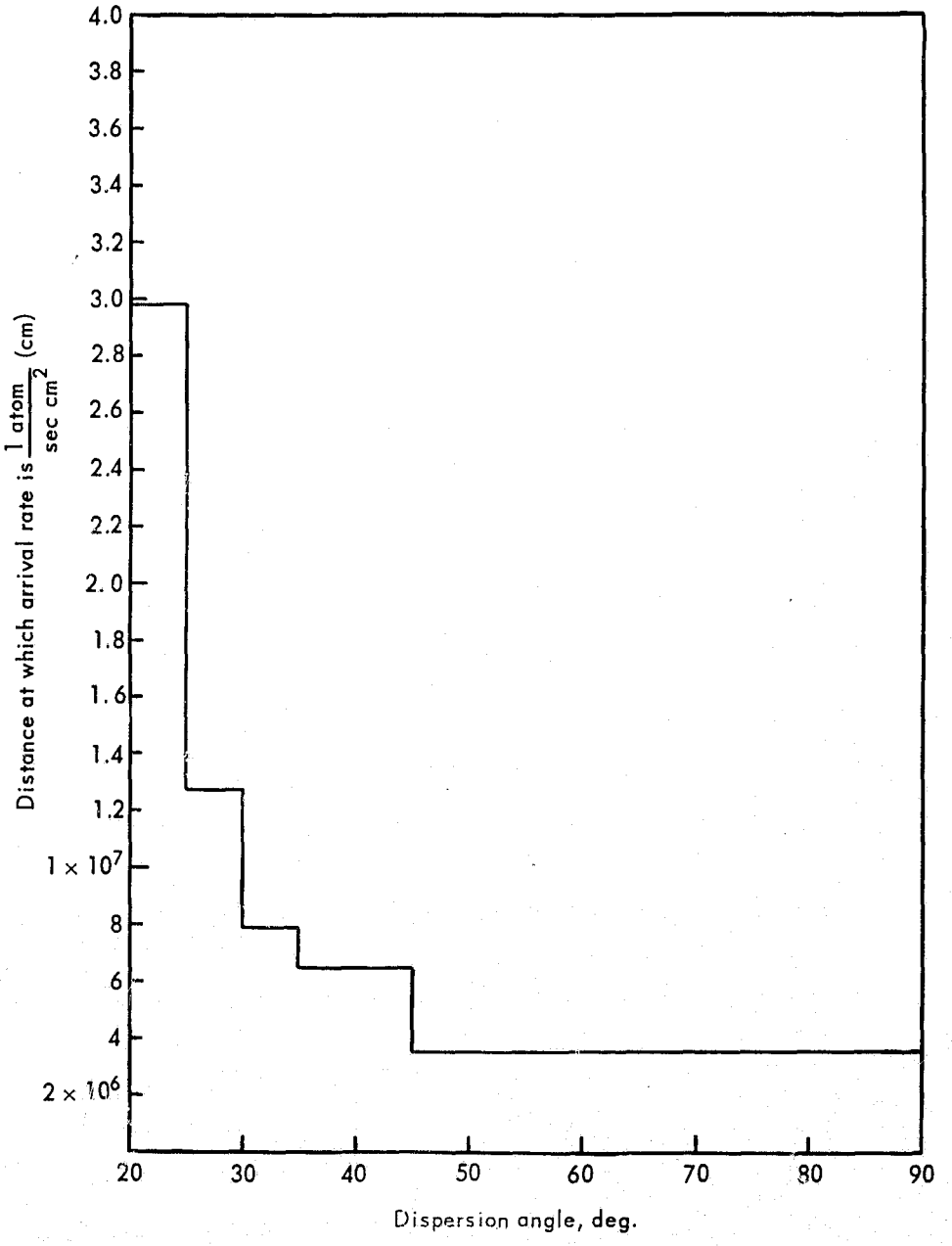

Figure I-5. Distance at Which Group 2 Arrival Rate is One Atom cm^{-2} sec^{-1}.

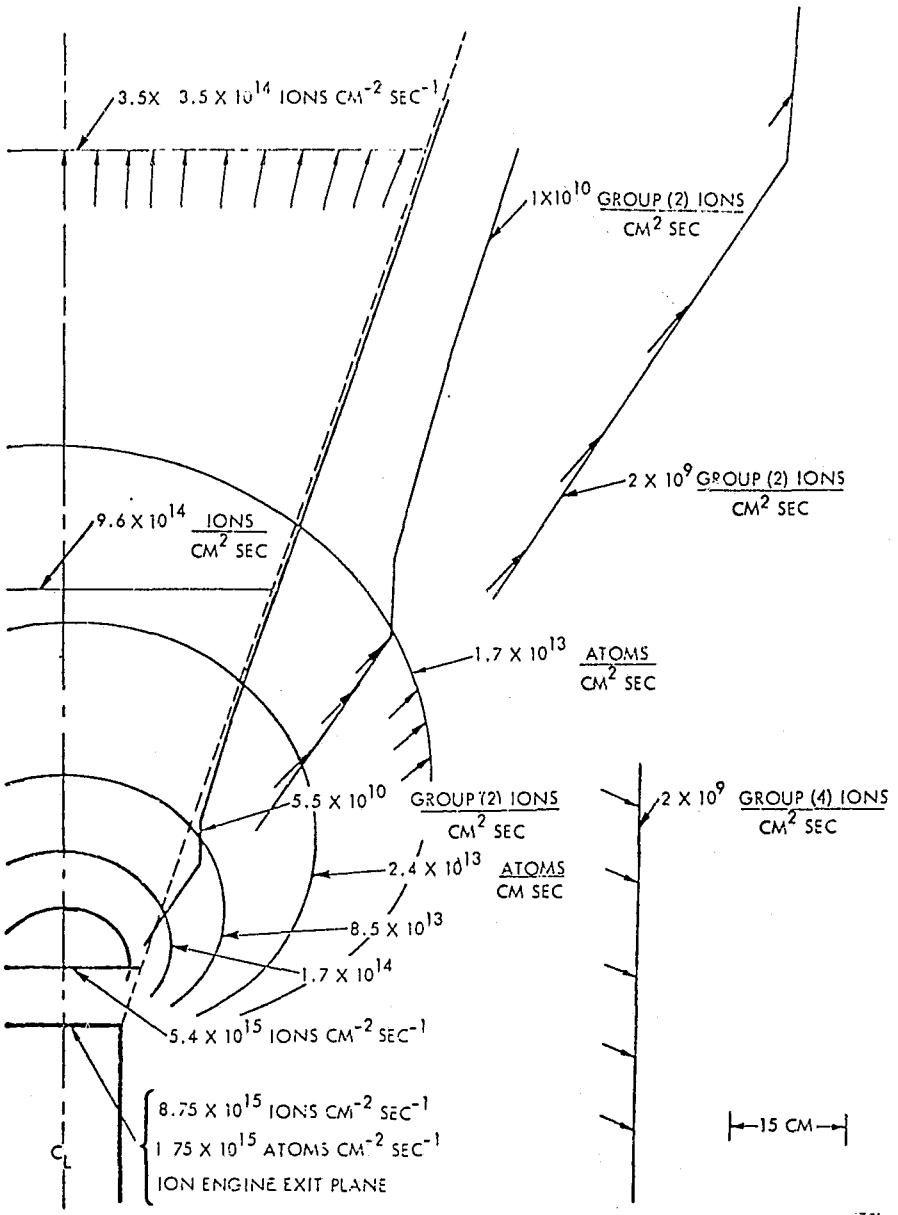

Figure I-6. Lines of Constant Arrival Rate of Particles from the 15 cm E-B Hg Thrustor.

flux is substantially higher; about 10^{13} . Neutral atom directions are about the same, although the distribution is significantly different. For most situations, the Group 2 ion arrival rate probably will be so far below the neutral atom arrival rate that it can be neglected. Nevertheless, we will check this statement by obtaining the scaling relationships which can be used to apply Stagg's data to the cesium engine we wish to evaluate. Further, a portion of this development will be applicable to the Group 4 ion behavior where, because of the difference in the angular characteristics, there may be a significant effect upon the cryogenic radiator. Finally, Group 2 ions may cause sputtering (which we will discuss later) whereas the neutral atoms are not energetic enough to cause significant surface erosion.

The behavior of Group 2 ions is determined within the ion engine (upstream of the exit plane). For purposes of scaling Stagg's data, we will assume a uniform density of neutral atoms within the entire extraction system (see Figure I-3). The charge exchange ion production rate is:

Production rate = exchange cross section × volume × ion arrival rate × neutral atom density (I-6)

This is:

$$N = Q \Delta L \, a \, n \, n_0 \tag{2}$$

where:

N = number of charge exchange ions produced per unit time in the volume ($a \Delta L$)

Q = charge exchange cross section

ΔL = increment of length

a = cross sectional area

n = number of ions arriving at volume per unit time per unit area

n_0 = neutral atom density.

The space-charge limited current flow between coaxial cylinders can be written (Ref. I-14):

$$J = \frac{4}{9} \epsilon_0 \left(\frac{2\ e}{m}\right)^{1/2} E^{3/2} \, (r_0 \ r \ \beta^2)^{-1} \tag{I-7}$$

where:

ϵ_0 = free space permittivity

e/m = particle charge to mass ratio (assuming single ionization)

e = electron charge

E = potential at radius r

r_0 = emitter radius

β = nondimensional function of r/r,

and, for parallel plane electrodes (Refs. I-15 and I-16):

$$I = K \left(\frac{e}{m}\right)^{1/2} \frac{E^{3/2}}{d^2} \tag{I-8}$$

where:

I = current density

K = a constant

e = electron charge

m = mass

E = potential difference between the electrodes

d = electrode separation distance

In effect, these state that current density is proportional to the inverse square root of mass. Therefore:

$$n \propto m^{-1/2} \tag{I-9}$$

where $\propto$ indicates proportionality. The neutral atom density, n_0, is not a function of mass. We therefore may write, from Equations 2 and I-9:

$$N \propto Q m^{-1/2} \tag{I-10}$$

Finally, if all other variables are constant except the propellant:

$$\frac{N_1}{N_2} = \frac{Q_1}{Q_2}\left(\frac{m_2}{m_1}\right)^{1/2} \tag{7}$$

where, in addition, we have assumed the charge to be the same in both cases. This equation allows calculation of the charge-exchange ion formation rate if we change propellant.

The effect of changing accelerating voltage also may be obtained from the Childs-Langmuir Law, which shows a 3/2 power dependency. Hence:

$$n \propto E^{3/2} \tag{I-11}$$

Equation 2 shows that:

$$N \propto n\, n_0 \tag{I-12}$$

Now, we may write:

$$n_0 = \frac{\mu_0\, t\, a}{V} \tag{I-13}$$

where:

μ_0 = neutral atom arrival rate per unit area

t = time

V = volume

which may be rewritten:

$$n_0 = \frac{\mu_0 \, t}{\Delta L} \tag{I-14}$$

$$n_0 = \frac{\mu_0}{v} \tag{I-15}$$

where:

v = neutral atom velocity

The propellant utilization efficiency is:

$$\eta = \frac{n}{n + \mu_0} \tag{12}$$

(this is exact if there are no Group 2 ions. The Group 1 ion flux is so much larger than the Group 2 flux that there is negligible error.) This can be rewritten as:

$$\mu_0 = \frac{(1 - \eta)\, n}{\eta} \tag{I-16}$$

which shows that:

$$\mu_0 \propto n \tag{I-17}$$

From Equation I-15 we see that:

$$n_0 \propto \mu_0 \tag{I-18}$$

Therefore:

$$n_0 \propto n \tag{I-19}$$

Equations I-12 and I-19 now show that:

$$N \propto n^2 \tag{I-20}$$

We now combine Equations I-11 and I-20 to obtain:

$$N \propto E^3 \tag{I-21}$$

so that the effect of changing accelerator voltage is:

$$\frac{N_1}{N_2} = \left(\frac{E_1}{E_2}\right)^3 \tag{9}$$

The effect of changing propellant utilization efficiency can be obtained by noting that Equation I-16 is:

$$\mu_0 = \frac{1 - \eta}{\eta} n \tag{I-22}$$

If we hold n constant, Equation I-13 shows that:

$$N \propto n_0 \tag{I-23}$$

But Equation I-15 gives:

$$n_0 \propto \mu_0 \tag{I-24}$$

So that:

$$N \propto \mu_0 \tag{I-25}$$

and Equation I-22 then provides:

$$N \propto \frac{1 - \eta}{\eta} \tag{I-26}$$

Thus, the effect of changing efficiency is given by:

$$\frac{N_1}{N_2} = \frac{1 - \eta_1}{\eta_1} \frac{\eta_2}{1 - \eta_2} \tag{10}$$

The effect of changing temperature may be obtained by noting that mean velocity is given by (Ref. I-17):

$$v = \left(\frac{8\,k\,T}{\pi\,m}\right)^{1/2} \tag{I-27}$$

where:

k = Boltzmann constant

T = temperature

m = atom mass

Hence:

$$v \propto T^{1/2} \tag{I-28}$$

Substituting Equation I-15 into 2 yields:

$$N = \frac{Q\,\Delta L\,a\,n\,\mu_0}{v} \tag{I-29}$$

Or:

$$N \propto \frac{1}{v} \tag{I-30}$$

Combining with Equation I-28 yields:

$$N \propto \sqrt{\frac{1}{T}} \tag{I-31}$$

so that the effect of changing temperature is given by:

$$\frac{N_1}{N_2} = \sqrt{\frac{T_2}{T_1}} \tag{8}$$

3.3 Group 4 Ion Behavior

Staggs calculated the Group 4 charge-exchange ions with the assumptions:

- Neutrals are emitted uniformly over the thruster diameter and follow a cosine law with distance
- The ion flux is paraxial and of uniform density

The first assumption has been discussed. The second is reasonable because the ion flux does not change significantly in the vicinity of the spacecraft within the 15-20° cone of the primary flux. Further, the same number of Group 4 ions would be considered regardless of where they were generated. All Group 4 ions, no matter where produced, will be accelerated perpendicular to the ion beam.

The Group 2 ion concentration is very small in comparison to Group 1. It may be neglected for purposes of calculating Group 4 ion production because the number of Group 4 ions so produced is negligible. Similarly, the number of scattering collisions which occur between the generation point and the spacecraft is negligibly small in comparison to the number which occur in the Group 1 ion beam. (The flux in the beam is several decades higher.) Therefore, we may neglect ion-ion, ion-atom, and atom-atom collisions except within the ion beam. This greatly simplifies the calculations and Equation 2 may be used to compute the Group 4 ion generation rate.

Equation 1 describes the neutral atom distribution. If we substitute $\theta = 0$ in this distribution and use D for the engine exhaust diameter, then this becomes:

$$\Gamma(r) = \frac{\Gamma_0 \frac{D^2}{r^2}}{\left[16 + \frac{8\,D^2}{r^2} + \frac{D^4}{r^4}\right]^{1/2}} \qquad \text{(I-32)}$$

where:

Γ = neutral current density parallel to the thrust vector

r = distance from exhaust plane

The cross sectional area of the exhaust plume at the engine is $\pi D^2/4$. If we take the unit of length, ΔL, in Equation 2 to be unity, then the number of charge exchange ions produced per unit length is (from Equations 1 and I-32):

$$N(r) = \frac{\pi\, Q\, D^2\, n\, n_0'}{4\left[16\,\frac{r^4}{D^4} + 8\,\frac{r^2}{D^2} + 1\right]^{1/2}} \qquad (3)$$

where: n_0' = neutral atom density at the exhaust plane. Equations I-27 and I-15 yield:

$$n_0' = \mu_0' \sqrt{\frac{\pi\, m}{8\, k\, T}} \qquad \text{(I-33)}$$

where: μ_0' = rate at which neutral atoms leave the engine per unit area (at the engine). Substituting, we find:

$$N(r) = \frac{\pi\, Q\, D^2\, n\, \mu_0' \sqrt{\frac{\pi\, m}{8\, k\, T}}}{4\left[16\,\frac{r^4}{D^4} + 8\,\frac{r^2}{D^2} + 1\right]^{1/2}} \qquad \text{(I-34)}$$

Now we wish to find the number of Group 4 charge exchange ions impacting on the spacecraft per unit area. To do this requires a knowledge of the charge exchange ion behavior. Prior to interaction, the neutral atoms possess energies in the thermal range (~0.025 ev). The charge exchange process is inelastic and the only effect is one of stripping an electron from the atom. Its energy remains, for practical purposes, unchanged. This means the charge exchange ion retains the velocity and direction it had before the collision. However, it now is a changed particle and is subject to any magnetic or electrical fields which may exist. Sellen (Ref. I-18) has shown that in a neutralized ion beam the dominent field effect is due to electrical charge differential in the radial direction. A small charge gradient also exists in the axial direction, but this is small and will not concern us here.

The ion density as a function of radial position is shown in Figure I-7. Cole (Ref. I-19) divides the plasma beam into an inner core and an exponential wing. He states that the electrical potential in the inner core and in portions of the exponential wing has been determined by Kemp (Ref. I-20) using emissive probe techniques. The outer portion of the exponential wing has not been investigated successfully and we can only postulate that an electron sheath region exists, as shown in Figure I-8. (However, it appears reasonable to assume such a sheath exists.) The experimental data show a slight negative curvature in the inner core which indicates a small excess of ions. The potential is almost constant, however. In the exponential wing a constant negative slope exists, indicating that the electric field is virtually uniform. In the assumed electron sheath, the curvature of potential is positive, as would be expected with an excess of electrons near the beam boundary.

The potential within the inner core and exponential wing regions is described by:

$$V - V_0 = \frac{k\,T_e}{e}\,\ln\left(\frac{\rho_+}{\rho_{+0}}\right) \tag{I-35}$$

where:

V = potential

k = Boltzmann constant

e = charge of an electron

T_e = electron temperature

ρ_+ = positive ion density

and o refers to the zero radius position. The radial density distribution is given by:

$$\left.\begin{aligned} \rho_+ &= \rho_{+0} \quad r < r_0 \\ \rho_+ &= \rho_{+0}\,\exp\left(-\frac{r - r_0}{C}\right) \quad r > r_0 \end{aligned}\right\} \tag{I-36}$$

where:

r = radius

C = a constant with respect to r

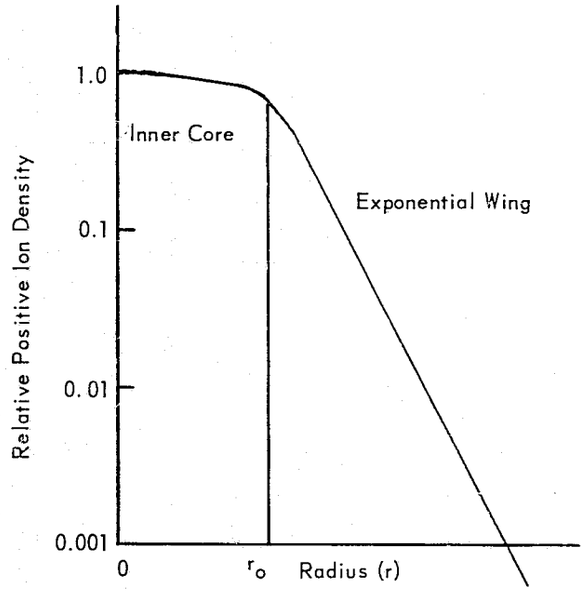

Figure I-7. Ion Density as a Function of Radial Position at a Fixed Axial Location (Ref. I-19).

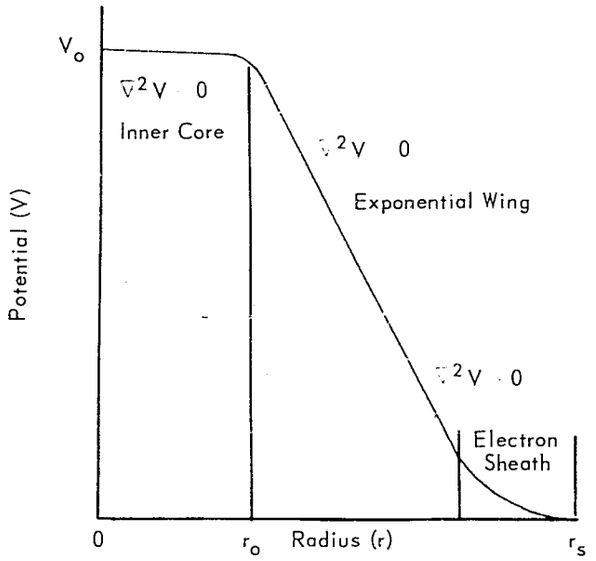

Figure I-8. Plasma Potential as a Function of Radial Postion at a Fixed Axial Location (Ref. I-19).

These equations provide a good correlation between ion density and plasma potential data in the inner core and a portion of the exponential wing. As previously mentioned, the lower portion of the exponential wing and the electron sheath potential variation is only postulated. However, if the beam is neutral then the total number of changes from positive ions and negative electrons must be equal. This means that the electric field at the edge of the outer sheath region must be zero. Sellen (Ref. I-21) has searched for a non-zero boundary. He found no evidence that such a non-zero boundary could exist.

Figure I-8 provides some insight into the electron motion. The electron mean radial amplitude is about r_0. The maximum amplitude is r_s. According to Code (Ref. I-19) this limitation follows from the electron temperature and the potential differences which would be generated by any further charge separation between the electron and ion colonies. This means that the neutralizing electrons cannot escape from the plasma column. When we make this statement we imply no perturbing influences. Cole also considers an interaction between the plasma column and some other plasma which contains low energy electrons. In such a reaction, an interchange between the high energy plasma electrons and the low energy plasma electrons may take place. In this case, low energy electrons enter the exhaust plume and high energy electrons escape. The charge balance is maintained. A reasonable postulate appears to be that a similar charge balance will be maintained if positive ions are removed. In this case, ion removal via such means as charge exchange reactions would also result in loss of electrons. If each charge exchange ion leaving the plasma column were to have an associated electron, then any surface intercepting this type of ion probably would not accumulate a charge. On the other hand, if the electron simply were lost because of a charge inbalance and it did not follow the ion, then intercepting surfaces could become charged. Possibly, such a charged surface then would attract electrons so that the overall effect would be one of neutralization. We have not investigated these various possibilities.

The important conclusion is that charge exchange ions which have a low velocity upon formation would be accelerated in a radial direction and leave the exhaust plume because of the overall neutrality of the plume.

Since they will leave the exhaust plume roughly perpendicular to the surface, the number which escape and intersect a surface parallel to the plume can be represented by:

$$N(r, x) = \frac{N(r)}{2 \pi x} \tag{I-37}$$

where:

x = distance from exhaust plume centerline to surface receiving the ions measured perpendicular to the exhaust plume

Substituting Equation I-34 gives:

$$N(r, x) = \frac{Q D^2 n \mu_0' \sqrt{\frac{\pi m}{8 k T}}}{8 x \left[16 \left(\frac{r}{D}\right)^4 + 8 \left(\frac{r}{D}\right)^2 + 1\right]^{1/2}} \tag{6}$$

4. REFERENCES

I-1. Hall, David F., "Evaluation of Electric Propulsion Beam Divergence and Effects on Spacecraft," Final Report Draft, MJO: 4795, TRW Systems, December 2, 1968.

I-2. White, A., GSFC, Personal Communication to W. Lyon, Hittman Associates, April 1969.

I-3. Staggs, J. F., W. P. Gula, and W. R. Kerslake, "The Distribution of Neutral Atoms and Charge-Exchange Ions Downstream of an Ion Thrustor," NASA Technical Memo TM-X-52259, January 1967.

I-4. Staggs, J. F., Edward A. Richley, and William P. Gula, "Ion Extractor System Design," AIAA Journal, Volume 5, No. 2, February 1967, pp. 359-360.

I-5. Hamza, V. and E. A. Richley, "Numerical Solution of Two-Dimensional Poisson Equation: Theory and Application to Electrostatic-Ion-Engine Analysis," NASA Lewis Research Center TN D-1323 (October 1962).

I-6 Kirstein, P. T. and J. S. Hornsby, "A Fortran Programme for the Emitting Surface," Centre of European Nuclear Research Report 63-16 (1963).

I-7. Hamza, V., "Numerical Solution of Axially Symmetric Poisson Equation: Theory and Application to Ion Thrustor Analysis," NASA Lewis Research Center TN D-1711 (May 1963).

I-8. Bogart, C. D. and E. A. Richley, "A Space-Charge-Flow Computer Program," Lewis Research Center NASA TN D-3394 (April 1966).

I-9. Hollway, D. L., "An Electrolytic-Tank Equipment for the Determination of Electron Trajectories, Potential and Gradient," I.E.E. Proc. 103, 155-160, Paper 1837 M (March 1963).

I-10. Loukochkov, V. S., "Electrolytic Tank With Current Leading Elements for Studying Space Charge Distribution in Electron Tubes," LeVide 11, 328-337 (September-October 1956).

I-11. Van Duzer, T. and G. R. Brewer, "Space Charge Simulation in an Electrolytic Tank," J. Appl. Phys. 30, 291-301 (March 1959).

I-12. Staggs, J. F., "An Electrolytic Tank Analog for Two-Dimensional Analysis of Electrostatic-Thruster Optics," NASA Lewis Research Center TN D-2803 (May 1965).

I-13. Staggs, J. F., William P. Gula, and William R. Kerslake, "Distribution of Neutral Atoms and Charge-Exchange Ions Downstream of an Ion Thruster," Journal of Spacecraft and Rockets, Volume 5, No. 2, February 1968, pp. 159-164.

I-14. Lockwood, D. L., W. R. Mickelsen, and V. Hamza, "Analytic Space Charge Flow and Theoretical Electrostatic Rocket Engine Performance," ARS Paper 2400-52, 1962.

I-15. Terman, F. E., Radio Engineers' Handbook, McGraw Hill, 1943, p. 287.

I-16. Condon, E. U., and Hugh Odishaw, Handbook of Physics, McGraw-Hill, second ed., 1967.

I-17. Lee, John F., Francis W. Sears, and Donald L. Turcotte, Statistical Thermodynamics, Addison-Wesley, 1963.

I-18. Sellen, J. M., Jr., R. F. Kemp, and R. H. Hieler, "Observations of Neutralized Ion Thrust Beams in the 25-Meter NASA Testing Chamber," NASA CR-53634, TRW, April 1964.

I-19. Cole, Robert K., H. S. Ogawa, and J. M. Sellen, Jr., "Study of Electric Spacecraft Plasma and Field Interactions," 07677-6013-R000, TRW Systems, May 1, 1968.

I-20. Kemp, R. F. and J. M. Sellen, Jr., "Plasma Potential Measurements by Electron Emissive Probes," Rev. Sci. Inst., Volume 37, 1966, pp. 455-461.

I-21. Sellen, J. M., Jr. and R. F. Kemp, "Cesium Ion Beam Neutralization in Vehicular Simulation," ARS Reprint 61-84-1778, June 1961.

APPENDIX II

SURFACE EFFECTS

1. INTRODUCTION

If a low energy atom collides with a surface it may stick to that surface. Its behavior after the initial interaction then is determined in part by the surface temperature. If surface attraction effects are neglected, the probability of escape can be correlated to the vapor pressure exhibited by the adsorbed atoms. Atoms which evaporate from the surface have an equal probability of being given a velocity vector in any direction.

As the energy, and therefore velocity, of the incoming atoms is increased, the adsorption phenomena change. Atoms may penetrate into the surface and the energy may be high enough that surface atoms are ejected in a manner analogous to ejection of debris by an impacting body. This phenomenon is known as sputtering.

Contaminant atoms which stick to a surface will change the surface characteristics. Obviously, as more and more contaminant is accumulated, a surface becomes more "contaminant like" in its appearance. Since we are investigating the effect upon thermal radiators, the change of relative emissivity and absorptivity is of interest. Very thin contaminant layers may have little effect. If the layer is thick enough, the surface will absorb and emit thermal energy as though it were pure contaminant.

Many thrusters use a reactive propellant. Hence, surface resistance to chemical attack is an important consideration.

Each of these effects will be considered in this appendix.

2. SURFACE CONTAMINATION

From a theoretical viewpoint, all surfaces are contaminated when fabricated since the spacecraft is assembled in a environment which contains gaseous molecules. Further contamination, such as occurring due to fingerprints, grease, or so forth, also is common. Clean room assembly and careful handling can minimize these effects, but proximity to the sea coast for most of our spacecraft launches will result in contamination due to salt in the air. Typical contaminate thicknesses under atmospheric conditions are a layer of water which is 55 molecules deep, 4.8 molecules thickness of carbon dioxide, and a monolayer of nitrogen (Ref. II-1). Such contamination does not concern us unless the surface function is compromised. For example, adsorption of photons in a coating of contaminate can be described by Lambert's law (Ref. II-1):

$$\log\left(\frac{I}{I_0}\right) = -A\ell \qquad \text{(II-1)}$$

where:

I_0 = incident spectral intensity (a function of wavelength)

I = transmitted spectral intensity

A = absorptivity

ℓ = thickness

Thus, if a certain thickness of contaminant would decrease the light intensity by 50%, doubling the thickness would cut the intensity by 75%. Since adsorptivity is a function of wave length, distribution of solar energy will change with thickness of contaminant. Further, transmission losses are a function of the type of contaminant. Regardless of the effect, provided one occurs, one of the first steps is to determine the quantity which can accumulate.

Langmire (as reported by Ref. II-2) has stated that in general molecules which impinge upon a clean surface do not rebound but condense and are held by the surface atom force field. Condensed molecules subsequently may evaporate with the behavior dependent upon surface force intensity, adsorbent characteristics, environmental pressure, and temperature. Considerable work has been expended to describe this behavior. For purposes of this study, we will bypass the detailed characteristics in favor of a more general approach.

If an incident molecule is not adsorbed, then it obviously will be reflected. Raff (Ref. II-3) lists the following general behavior of gases that are interacting with solids:

(1) The spatial distributions of reflected gaseous particles tend to be specular (i.e., reflection angle tends to equal the incidence angle) for clean surfaces but becomes more diffuse (cosine-type scattering) as the surface becomes contaminated.

(2) As the attractive interaction between gaseous particle and surface increases, the spatial distribution shifts towards the surface normal and tends to become more diffuse.

(3) As the average incident beam energy decreases, the angular distributions tend to shift toward the surface normal. Helium, however, seems to be an exception to this general rule . . . .

(4) The nature of the spatial distribution is strongly dependent upon incidence angle of the beam and the nature of this dependence seems to vary from one gas to another.

(5) The spatial distributions tend to shift toward the surface normal (i.e., become subspecular) as the surface temperature increases.

Obviously, we are dealing with a complex phenomenon. To avoid these complexities, a simplified approach is to assume either specular or diffuse reflection, depending upon which is worst, and evaluate the results. In most cases, this will be sufficient to establish whether a problem may or may not exist.

3. STICKING

The sticking probability or coefficient is the ratio of the number of particles which do not instantaneously bounce from a surface to the number which are incident upon the surface. Sticking probability normally ranges from about 0.3 to 1.0. The value is a strong function of surface conditions, and, to be conservative, one normally assumes a sticking probability of one in calculating accumulation rate upon a surface. With this assumption, the predicted accumulation rates are greater than achieved in practice.

3.1 Ammonia

May (Ref. II-4) has studied interaction of NH_3 with a tungsten surface. He found it to be absorbed at room temperature in an undissociated state. When the surface was heated to 500°K a partial decomposition occurred with evolution of hydrogen but not nitrogen. The residue had the stoichiometry NH_2. The NH_2 groups ordered into a centered rectangular array at 800°K and partial evaporation of NH_2 began at 900°K. The rectangular array became unstable at 1050°K but retained the NH_2 composition. Nitrogen and atomic hydrogen evaporate at 1200°K and surface cleanliness is achieved at 1300°K.

Adsorption of the second layer occurs as weakly held NH_3 on top of the NH_2 layer. The tungsten work function is barely changed by a layer of NH_2, but is reduced by about one volt by a layer of NH_3. It makes little difference whether the NH_3 is on top of bare tungsten or is adsorbed on top of a layer of NH_2.

Behavior of ammonia on W (211) is similar in many ways to its behavior on W (100) although the surface structures are very different during decomposition.

Hydrogen was found to interfere with the adsorption of ammonia, but ammonia was adsorbed at room temperature in all of the experiments. A sufficiently long exposure to NH_3 will result in complete displacement of the hydrogen. Nitrogen does not adsorb in the presence of hydrogen since its sticking probability is much lower. It also does not interfere with NH_3 adsorption at room temperature, but interference is expected from strongly held nitrogen at elevated temperatures.

A sticking probability of 0.8 is reported by May for NH_3 on W (211). A value of 0.45 for clean W(100) also is referenced. The sticking probability of hydrogen is reported by May as 0.3. For our purposes, it probability will be sufficient to assume a sticking probability of one to evaluate accumulation effects. (While at the same time using a non-sticking probability of one to evaluate reflection effects. Of course, these are incompatible, but are completely sufficient for determining if a problem may exist.)

3.2 Cesium

Hall (Ref. II-5) states that cesium wets most surfaces and further states that condensation rate should be independent of arrival velocities up to about 500 m/sec. (Cesium velocity at room temperature is about 200 m/sec.). This means neutral cesium atom accumulation rate should be predictable since if a liquid wets a surface, it has a higher binding energy to the surface than to itself. In this case, the initial monolayer probably will be formed easily if the arrival rate exceeds the bulk evaporation rate. (The "probably" is included because impurities could change the conclusion. If the surface were not wetted we could still obtain accumulation due to impurities or perhaps geometric effects. If, for example, one atom sticks to the surface, then other atoms may stick to the initial one. Then conditions might become favorable for whisker formation.) This behavior is consistent with Dushman's (Ref. II-2) quote of an investigator who determined a sticking coefficient of one for metal atoms condensing upon metal surfaces.

3.3 Teflon

Behavior of exhaust from a Teflon thruster is different in many respects when compared to other thrusters. The principal exhaust product appears to be monomer plus (perhaps) atomic species. These will have high vapor pressures and would evaporate quickly from a surface if they retained their original identity. But, the Teflon monomer repolymerizes upon surfaces, forming a Teflon-like polymer which has a low vapor pressure and will not readily re-evaporate. The extent of condensation, chemical recombination, and re-evaporation has not been determined. Therefore we have not attempted a quantitative treatment. Further background is provided in Appendix VII.

4. ACCUMULATION

4.1 Theoretical Treatment

Accumulation rate may be estimated from the equation:

$$\begin{matrix}\text{Rate of change of number} \\ \text{of cesium atoms}\end{matrix} = \begin{matrix}\text{Condensation} \\ \text{or sticking} \\ \text{rate}\end{matrix} - \begin{matrix}\text{Evaporation} \\ \text{rate}\end{matrix} \qquad \text{(II-2)}$$

We further can write:

$$\begin{matrix}\text{Condensation} \\ \text{rate}\end{matrix} = \begin{bmatrix}\text{Arrival} \\ \text{rate}\end{bmatrix} \begin{bmatrix}\text{sticking} \\ \text{coefficient}\end{bmatrix} \qquad \text{(II-3)}$$

Treating the case of unity sticking coefficient to predict build up rate will never underestimate the amount of contaminant. Therefore we make that assumption. Next we neglect sputtering of condensed contaminant and consider a pure material. This means evaporation rate may be computed from the vapor pressure.

Lee (Ref. II-6) has shown that the total number of atoms crossing an incremental area from either side per unit area per unit time is:

$$N = \frac{m\,\bar{v}}{4} \qquad \text{(II-4)}$$

where:

m = atom density

$\bar{v}$ = mean atom velocity

Vapor pressure is the pressure exerted against a container wall by the atoms inside the container provided the temperature is at the point where vapor and liquid are at equilibrium. The pressure exerted against a container, and hence simply pressure, is given by (Ref. II-6, Eq. 2-14):

$$P = \frac{n\,m\,\overline{v^2}}{3} \qquad \text{(II-5)}$$

Further (Ref. II-7, Eq. 2.33):

$$\overline{v^2} = \frac{3\,k\,T}{m} \qquad \text{(II-6)}$$

so that:

$$P = n\,k\,T \qquad \text{(II-7)}$$

Mean velocity is given by (Ref. II-6, Eq. 3-32):

$$\bar{v} = \sqrt{\frac{8\,k\,T}{\pi\,m}} \qquad \text{(II-8)}$$

where:

k = Boltzmann constant

T = temperature

m = atom mass.

Substitution gives:

$$N = m\sqrt{\frac{k\,T}{2\,\pi\,m}} \qquad \text{(II-9)}$$

Or:

$$n = \frac{P}{k\,T} \qquad \text{(II-10)}$$

Substitution now yields:

$$N = \frac{P}{\sqrt{2\,\pi\,m\,k\,T}} \qquad \text{(II-11)}$$

We now may complete the rate balance:

$$\frac{dN}{dt} = \Gamma_a - \frac{P}{\sqrt{2\,\pi\,m\,k\,T}} \qquad \text{(15)}$$

where:

$\frac{dN}{dt}$ = rate of change of the number of contaminant atoms or molecules per unit area of surface

Γ_a = contaminant atom or molecular arrival rate

The rate at which contaminant evaporates as fast as it is received is of interest. Hence, we set $dN/dt = 0$ to obtain (see also, for example, Ref. II-8):

$$\Gamma_a = \frac{P}{\sqrt{2\,\pi\,m\,k\,T}} \qquad \text{(II-12)}$$

If Equation 15 shows an increasing quantity of contaminant with time, we know that the section of spacecraft under consideration probably will become coated. Conversely, if the quantity decreases with time, the thickness will be at most only a few monolayers (and probably less) provided chemical reactions are not taking place. (Contaminant on a surface will behave as bulk material if more than a few monolayers thick.) Equation II-12 predicts the case for which evaporation and arrival rates are equal. In practice, we compute the arrival rate and compare with the Eq. II-12 arrival rate. If the Eq. II-12 value is smaller contaminant will accumulate; if larger, it will not.

4.2 Cesium

To compute rates, one first must obtain the vapor pressure. The rate information then will follow immediately from Eq. 15 or II-12.

Cesium vapor pressure data from Nottingham (Ref. II-9) and from Hatsopoulos (Ref. II-8) are presented in Figure II-1. Nottingham's values labeled "Best Fit" are based upon experimental vapor pressure data and are consistent with most of the data used in thermionic research. The fitted curve is:

$$\log (P) = - \frac{3920.38}{T} - 0.519781 \log (T) + 10.71914 \qquad \text{(II-13)}$$

where:

P = pressure, N/m^2

T = temperature, °K.

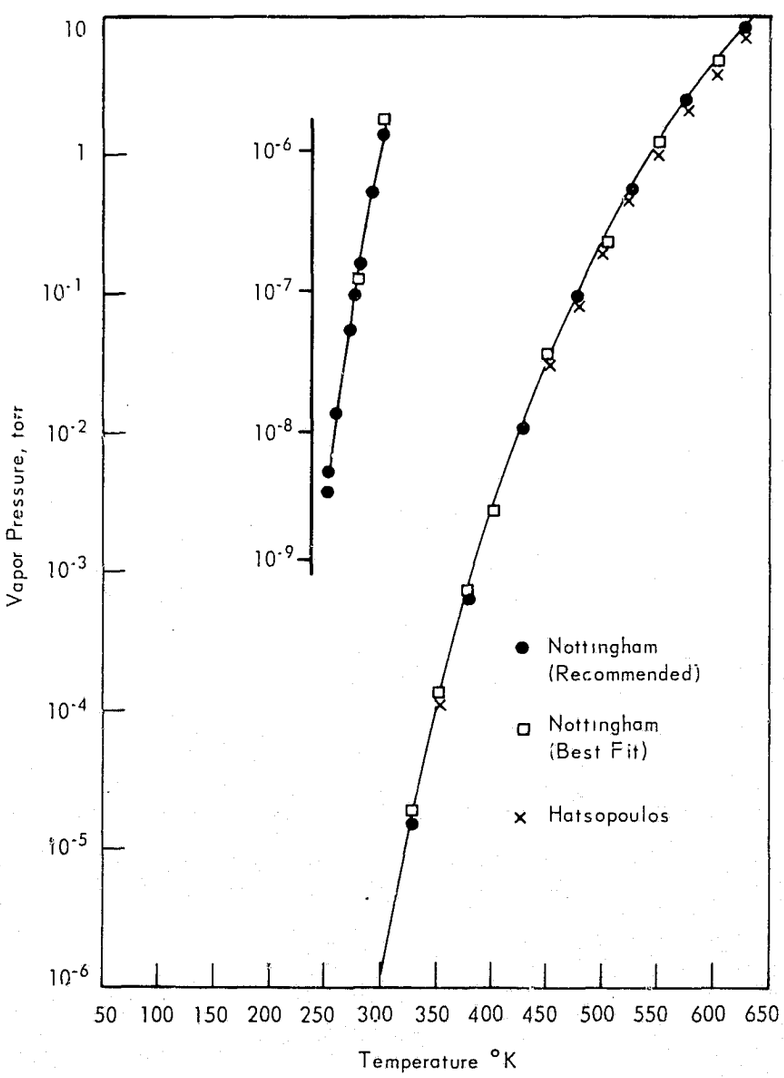

Figure II-1. Cesium Vapor Pressure.

But this equation leads to inconsistences in the heat of condensation at 0°K. For this reason, Nottingham presents a thermodynamically consistent equation:

$$\log (P) = -\frac{4053.30}{T} - 0.915282 \log (T) + 12.05025 \qquad \text{(II-14)}$$

This is the "Recommended" portion of Figure II-1. Data taken from Hatsopoulos are presented for comparison. (Although the agreement appears to be excellent, this is due to the scale. Variations of 30 percent are common.) We will follow Nottingham's recommendations and use the thermodynamically consistent relationship. An important reason for this selection is the large extrapolation we plan to about 100°K. It will be important that the equation extrapolate to this range with reasonable accuracy. Thermodynamic consistency at 0°K will help assure this.

Equation II-14 provides the following data:

Temperature, °K	Vapor Pressure, N/m^2	Vapor Pressure, torr
50	1.72×10^{-71}	1.29×10^{-73}
100	4.90×10^{-31}	3.68×10^{-33}
150	1.09×10^{-17}	8.18×10^{-20}
200	4.79×10^{-11}	3.59×10^{-13}
250	4.41×10^{-7}	3.31×10^{-9}

With the selections:

$k = 1.3805 \times 10^{-23}$ J/°K

$m = 2.20 \times 10^{-25}$ kg

we obtain:

Temperature, °K	Γ_a atoms/m^2 sec	Γ_a atoms/cm^2 sec
50	5.56×10^{-49}	5.56×10^{-53}
100	1.121×10^{-8}	1.121×10^{-12}
150	2.04×10^{5}	2.04×10^{1}
200	7.08×10^{11}	7.08×10^{7}
250	6.39×10^{15}	6.39×10^{11}
300	$2.47 \times 10^{18*}$	2.47×10^{14}
350	$1.690 \times 10^{20*}$	1.690×10^{16}
400	$3.92 \times 10^{21*}$	3.92×10^{17}
450	$4.44 \times 10^{22*}$	4.44×10^{18}
500	$3.04 \times 10^{23*}$	3.04×10^{19}

The allowable arrival rate (really evaporation rate) is statistically meaningless below about 180 or 190°K. For practical purposes, the important conclusion is that no cesium atoms will evaporate below about 150°K and therefore, if evaporation is the only escape mechanism, the build-up rate will equal the arrival rate for a surface below 150°K. The behavior is plotted in Figure II-2 and 2.

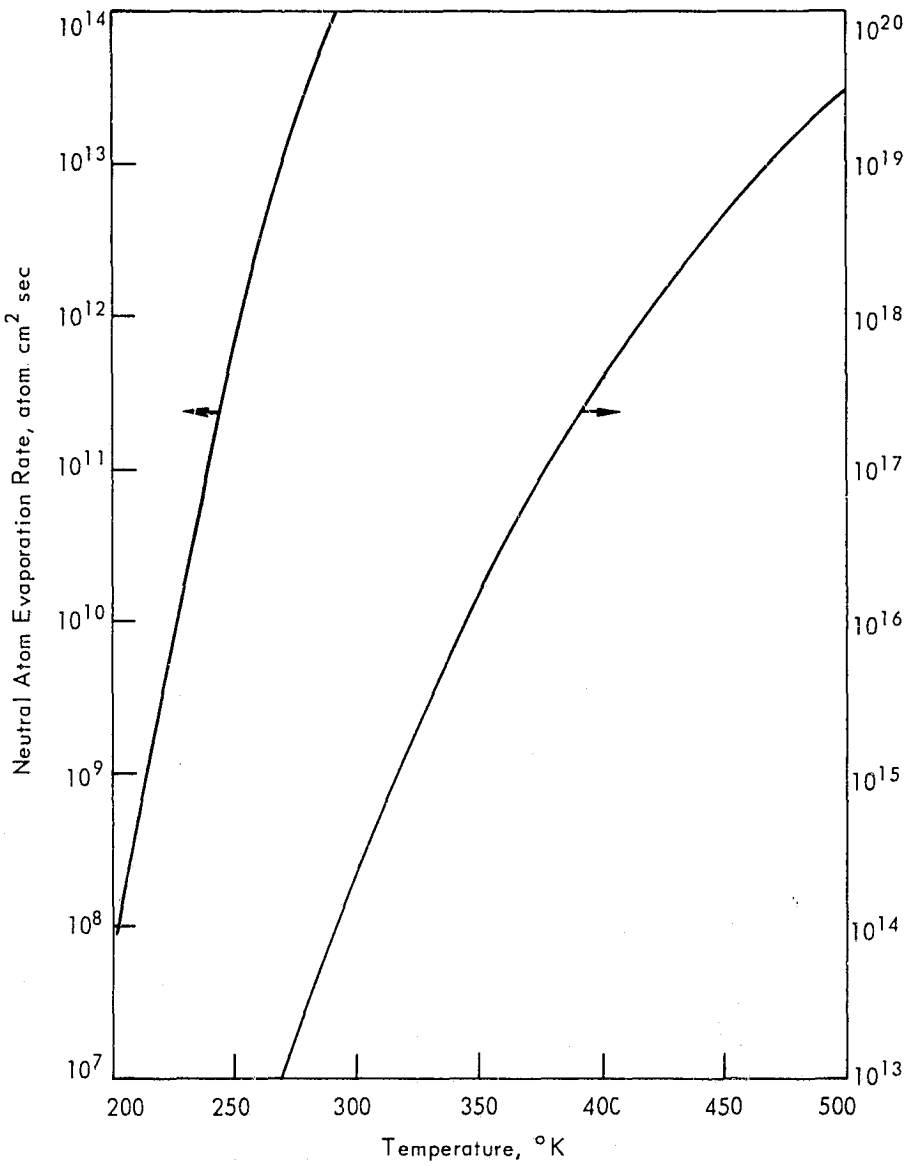

Figure II.2. Cesium Atom Evaporation Rate

4.3 Ammonia

Adsorption of the first monolayer of ammonia on tungsten is relatively strong, and a temperature of about 1300°K is required to remove all of it. Adsorption of the second layer is reported to be relatively weak with a subsurface of tungsten. If this phenomenon is true with other surfaces as well, then treatment of more than two or three monolayers can be based strictly upon the vapor pressure of the ammonia and the rate at which incoming ammonia hits the surface. Even if the uppermost layers are held more strongly, after accumulation of a few monolayers, this assumption will be valid. Consequently, we may apply the theoretical treatment of Section 4.1.

Ammonia vapor pressure data from References II-10 through II-13 are summarized in Figure II-3. Since these data did not cover the range of interest, we replotted them on the compressed scale of Figure II-4 (see also Figure 10). The thermodynamic consistency was perfect (see Section II.4.4 for the technique) and further, the line passed through one point we obtained at 100°K (Ref. II-14, a verbal communication) lending further substantiation to the extrapolation.

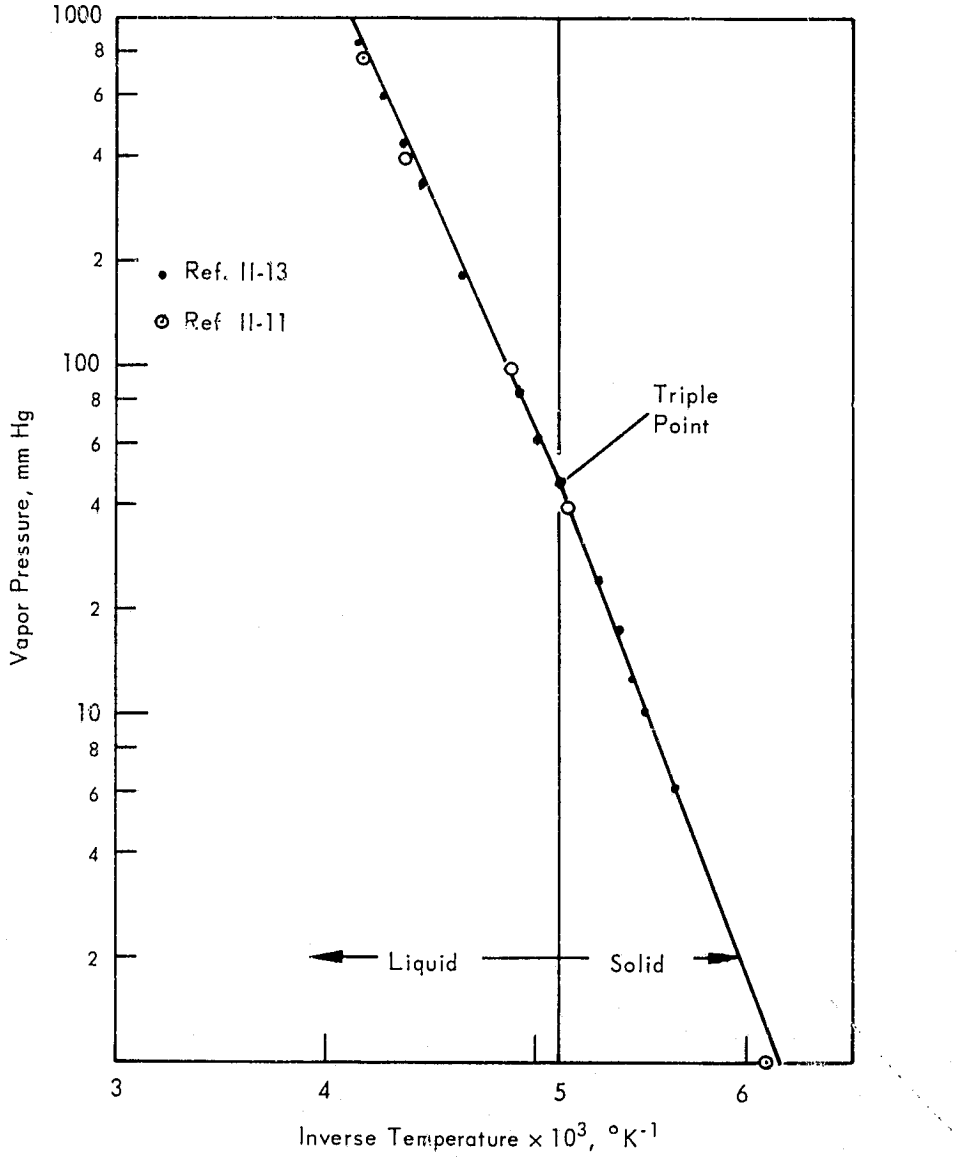

Figure II-3. Ammonia Vapor Pressure.

The ATS-F and -G design incorporates a radiator that is to operate at 100°K. Equation II-12, for this condition, gives an NH_3 evaporation rate of:

$$\Gamma_A = \frac{(6 \times 10^{-7})\ (1333)}{[(2)\ (\pi)\ (17/6.02 \times 10^{23})\ (1.38 \times 10^{-16})\ (100)]^{1/2}}$$

$$= 5 \times 10^{14} \text{ molecules/cm}^2 \text{ sec}$$

Any incoming rate greater than this might result in accumulation of NH_3 on the radiator. Most of the spacecraft will operate at a higher temperature. Taking 250°K as a lower limit for most components or surfaces, we obtain:

$$\Gamma_A = (5)\ (10^{14})\ \frac{10^3}{6 \times 10^{-7}}\ \sqrt{\frac{100}{250}}$$

$$= 5 \times 10^{23}$$

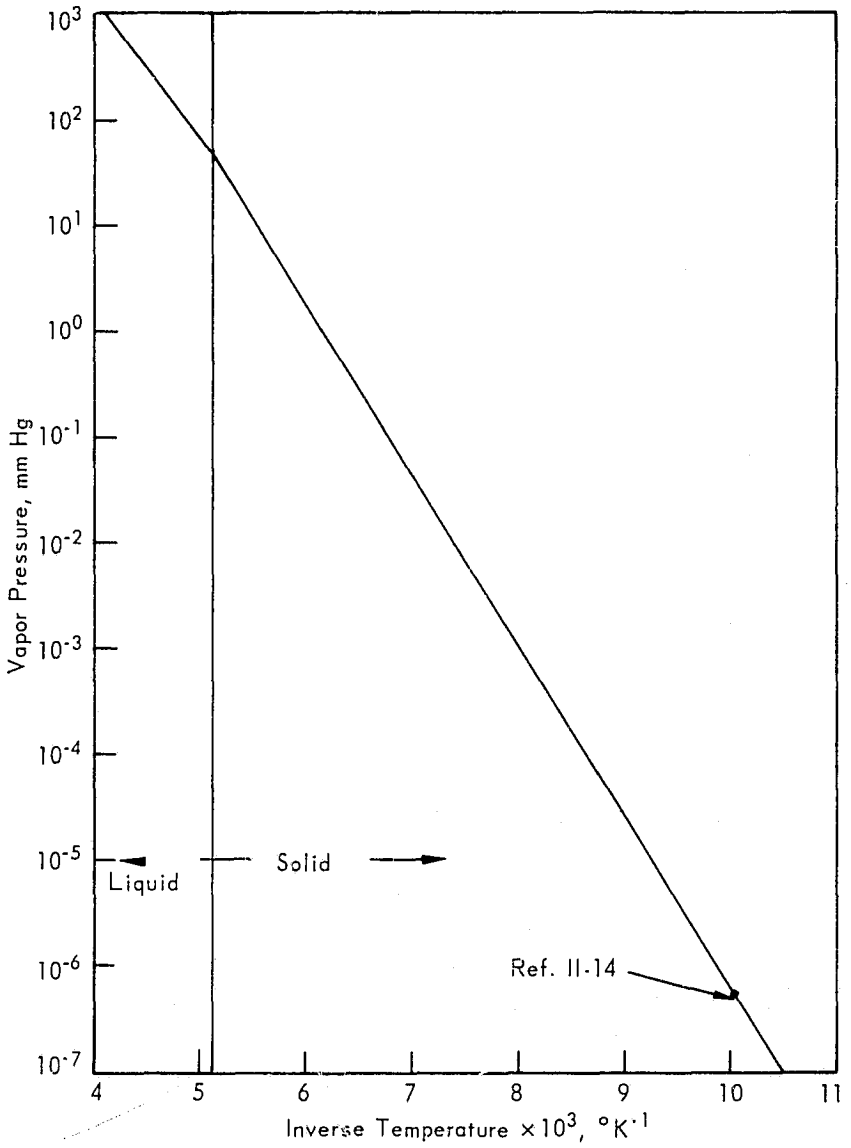

Figure II-4. Ammonia Vapor Pressure.

SMS uses a radiator at 70°K. To compute the evaporation rate at this temperature, we first note two values from Figure II-4. At $1/T = 10.49 \times 10^{-3}\ ^{\circ}K^{-1}$, $P = 10^{-7}$ mm Hg; at 5.43×10^{-3}, 10^{+1}. The vapor pressure behaves according to:

$$\ln P = m\left(\frac{1}{T}\right) + C \qquad \text{(II-15)}$$

where:

m = slope

C = intercept

Using the above values:

$$\ln P = -\frac{3640}{T} + 22.1 \qquad \text{(II-16)}$$

At 70°K, P = 1.04×10^{-13} mm Hg. (This is significantly below the 100°K value of 6.2×10^{-7}.) At 70°K, Eq. II-12 gives an evaporation rate of:

$$\Gamma = \frac{(1.04)\,(10^{-13})\,(1333)}{[(2\pi)\,(17/6.02 \times 10^{23})\,(1.38 \times 10^{-16})\,(70)]^{1/2}}$$

$$= 1.06 \times 10^{8} \text{ molecules/cm}^2 \text{ sec}$$

This is a very low evaporation rate.

4.4 Hydrazine

Vapor pressure data exist in the literature for the liquid above 0°C, including References II-15, -16, -17, and -18. We found only one data point for the solid during our search for hydrazine effects. This includes a literature search for exhaust effects, etc., the Chemical Abstracts (1907 through 1969), and the Engineering Index (1961-1969). We next tried the Chemical Thermodynamics Data Group (Ref. II-19), the Cyrogenic Data Center (Ref. II-20), and the Thermophysical Properties Research Center (Ref. II-12). No luck. (Each of these centers conducted searches of their files for us. Shafer, of the Thermophysical Properties Research Center, found Ref. II-18 for us. Consequently, we have estimated the vapor pressure of $N_2 H_4$ (solid) at low temperatures by taking into account the change in phase characteristics as predicted by basic thermodynamics. The accuracy of this technique probably will be within an order of magnitude (according to Wagman, Ref. II-19).

We first note the Clausius-Clapeyron equation (Ref. II-21):

$$\frac{dP}{dT} = \frac{\lambda}{T \Delta v} \qquad \text{(II-17)}$$

where:

P = pressure

T = temperature

λ = latent heat of phase change

Δv = volume change accompanying phase change

This equation is thermodynamically rigorous - it follows directly from the basic premises of thermodynamics - and as such is an exact representation of vapor pressure behavior. If the volume of liquid or solid is small in comparison to that of the vapor, then $\Delta v \approx v_v$, the volume of the vapor, and:

$$\frac{dP}{dT} = \frac{\lambda}{T v_v} \qquad \text{(II-18)}$$

An ideal gas behaves according to:

$$P v_v = R T \tag{II-19}$$

where

R = gas constant

Hence, we may eliminate v_v to obtain:

$$\frac{d \ln P}{d T} = \frac{\lambda}{R T^2} \tag{II-20}$$

If we treat λ as a constant, this may be integrated directly to obtain:

$$\ln P = \frac{\lambda}{R T} + C \tag{II-21}$$

where:

C = integration constant.

This implies that a plot of ln P vs 1/T should be a straight line (provided λ is constant). The constant λ assumption is reasonably good (although not perfect) everywhere except at the melting point. Here there is a discontinuity in the slope, but not the function; behavior which provides an excellent extrapolation technique. We need only change the slope at the melting point to extrapolate from liquid to solid and thence downward in temperature.

The plot of vapor pressure for liquid N_2H_4, using data from Haws (Ref. II-16) is shown in Fig. II-5. The end points of this curve are P = 1 @ $1/T = 3.91 \times 10^{-3}$ and P = 10^5 @ $1/T = 1.57 \times 10^{-3}$. The slope is:

$$m = \frac{\ln 10^5 - \ln 1}{(1.57 - 3.91)\,(10^{-3})} = -4.91 \times 10^3$$

But the slope is also $m = \lambda / R$. At the melting point, the heat of fusion is 3025 cal/mole (Ref. II-18) and at 25°C it is 3200 cal/mole (from equations in Ref. II-15). Equations and experiment (Ref. II-15) provide a heat of vaporization of 10,700 cal/mole at 25°C. The heat of vaporization of the solid at 25°C therefore is 10,700 + 3200 = 13,900 cal/mole. The slope of the solid vapor pressure curve therefore is (4.91×10^3) (13,900/10,700) = -6.39×10^3. Taking the freezing point as 2°C (Refs. II-15 and -16), 1/T = 0.00364. Since the vapor pressure of the solid and liquid is the same at this point, we now have enough information to construct the vapor pressure line. We wish to go to ~100°K (1/T = 0.01). Hence, we write

$$\frac{\ln 3.85 - \ln p}{.00364 - .01} = -6.39 \times 10^3$$

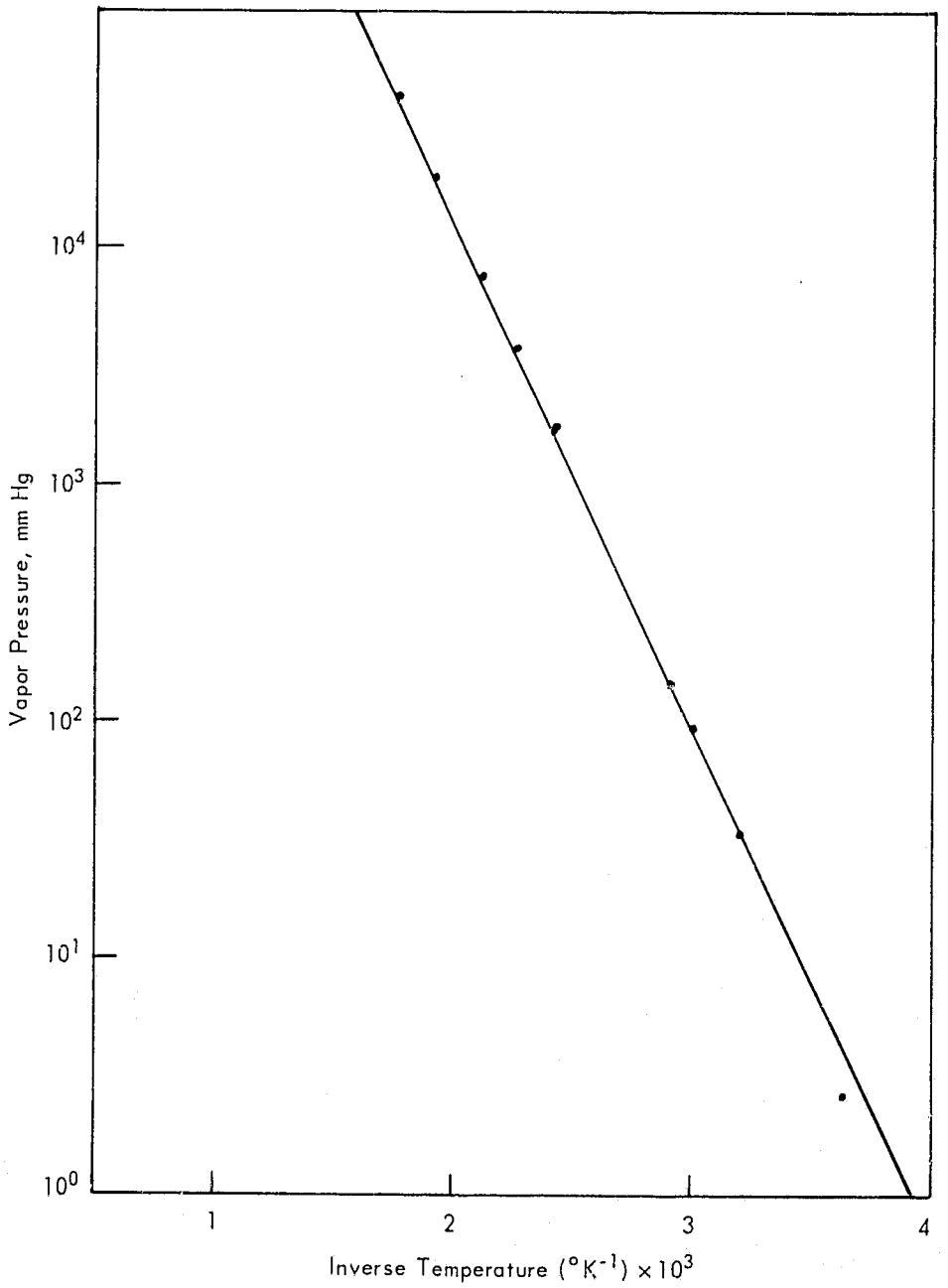

Figure II-5. Liquid/Hydrazine Vapor Pressure.

where p is the vapor pressure at 100°K. Immediately, $p = 8.62 \times 10^{-18}$ mm Hg. Now we may construct the vapor pressure line shown in Figures II-6 and 11. For comparison, we have shown the only existing experimental point. At 70°K, the only point not on the curve that is of interest, $p \approx 10^{-29}$ mm Hg.

If needed, better accuracy in the extrapolation can be obtained. One merely needs to incorporate the enthalpy (and/or heat capacity) information that is available.

The hydrazine evaporation rate at 70°K is:

$$(1.06 \times 10^8)\left(\frac{10^{-29}}{1.04 \times 10^{-13}}\right)\left(\frac{17}{32}\right)^{1/2}$$

$$= 7 \times 10^{-9} \text{ molecules/cm}^2 \text{ sec}$$

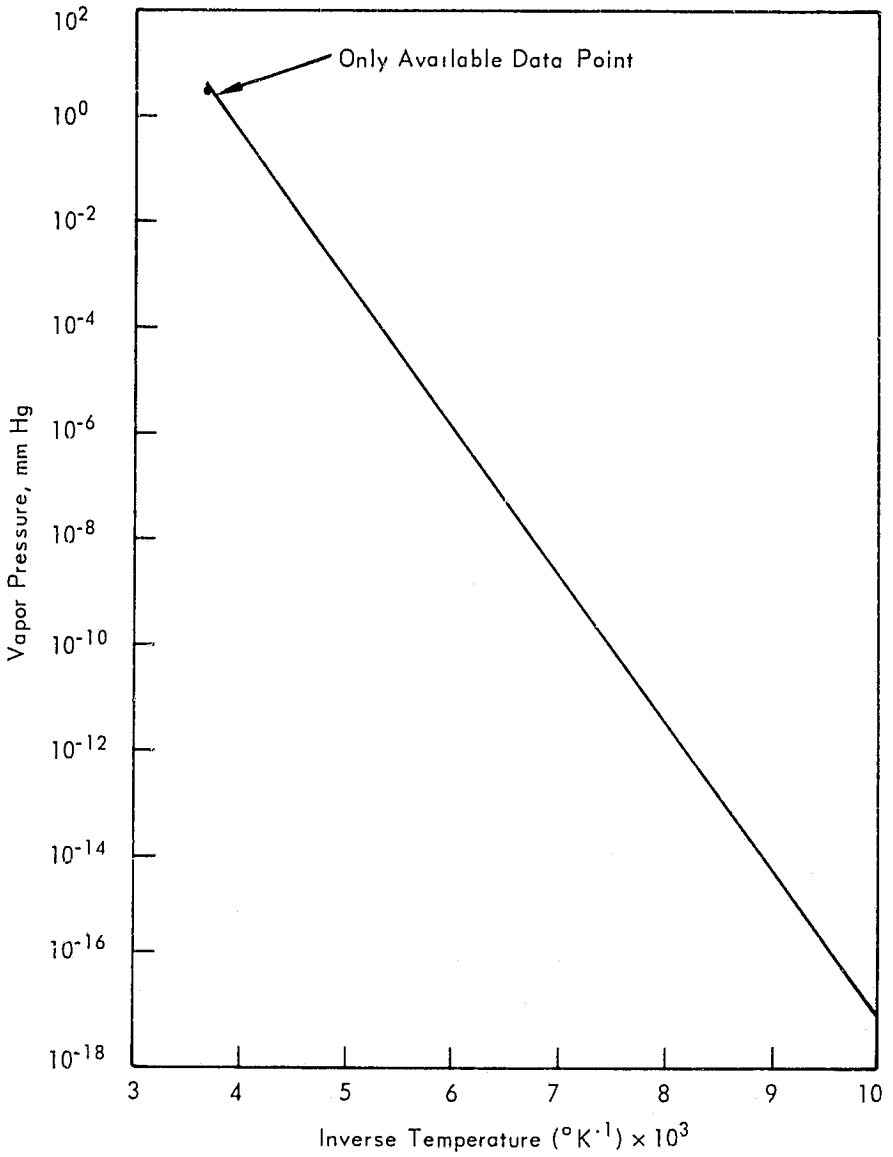

Figure II-6. Solid/Hydrazine Vapor Pressure.

This rate is so low as to be statistically meaningless. No hydrazine evaporates!

Propellant grade N_2H_4 probably will contain 0.3 to 0.5% H_2O. To check on its behavior, we first note the vapor pressure as shown in Fig. II-7. The lowest point on the curve occurs at a pressure of 10^{-8} mm Hg and an inverse temperature of 6.88×10^{-3} $°K^{-1}$ (145°K). The evaporation rate at this temperature is, from Eq. 15:

$$\frac{(10^{-8})\,(1333)}{[(2\pi)\,(18/6.02\times 10^{23})\,(1.38\times 10^{-16})\,(145)]^{1/2}}$$

$$= 6.91 \times 10^{12} \text{ molecules/cm}^2 \text{ sec}$$

which is relatively small. We can obtain the vapor pressure at 100°K by noting the ratio equation:

$$\frac{\ln(10^{-1}) - \ln(10^{-8})}{4\times 10^{-3} - 6.88\times 10^{-3}} = \frac{\ln(10^{-1}) - \ln(p)}{4\times 10^{-3} - 10\times 10^{-2}}$$

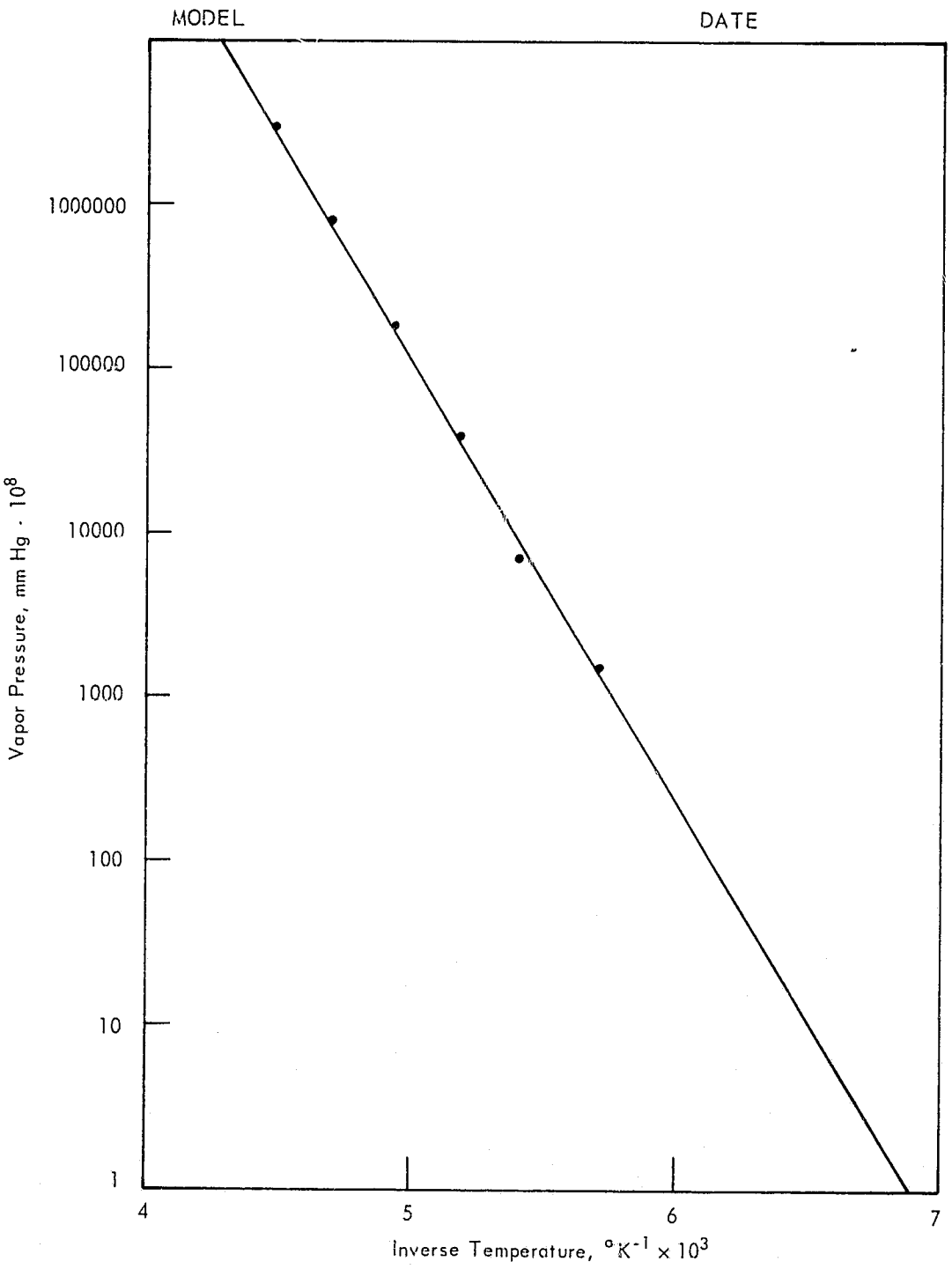

Figure II-7. Vapor Pressure of Ice (Ref. II-11).

where p is the vapor pressure at 100°K ($1/T = 10 \times 10^{-2}$). Immediately, $p \approx 2.5 \times 10^{-16}$. The evaporation rate at 100°K then is:

$$\left[\frac{(2.5)\ (10^{-16})}{10^{-8}}\right]\left[\frac{145}{100}\right]^{1/2} (6.91 \times 10^{12})$$

$$\approx 2 \times 10^5 \text{ molecules/cm}^2 \text{ sec}$$

This is extremely low. For example, one monolayer contains $(6.02 \times 10^{23}/18)^{2/3} = 1.08 \times 10^{15}$ molecules/cm^3. For practical purposes, water does not evaporate at temperatures lower than ~130 to 150°K.

4.5 Nitrogen and Hydrogen

These gases, which result from decomposition of N_2H_4, have high vapor pressures which will prevent bulk accumulation on spacecraft surfaces. Nitrogen has a one atm. vapor pressure at -196°C; hydrogen at -252°C. Since these appear to be no problem we have not studied their evaporation characteristics.

5. SPUTTERING

A large amount of work has been performed in the investigation of sputtering by atoms and ions. Despite this effort, we do not fully understand the phenomenon. Dunnill (Ref. II-22) investigated the literature and the basic physical processes of sputtering. He could find no relationship which would predict the sputtering phenomenon with any degree of accuracy as a function of the various operating parameters of an ion beam and the target material. As a consequence, he arrived at a semiempirical relationship which he recommends for preliminary design work:

$$S = S_m \left[1 - e^{-K(E - E_t)}\right] \qquad \text{(II-22)}$$

where:

S = sputtering ratio

= number of target atoms ejected per incoming particle

E = energy of incoming particle

E_t = threshold energy for sputtering

and S_m and K are functions of the target and ion beam properties. This equation gives a linear behavior for low energies and provides a sputtering ratio which approaches a constant at higher energies. It is not applicable for very high energies (considerably above those of interest for the cesium ion engine) because, as reported by Trollinger (Ref. II-23), the sputtering ratio eventually decreases with increase in ion energies. Trollinger also reports that the maximum value occurs at lower energies for lower molecular weight beams and that the decrease with increasing energy is defined more sharply in such cases.

Hall (Ref. II-5) reports a threshold energy in the vicinity of 25 electron volts. Trollinger presents a number of graphs of sputtering ratio as a function of energy which exhibit threshold energies in the vicinity of 50 electron volts for solids and 30 electron volts for liquids. We immediately conclude that sputtering will not occur due to the neutral atom effluent from the ion engine. Since the Group 1 ions never intersect the spacecraft components, these are no problem. Group 4 ion energies will be, for practical purposes, below the threshold value and will not cause sputtering. Therefore, we need only be concerned with sputtering due to the Group 2 ions. Energies of these ions will vary from close to the Group 1 energy downward to the Group 4 level. Some of these may cause sputtering since energies will be above the threshold values.

The direction of sputtered material will be of interest because of possible effects in the cryogenic radiator. Correlation of experimental data from several investigators is good with respect to the angular distribution. In general, for incident particle energies below approximately 3 kev, an under cosine distribution results. This distribution becomes very nearly a cosine distribution for energies between 3 and 5 kev. The cosine distribution takes the form:

$$S = \frac{S_0}{\cos \theta} \tag{II-23}$$

where S_0 = sputtering yield at normal incidence ($\theta = 0$). According to Hall this relationship is good for angles as high as 85°. As 90° is approached, little or no sputtering occurs and the yield drops rapidly to zero.

Hall also shows that the increase in removal rate with increasing incidence angle is compensated for by the change in projected target area since:

$$A = A_0 \cos \theta \tag{II-24}$$

where:

A = projected target area

A_0 = actual target area

If the incident flux at an angle θ is Γ, then the number of particles striking a particular target is:

$$\begin{aligned} \Gamma' &= \Gamma A \\ &= \Gamma A_0 \cos \theta \end{aligned} \tag{II-25}$$

If each of these was perpendicular to the surface, each of the Γ incoming particles would produce S_0 particles. By Equation II-26, each particle produces $S_0/\cos \theta$ particles. Hence, the number of sputtered particles in the area A is:

$$\begin{aligned} S' &= \frac{S_0}{\cos \theta} A_0 \cos \theta \\ &= S_0 A_0 \end{aligned} \tag{II-26}$$

which is independent of θ. Of course, Equation II-26 is only good so long as the cosine sputtering yield equation, Equation II-23, holds. Hence, Equation II-26 is not true for angles above about 85 degrees.

The effect for θ approaching 90° can lead to production of holes in surfaces which intersect. This occurs if the incident particles intersect one of the surfaces at a large θ. The incident particle then is simply deflected toward the other surface. Normally, a hit

on the other surface will cause sputtering. Since more incoming particles will intersect such a surface zone than over the entire surface, a hole will be produced which is self perpetuating.

The energy of the sputtered particles also is of interest because of the possibility of sputtered particles hitting surfaces which cause further sputtering. For low energy sputtering, Trollinger (Ref. II-23) reports energy distributions which closely approximate a Maxwellian distribution. The average energy of sputtered neutral particles is stated to vary only slightly with impingement energy to about 3 kev. Average energy of sputtered ions is stated to be slightly higher than that of neutrals. Trollinger presents several curves for incident mercury ions which show average velocities of the sputtered particles to be a factor of 10 or 20 lower in energy than the incident ion. The nature of the Boltzmann distribution shows that, for practical purposes, sputtered particles will not have high enough energies to cause further sputtering in the case of the 600 electron volt ions from our cesium engine.

A target also can cause re-emission of the beam material once it becomes coated. Most of the sputtered beam material will be comprised of neutral atomic particles. Energies of these particles appear to lie between that corresponding to the localized target temperature and that of a sputtered particle (as previously discussed). The angular distribution of particles of this type should be in the form of a cosine because of collision effects within the target lattice.

The impingement characteristics are such that the Group 2 ions which enter the cryogenic radiator opening and impact on the lower surface will not cause sputtering beyond that resulting from the initial impact. Two phenomena may take place. If some cesium is adsorbed on the lower surface due to surface effects, then it may be sputtered off in a cosine type of distribution. In this case, it will behave in precisely the same manner as the neutral atom re-evaporation situation which we previously analyzed. If, on the other hand, sputtering of a target atom were to occur, the preferred direction would be away from the radiator opening because of the angled construction of the lower radiator surface.

Impacts also can cause secondary electron emission. This phenomenon will not change the characteristics of the surfaces and hence need not concern us.

Hall presents the following equation for target erosion rate which he states to hold after an initial period during which the target is becoming saturated with propellant atoms:

$$\frac{dx}{dt} = -\frac{\Gamma S}{n} \qquad \text{(II-27)}$$

where:

$\frac{dx}{dt}$ = rate of change of target thickness with respect to time, cm/sec

Γ = bombarding ion flux density, ions/cm^2 sec

S = sputtering yield, target atoms/ion

n = target number density, atoms/cm^2

Daley (Ref. II-24) presents the curve shown in Figure II-8. This shows that the sputtering yield is about one atom per incident ion for an energy of 600 electron volts.

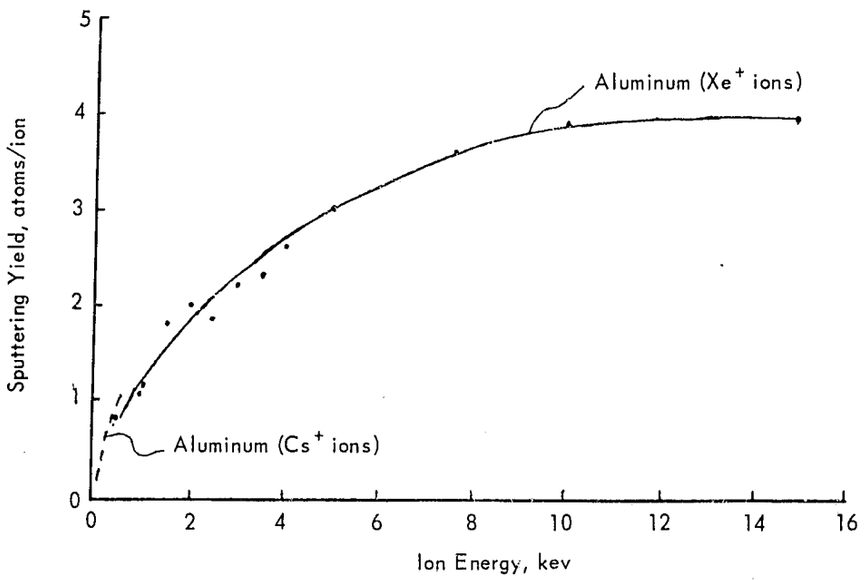

Figure II-8. Sputtering Yield of Aluminum.

Sputtering due to the atoms in the exhaust of NH_3 and N_2H_4 thrusters does not appear to be a problem because of the low atomic energies. The ammonia thruster further does not emit particulate matter and there is no source of sputtering due to that effect. This is not necessarily the case with the hydrazine thruster since catalyst loss has been reported (see Appendix VIII). Only limited data are available which indicate there is little problem.

Recent data from thruster tests, particularly with mercury, indicate considerable sputtered grid material which may cause problems. These data were obtained after this study was completed and the results have not been covered in this report.

6. CHEMICAL COMPATIBILITY

6.1 Cesium Compatibility

Considerable research has been performed with cesium compatibility in support of the thermionic conversion programs. Unfortunately, few materials utilized in thermionic diodes are used in spacecraft. Of specific interest to us are aluminum, 3M velvet paint, and perhaps gold. None of these materials are used in thermionic diodes. Hence, little of the thermionic program research can be applied with the exception of the theoretical characteristics which have been obtained.

Hall (Ref. II-5) has reported the results of a literature search on this subject. (We have not searched further, but we will list his references in support of the specific information so that the reader can go back to original data sources where desired.) This work is continuing and more experimental data are being prepared for documentation.

Hall has made no distinction between ions and atoms in considering compatibility with metals. Range of ions in metals is only a few angstroms and then the ions become neutralized. Overall chemical effect should be similar. The Armour Research Foundation (Ref. II-25) reports that aluminum and cesium are almost completely immisicible in both the liquid and the solid states. Little interaction between a layer of cesium and an aluminum surface is to be expected. There is a corrosive reaction reported between cesium and aluminum in the presence of moist air. However, such a reaction is unlikely in a spacecraft environment. A surface coating of cesium should have total relative

emissivities and absorptivities about the same as 6061 aluminum alloy. On this basis, a cesium coating would have little effect upon a radiator. We have not checked the specular behavior and these curves could be quite different. If this were to be true, then coolers (which are strongly dependent upon specular behavior for proper operation) could be affected. No distinction is made between the effect of cesium in contact with aluminum and the effect which would occur if aluminum were bombarded by cesium. In the latter case, some surface penetration would occur. The effect probably is small or negligible.

An intermetallic compound of gold and cesium has been reported (Ref. II-26). The solubility of cesium in gold is limited, but liquid cesium appears to dissolve gold at temperatures slightly above room temperature. The equilibrium data indicate formation of an intermetallic compound at the reaction interface which would change the surface properties, but would have a negligible effect upon bulk properties of metallic gold. This may have a significant effect on the relative emissivities. Some idea of the effect can be obtained by considering the bulk electrical resistivity. Parker (Ref. II-27) reports that the relative emissivity is proportional to $(\rho T)^{0.5}$ where ρ is the bulk electrical resistivity and T is the absolute temperature. Hall could not find electrical resistivity information on the desired cesium alloys. However, he did examine other alloys to obtain an engineering feel for the problem. He found instances where the bulk resistivity of an alloy was considerably larger than the bulk resistivity of either pure constituent. This implies that the relative emissivity also should be higher. Note we have not mentioned solar absorptance. The change in this property with formation of intermetallic compounds cannot be predicted. We conclude that specific tests are necessary. This even is true for aluminum where chemical reactions were not reported, but still to be safe one should perform an experimental investigation.

The 3M black velvet paint used on the ATS-F cooler cold patch is not mentioned by Hall. His discussion of other coatings, such as Cat-A-Lac black, S-13 (a paint), and other coatings indicates that reactions with cesium can be expected at temperatures in the vicinity of room temperature. Hall does not mention cesium reactions at low temperatures. About the only conclusion we can draw is that the 100°K operational temperature should greatly slow any reactions which may occur.

6.2 Ammonia Compatibility

Boyd (Ref. II-28) has compiled data covering the compatibility of NH_3 with containment materials. He divided the materials into four classes:

(a) Materials which exhibit a corrosion rate of less than one mil per year. When used as a container, the material does not promote decomposition and is free of impact sensitivity.

(b) Similar to Class 1 except the corrosion rate may be as great as 5 mil/year.

(c) Five to 50 mils/year corrosion rate with moderate breakdown of the propellant. Not shock sensitive.

(d) Corrosion rates greater than 50 mils/year. These may cause extensive decomposition of the propellant, spontaneous ignition, or reactions upon impact.

Boyd's ammonia data are compiled in Table II-1. These and similar data should be interpreted from the reporters standpoint. Some reported compatibility conclusions are based upon the planned application. For example, a metal may be satisfactory if air oxidation of the surface can be prevented but unsatisfactory if air exposure is necessary.

Table II-1
Compatibility of Materials With Ammonia (Reproduced from Ref. II-28)

Material	Temperature, F							
	Gas				Liquid			
	Class 1	Class 2	Class 3	Class 4	Class 1	Class 2	Class 3	Class 4
Metals								
Aluminum	212	100	175	> 175			175	175
302 Stainless Steel	75			< 900				
304 Stainless Steel	600			< 900				
316 Stainless Steel	600			< 900				
347 Stainless Steel			75					
410 Stainless Steel	600			850				
430 Stainless Steel	600			< 900				
Worthite	75			< 900				
Durimet 20	75			< 900				
Carpenter 20	600							
Mild Steel	600			< 900		75		
Cast Iron	600			< 900		75		
Si-Iron	212	75					75	
Ni-Cast Irons, Low Cu	75					160		
Ni-Cast Irons, High Cu	75							All
Nickel	500		500	<1100				75
Inconel	700		1100	>1100		75		
Monel	500		500	<1100				75
Hastelloy B	600	600		>1000				
Hastelloy C	600	600		>1000				
Hastelloy D	600	600		>1000				
Hastelloy F		600		>1000				
Chlorimet 2-3	75							
Nickel-Copper	75							
Copper		75		High				Low
Yellow Brass		75		High				Low
Red Brass		75		High				Low
Tin Bronze		75		High				Low
Al Bronze		75		High				Low
Si Bronze		75		High				Low
Cu-Nickel		75		High				Low
Gold	212				High			
Lead		75		> 260		75		
Dow Metal C		Low						
Dow Metal F-1		Low						
Dow Metal H		Low						
Dow Metal J-1		Low						
Dow Metal M		Low						

Material	Temperature, F							
	Gas				Liquid			
	Class 1	Class 2	Class 3	Class 4	Class 1	Class 2	Class 3	Class 4
Platinum	212				High			
Ir-Platinum	High				High			
Rh-Platinum	High				High			
Silver	75							Hot
Ag-Cu				All				All
Titanium	175							
Tantalum	212			High	212		High	
Zinc	75							
Zirconium	175							
Organic Materials								
Rubber, Hard Linings				75			75	
Rubber, Soft Linings				75				75
Rubber, Natural		75		Hot				
GRS		75		Hot				
Neoprene		75		Hot				
Butyl Rubber		75		Hot				
Thiokol			Cold					
Glass Fabric and Silicone Elastomer*		Hot						
Silicone Greases		Hot	75					
Haveg 41 Epon	212							
Silicone Elastomer		75						
Silicone Resins			75					
Teflon	Hot							
Cork				75				
Vinyl Copolymers		Hot				Hot		
Phenolics		Hot				Hot		
Furans		Hot				Hot		
Polyethylene		Hot				Hot		
Kel-F		Hot				Hot		
Vinylidene Chloride			Cold				Cold	
Sulfur Cement			Cold				Cold	
Bituminous Composition			Cold				Cold	
Polystyrene				75				
Polyesters				75				
Phenol Formaldehyde				75				
Nonmetals								
Glass	212							
Stoneware	212							
Karbate	> 2000							
Carbon	> 2000							
Graphite	> 2000							

*Glass Fabric and Silicone Rubber

Ammonia is alkaline in nature. The stainless steels, carbon steels, nickel alloys, silver, platinum, gold, and tantalum are placed in Class 1 with anhydrous NH_3. Inconel, gold, platinum, and tantalum are Class 1 materials in moist ammonia. Carbon steel and cast iron are also resistant. Copper alloys are less resistant than steel and are susceptible to cracking in an ammonia atmosphere. The upper temperature limit of many metals is related to the initiation of nitriding. Inconel is more resistant to nitriding than other nickel alloys, mild steel, or stainless steel.*

Many organic materials are suitable for ammonia service. Plastics and elastomers usually resist attack up to their softening point. Most inorganic construction materials are not attacked by ammonia.*

6.3 Hydrazine Compatibility

Most metallic materials are compatible with N_2H_4. Many plastics and rubber are compatible at room temperature. In considering the compatibility, one must realize that two criteria are applied:

(1) The corrosive effects on the material.

(2) The effect upon hydrazine.

For the most part, we are concerned only with the former. Whether the hydrazine is affected is of little concern for our application EXCEPT the change in behavior that occurs as a result of an induced chemical reaction. Normally, any reaction will be one of hydrazine decomposition. This would tend to produce higher vapor pressure products which would evaporate faster than the parent material. The effect of this type of chemistry on the surface could be interesting. The surface itself could easily be involved, with possible changes in surface properties as a result.

Hydrazine compatibility data are summarized in Table II-2.

Hydrazine is known to form many coordination compounds with metals. It has high reactivity and excellent solvent properties. It will degrade and dissolve polymeric materials, such as elastomers. Copper, zinc, and nickel are known to form coordination compounds. Iron and aluminum are less prone to this reaction, but still must be considered because of the quantity in which these substances typically are present (Ref. II-29). Sutherland (Ref. II-30) also comments upon compatibility. Titanium (6 Al/4V), most series stainless steels, and most aluminum alloys are satisfactory with hydrazine. Alloys containing copper, molybdenum, or lead should be avoided. Hydrazine-water blends are incompatible with aluminum alloys but are satisfactory with stainless steels.

6.4 Nitrogen

Nitrogen is very inert and, at ordinary temperatures, will not react with spacecraft materials. It should be no problem.

6.5 Hydrogen

Hydrogen is relatively inactive chemically at room temperature and, one would expect, even less active at lower temperatures. At elevated temperatures, it is an active reducing agent. A number of metals will absorb hydrogen, although the amount absorbed is not large. Platinum and palladium are notable exceptions and absorb large quantities of the gas.

---

*Paragraph taken from Ref. II-28.

Table II-2
Compatibility of Materials with Hydrazine (Reproduced Directly from Ref. II-28)

Material	Temperature, F								Material	Temperature, F							
	Gas				Liquid					Gas				Liquid			
	Class 1	Class 2	Class 3	Class 4	Class 1	Class 2	Class 3	Class 4		Class 1	Class 2	Class 3	Class 4	Class 1	Class 2	Class 3	Class 4
430 Stainless Steel					68			68	Nonmetals								
440 C Stainless Steel					80			75									
302 Stainless Steel					80	140			Teflon					140			
303 Stainless Steel						75											
304 Stainless Steel	140				140				Kel-F					80			160
316 Stainless Steel	200				200			160	Kel-E-1								140
317 Stainless Steel					80				Kel-E-5								140
321 Stainless Steel	140				140			68	Kel-F-300 (15% Glass Filled)								140
347 Stainless Steel	200				200				Polyethylene					80			160
Stainless W					75		160		Saran								68
17-4PH	140				140			160	Lucite						80		
17-7PH					75				Epon							75	
AM-350					160				Nylon							75	
AM-355					160				Tygon								68
Worthite	75								Polyvinyl Chloride							75	
Durimet 20	75								Polyvinyl Alcohol								75
Lead					68				Vinylite						75		
90Pb-10Sn			77		75			77	Polyester								75
Magnesium								80	Cellulose Acetate								75
Magnesium, AM100A				140					Ethyl Cellulose							75	
									Lactoprene								75
Molybdenum					75			80	Phenolic							75	
									Mylar, Type A								140
Nickel				140				140	Buna N Rubber						80	120	
									Neoprene Rubber						75	75	68
Electroless Nickel								68	Natural Rubber						80		75
Monel					80			80	Silicone Rubber						75		
K-Monel				200	140				U.S. Rubber L7825						77		
Inconel				200	200		140		Butyl Rubber Compound 805-70					140			
									U.S. Rubber M-20995						77		
Inconel X					80		140		SBR					75	160		160
Nichrome					80				Polybutadiene						75		
Chromel A					80			80	Hydropol						160		
Hastelloy C					125				Silastic 167						75		
									Silastic LS-53								140
Silver					80			75	Silicone DC-710							70	
Silver Solder					75		140		Koroseal							77	
									Haveg 61							200	
Tantalum					80			212	Delanium					140			
									Garlock Gasket 900							200	
Tin					80		140		Andok C							75	
									Carum 200							75	
Titanium, 6A1-4V					160				Dapon 35								140
Titanium, A110AT	140				140				Oxyseal							75	
Tungsten						75			An-C-53							75	
Zinc								RT	Glass					80		140	
Zirconium					75				Graphite					68	75		
									Graphitar 2 and 50					140		73	
									Asbestos					80		75	80

Since we expect hydrogen will not be a problem we have not provided further information in this area.

7. THERMAL RADIATION EFFECTS DUE TO CESIUM

A clean surface which is subjected to cesium bombardment initially will exhibit a relative emissivity and solar absorptivity which is characteristic of the surface material. As more and more cesium is absorbed upon the surface, its thermal radiation behavior will change and the surface properties will be influenced by both the base material and the cesium. During the initial condensation phase, the cesium layer will not be opaque. A significant amount of thermal energy can be transmitted to the original surface as long as the cesium coating is less than about 2500 angstroms thick. (Cesium, as with other alkali metals, is somewhat unique in this respect. Most metals begin to exhibit opaqueness at several hundred angstroms.) This effect is shown in Figure II-9 which presents calculated transmittance as a function of wavelength and cesium film thickness. (Note that these are calculated data which we abstracted from Reference II-5. Most of the data in this section are taken from the same reference. We also will list the original articles to provide immediate access to the data.)

The only reflectance data Hall (Ref. II-5) could find are shown in Figure II-10. These data were very sparse, and Hall had to estimate the behavior from 0.7 to 3.0 microns.

Hall derived the solar absorptance from the Figure II-10 data and calculated the hemispherical emittance using equations presented by Parker (Ref. II-27). These data are shown in Table II-3.

The solar absorptance of highly polished 6061-T6 aluminum alloy is 0.16 to 0.25. A thick coating of cesium therefore might have a slight effect on total absorption of solar energy. The increase would vary with the aluminum sample and, if the sample happened to have a solar absorptance of 0.25, the change which would occur by coating it with a thick layer of cesium might be negligible. The hemispherical emittance of the same aluminum alloy is 0.03 to 0.04 at a temperature of 300°K. The data in Table II-3 show that the overall effect of coating such a surface with a thick layer of cesium might be negligible. Since there appears to be no chemical reaction between aluminum and cesium (subject to our previously discussed postulations), there may be few effects occurring

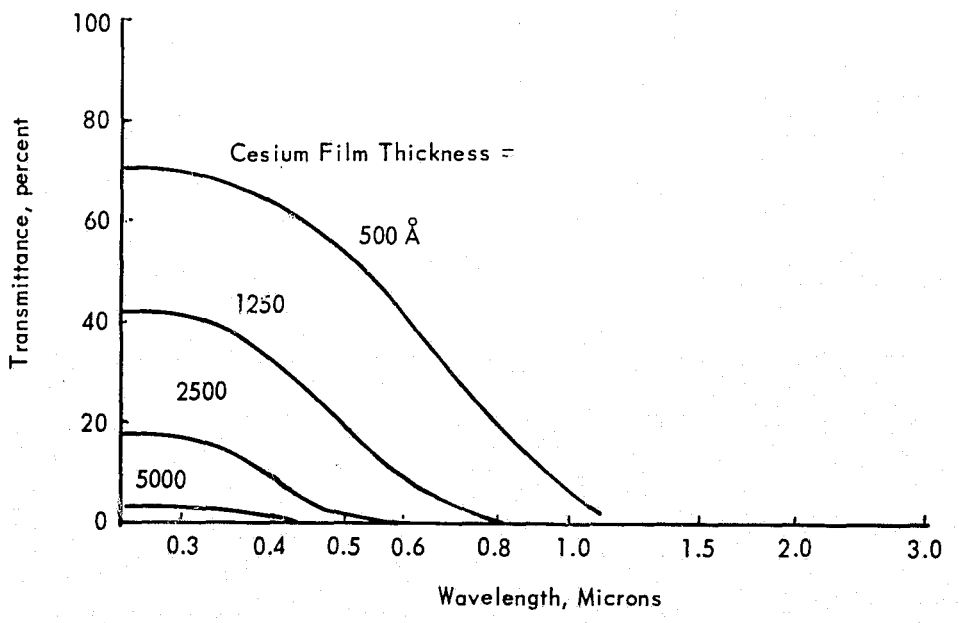

Figure II-9. Calculated Transmittance of Cesium Films (Ref. II-31).

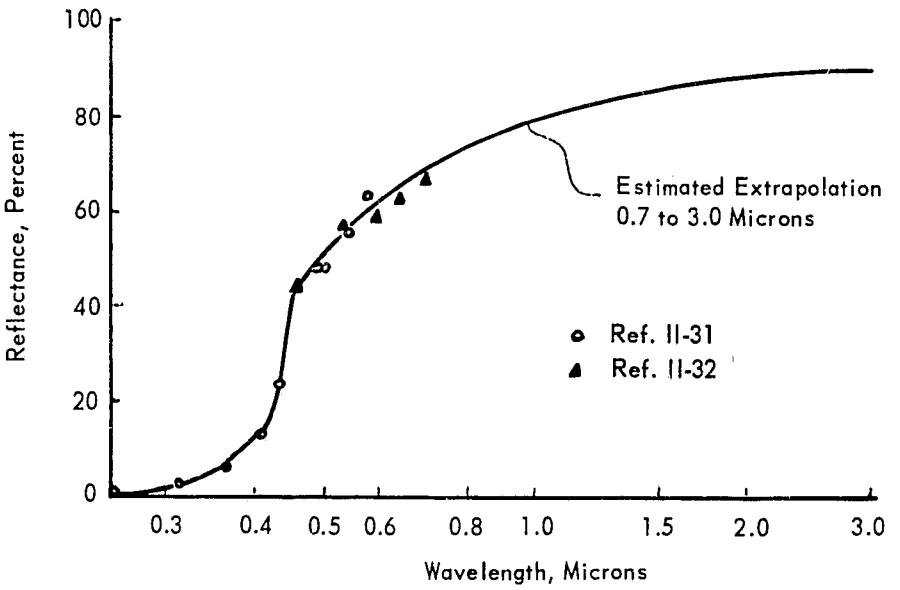

Figure II-10. Spectral Reflectance of Cesium.

Table II-3
Thermal Radiation Properties of Cesium (Ref. II-5)

Temperature, °K	Physical State	Hemispherical Emittance*
248	Solid	0.02
301	Solid	0.03
302	Liquid	0.04
373	Liquid	0.05
Solar absorptance = 0.25 ± 0.05		

*Probably - 0.00, +0.01.

during cesium deposition which change the thermal radiation properties. We may, on a preliminary basis conclude that aluminum surfaces may not be affected by cesium, regardless of the thickness of the layer which is deposited. The conclusions have been qualified because of possible specular effects. The spectral characteristics of the cooler are very important to proper operation. We would have to show no spectral effect to positively conclude cesium would not affect the cooler reflecting walls.

This is not true of 3M black velvet paint. This paint probably has a relative emissivity and absorptivity in the vicinity of 0.9 to 0.98. Table II-3 shows that the cesium is precisely the opposite. In other words, a cesium layer is highly reflective and emits very little radiation whereas the 3M black velvet paint absorbs and emits with characteristics very similar to those of a black body. A thick layer of cesium will have a drastic effect upon black velvet paint characteristics, even if no chemical reaction takes place. Just how much cesium constitutes a large quantity can be obtained by considering Figure II-9. This shows that a significant change in transmittance occurs in the vicinity of 500 angstroms or 5×10^{-6} cm. The thickness of one monolayer is about 5×10^{-8} cm. The 500 angstrom thickness therefore is $5 \times 10^{-6} / 5 \times 10^{-8} \approx 100$ monolayers. Consequently, a build-up of about 100 monolayers may represent a significant change in its emission characteristics. On the other hand, one or two monolayers should not represent a significant perturbation.

8. REFERENCES

II-1. "Program To Study and Resolve Rocket Engine Installation Problems Related To Maneuvering Satellite Vehicles," AFRPL-TR-65-42, AD-458637, Air Force Systems Command, February 1965.

II-2. Dushman, S., Scientific Foundations of Vacuum Technique, Wiley, 1962.

II-3. Raff, L. M., Jerry Lorenzen, and B. C. McCoy, "Theoretical Investigations of Gas-Solid Interaction Phenomena. I," Journal of Chemical Physics, Vol. 46, No. 11, 1 June 1967, pp. 4265-4274.

II-4. May, John W., Roland J. Szostak, and Lester H. Germer, "Ammonia Adsorption and Decomposition on a Tungsten (211) Surface," NASA-CR-95706, N68-29424, 1968 (?).

II-5. Hall, David F., "Evaluation of Electric Propulsion Beam Divergence and Effects on Spacecraft," Final Report Draft, MJO: 4795, TRW Systems, Dec. 2, 1968.

II-6. Lee, John F., Francis W. Sears, and Donald L. Turcotte, Statistical Thermodynamics, Addison-Wesley, 1963.

II-7. Soo, S. L., Analytical Thermodynamics, Prentice-Hall, 1962.

II-8. Hatsopoulos, G. N., and E. P. Gyftopoulos, Thermionic Energy Conversion, Draft Copy of book prepared for the Atomic Energy Commission, Part I, no date (Received 1968).

II-9. Nottingham, Wayne B. and Roland Breitwieser, "Theoretical Background for Thermionic Conversion Including Space-Charge Theory, Schottky Theory, and the Isothermal Diode Sheath Theory," NASA TN D-3324, March 1966.

II-10. Knox, Bruce P., and Henry R. Eberle, "Propellant Performance Handbook, Vol. IV, Part A, Fluorine/Ammonia, "Bell Aerosystems, 8173-902008- Vol. 4, Part A, AD802908, June 1964.

II-11. Weast, Robert C.,and Samuel M. Selby, Handbook of Chemistry and Physics, 48th Edition, 1967.

II-12. Shafer, Wade H., Personal Communication, Thermophysical Properties Research Center, West Lafayette, Ind. 47906, 317-463-1581, June 8 and 9, 1970.

II-13. Overstreet, Roy, and W. F. Gisuque, "Ammonia. The Heat Capacity and Vapor Pressure of Solid and Liquid. Heat of Vaporization. The Entropy Values from Thermal and Spectroscopic Data," Journal of the American Chemical Society, Vol. 59, February 1937, pp. 254-259.

II-14. Suddeth, D., Personal Communication, GSFC, October 1, 1969.

II-15. Audrith, L. F., and B. A. Ogg, The Chemistry of Hydrazine, Wiley, 1951.

II-16. Haws, Jimmy L., and Darrel G. Harden, "Thermodynamic Properties of Hydrazine," Journal of Spacecraft and Rockets, Vol. 2, No. 6, November-December, 1965, pp. 972-974.

II-17. Washburn, Edward W., et al, International Critical Tables . . . , Vol. III, McGraw-Hill, 1928.

II-18. Scott, D. W., G. D. Oliver, Margaret E. Gross, W. N. Hubbard, and Hugh M. Huffman, "Hydrazine: Heat Capacity, Heats of Formation and Vaporization, Vapor Pressure, Entropy, and Thermodynamic Functions," Journal of the American Chemical Society, Vol. 71, 1949, pp. 2293-7.

II-19. Wagman, Dr. Donald D., Personal Communication, Chemical Thermodynamics Data Group, NBS, Washington, D.C. 20234, 301-921-2773, June 8, 1970.

II-20. Williamson, Frank, Personal Communication, Cryogenic Data Center, NBS, Boulder, Colorado 80302, 303-447-1000, ext. 3797, June 8, 1970.

II-21. Kiefer, Paul J., Gilbert Ford Kinney, and Milton C. Stuart, Principles of Engineering Thermodynamics, 2nd Ed., Wiley, 1954.

II-22. Dunnill, W. A., D. B. Brayton, and W. H. Goethert, "Electrical Propulsion Test Facility Development Study Summary Report," AEDC-TR-67-106 (AD817802), Arnold Engineering Development Center, July 1967.

II-23. Trollinger, J. D., J. I. Shipp, and E. A. Lennert, "Basic Processes of Ion Beam Termination," AEDC-TDR-64-105 (AD603905), Arnold Engineering Development Center, August 1964.

II-24. Daley, Howard L., and Julius Perel, "Cesium Ion Sputtering of Aluminum, Copper, and Titanium," Paper 66-203 (A66-21445), AIAA 5th Electric Propulsion Conf., March 7-9, 1966.

II-25. Armor Research Foundation (ITT), "Determination of Some Aluminum Alloys in the Presence of Mercury and Cesium," Summary Report, ARF Project No. R3501-B41, September 4, 1962.

II-26. Kienart, G. and J. Verna, Z. Anorg. Allgem. Chem., Volume 310, pp. 143-169, 1961.

II-27. Parker, W. J. and G. C. Abbott, "Theoretical and Experimental Studies of the Total Emittance of Metals, "Symposium on Thermal Radiation of Solids, NASA SP-55, pp. 11-28 (1965).

II-28. Boyd, W. K., W. E. Berry, and E. L. White, "Compatibility of Materials with Rocket Propellants and Oxidizers," DMIC Memo 201, January 29, 1965.

II-29. Salvinski, R. J., "Investigation of the Formation and Behavior of Clogging Material In Earth and Space Storable Propellants," Interim Report, No. 08113-6016-R000, NASA-CR-191569 (X69-16132), TRW Systems, October 1968.

II-30. Sutherland, George S., et. al., "Monopropellant Hydrazine Reaction Control Systems - A Five Year Status Report," obtained from AIAA under A68-33429.

II-31. Ives, H. and H. B. Briggs, "Optical Constants of Rubidium and Cesium," J. Optical Soc. Am., Volume 27, pp. 395-400, 1937.

APPENDIX III

ION THRUSTER-RADIATOR INVESTIGATION

1. SPACECRAFT-RADIATOR GEOMETRY

The assumed spacecraft-engine-radiator geometry is shown in Figures III-1 through III-3. We will use this assumed geometry as the basis for computing cesium accumulation rates within a low temperature radiator.

2. NEUTRAL ATOM BEHAVIOR

The geometric relationship between the center of the engine exhaust plane (point P) and the center of the radiator opening is shown in Figure III-4. The angle γ can be determined from:

$$\tan \gamma = \frac{c}{b} \qquad \text{(III-1)}$$

Then:

$$\delta = \pi - \gamma - \alpha \qquad \text{(III-2)}$$

From the geometry:

$$b = \frac{c + s}{\cot \epsilon + \cot \Phi} \qquad \text{(III-3)}$$

$$\epsilon + \gamma + \delta + \Phi = \pi \qquad \text{(III-4)}$$

$$t = \sqrt{b^2 + s^2} \qquad \text{(III-5)}$$

Substituting Equation III-2 into III-4 yields:

$$\epsilon + \Phi - \alpha = 0 \qquad \text{(III-6)}$$

But:

$$\cot \epsilon = \frac{c}{b} \qquad \text{(III-7)}$$

$$\cot \Phi = \frac{s}{b} \qquad \text{(III-8)}$$

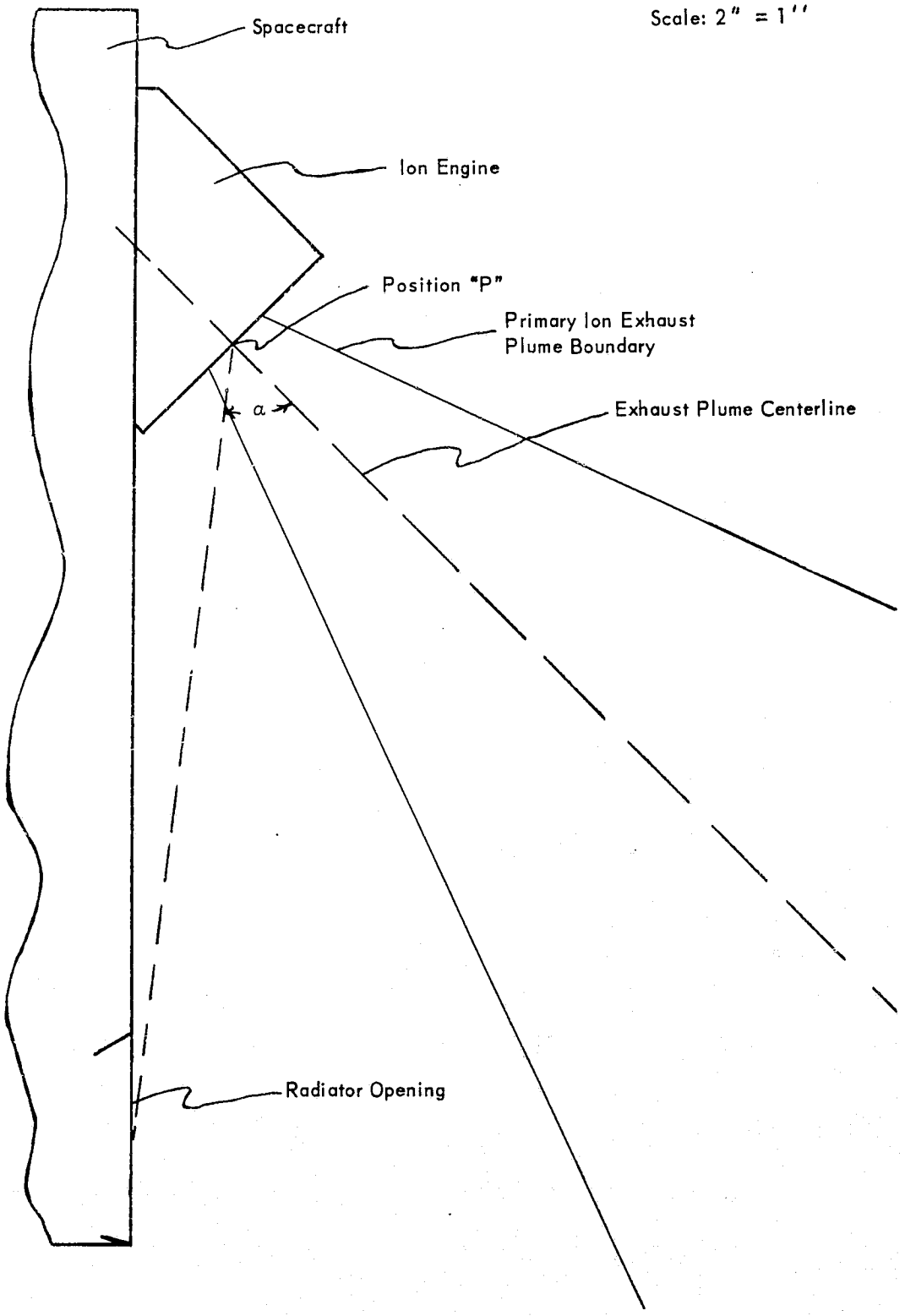

Figure III-1. Spacecraft-Engine-Radiator Geometry.

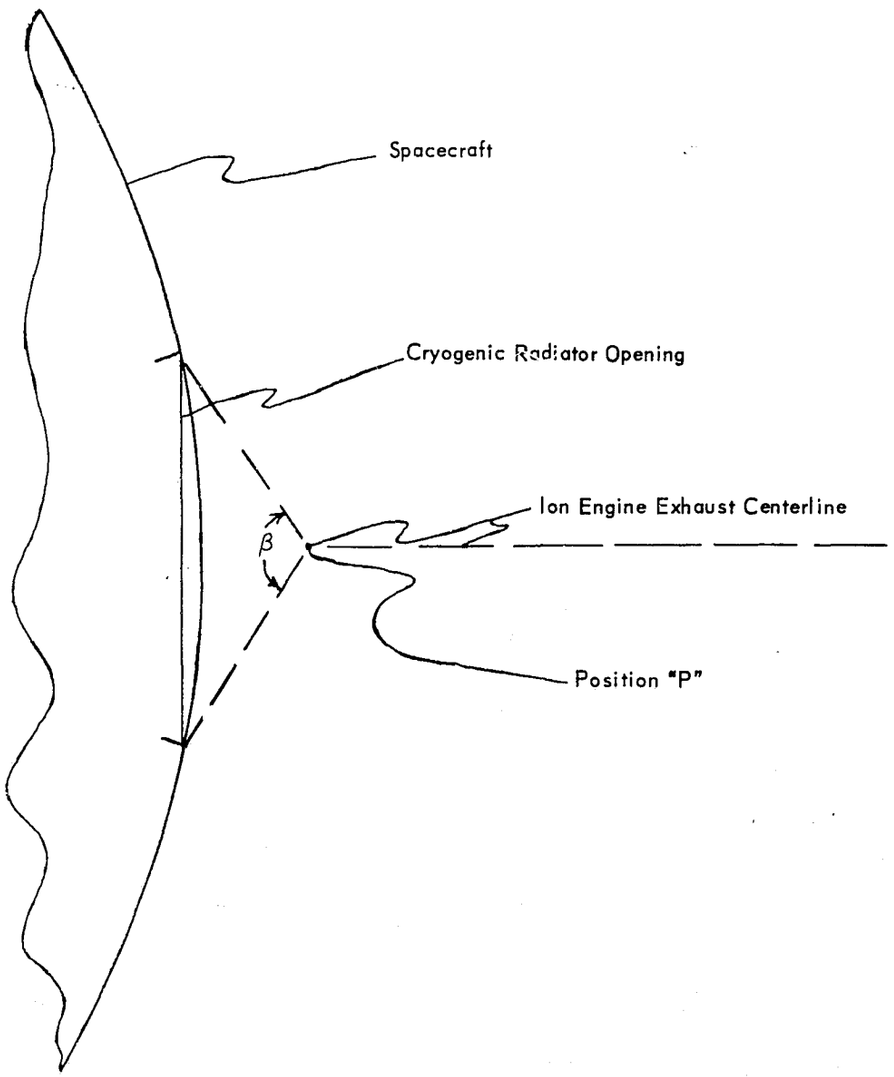

Figure III-2. Spacecraft-Engine-Radiator Geometry.

So that Equation III-6 becomes:

$$\alpha = \cot^{-1}\left(\frac{c}{b}\right) + \cot^{-1}\left(\frac{s}{b}\right) \qquad \text{(III-9)}$$

Equations III-5 and III-9 describe the exhaust plume behavior in terms of the separation distance, s.

The cryogenic radiator opening is positioned between s - h/2 and s + h/2. The angles corresponding to this are:

$$\alpha_1 = \cot^{-1}\left(\frac{c}{b}\right) + \cot^{-1}\left(\frac{s - \frac{h}{2}}{b}\right) \qquad \text{(III-10)}$$

$$\alpha_2 = \cot^{-1}\left(\frac{c}{b}\right) + \cot^{-1}\left(\frac{s + \frac{h}{2}}{b}\right) \qquad \text{(III-11)}$$

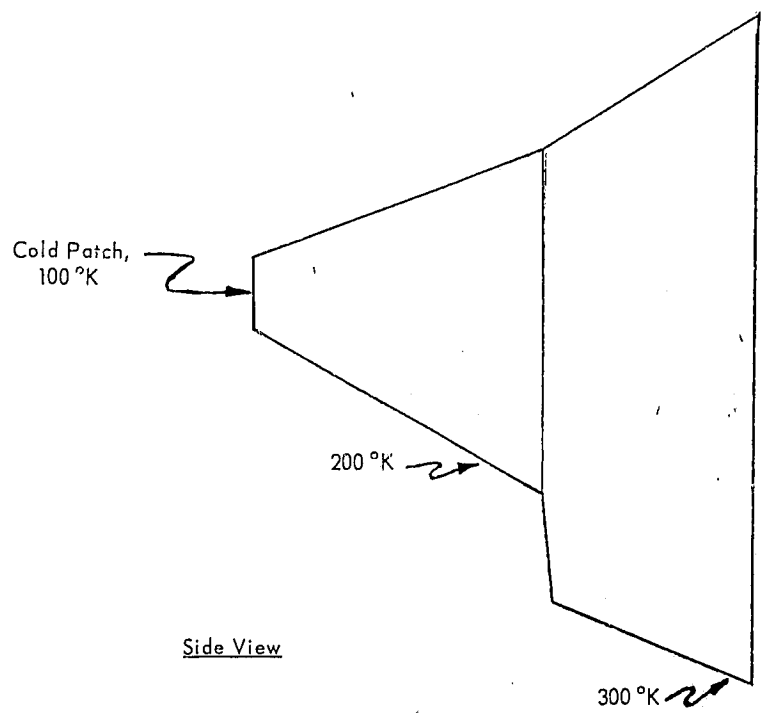

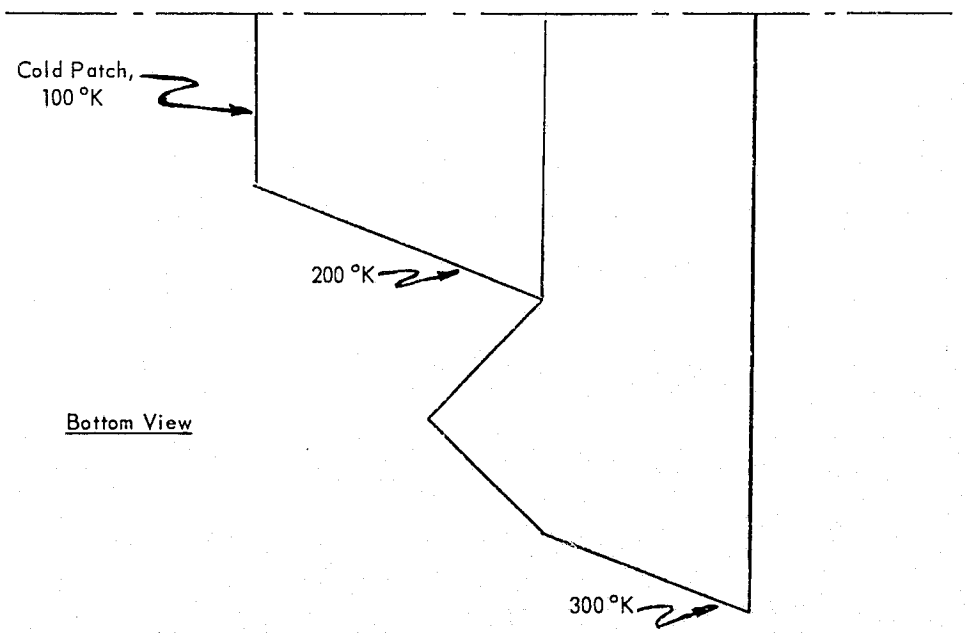

Figure III-3. Cryogenic Radiator Configuration.

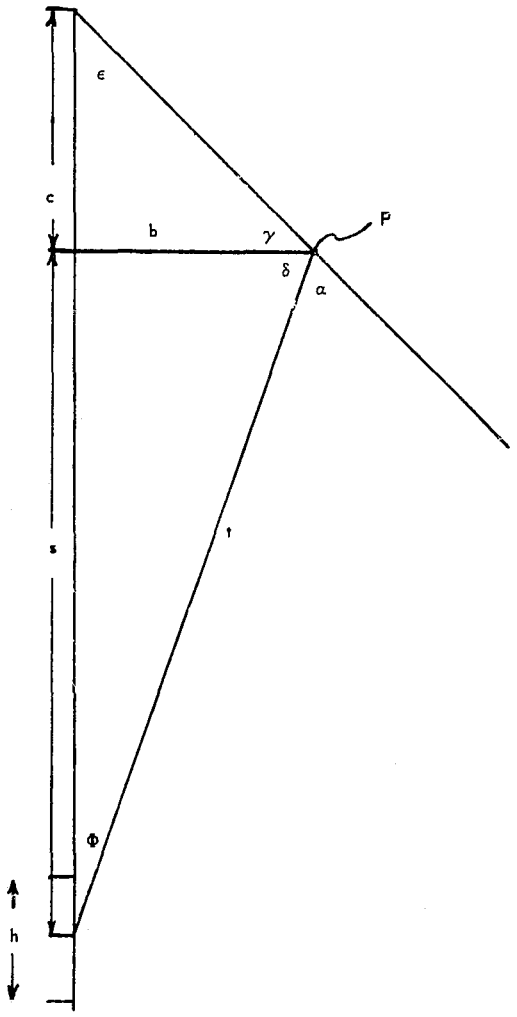

Figure III-4. Geometric Relationships.

Roughly, any atoms emitted by the engine which are outside the range of $\alpha_1 \leq \alpha \leq \alpha_2$ cannot enter the radiator directly.

If we look at the spacecraft from the side we obtain the following geometry:

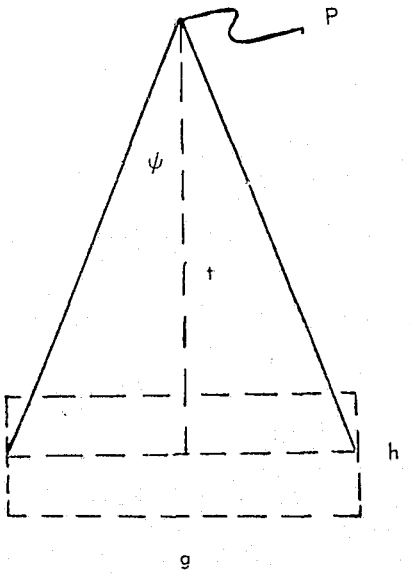

Immediately:

$$\tan \psi = \frac{g}{2t} \qquad \text{III-12}$$

Or:

$$\psi = \tan^{-1} \left(\frac{g}{2t}\right) \qquad \text{III-13}$$

Substituting Equation III-5 gives:

$$\psi = \tan^{-1}\left(\frac{g}{2\sqrt{b^2 + s^2}}\right) \qquad \text{(III-14)}$$

At positions s - h/2 and s + h/2 we find:

$$\psi_1 = \tan^{-1}\left(\frac{g}{2\sqrt{b^2 + \left(s - \frac{h}{2}\right)^2}}\right) \qquad \text{(III-15)}$$

$$\psi_2 = \tan^{-1}\left(\frac{g}{2\sqrt{b^2 + \left(s + \frac{h}{2}\right)^2}}\right) \qquad \text{(III-16)}$$

For most engine positions s >> h and little error will be involved in using Equation III-14 instead of Equations III-15 and III-16 to compute the rate at which cesium atoms enter the radiator. If we make this assumption, then only those atoms which satisfy $\alpha_1 \leq \alpha \leq \alpha_2$ and have an angle between 0 and $\pm\psi$ will enter the radiator.

The flux, Γ, at an angle θ and distance, r (see Figure I-1), can be obtained from Figure I-2. The number of atoms entering the radiator opening is then:

$$N = \Gamma A \qquad \text{(III-17)}$$

where A is the projected opening area as seen from the ion engine. This is approximately:

$$A = 2r^2\,\Delta\alpha\,\psi = 2r^2\,\psi(\alpha_2 - \alpha_1) \qquad \text{(III-18)}$$

so that:

$$N = 2\,\Gamma r^2\,\psi(\alpha_2 - \alpha_1) \qquad \text{(III-19)}$$

The behavior of the intercepting surface changes with distance, s, (the variable which describes movement of the engine relative to the radiator opening). The intercepting surface behavior relative to the center of the engine exhaust plane for the lowest surface in the radiator is shown in Figure III-5. The s = 30.8 inch point corresponds to the engine in the position furthest from the radiator (as shown in Figure III-1). The s = 7.5 inch point corresponds to the lower corner of the engine even with the radiator opening. In this latter configuration, a portion of the engine shields the opening so that part of the cesium is deflected. Note that, no matter where the engine is located, no cesium arrives on the cold patch directly. The radiator geometric arrangement prevents this.

When the engine is far removed from the opening, little cesium is intercepted by the radiator side walls. As the engine moves closer, the angular distribution results in a greater side wall interception rate. For the time being, we will neglect the side wall accumulation due to direct impingement.

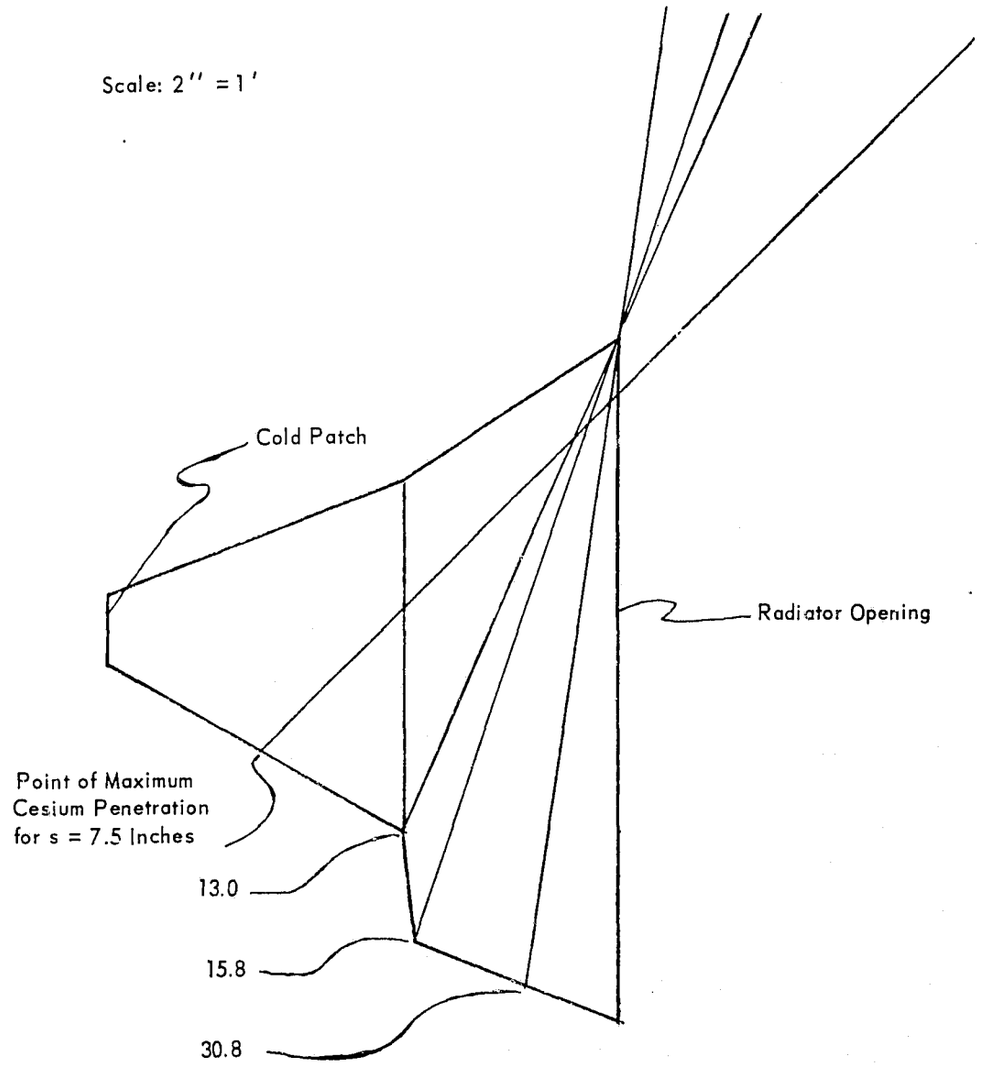

Figure III-5. Cesium Atom First Collision Boundaries.

The lowest accumulation rate within the radiator structure occurs when the engine is furthest removed from the opening. When this occurs, the lower surface is coated by direct cesium impingement as shown by the shadowed area in Figure III-6. The flux impinging on this surface represents a 52° angle from the exhaust plume centerline. The distance is 31.5 inches. The flux at this point is 2.3×10^{12} atoms/cm^2 sec. From Figure II-2 we find the emission rate from this surface (300°K) is 2.4×10^{14} atoms/cm^2 sec. This means no cesium will accumulate, but will evaporate as fast as it arrives.

Again neglecting the side wall effect, the evaporating cesium will be distributed as shown in Figure III-7. The percentage behavior is:

	Destination	Percent
(1)	Upper surface at 300°K	12.2
(2)	Upper surface at 200°K	15.0
(3)	Left surface at 300°K	12.7
(4)	Space	60.1

None of the evaporated cesium reaches the cold patch directly.

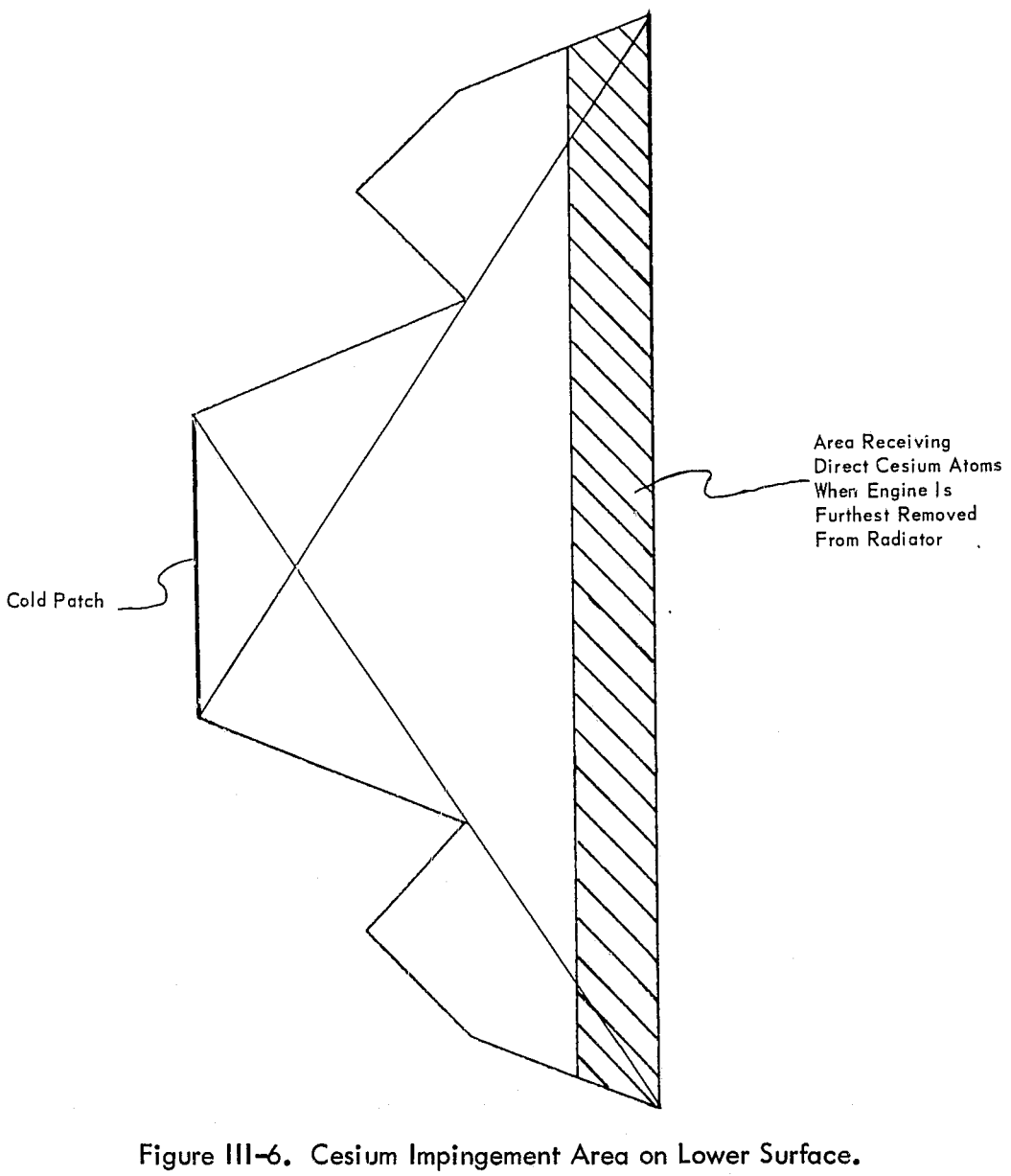

Figure III-6. Cesium Impingement Area on Lower Surface.

This distribution will be perturbed by the side walls since a large proportion of the inward traveling cesium will be caught in the "valleys" (see Figure III-6). If we assume the side effect may be proportioned directly with length of the shadowed area in Figure III-6, then the distribution is changed to:

Destination	Percent
(1)	12.2
(2)	7.5
(3)	20.2
(4)	60.1

where only about half of the original leftward traveling cesium (Figure III-7) reaches Surface (2). The other half is trapped by the side walls. The shaded area in Figure III-6 receives 2.08×10^{14} atoms/sec. These are distributed as follows:

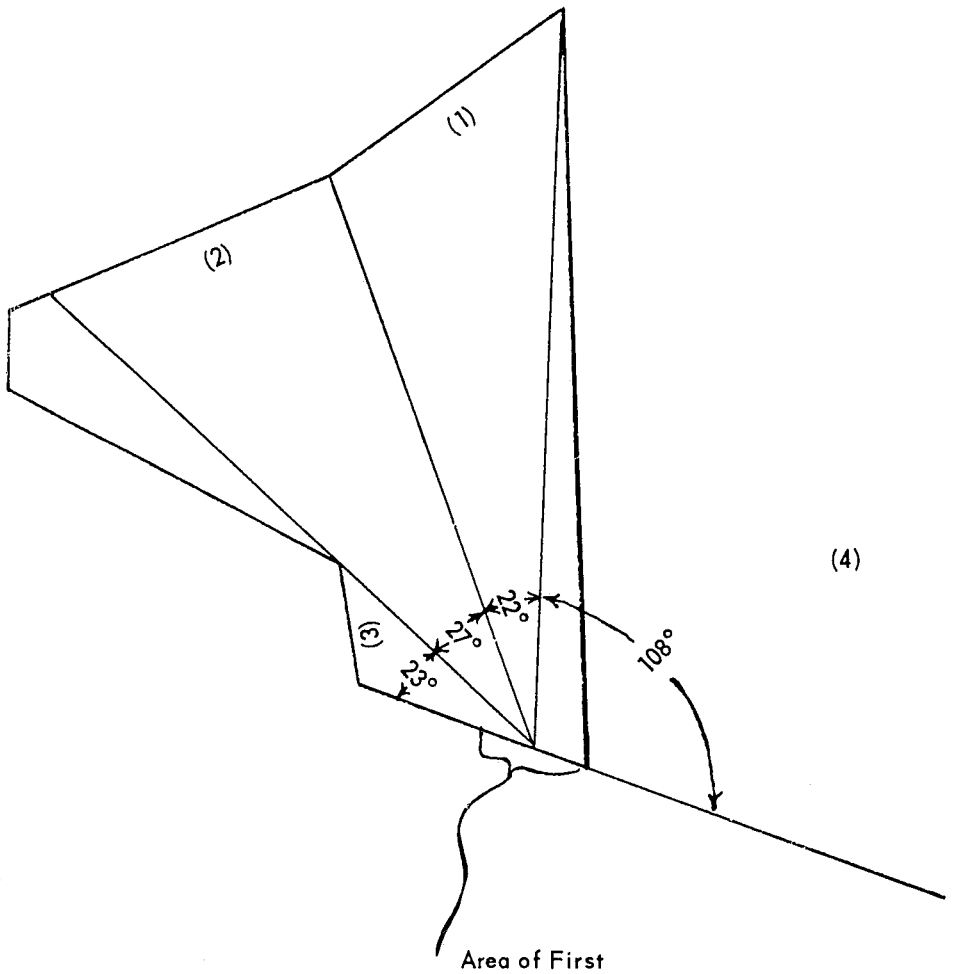

Figure III-7. Geometry for Evaporation After First Interception.

	Destination	Atoms/Sec	Atoms/cm^2 sec
(1)	Upper surface at 300°K	2.54×10^{13}	1.14×10^{11}
(2)	Upper surface at 200°K	1.56×10^{13}	1.26×10^{11}
(3)	Left surface at 300°K	4.20×10^{13}	–
(4)	Space	1.25×10^{14}	–

The evaporation rate for Surface (2) at 200°K is 7.1×10^{7} atoms/cm^2 sec (from Figure II-2). Hence, for practical purposes, the cesium accumulation rate on this surface is equal to the rate at which cesium atoms arrive. The time required to build a monolayer is:

$$\frac{4.11 \times 10^{14}}{1.26 \times 10^{11}} = 3300 \text{ sec}$$

In a few days this surface will behave as though it were composed of cesium.

Surface (1) receives no direct atoms but receives a number of atoms as a result of the first "reflection." Since the surface is at 300°K, the atoms are immediately re-evaporated. These are distributed as shown in Figure III-8. Again, note that none of the evaporated atoms hit the cold patch. Those evaporated in a 42° arc hit the lower 200°K surface if not intercepted by the sides. Taking this side effect as a factor of two reduction (as before), the number hitting the lower 200°K surface is (2.54×10^{13}) (0.5) (42)/ 180 = 2.96×10^{12} atoms/sec. This corresponds to a flux of 2.39×10^{10} atoms/cm^2/sec

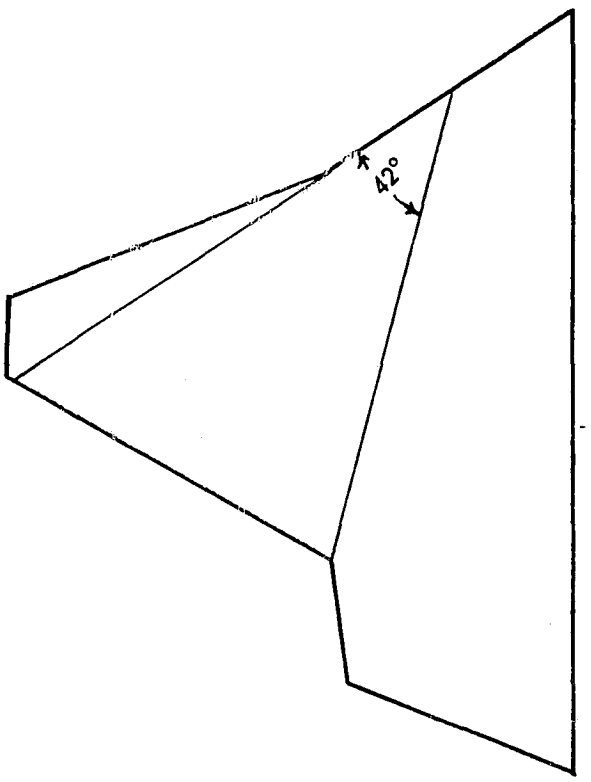

Figure III-8. Evaporation from Upper Surface at 300°K.

which also is approximately the accumulation rate. The time to accumulate one monolayer is:

$$\frac{4.11 \times 10^{14}}{2.39 \times 10^{10}} = 17{,}200 \text{ sec}$$

or about five hours. Again, in a few days the surface should behave as though it is cesium.

We have not calculated cesium accumulation rates on the 200°K sides of the radiator structure. These will receive cesium in much the same manner as the other surfaces and will become coated in a few hours or, at most, in a few days. Again, the cold patch will not see any sides at 300°K.

Moving the engine closer to the radiator opening will increase the rate at which cesium enters the hole and will increase the buildup rate of cesium on the 200°K walls. The following conclusions still hold:

(1) The cold patch "sees" only space or the 200°K walls.

(2) The 200°K walls quickly become coated with cesium to a depth of more than several monolayers.

(3) No atoms hit the cold patch except those evaporated from the 200°K walls.

The interesting conclusion which follows is:

- Cold patch cesium accumulation rate is independent of engine position

We made a number of assumptions in calculating the cesium arrival rates with respect to geometry, etc. The calculation results shows that assumption errors would have made no difference in the conclusions. The important effect is that the 200°K walls determine the rate at which the cold patch becomes coated with cesium.

We now are in a position to compute the cesium arrival rate on the cold patch. This can be accomplished by considering a differential area, dx dy, on the cold patch and by considering a similar area, ds dt, on a 200°K surface. The geometric relationship for the lower 200°K surface is shown in Figure III-9. The mathematical analysis of this configuration is horrendous. Fortunately, the work has already been accomplished in the heat transfer field. This problem is identical to the calculation of the view factor in radiation heat transfer.

Kreith (Ref. III-1) presents an analysis of the configuration shown in Figure III-10. The result is shown graphically in Figure III-11. These data may be used to analyze the Figure III-12 configuration by the relationship:

$$F_{3(2.4,6)} = \frac{1}{2A_3}\left[A_{(1,3)}\,F_{(1,3)(2,4)} + A_{(3,5)}\,F_{(3,5)(4,6)} - A_1\,F_{12} - A_5\,F_{56}\right] \qquad \text{(III-20)}$$

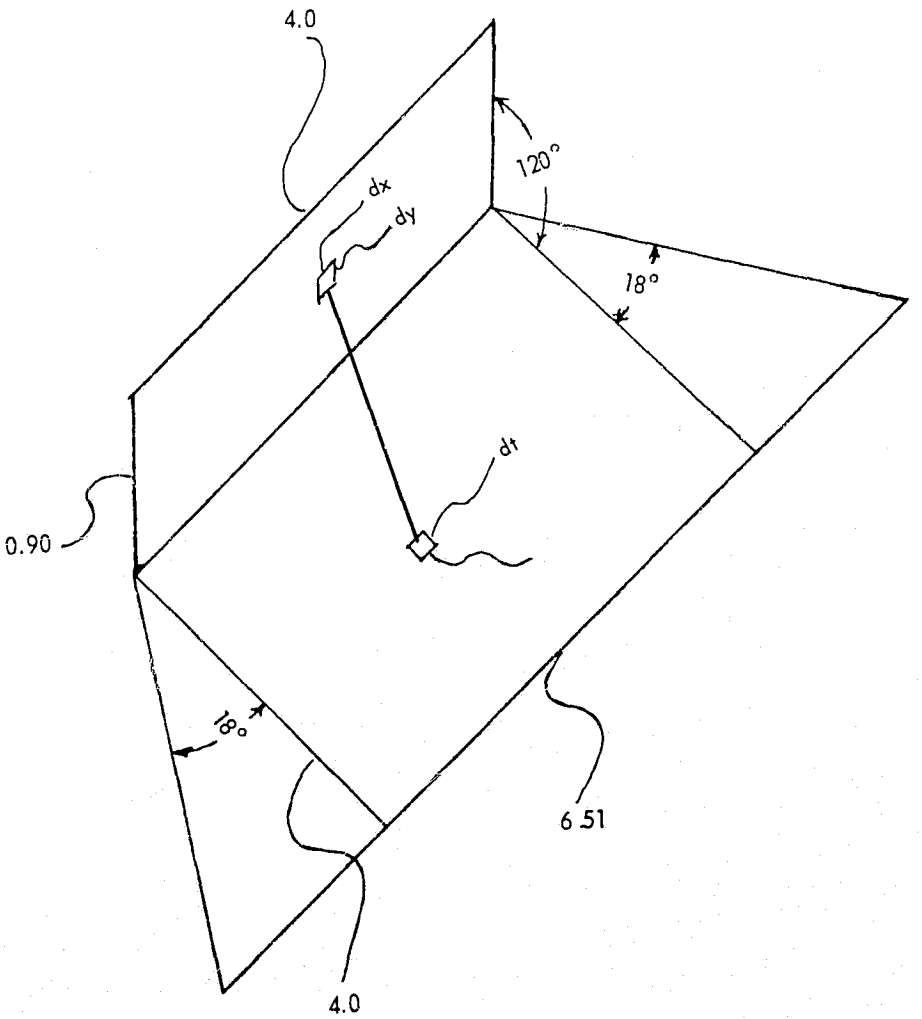

Figure III-9. Cold Patch Geometry Relative to Lower Surface.

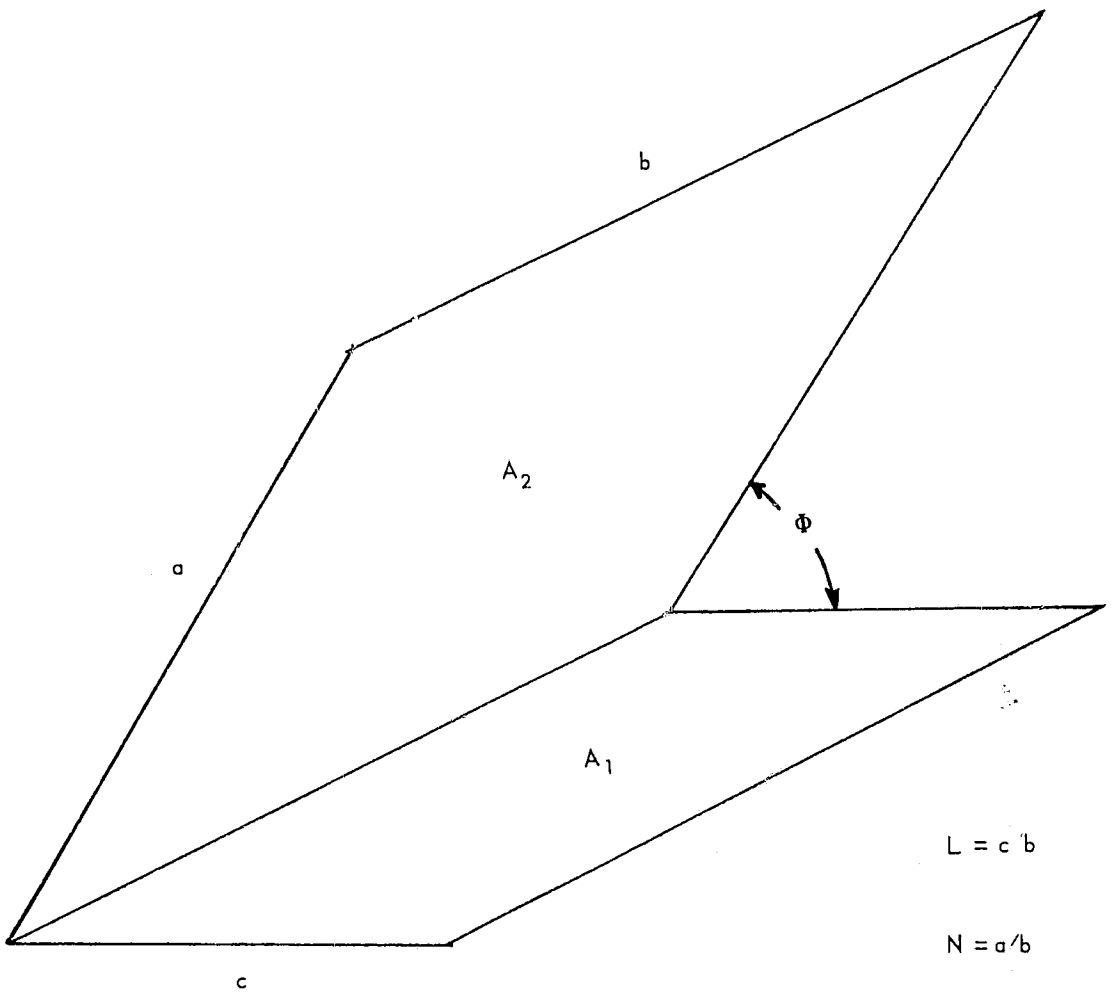

Figure III-10. View Factor Geometry for Two A_1 and A_2 Rectangles.

The computed view factor excludes A_1 and A_5. We are "looking" only at A_2, A_4, and A_6 as "seen" from A_3. This geometry is not precisely the same as shown in Figure III-9, but with proper selection of areas the error will be small enough that it may be neglected for our purposes. The edge perturbation will be small and most of the effect will be due to A_4. We will select A_2 and A_6 so that the areas are identical to the triangular shaped portions of Figure III-9.

One simplification is immediately possible because of the equal areas:

$$A_1 = A_5$$

$$A_2 = A_6$$

This means Equation III-20 may be written:

$$F_{3(2,4,6)} = \frac{1}{A_3} \left[A_{(1,3)} F_{(1,3)(2,4)} - A_1 F_{12} \right] \qquad \text{(III-21)}$$

Or:

$$F_{3(2,4,6)} = \frac{1}{A_3} \left[A_{(2,4)} F_{(2,4)(1,3)} - A_2 F_{21} \right] \qquad \text{(III-22)}$$

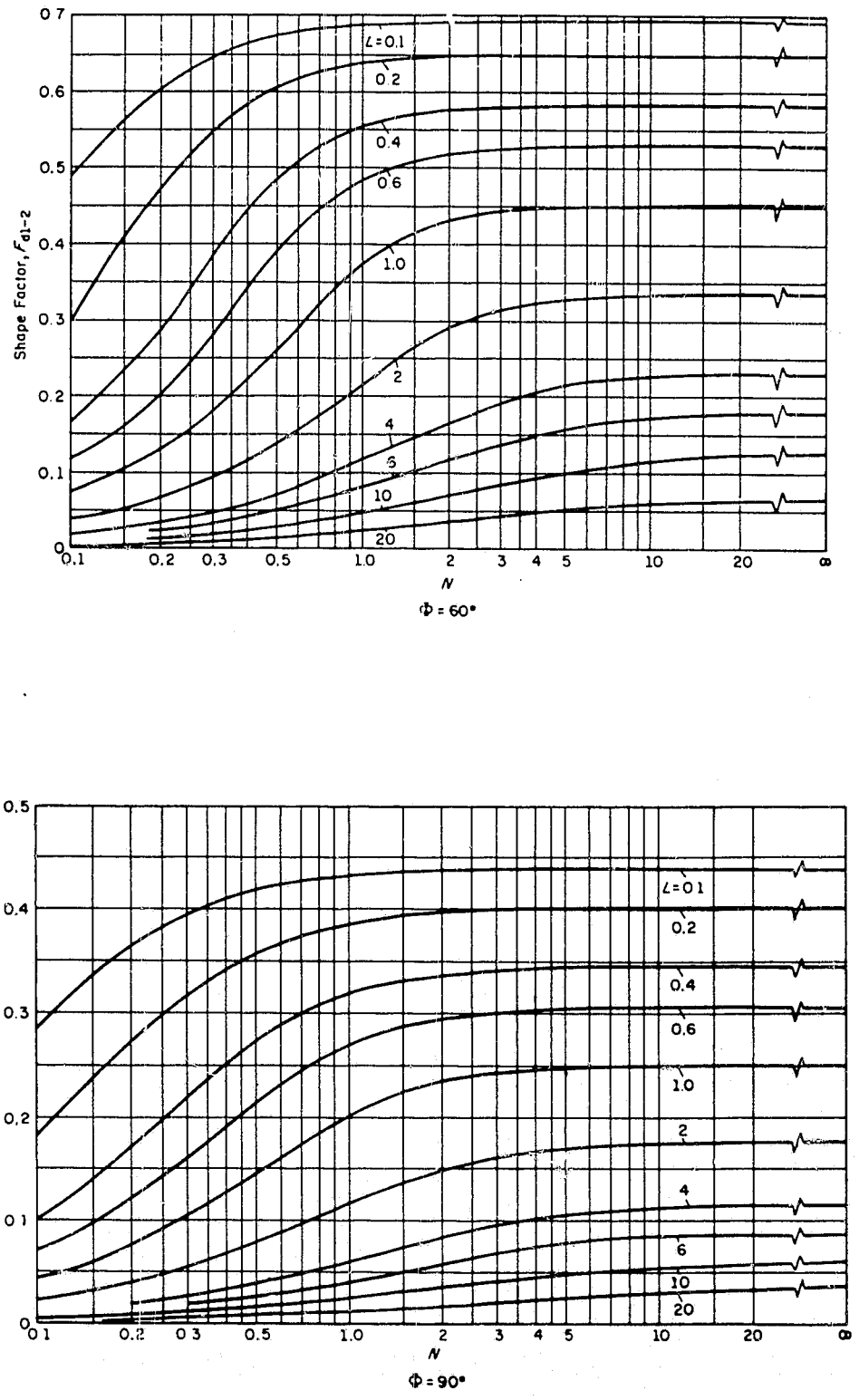

Figure III-11. View Factors (Reproduced from Ref. III-1).

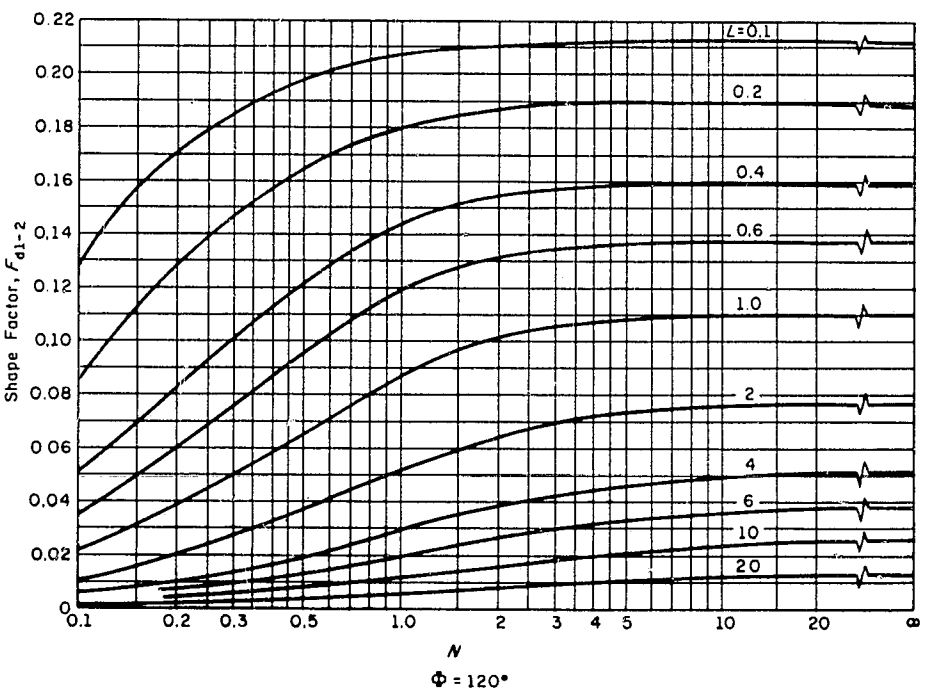

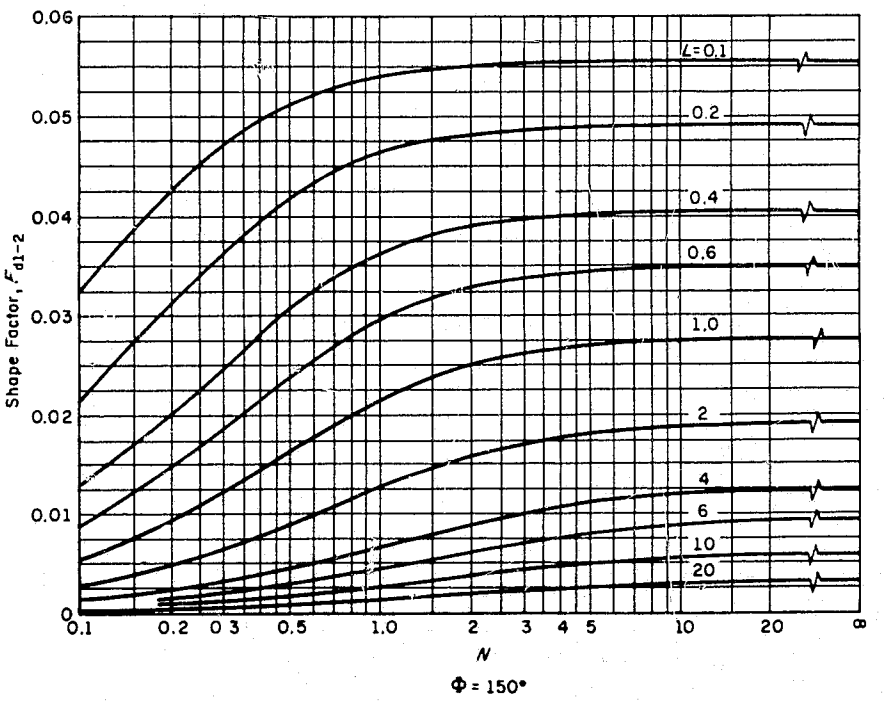

Figure III-11. View Factors (Continued).

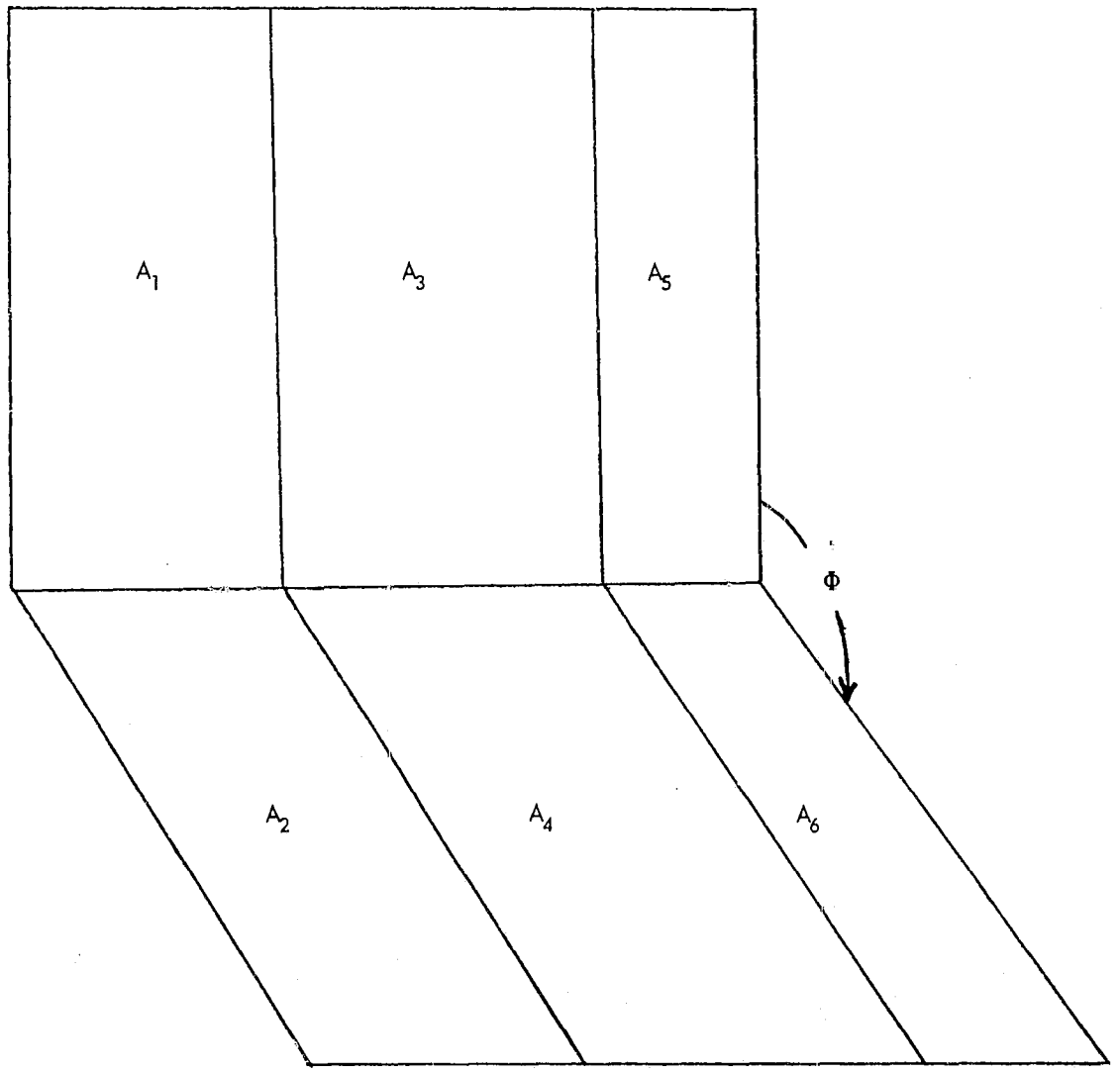

Figure III-12. View Factor Geometry.

Figure III-9 provides the following:

$\Phi = 120°$

$A_2 = (0.5)(4.0)(1.25) = 2.50 \text{ in}^2$

$A_4 = (4.0)(4.0) = 16.00 \text{ in}^2$

$A_3 = (0.90)(4.0) = 3.60 \text{ in}^2$

$A_{(2,4)} = A_2 + A_4 = 18.50 \text{ in}^2$

For A_2 to A_1:

$b = 0.625$ in

$a = 0.90$ in

$c = 4.0$ in

$L = \frac{4.0}{0.625} = 6.40$

$N = \frac{0.90}{0.625} = 1.440$

For $A_{(2,4)}$ to $A_{(1,3)}$:

$b = 4.62$ in

$a = 0.90$ in

$c = 4.0$ in

$L = \frac{4.0}{4.62} = 0.865$

$N = \frac{0.90}{4.62} = 0.1946$

Figure III-11 yields:

$$F_{(2,4)(1,3)} = 0.047 \qquad F_{21} = 0.024$$

Equation III-22 now yields:

$$F_{3(2,4,6)} = \frac{1}{3.60} [(18.50)(0.047) - (2.50)(0.024)] = 0.225$$

The same analysis will hold for the upper surface. In this case the dimensions are slightly different, as shown in Figure III-13. However, the effect of the smaller angle will balance the smaller dimensions so that the upper surface and lower surface view factors multiplied by the respective areas are identical. (The surfaces appear the same when viewed from the cold patch.) Hence, the same 0.225 view factor may be used to describe the upper surface as well as the lower one.

The sides are identical and can be treated by considering Figure III-14. The analysis is the same. Hence:

$A_2 = (0.5)(3.75)(1.55) = 2.90$ in^2
$A_3 = (0.90)(4.0) = 3.60$ in^2
$A_4 = (0.90)(3.75) = 3.38$ in^2

$A_{(2,4)} = 2.90 + 3.38 = 6.28$ in^2
$\Phi = 110°$

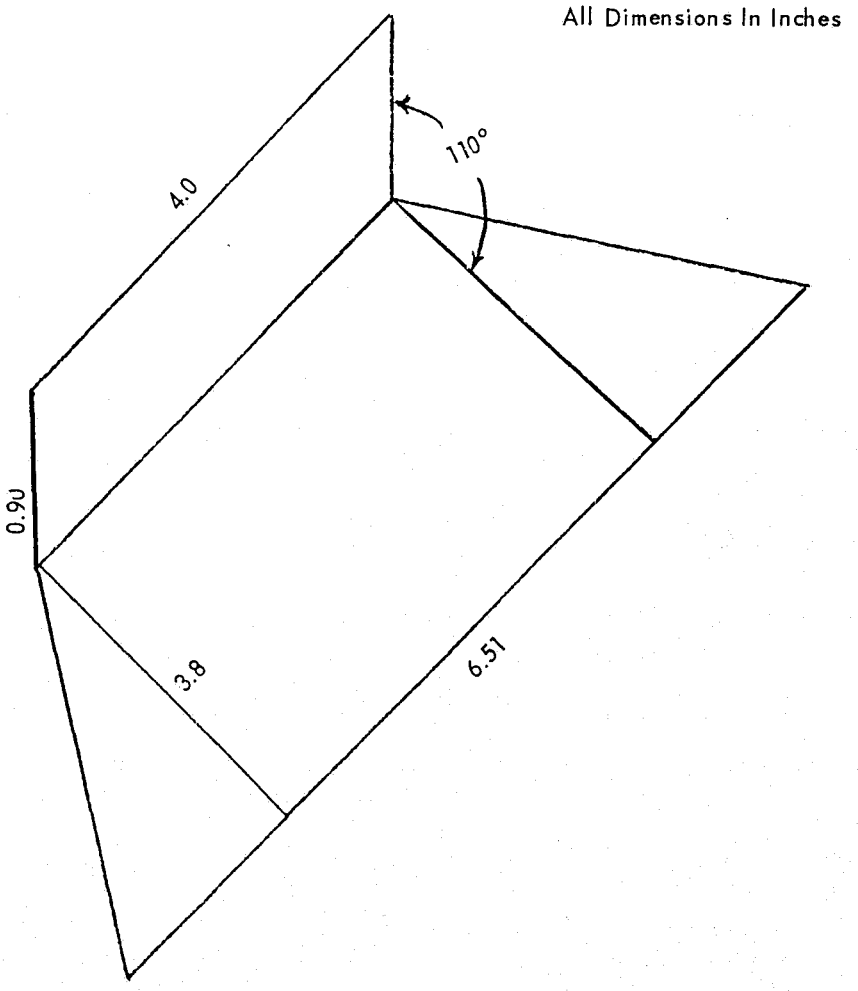

Figure III-13. Cold Patch Geometry Relative to Upper Surface.

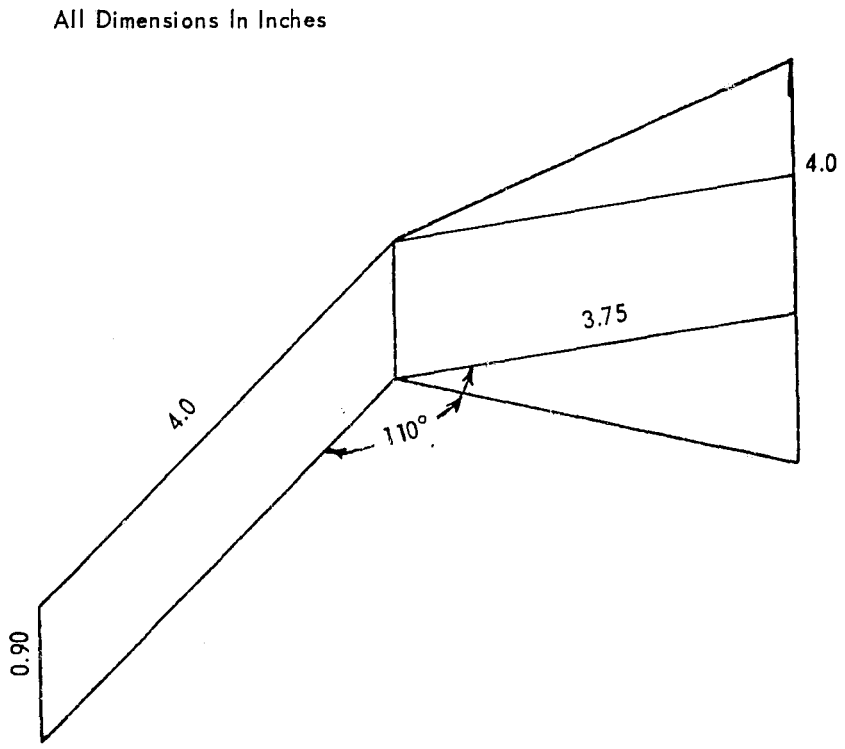

Figure III-14. Cold Patch-Side Wall Geometry.

For A_2 to A_1:

$b = 0.78$ in

$a = 4.0$ in

$c = 3.75$ in

$L = \frac{3.75}{0.78} = 4.80$

$N = \frac{4.0}{0.78} = 5.13$

For $A_{(2,4)}$ to $A_{(1,3)}$:

$b = 1.68$ in

$a = 4.0$

$c = 3.75$

$L = \frac{3.75}{1.68} = 2.23$

$N = \frac{4.0}{1.68} = 2.38$

From Figure III-13:

$F_{21} = 0.057$

$F_{(2,4)(1,3)} = 0.089$

Using Equation III-22, we obtain:

$$F_{e(2,4,6)} = \frac{1}{3.60}\left[(6.28)\,(0.089) - (2.90)\,(0.057)\right] = 0.110$$

The total view factor of the cold patch to the side walls is $(0.225 + 0.110)(2) = 0.670$. These walls are emitting cesium at a rate of 7.1×10^7 atoms/cm^2 sec when viewed from any angle. Therefore, the mean flux "seen" by the cold patch is $(0.670)(7.1)(10^7) = 4.8 \times 10^7$ atoms/cm^2 sec. The time to accumulate one monolayer is:

$$\frac{4.11 \times 10^{14}}{4.8 \times 10^7} = 8.6 \times 10^6 \text{ sec} = 2400 \text{ hrs}$$

Cesium accumulation on the cold patch is not a significant problem. About one monolayer will accumulate during 3000 hours of operation.

3. GROUP 4 ION BEHAVIOR

In Section III.2 we found the neutral cesium atoms caused only one monolayer of cesium on the cold patch after 2400 hours of continuous operation. The Group 4 ions, although of a lower quantity, exhibit a different angular behavior. Neutral atoms travel in a straight line from the engine to the radiator. Charge exchange atoms enter the radiator from the exhaust plume. Whereas neutral atoms must undergo at least two interactions within the radiator to reach the cold patch, Group 4 ions may travel directly to the cold patch.

According to White (Ref. III-2), the engine probably would operate with a 600 volt accelerator. The energy provided by a 600 volt field is:

$$(600\ \text{v})\ (1.60 \times 10^{-12}\ \text{erg/ev}) = 9.60 \times 10^{-10}\ \text{erg}$$

Since kinetic energy is:

$$E = \frac{m V^2}{2} \qquad \text{(III-23)}$$

where:

m = mass

V = velocity

the velocity is:

$$V = \sqrt{\frac{2E}{m}}$$

$$= \left[\frac{(2)\ (9.60)\ (10^{-10})\ (6.02)\ (10^{23})}{132.9}\right]^{1/2} = 2.95 \times 10^{6}\ \text{cm/sec} \qquad \text{(III-24)}$$

Speiser (Ref. III-3) gives the charge exchange cross section for cesium as:

$$\left.\begin{aligned} \sqrt{Q} &= A - B \log (V/10^{6}) \\ A &= 1.96 \times 10^{-7}\ \text{cm} \\ B &= 0.85 \times 10^{-7}\ \text{cm} \end{aligned}\right\} \qquad \text{(III-25)}$$

where:

Q = cross section, cm^2

V = ion velocity, cm/sec

= 2×10^{6} to 1.2×10^{7} cm/sec (300 ev - 10 kev)

The cross section therefore is:

$$Q = [(1.96)\ (10^{-7}) - (0.85)\ (10^{-7})\ \log\ (2.95)]^2 = 2.43 \times 10^{-14}\ cm^2$$

which is about a decade larger than reported for typical charge exchange reactions by Jahn (Ref. III-4) for inert gases. (Staggs used 6×10^{-15} cm^2 for mercury.) Marino (Refs. III-5 and -6) and Perel (Ref. III-7) obtained numerous cross section data. Zuccaro (Ref. III-8) concluded that the cross section was well established and used cesium as a check upon his experiments to obtain mercury charge exchange cross sections. These cesium data are summarized in Figure III-15. The experimental values are Zuccaro's. An ion energy of 600 ev results in a cross section of 3.06×10^{-14} cm^2 according to Marino and 2.40×10^{-14} cm^2 according to Perel. The agreement with 2.43×10^{-14} cm^2 calculated by Equation III-25 is excellent. We will use the calculated value.

The Group 4 ion behavior is given by:

$$N(r, x) = \frac{QD^2\ n\mu_0'\ \sqrt{\frac{\pi m}{8kT}}}{8x\ \left[16\left(\frac{r}{D}\right)^4 + 8\left(\frac{r}{D}\right)^2 + 1\right]^{1/2}} \qquad (6)$$

where:

N = ion impact rate per unit area

D = engine exhaust diameter = 7.62 cm

μ_0 = neutral atom emission rate per unit area = 4.54×10^{15} atoms/cm^2 sec

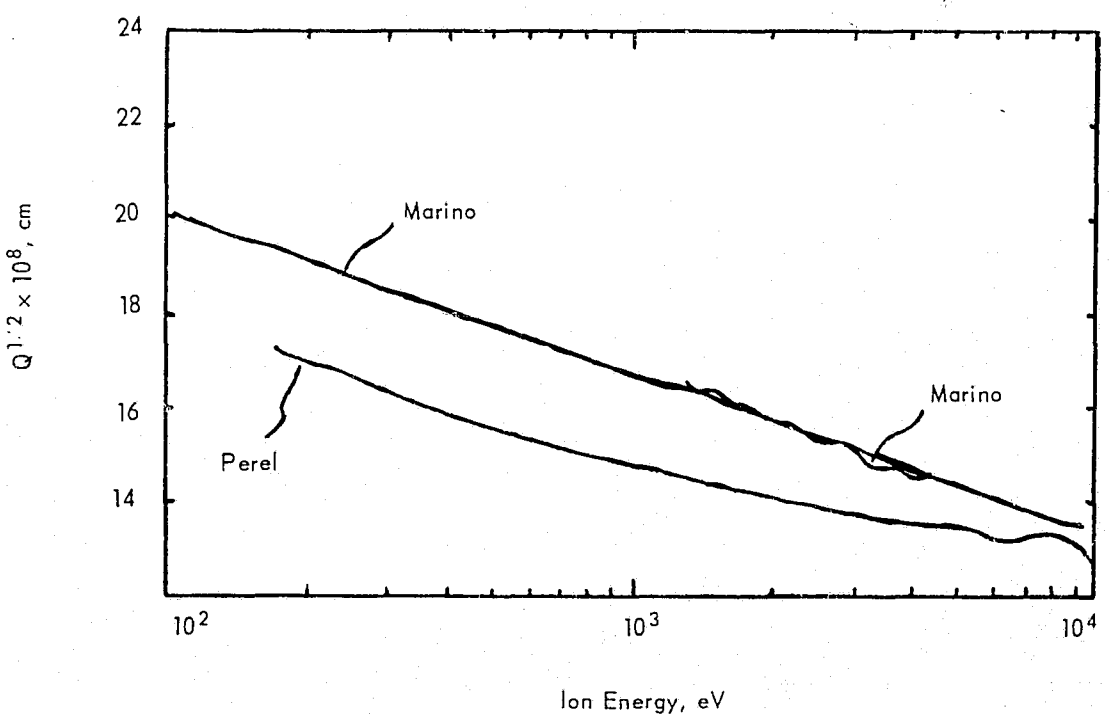

Figure III-15. Cesium Charge Exchange Cross Sections (Ref. III-8).

x = distance from exhaust plume centerline to surface receiving ions

r = distance from exhaust plane along axis

Q = charge exchange cross section

$= 2.43 \times 10^{-14}$ cm^2

n = ion arrival rate per unit area

$= 1.816 \times 10^{16}$ ions/cm^2 sec

k = Boltzmann constant

$= 1.380 \times 10^{-16}$ erg/°K

T = temperature = 533°K

m = mass = 2.20×10^{-22} gms/atom (or ion)

With these values, Equation (6) becomes:

$$N(r, x) = \frac{4.95 \times 10^{14}}{x \left[16 \left(\frac{r}{D}\right)^4 + 8\left(\frac{r}{D}\right)^2 + 1\right]^{1/2}} \qquad \text{(III-26)}$$

The behavior of this equation was shown in Figure 4. For the configuration shown in Figure III-1, r ≈ 65 cm and x ≈ 81 cm. The Group 4 flux is ~2.2×10^{10} ions/cm^2 sec. The time to accumulate a one monolayer thickness is:

$$\frac{4.11 \times 10^{14}}{2.2 \times 10^{10}} = 19000 \text{ sec} \equiv 5 \text{ hours}$$

One hundred monolayers will build up in about 20 days if all incoming ions are adsorbed on the surface. This indicates a potential problem because of change in cold patch emissivity. Moving the engine closer to the radiator decreases both r and x, with corresponding drastic increase in the ion flux hitting the cold patch.

One assumption we made in the derivation of Equation 6 was that the number of neutral atoms in the exhaust plume obeyed the cosine distribution as stated in Equation 1. This equation does not allow for conversion of neutral atoms to charge exchange ions. Now we have found a significant flux of charge exchange ions. This raises the question "Are a sufficient number of atoms converted to ions to invalidate the assumption?" We also assumed a constant Group 1 ion flux. Since each Group 4 ion which is produced reduces the number of Group 1 ions by one, the validity of this assumption also is open to question. To investigate the assumption, we note that the Group 4 ion flux is, from Equation 6:

$$N(r, x) = \frac{K n \mu_0'}{x \left[16 \left(\frac{r}{D}\right)^4 + 8 \left(\frac{r}{D}\right)^2 + 1\right]^{1/2}} \qquad \text{(III-27)}$$

where K is a constant.

The number of Group 4 ions produced per unit length of exhaust plume is:

$$N(r) = \frac{2 K n \mu_0' \pi}{\left[16 \left(\frac{r}{D}\right)^4 + 8 \left(\frac{r}{D}\right)^2 + 1\right]^{1/2}} \tag{III-28}$$

The total number produced for any distance R is:

$$N_t(R) = 2\pi K n u_0' \int_0^R \frac{dr}{\left[16 \left(\frac{r}{D}\right)^4 + 8 \left(\frac{r}{D}\right)^2 + 1\right]^{1/2}} \tag{III-29}$$

Since this equation neglects the depletion of n and μ_0, the N(R) it predicts is too high by an undetermined amount. Despite the error, its behavior will be illuminating. To solve the equation, first define:

$$\Phi = \frac{1}{\left[16 \left(\frac{r}{D}\right)^4 + 8 \left(\frac{r}{D}\right)^2 + 1\right]^{1/2}} \tag{III-30}$$

so that:

$$N_t(R) = 2\pi K n \mu_0' \int_0^R \Phi \, dr$$

$$= 2\pi K n \mu_0' D \int_0^{R/D} \Phi d\left(\frac{r}{D}\right) \tag{III-31}$$

But $\int_0^{R/D} \Phi \, d\,(r/D)$ can be obtained numerically. This is shown in Figure III-16. There is very little change in Φ for $R/D > \sim 5$, showing that few charge exchange ions are being formed beyond this point (in comparison to those formed near the engine).

Figure III-16 and Equation III-31 give:

$$N_t(R/D = 5) = 2\pi K n \mu_0' D(0.725) \tag{III-32}$$

From this and Equation III-28:

$$\frac{N\left(\frac{r}{D} = 5\right)}{N_t\left(\frac{R}{D} = 5\right)} = \frac{2\pi K n \mu_0'/10^2}{2\pi K n \mu_0' D(0.725)} = 1.81 \times 10^{-3} \tag{III-33}$$

An r/D = 5 corresponds to r = (5)(3)(2.54) = 38.1 cm. For x = 10 cm, Figure 4 gives N (r,x) = 4.8×10^{11} ions/cm^2 sec. This means N(r) for this position is $(4.8)(10^{11})(10)(2)(\pi)$ = 3.02×10^{13} ions/cm sec. The total number of charge exchange ions produced to this point (r/D = 5) is, from Equation III-33:

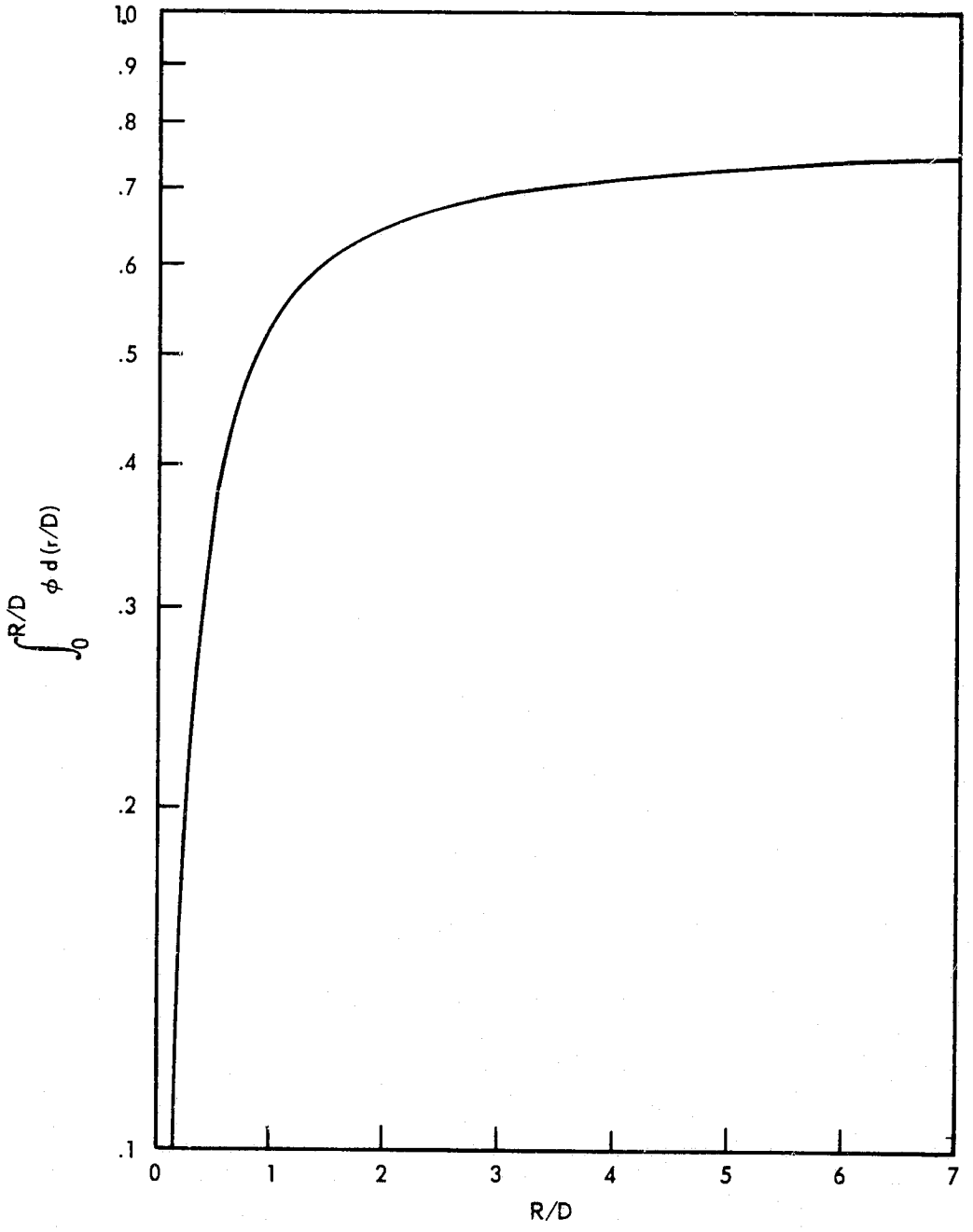

Figure III-16. $\int_0^{R/D} \Phi d\,(r/D)$.

$$N_t\left(\frac{R}{D} = 5\right) = \frac{3.02 \times 10^{13}}{1.81 \times 10^{-3}} = 1.670 \times 10^{16} \text{ ions/sec} \qquad \text{(III-34)}$$

The engine emits 2.06×10^{17} atoms/sec and 8.28×10^{17} Group 1 ions/sec. The Group 1 ions, by definition, remain in the primary beam. Removal of 1.67×10^{16} from 8.28×10^{17} will not change the calculated results significantly. Hence, the assumption of a constant number of Group 1 ions is valid. The validity of assuming the number of atoms in the beam remains constant is not obvious. Not all of the 2.06×10^{17} atoms/sec are emitted so as to remain in the beam.

Consider Equation 1 for a/r = 1 (the maximum ratio for which it is valid):

$$\Gamma(a, \theta) = \frac{\Gamma_0 \cos^4 \theta}{[2 + 2 \cos \theta]^{1/2}} \qquad \text{(III-35)}$$

at $\theta = 20°$ this gives:

$$\frac{\Gamma(a, 20°)}{\Gamma_0} = 0.477 \qquad \text{(III-36)}$$

and at $\theta = 0°$ it is:

$$\frac{\Gamma(a, 0°)}{\Gamma_0} = 0.500 \qquad \text{(III-37)}$$

For practical purposes, $\Gamma = \Gamma_0/2$ for $0 \leq \theta \leq 20°$ and r = a.

Now consider the geometry:

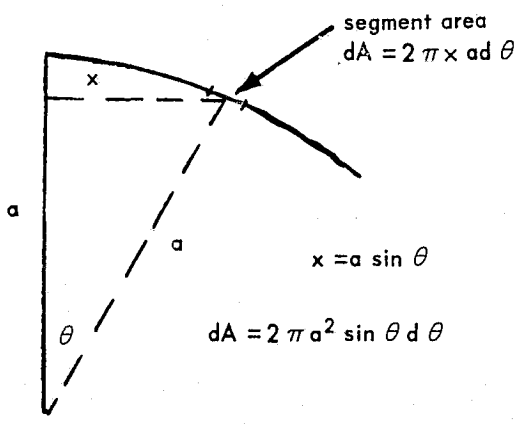

The area on the surface between $\theta = 0$ and 20° is:

$$A = 2\pi a^2 \int_{\theta=0}^{20°} \sin \theta \, d\theta = 0.378 \, a^2 = 5.48 \text{ cm}^2 \qquad \text{(III-38)}$$

The neutral atom flux at this surface is $4.54 \times 10^{15}/2 = 2.27 \times 10^{15}$ atoms/cm^2 sec. The total atoms passing through the surface (without Group 4 ion production) is $(2.27)(10^{15})$

(5.48) = 1.24×10^{16} atoms/sec. This is the number we assumed was constant in computing Group 4 ion production. The total ions produced with this assumption were 1.67×10^{16} per second. This indicates that all of the atoms have been used up, which in turn shows that the assumption of constant neutral atom flux was incorrect.

Without this assumption, we may write, for a differential element of length, Δr:

Rate at which Group 4 atoms are produced = Rate at which neutral atoms enter element - Rate at which neutral atoms leave element (III-39)

which assumes no atoms escape the exhaust plume (a good assumption unless we are close to the engine). Equation 2 gives the first part of Equation III-39 as:

$$Q\,\Delta r\,\pi x^2\,n\,n_0$$

where x is the exhaust plume radius. From Equation I-33 we see that:

$$n_0 = \mu_0 \sqrt{\frac{\pi m}{8kT}} \tag{III-40}$$

Hence, the Group 4 production rate is:

$$Q\Delta r\,\pi x^2\,n\,\mu_0 \sqrt{\frac{\pi m}{8kT}} \tag{III-41}$$

and Equation III-39 becomes:

$$Q\pi x(r)^2\,n(r)\,\mu_0(r) \sqrt{\frac{\pi m}{8kT}}\;\Delta r = \pi \left[x\left(r - \frac{\Delta r}{2}\right)^2 \mu_0 \left(r - \frac{\Delta r}{2}\right) - x\left(r + \frac{\Delta r}{2}\right)^2 \mu_0 \left(r + \frac{\Delta r}{2}\right)\right] \tag{III-42}$$

where the functional dependence of r is indicated. But we have shown that the number of Group 1 ions passing through a plane perpendicular to the exhaust plume is constant. Therefore, $x(r)^2\,n(r)$ is a constant, K', and Equation III-42 becomes:

$$QK'\,\mu_0(r) \sqrt{\frac{\pi m}{8kT}} = -\frac{d}{dr}\left(x(r)^2\,d\mu_0(r)\right) \tag{III-43}$$

which we may write:

$$\frac{QK' \sqrt{\frac{\pi m}{8kT}}}{x(r)^2}\,dr = -\frac{d\left(x(r)^2\,d\,\mu_0(r)\right)}{x(r)^2\,\mu_0(r)} \tag{III-44}$$

Or:

$$d \ln(x(r)^2 \mu_0(r)) = - QK' \sqrt{\frac{\pi m}{8kT}} \frac{dr}{x(r)^2} \qquad \text{(III-45)}$$

Which integrates to:

$$\ln (x(R)^2 \mu_0(R)) - \ln (x_0^2 \mu_0') = - QK' \sqrt{\frac{\pi m}{8kT}} \int_0^R \frac{dr}{x(r)^2}$$

But

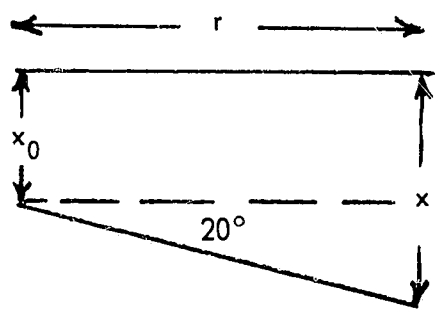

$$x(r) = x_0 + r \tan (20°) \qquad \text{(III-47)}$$

so that Equation III-46 becomes:

$$x(R)^2 \mu_0(R) = x_0^2 \mu_0' \exp \left(- QK' \sqrt{\frac{\pi m}{8kT}} \int_0^R \frac{dr}{[x_0 + r \tan (20°)]^2} \right) \qquad \text{(III-48)}$$

$$x(R)^2 \mu_0(R) = x_0^2 \mu_0' \exp \left[\frac{- QK'}{\tan (20°)} \sqrt{\frac{\pi m}{8kT}} \left(\frac{1}{x_0} - \frac{1}{x_0 + R \tan (20°)} \right) \right] \qquad \text{(III-49)}$$

Substituting values for $x_0 = 1.50$ in (3.81 cm) and R = 38.1 cm gives:

$$\frac{x(R)^2 \mu_0(R)}{x_0^2 \mu_0'} = 0.88$$

This is the ratio of the number of atoms remaining at a distance of 38.1 cm to those leaving the engine. Hence, the Group 4 charge exchange production rate will be within 10 or 15 percent of the previous prediction when the calculation is made as shown above. The difference between this conclusion and that obtained from Equation III-33 is due to two effects in Equation III-33:

(1) Neglecting the reduction in atom removal rate

(2) Applying the distribution given by Equation 1 in the region r < a.

The first effect becomes very strong when integrated over a distance. The second introduces a sizable error near the engine.

We conclude that the Group 4 ions remain a problem. The fluxes previously calculated may be a few percent high, but the error is not great enough to be of consequence.

4. GROUP 2 ION BEHAVIOR

We will use the scaling relationships developed in Section I.3.2 to calculate the Group 2 ion concentrations. The total number of ions produced by the mercury engine, which serves as the calculation basis, is 1.54×10^{18} ions/sec. The cesium engine produces 8.28×10^{17} ions per second. If all other variables were the same the Group 2 ion concentrations would be a factor of $8.28 \times 10^{17} / 1.54 \times 10^{18} = 0.536$ times the mercury engine concentrations. (Ion exchange reactions are directly proportional to the number of Group 1 ions passing through the exhaust plane.) The effect of the propellant change is given by:

$$\frac{N_1}{N_2} = \frac{Q_1}{Q_2} \left(\frac{m_2}{m_1}\right)^{1/2} \tag{7}$$

$$= \frac{2.43 \times 10^{-14}}{6 \times 10^{-15}} \left(\frac{201}{132.9}\right)^{1/2} = 4.98$$

The accelerating voltage perturbation is:

$$\frac{N_1}{N_2} = \left(\frac{E_1}{E_2}\right)^3 = \left(\frac{600}{3000}\right)^3 = 8 \times 10^{-3} \tag{9}$$

Temperature of the neutral atoms gives:

$$\frac{N_1}{N_2} = \sqrt{\frac{T_2}{T_1}} = \left(\frac{500}{533}\right)^{1/2} = 0.970 \tag{8}$$

Efficiencies are roughly identical. Hence the cesium engine Group 2 ion behavior may be obtained by multiplying Staggs' data by $(0.536)(4.98)(8 \times 10^{-3})(0.970) = 0.0207$.

With the engine positioned as shown in Figure III-1, the Group 2 ions entering the radiator opening make an angle of about 52° with the exhaust plume centerline. Figure I-4 gives a group 2 ion flux of about 1.3×10^{13} ions/steradian sec for this angle. The corresponding cesium engine flux is $(0.0207)(1.3)(10^{13}) = 2.7 \times 10^{11}$ ions/steradian sec. Separation distance is 80 cm. The area at this radius corresponding to one steradian is $(80)^2 = 1600$ cm^2. The normal flux therefore is $2.7 \times 10^{11} / 1600 = 1.7 \times 10^8$ ions/cm^2. The neutral atom flux at this same position is 2.3×10^{12} atoms/cm^2 sec. The Group 2 ion flux is completely negligible in comparison.

The point where the engine is closest to the spacecraft represents a separation distance of 13.3 cm at a 90° angle with the exhaust plume. Figure I-4 shows the same Group 2 flux as at a 52° angle. Taking this value (the real value will approach zero at 90°), we obtain a Group 2 ion flux of $(1.7)(10^8)(80/13.3)^2 = 6.1 \times 10^9$ ions/cm^2 sec. Again, this is negligible in comparison to the neutral atom flux.

In Section 2.1.4 we presented an alternate technique for calculating Group 2 behavior. Application of this approach (Section 2.2.4) gave the equation

$$N_{Cs} = 3.5\, N_{Hg} \tag{25}$$

In the previous section we found:

$$N_{Cs} = 0.0207\, N_{Hg} \tag{III-50}$$

The agreement is terrible! As a consequence, we must use the Group 2 ion flux calculations as a guide only. Treating the results quantitatively would be a mistake.

5. REFERENCES

III-1. Kreith, Frank, Radiation Heat Transfer for Spacecraft and Solar Power Plant Design, International Textbook, 1962.

III-2. White, A., Goddard Space Flight Center, Personal Communication, May 16, 1969.

III-3. Speiser, R. C., "Cesium Ion -Atom Charge Exchange Scattering," Electro-Optical Systems Rept. No. 1583, (AD-263-725), September 30, 1961.

III-4. Jahn, Robert G., Physics of Electric Propulsion, McGraw Hill, 1968, p. 66.

III-5. Marino, Lawrence, L., A. C. H. Smith, and E. Caplinger, "Charge Transfer Between Positive Cesium Ions and Cesium Atoms," Physical Review, Volume 128, No. 5, p. 2243, December 1, 1962.

III-6. Marino, Lawrence, L., "Charge Transfer Between Alkali-Metal Ions and Cesium Atoms," Physical Review, Volume 152, No. 1, p. 46, December 2, 1966.

III-7. Perel, Julius, Richard H. Bernon, and Howard L. Daley, "Measurement of Cesium and Rubidium Charge-Transfer Cross Sections," Physical Review, Volume 138, No. 4A, p. A937, May 17, 1965.

III-8. Zuccaro, David, "Measurement of the Charge Exchange Cross Section of Mercury," NASA CR-72398 (N68-30824), Hughes Research Laboratories, April 1968.

PRECEDING PAGE BLANK NOT FILMED

APPENDIX IV

ION THRUSTER-STAR TRACKER-SPACECRAFT DESCRIPTION

1. PHYSICAL APPEARANCE AND CHARACTERISTICS

1.1 Spacecraft

Figure 6 presented an overall view of the spacecraft assumed for this study. The X-Y-Z relationship is shown in Figure IV-1. In the X-Y plane (north, south, east, west parallel to a plane tangent to the earth's surface) the nominal thruster exhaust is directed 13° west of north. Since the Polaris tracker looks northward, the effect is to direct the exhaust away from the tracker field of view.

View A-A (Figure IV-1) shows the earthward components of the nominal exhaust centerline. The 35° downward (from X-Y) component brings the exhaust plume closer to the tracker field of view.

1.2 Cesium Thruster

An overall sketch of the cesium thruster is shown in Figure IV-2. Most of the Group 1 (primary) ions are assumed to be contained within a 15° (half angle) cone. Behavior of the Group 2 ions and neutrals is as previously described, except assumed efficiency is better (90% vs. the previous 80%. This is still low and higher values can be achieved.)

Neutral cesium also is produced by the neutralizer, shown in Figure IV-3. This is a tubular structure and acts much like a small nozzle, ejecting cesium toward the centerline of the main exhaust plume. This neutralizer is similar to that described by Ernstene (Ref. IV-5). This neutralizer uses plasma from a small cesium discharge to couple electrons to the ion beam. A hot cesiated surface supplies between 100 and 500 times as many electrons as neutral cesium atoms to the discharge, as well as supplying some slow ions. The latter creates a plasma bridge which connects the neutralizer to the beam and allows the electrons to flow. The discharge chamber is operated at 600°C. Beam potential runs at about 6 volts.

Ernstene made an interesting comment regarding the operation of the neutralizer. "When the discharge strikes, the blue glow of the ion beam becomes very faint. An explanation could be that the neutralizer supplies cool electrons that lack the energy required to excite Cs or residual chamber gas and so cause the blue radiation. If so, this type of neutralizer can be expected to produce a more thoroughly neutralized, cooler, and quieter beam."

The proposed mode of operation is referred to as the spot mode. This is a high vapor flow mode, characterized by only a small spot of visible plasma at the orifice. According to Rawlin (Ref. IV-6), lower flows result in a more pronounced visible plume extending from the neutralizer to the beam. He adds: "The plasma-bridge neutralizer is a relatively new device and additional testing is required to increase the understanding of its discharge." This view is reinforced by Cole (Ref. IV-7) who states "Precise definition of the properites of these neutralizers remain to be determined." According to Speiser (Ref. IV-8), the neutralizer beam has no optical thickness. He stated that the atoms which flow through the 7 mil aperture become ionized within roughly a centimeter.

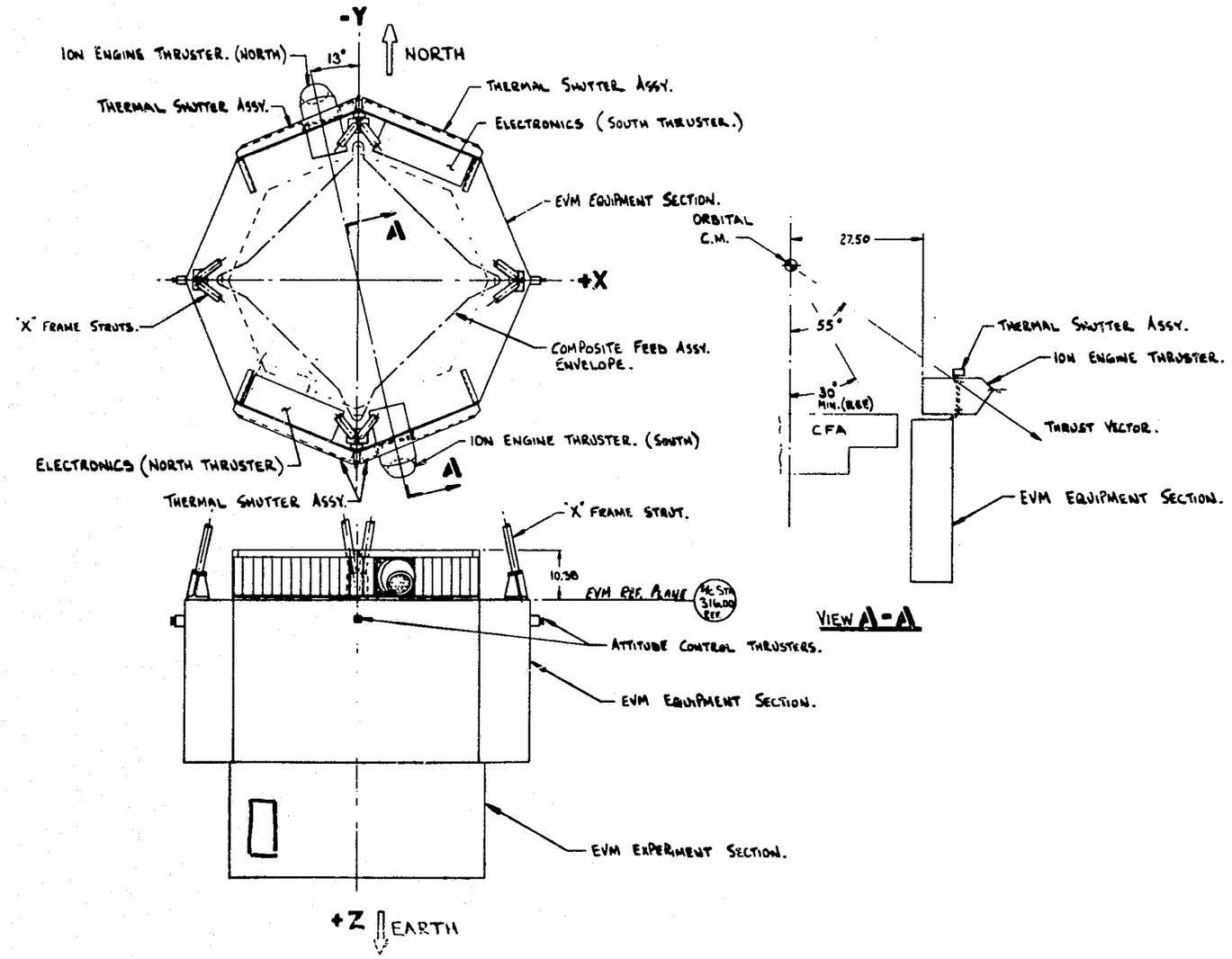

Figure IV-1. ATS-F and -G Configuration (Ref. IV-1).

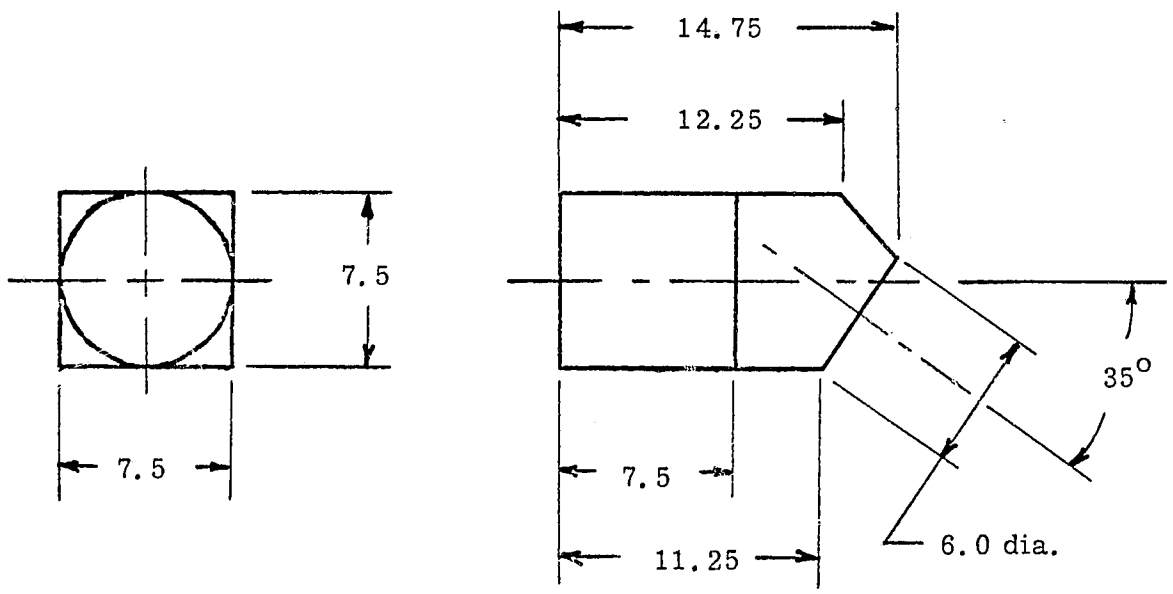

Figure IV-2. Ion Engine Sketch (Ref. IV-3).

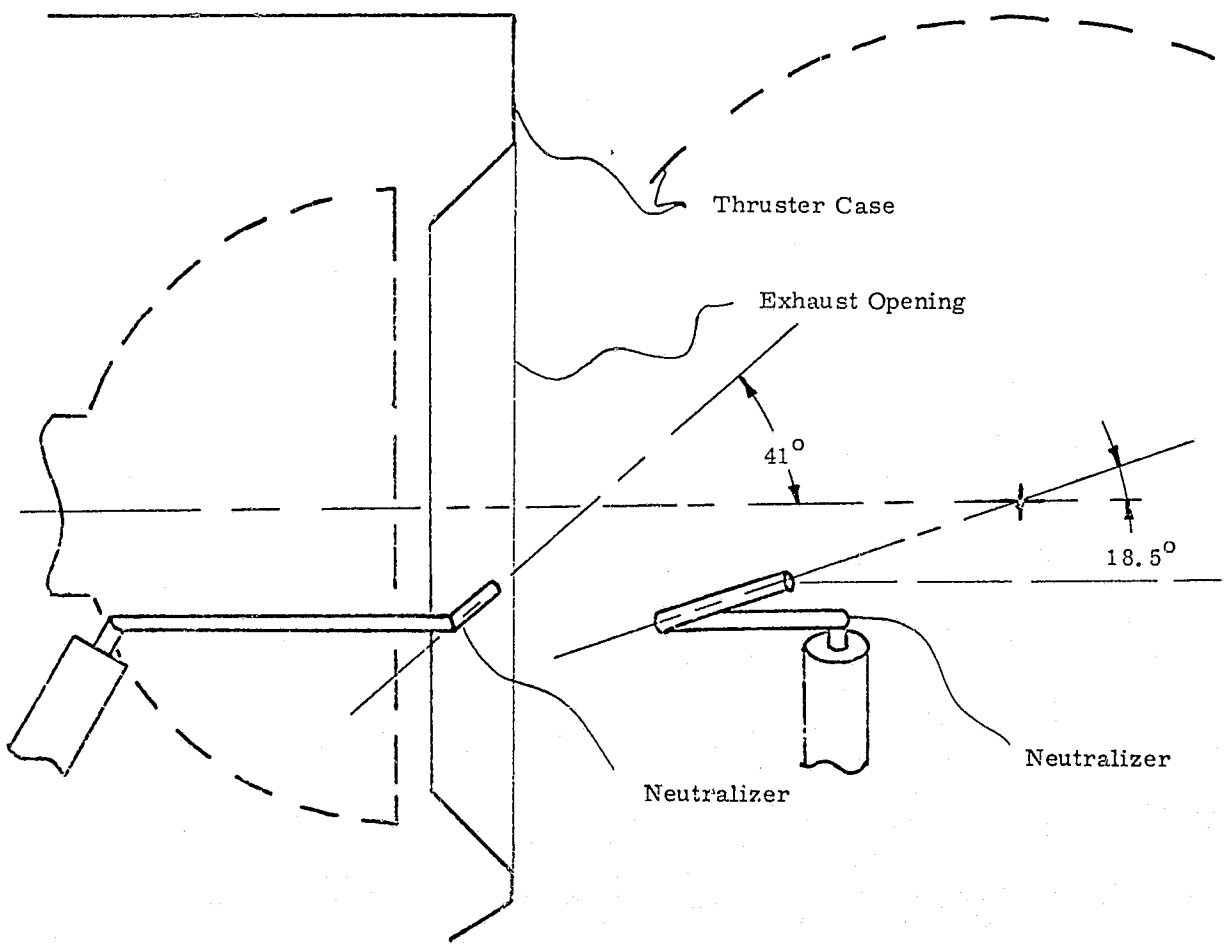

Figure IV-3. Neutralizer Orientation (Ref. IV-4).

He added that these don't cause a problem. The problem results from atoms that reach the first or second excited levels and then decay with emission of radiation. He further added that one must ionize a good portion of the cesium from the neutralizer or it simply doesn't work. Evidence of this ionization is the visible spot located at the neutralizer opening.

In any event, the actual operating characteristics of the neutralizer should not seriously perturb our results. A change in one of the components by something like a factor of two will not change any conclusions. (Calculation of line strengths is notoriously inaccurate. Further, what we are looking for are effects which differ from each other by decades, not factors.) We have based our calculations upon exhaust characteristics without a contribution from the neutralizer, with the exception of assuming that the exhaust beam is neutral.

1.3 Polaris Tracker

The tracker on which we have based the study is a Ball Brothers Research Corporation tracker which does not provide spectral discrimination. The maximum field of view is $8° \times 30°$. The two-axis tracker has a $0.7° \times 2.1°$ instantaneous field of view in the yaw and roll directions, respectively. The sensor is a ITT F4004-S-20 image tube. In this report, we have not been concerned with the lens system since all calculations have been upon available fields of view and a unit lens area. This assumption will introduce an error into the response calculation since portions of the instantaneous field of view will focus upon different portions of the sensor. The error is zero at an infinite distance and becomes finite as the tracker is approached. Error should be small for distances of more than a few inches from the tracker.

2. THRUSTER-STAR-TRACKER-SPACECRAFT GEOMETRY

2.1 Introduction

A rectangular coordinate system is used to describe the ATS spacecraft. The point (0, 0, 0) is located at the spacecraft center of mass. The +x coordinate describes east, -y is north, and +z is toward the earth. This system, showing the tracker and thruster locations, is indicated in Figure IV-4.

The "focus" of the thruster is located at the point (-a, -b, c). A line connecting this point with the spacecraft center of mass at (0, 0, 0) can be represented by the equations*:

$$\frac{x}{-a} = \frac{y}{-b} = \frac{z}{c} \qquad \text{(IV-1)}$$

The "focus" of the Polaris tracker is located at the point (h, -j, g). Traveling in the plus y direction to the xz plane gives the point (h, 0, g). The equation of a line connecting these two points, which also represents the line of nominal sight to Polaris, is represented by (h, y, g) with $0 \geq y \geq -\infty$.

2.2 Thruster Exhaust Plume

The plume can be described by a cone. The equation of a right circular cone with its axis corresponding to the z' axis and its apex at (0, 0, 0) is given by:

$$x'^2 + y'^2 - k^2 z'^2 = 0 \qquad \text{(IV-2)}$$

This can be regarded as a surface of revolution generated by the rotation of the line x' = kz' about the z' axis. We will take the z' axis as being identical to the line defined by Eq. (IV-1).

*See any solid geometry book. We are using Reference IV-9.

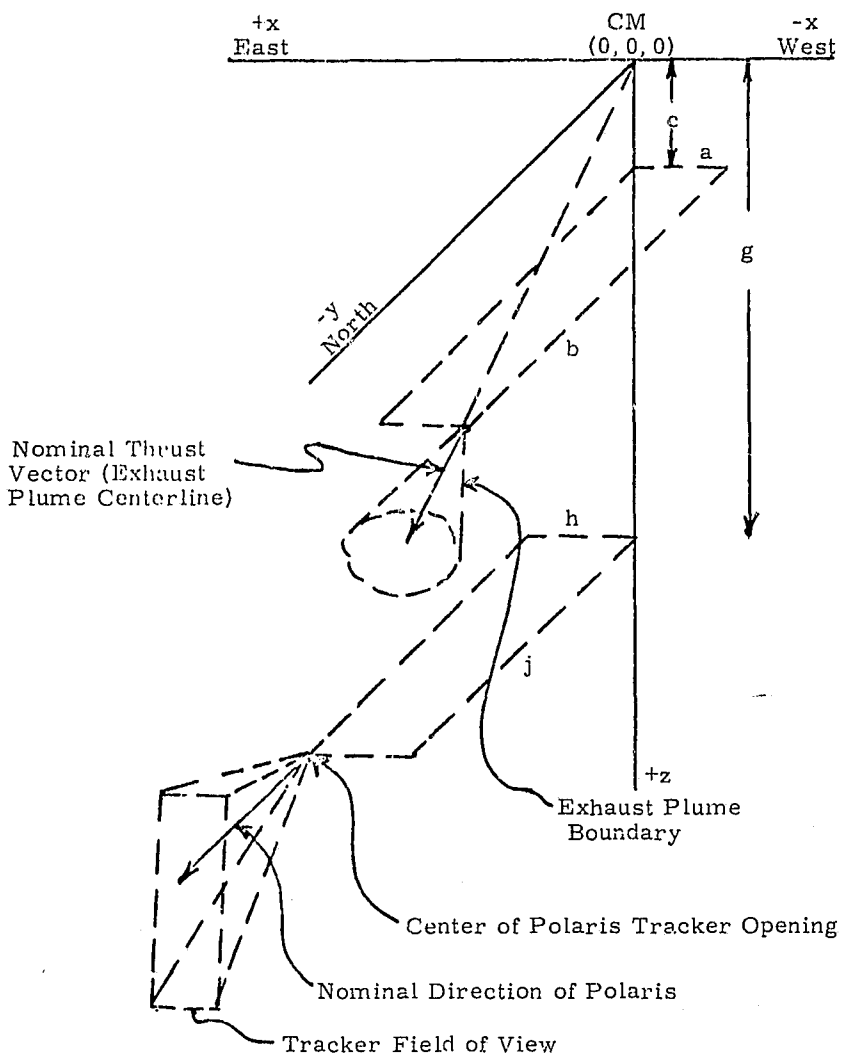

Figure IV-4. Thruster-Tracker-Spacecraft Geometry.

Now construct a plane which passes through the z axis and the point (-a, -b, c). There results the geometry shown in Figure IV-5. Note that there are only two basic positions for which the point (x, y, z) lies in the plane as shown in Figure IV-5. Other positons of δ, as indicated by the rotation arrow, will remove it from the plane.

Hall (Refs. IV-10 and IV-11) gives the neutral atom distribution by:

$$\Gamma(r, \theta) = \frac{\Gamma_0 A^2 \cos\theta}{r^2 \left[1 + 2\left(\frac{A}{r}\right)^2 \cos\theta + \left(\frac{A}{r}\right)^4\right]^{1/2}} \qquad \text{(IV-3)}$$

where:

A = radius of exhaust plane

Γ = atom flux

0 = refers to initial value

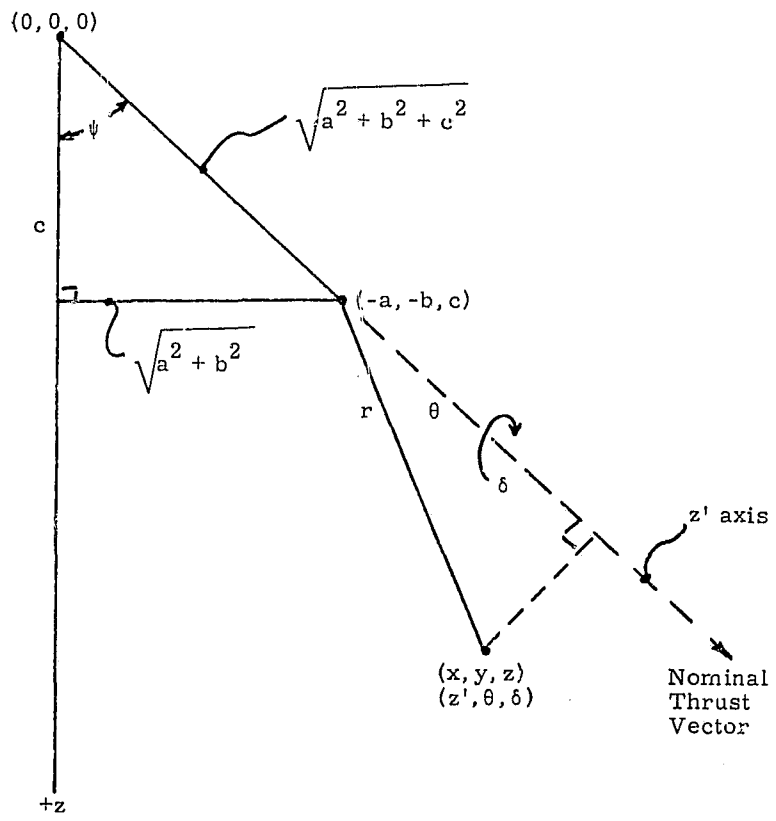

Figure IV-5. Thruster Orientation.

The neutral atom density is given by:

$$\rho = \frac{\Gamma}{v} \tag{IV-4}$$

where:

v = atom velocity

Therefore, if we have frozen flow so that v is constant:

$$\rho(r, \theta) = \frac{\rho_0 \left(\frac{A}{r}\right)^2 \cos\theta}{\left[1 + 2\left(\frac{A}{r}\right)^2 \cos\theta + \left(\frac{A}{r}\right)^4\right]^{1/2}} \tag{IV-5}$$

Note the restrictions:

$$0 \leq \theta \leq \pi/2$$

$$r > A$$

If $r \gg A$, Equation (IV-5) reduces to:

$$\rho(r, \theta) = \rho_0 \left(\frac{A}{r}\right)^2 \cos\theta \tag{IV-6}$$

which we will use as an approximation to determine the number of atoms "seen" by the tracker. (The effect of the approximation is to predict a higher density than is actually the case for positions near to the thruster. The error is expected to be small since the tracker cannot "see" the close-in position of the plume. In any event, the assumption is conservative.)

2.3 Tracker Geometry

The line-of-sight from the tracker along the centerline is straightforward. We merely select $x = h$, $z = g$, $-j \geq y \geq -\infty$. Angular changes will require different selections of x and z. To investigate these effects, we consider the geometry shown in Figure IV-6. The angle α describes motion in the xy plane (positive for movement in the positive x direction) and the angle β describes yz plane motion (positive with positive z movement).

Note the following:

$$j_2 = j_3 \tan \alpha \qquad \text{(IV-7)}$$

$$j_1 = j_3 \tan \beta \qquad \text{(IV-8)}$$

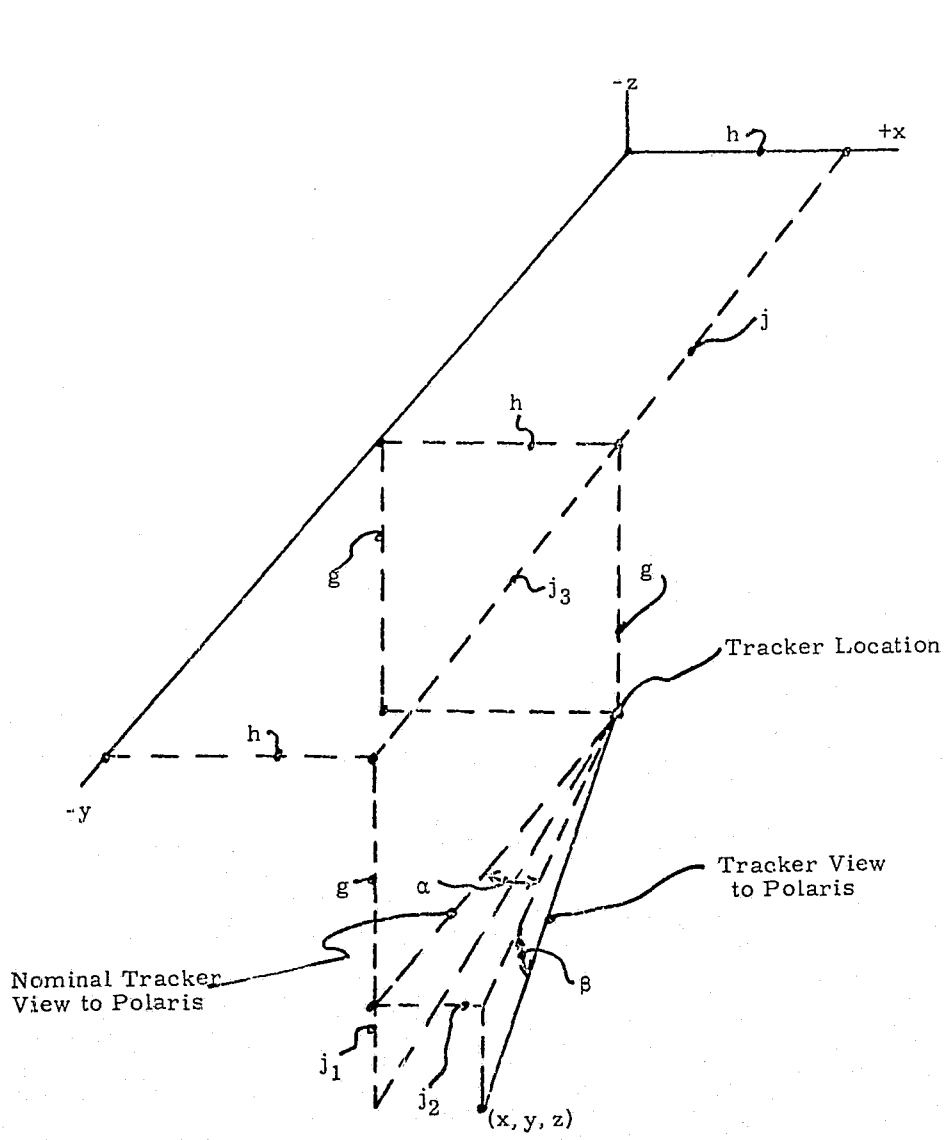

Figure IV-6. Tracker Line-of-Sight Geometry.

Immediately:

$$y = -(j + j_3)$$

$$j_3 = -y - j \tag{IV-9}$$

$$x = h + j_2$$

$$x = h + j_3 \tan \alpha \tag{IV-10}$$

$$z = g + j_3 \tan \beta \tag{IV-11}$$

Or:

$$x = h - (j + y) \tan \alpha \tag{IV-12}$$

$$z = g - (j + y) \tan \beta \tag{IV-13}$$

2.4 Tracker Sight Through Plume

The previous section provides x, y, and z along any line-of-sight. We next must obtain the density corresponding to these coordinates.

The distance between the point (x, y, z) and the thruster opening at (-a, -b, c) is r. This is given by:

$$r = [(x + a)^2 + (y + b)^2 + (z - c)^2]^{1/2} \tag{IV-14}$$

Substituting, we obtain:

$$r = [\{h + a - (j + y) \tan \alpha\}^2 + (y + b)^2 + \{g - c - (j + y) \tan \beta\}^2]^{1/2} \tag{IV-15}$$

If the direction cosines of a line connecting these points are α_1, β_1, and γ_1, then:

$$\cos \alpha_1 = \frac{x + a}{r} \tag{IV-16}$$

$$\cos \beta_1 = \frac{y + b}{r} \tag{IV-17}$$

$$\cos \gamma_1 = \frac{z - c}{r} \tag{IV-18}$$

The thrust vector connects the point (0, 0, 0) and (-a, -b, c). The direction cosines of this line, indicated by the subscript 2, are:

$$\cos \alpha_2 = \frac{-a}{r_2} \tag{IV-19}$$

$$\cos \beta_2 = \frac{-b}{r_2} \tag{IV-20}$$

$$\cos \gamma_2 = \frac{c}{r_2} \tag{IV-21}$$

where:

$$r_2 = (a^2 + b^2 + c^2)^{1/2} \tag{IV-22}$$

The angle between the two lines is the angle θ which describes the exhaust plume behavior. This is given by:

$$\cos \theta = \cos \alpha_1 \cos \alpha_2 + \cos \beta_1 \cos \beta_2 + \cos \gamma_1 \cos \gamma_2 \tag{IV-23}$$

Substituting, we find:

$$\cos \theta = \frac{1}{r} [(x + a) \cos \alpha_2 + (y + b) \cos \beta_2 + (z - c) \cos \gamma_2] \tag{IV-24}$$

But the density expression can now be applied to get:

$$\rho = \frac{\rho_0 A^2}{r^3} [(x + a) \cos \alpha_2 + (y + b) \cos \beta_2 + (z - c) \cos \gamma_2] \tag{IV-25}$$

Next we substitute for x and z:

$$\rho = \frac{\rho_0 A^2}{r^3} \{[a + h - (j + y) \tan \alpha] \cos \alpha_2 + (y + b) \cos \beta_2 + [g - c - (j + y) \tan \beta] \cos \gamma_2\} \tag{IV-26}$$

A final substitution for r gives:

$$\rho = \rho_0 A^2 \{[a + h - (j + y) \tan \alpha] \cos \alpha_2 + [y + b] \cos \beta_2 + [g - c - (j + y) \tan \beta] \cos \gamma_2\}$$

$$\{[a + h - (j + y) \tan \alpha]^2 + [y + b]^2 + [g - c - (j + y) \tan \beta]^2\}^{-3/2} \tag{IV-27}$$

To obtain an algebraic simplification, define:

$$s_1 = a + h - j \tan \alpha \tag{IV-28}$$

$$s_2 = g - c - j \tan \beta \qquad \text{(IV-29)}$$

Thus

$$\frac{\rho}{\rho_0 A^2} = \{(s_1 \cos \alpha_2 + b \cos \beta_2 + s_2 \cos \gamma_2) + y (\cos \beta_2 \pm \tan \alpha \cos \alpha_2 - \tan \beta \cos \gamma_2\} \qquad \text{(IV-30)}$$

$$\{s_1^2 + b^2 + s_2^2) + y (-2 s_1 \tan \alpha + 2 b - 2 s_2 \tan \beta) + y^2 (\tan^2 \alpha + 1 + \tan^2 \beta\}^{-3/2}$$

Further define:

$$s_3 = s_1 \cos \alpha_2 + b \cos \beta_2 + s_2 \cos \gamma_2 \qquad \text{(IV-31)}$$

$$s_4 = \cos \beta_2 - \tan \alpha \cos \alpha_2 - \tan \beta \cos \gamma_2 \qquad \text{(IV-32)}$$

$$s_5 = s_1^2 + b^2 + s_2^2 \qquad \text{(IV-33)}$$

$$s_6 = 2 (-s_1 \tan \alpha + b - s_2 \tan \beta) \qquad \text{(IV-34)}$$

$$s_7 = \tan^2 \alpha + 1 + \tan^2 \beta \qquad \text{(IV-35)}$$

so that:

$$\frac{\rho}{\rho_0 A^2} = \frac{s_3 + s_4 y}{(s_5 + s_6 y + s_7 y^2)^{3/2}} \qquad \text{(IV-36)}$$

2.5 View of Polaris

The tracker will "see" space, Polaris, and cesium atoms. The effect upon Polaris will be determined by the number of atoms interposed in the field of view between the tracker and the star. This is given by:

$$dN = \rho \, du \qquad \text{(IV-37)}$$

where:

N = atoms per unit area

u = distance measured along the tracker line of sight

The tracker is located at (h, -j, g). The position under consideration is given as (h - [j + y] tan α , y, g - [j + y] tan β). (See Eqs. I-12 and I-13). The distance between these points is given by:

$$u = [\{h - (j + y) \tan \alpha - h\}^2 + (y + j)^2 + \{g - (j + y) \tan \beta - g\}^2]^{1/2} \quad \text{(IV-38)}$$

$$u = (j + y) (\tan^2 \alpha + \tan^2 \beta + 1)^{1/2} \quad \text{(IV-39)}$$

Differentiating, we find:

$$d u = (\tan^2 \alpha + \tan^2 \beta + 1)^{1/2} d y \quad \text{(IV-40)}$$

Substitution of Eqs. (IV-40) and (IV-36) into (IV-37) gives:

$$d N = \frac{\rho_0 A^2 (s_3 + s_4 y) (s_7) d y}{(s_5 + s_6 y + s_7 y^2)^{3/2}} \quad \text{(IV-41)}$$

Further define:

$$s_8 = \rho_0 A^2 s_7 \quad \text{(IV-42)}$$

$$s_9 = s_3 s_8 \quad \text{(IV-43)}$$

$$s_{10} = s_4 s_8 \quad \text{(IV-44)}$$

so that:

$$d N = \frac{(s_9 + s_{10} y) d y}{(s_5 + s_6 y + s_7 y^2)^{3/2}} \quad \text{(IV-45)}$$

and N is obtained by integrating:

$$N = - \int_{y_{min}}^{y_{max}} \frac{(s_9 + s_{10} y) d y}{(s_5 + s_6 y + s_7 y^2)^{3/2}} \quad \text{(IV-46)}$$

where y_{min} is the position nearest the spacecraft and y_{max} is furthest removed. Define:

$$q = 4 s_5 s_7 - s_6^2 \quad \text{(IV-47)}$$

$$k = 4 s_7 / q \quad \text{(IV-48)}$$

Then, this has the solution:

$$N = \left\{ \frac{2 [(2 s_7 s_9 - s_6 s_{10}) y + s_6 s_9 - 2 s_5 s_{10}]}{q (s_5 + s_6 y + s_7 y^2)^{1/2}} \right\}_{y_{min}}^{y_{max}} \quad \text{(IV-49)}$$

The limits, y_{min} and y_{max}, are determined, in part, by the plume restriction that $0 \leq \theta \leq \pi/2$. We may write:

$$\cos \theta = (s_3 + s_4\, y)\,(s_5 + s_6\, y + s_7\, y^2)^{-1/2} \qquad \text{(IV-50)}$$

For $\theta = \pi/2$, $\cos \theta = 0$, and, for a finite y:

$$y_0 = - s_3/s_4 \qquad \text{(IV-51)}$$

But, from a practical sense, y cannot be less than j. Therefore, if $j + y_0 > 0$, $y_{min} = -j$. Otherwise, $y_{min} = y_0$.

Reflection upon the geometry will show that $y_{max} = -\infty$. When we use this value, the value of the integral becomes infinite - also a realistic (mathematically) upper limit. In the practical sense, we do not go to ∞ because of the finite number of atoms ejected, finite thrusting time, exhaust interactions and removal mechanisms, etc. In the mathematical sense, the function behavior allows choice of a large value for y_{max}. Increase in N beyond this is so slow as to be negligible for realistic distances.

This solution for plume behavior was programmed for solution on a digital computer. The results of the analysis are summarized in Figure IV-8 with the input geometry which

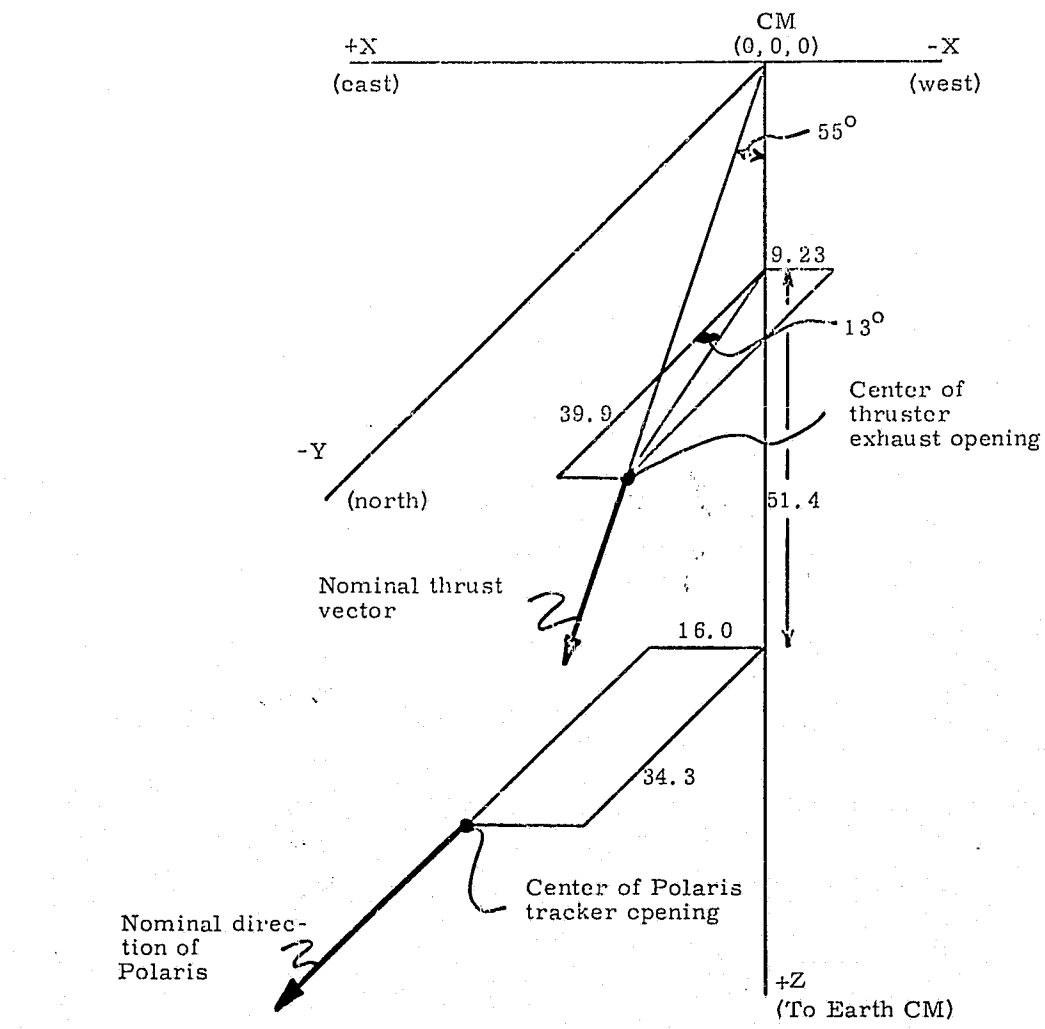

All dimensions in inches

Scale along major axes: 1/20

Figure IV-7. Tracker-Thruster Geometry.

is shown in Figures 7 and IV-7. The behavior with increasing distance from the tracker is shown in Figure IV-9. Beyond roughly 1000 inches, the increased number of atoms seen by the tracker is very small. Beyond 10^5 inches, the change is so slight that it is lost by the limited significant figures carried by the machine. (We used -10^{10} inches in place of $-\infty$ for y_{max} in our study.)

2.6 Reflected Sunlight

The basic assumptions (see Appendix V) allow us to set up a relatively simple geometry to handle sunlight interaction. If P_a is the probability of absorption per unit length and a photon passes through a distance dr, the probability of absorption is P_a dr. If the distance from the absorption point to the tracker lens is r, the probability that the reemitted photon will hit the lens is:

$$d P_h' = \frac{A'}{4 \pi r^2} \qquad \text{(IV-52)}$$

where:

A' = effective lens area

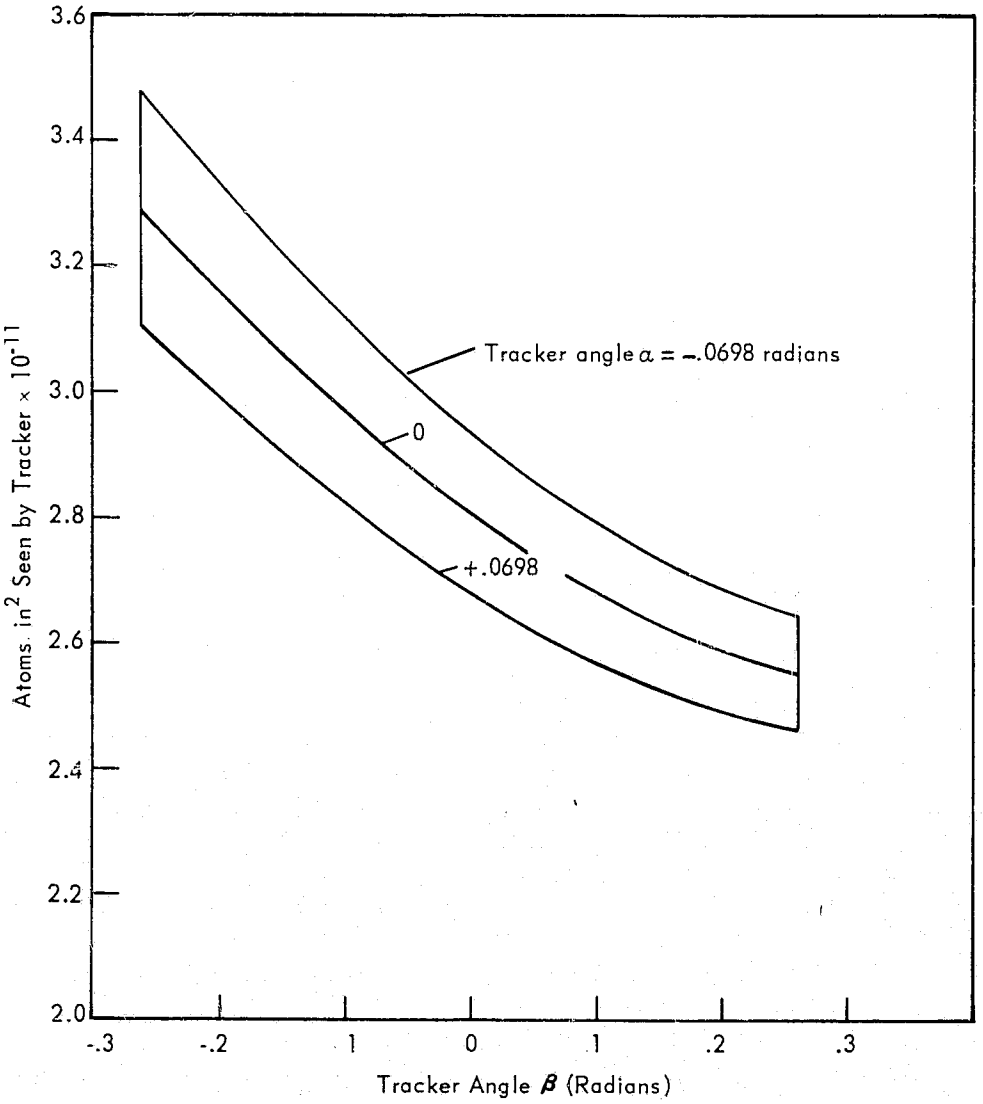

Figure IV-8. Atoms/in^2 Seen By Tracker.

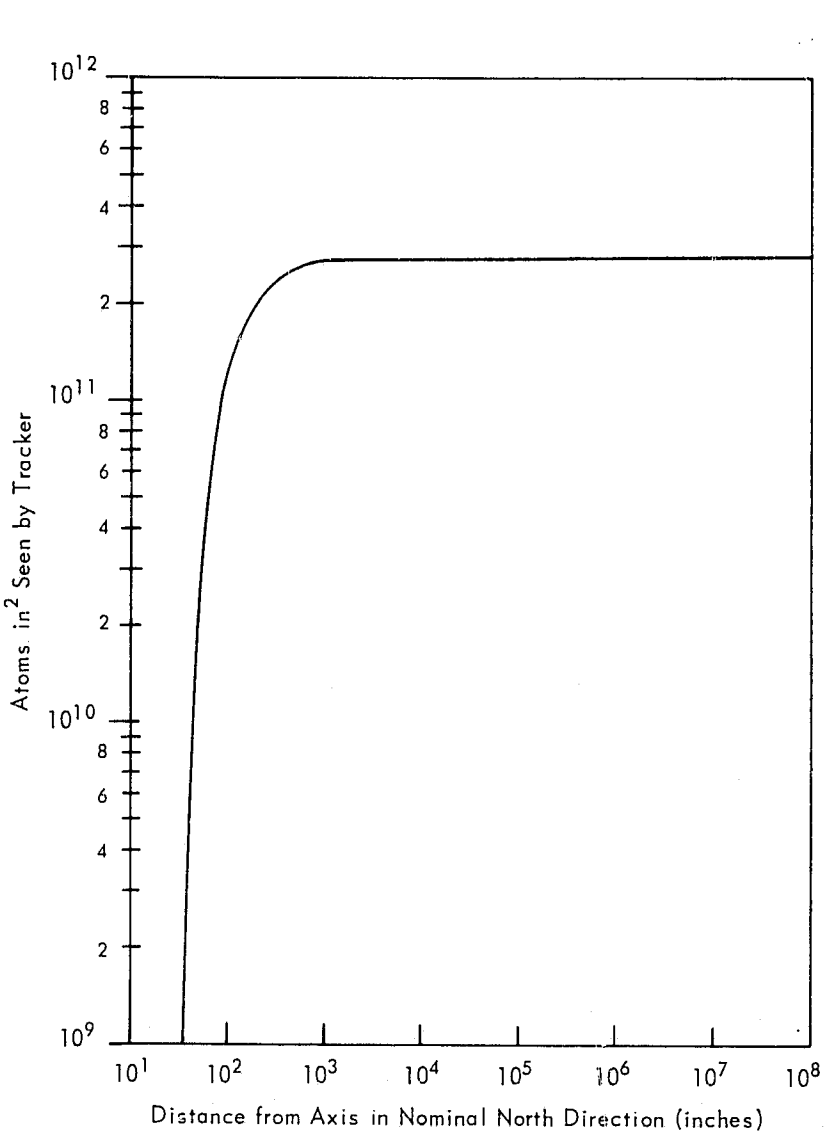

Figure IV-9. Atoms/in^2 Seen by Tracker.

Therefore, the probability of obtaining an absorption which hits the lens is:

$$d P_h = (P_a \, d \, r) \, d P_h' = \frac{A' \, P_a \, d \, r}{4 \pi \, r^2} \tag{IV-53}$$

for each photon passing through the plume which travels a distance dr. Our assumptions make the selection of sun position (relative to the plume) unimportant. It makes no difference what direction the sun generated photons are traveling. Once we consider the total plume volume, the number of interactions will be the same.

If I_0 is the sunlight intensity (energy per unit area per unit wavelength), then the intensity per unit wavelength intercepted by the plume is given by:

$$d^2 I' = I_0 \, d^2 S \tag{IV-54}$$

where d^2S is the incremental area of plume under consideration as seen by the sun. The geometrical arrangement can be obtained by considering Figure IV-10. The lens area

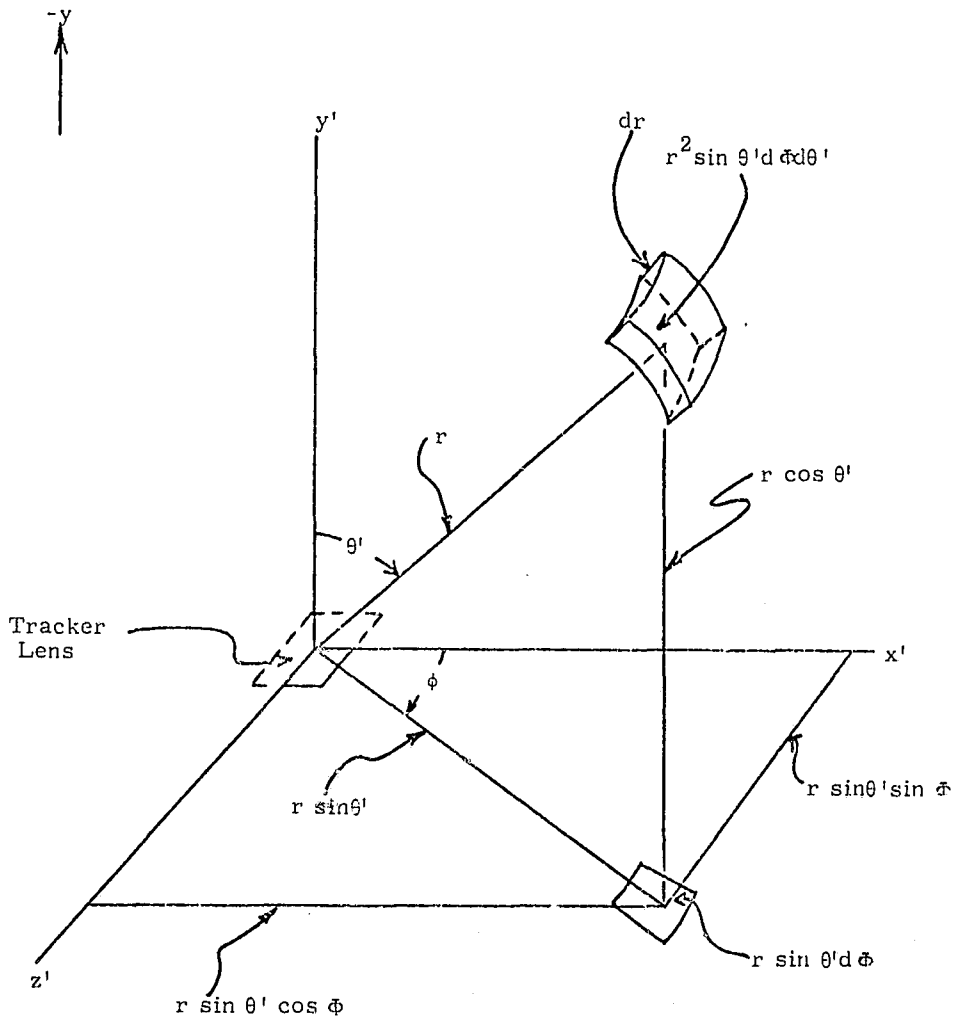

Figure IV-10. Sunlight Interaction Geometry.

seen by the sun is $d^2S = r^2 \sin\theta \, d\Phi d\theta$. In traversing the elemental volume, the photons will travel a distance dr. The intensity scattered into the lens is given by:

$$d^3 I = d P_h \, d^2 I' \tag{IV-55}$$

or

$$\begin{aligned} d^3 I &= d P_h \, I_0 \, d^2 S \\ &= \frac{A' \, I_0 \, P_a \, d r}{4 \pi} \sin\theta \, d\Phi \, d\theta \end{aligned} \tag{IV-56}$$

Note:

$$A' = A_\ell \cos\theta' \tag{IV-57}$$

where

A_ℓ = lens area

Therefore:

$$d^3 I = \frac{A_\ell I_0 P_a \cos \theta' \sin \theta' \, d r \, d \Phi \, d \theta'}{4 \pi} \tag{IV-58}$$

The instantaneous field of view is 0.7° (yaw) × 2.1° (roll) (Ref. IV-12). Unfortunately, this specification is not easy to apply to the selected geometry. However, we have included this as an easily understood illustration of the technique.

We next use the rectangular coordinate system illustrated in Figure IV-11. The equivalent of Eq. (IV-53) now is:

$$d P_h = \frac{A' P_a \, d y'}{4 \pi (x'^2 + y'^2 + z'^2)} \tag{IV-59}$$

where the sun now is considered as located at an (x', y', z') of (0, -∞, 0. The area seen by the sun is simpler than before: dx'dz'. The intensity per unit wavelength intercepted by the plume is:

$$d^2 I' = I_0 \, d x' \, d z' \tag{IV-60}$$

Using Eq. (IV-55), we find:

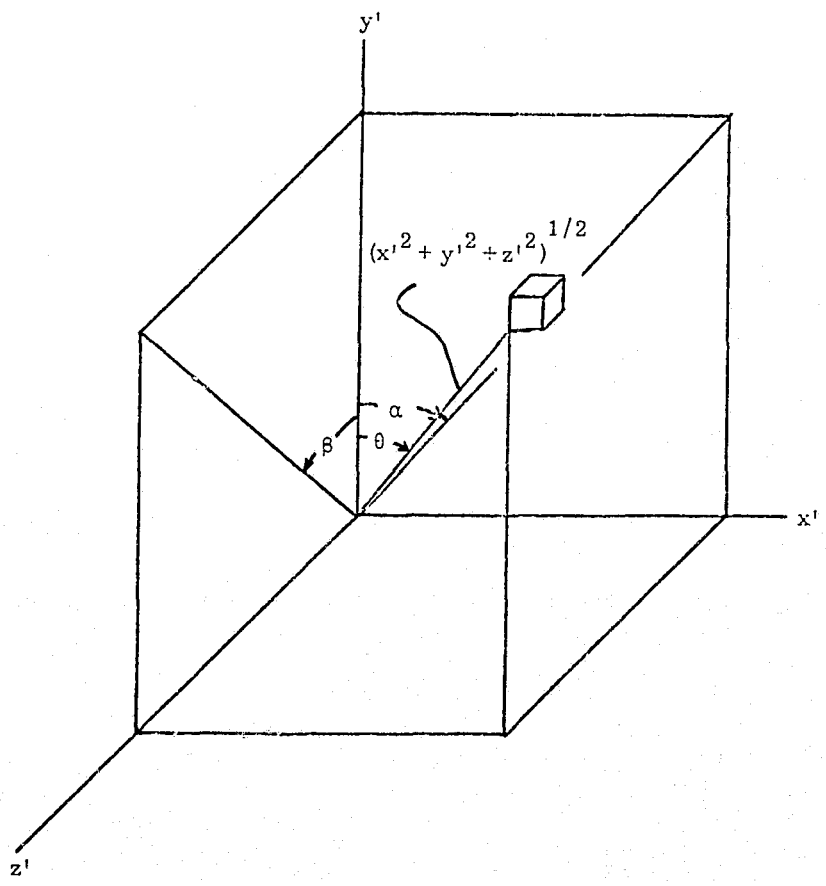

Figure IV-11. Sunlight Interaction Geometry.

$$d^3 I = \frac{A' P_a \, d y' \, I_0 \, d x' \, d z'}{4 \pi (x'^2 + y'^2 + z'^2)} \tag{IV-61}$$

Note that:

$$\cos \theta' = \frac{y'}{(x'^2 + y'^2 + z'^2)^{1/2}} \tag{IV-62}$$

This and Eq. (IV-57) now enable us to write:

$$d^3 I = \frac{A_\ell \, y' \, P_a \, I_0 \, d x' \, d y' \, d z'}{4 \pi (x'^2 + y'^2 + z'^2)^{3/2}} \tag{IV-63}$$

which is the equivalent of Eq. (IV-59) in the (x', y', z') coordinate system. Now (see also Figure IV-6):

$$x' = - (j + y) \tan \alpha \tag{IV-64}$$

$$y' = - (j + y) \tag{IV-65}$$

$$z' = - (j + y) \tan \beta \tag{IV-66}$$

Therefore, if:

$$\alpha'_1 \leq \alpha \leq \alpha'_2 \tag{IV-67}$$

and

$$\beta'_1 \leq \beta \leq \beta'_2 \tag{IV-68}$$

then:

$$- (j + y) \tan \alpha'_1 \leq x' \leq - (j + y) \tan \alpha'_2 \tag{IV-69}$$

$$- (j + y) \tan \beta'_1 \leq z' \leq - (j + y) \tan \beta'_2 \tag{IV-70}$$

Further:

$$0 \leq y' \leq \infty \tag{IV-71}$$

which defines the range of all independent variables. Immediately, Eq. (IV-63) becomes:

$$I = \int_{y' = 0}^{\infty} \int_{x' = y' \tan \alpha'_1}^{y' \tan \alpha'_2} \int_{z' = y' \tan \beta'_1}^{y' \tan \beta'_2} \frac{A_\ell \, y' \, P_a \, I_0 \, d x' \, d y' \, d z'}{4 \pi (x'^2 + y'^2 + z'^2)^{3/2}} \tag{IV-72}$$

Unfortunately, P_a is a function, not a constant, and we cannot immediately evaluate Eq. (IV-72). This completes the geometric portion of the sunlight interaction treatment.

2.7 Tracker View of the Primary Beam ($\theta \leq 15°$).

The angle θ is described by:

$$\cos\theta = (s_3 + s_4\, y)\,(s_5 + s_6\, y + s_7\, y^2)^{-1/2} \qquad \text{(IV-73)}$$

This function is a maximum when θ is at a minimum, provided $\theta \geq 0$. (The value $\theta \leq 0$ is meaningless for our purposes - it has no physical significance.) To find the maximum, we differentiate and set the result equal to zero:

$$\frac{d(\cos\theta)}{dy} = 0 = s_4\,(s_5 + s_6\, y + s_7\, y^2)^{-1/2} - \frac{1}{2}\,(s_3 + s_4\, y)\,(s_5 + s_6\, y + s_7\, y^2)^{-3/2}\,(s_6 + 2\, s_7\, y) \qquad \text{(IV-74)}$$

Rejecting $s_5 + s_6\, y + s_7\, y^2 = \pm\infty$, we can rewrite this as:

$$y = \frac{s_3\, s_6 - 2\, s_4\, s_5}{s_4\, s_6 - 2\, s_3\, s_7} \qquad \text{(IV-75)}$$

Beautiful!! We have found a simple expression for a change. The behavior of this function and Eq. IV-73 was obtained by writing a digital computer program and running a parametric study over the range of interest. The results are shown in Figure IV-12. Clearly, the primary beam just misses the maximum range of view of the tracker. Changing the beam direction by deflecting the beam will bring a portion into the tracker field of view.

3. REFERENCES

IV-1. "Ion Engine Installation," G. E. sketch drawn on November 14, 1969 (See Ref. IV-2).

IV-2. Bartlet, R., Personal Communications, GSFC. April 17, 1970.

IV-3. "Proposed Changes to ICD No. GD11711002, Figure 3-3," not otherwise identified (See Ref. IV-2).

IV-4. "Thruster Assy., 1 mlb M.E.S.C.," Electro-Optical Systems, Inc. sketch, Code ident. no. 12705, not otherwise identified (See Ref. IV-5).

IV-5. Ernstene, M. P., et al., "Surface Ionization Engine Development," Journal of Spacecraft and Rockets, Vol. 3, No. 5, May 1966, pp. 744-747.

IV-6. Rawlin, V. K., and E. V. Pawlik, "A Mercury Plasma-Bridge Neutralizer," Journal of Spacecraft and Rockets, Vol. 5, No. 7, July 1968, pp. 814-820.

IV-7. Cole, Robert K., H. S. Ogawa, and J. M. Sellen, Jr., "Study of Electric Spacecraft Plasmas and Field Interactions," 07677-6013-R000, TRW Systems, May 1, 1968.

IV-8. Speiser, Robert, Personal Communication, Electro-Optical Systems, Telephone No. 213-351-2351, April 20, 1970.

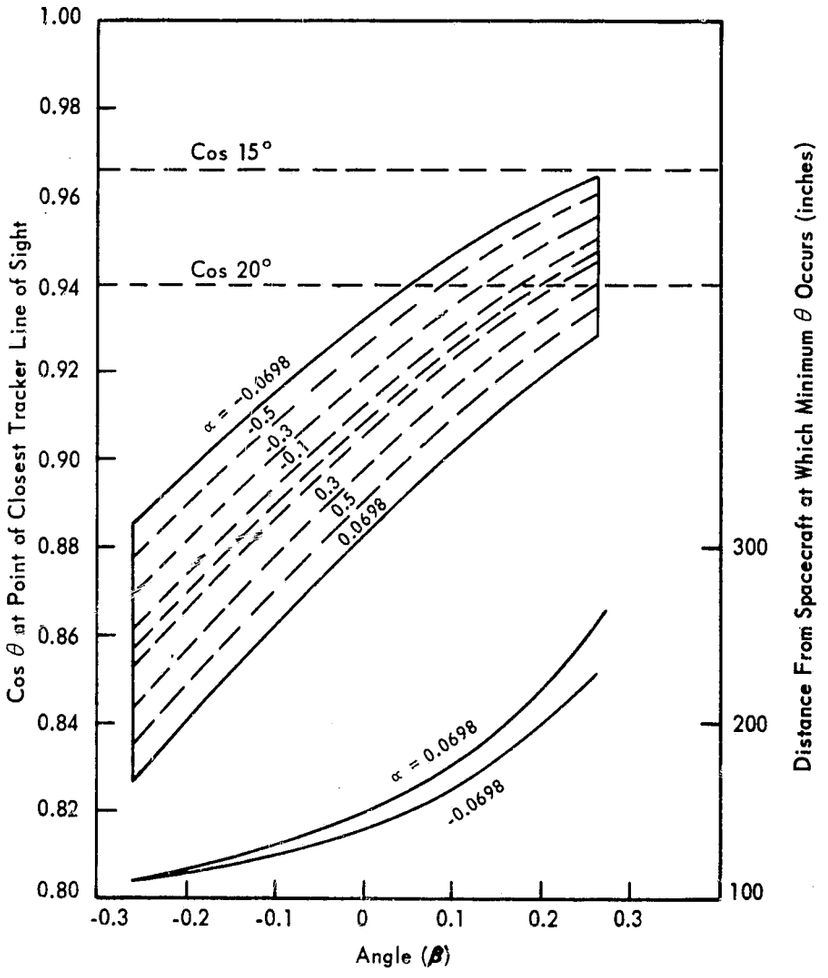

Figure IV-12. Thruster Primary Beam-Tracker Interaction.

IV-9. Brink, Raymond W., Essentials of Analytic Geometry, D. Appleton-Century Company, 1939.

IV-10. Hall, David F., "Evaluation of Electric Propulsion Beam Divergence and Effects on Spacecraft," Final Report Draft, MJO:4795, TRW Systems, December 2, 1968.

IV-11. Hall, David F., Brian E. Newman, and James R. Womack, "Electrostatic Rocket Exhaust Effects on Solar-Electric Spacecraft Subsystems," Journal of Spacecraft and Rockets, Vol. 7, No. 3, March 1970, pp. 305-312.

IV-12. "Proposal for Applications Technology Satellite F & G, Phase D," SD Proposal N-21630, General Electric Company, McDonnel Douglas, and Hughes, Book 1: Technical, Vol. 1C, Controls, 17 September 1969, pp. 4-108 (reference not available in total for the study-only applicable pages were made available).

PRECEDING PAGE BLANK NOT FILMED

APPENDIX V

SPECTRAL CHARACTERISTICS AND ABSORPTION PHENOMENA

1. TRACKER RESPONSE

The tracker is based upon an ITT F4004 image tube sensor which has an S-20 response (Ref. V-1). The S-20 curve is shown in Figures V-1 (ITT) and -2 (RCA). We are not concerned with magnification, etc. in the tracker since all calculations are based upon the total instantaneous field of view. Therefore, subject to the assumption that the spectrum is unperturbed by the tracker lens, we are not concerned with its other characteristics.

2. POLARIS SPECTRUM

The relative spectral energy distribution of Polaris is shown in Figure V-3. The integrated energy from Polaris is 1.18×10^{-13} w/cm (Ref. V-5). A curve providing absolute values as a function of wavelength is shown in Figure V-4.

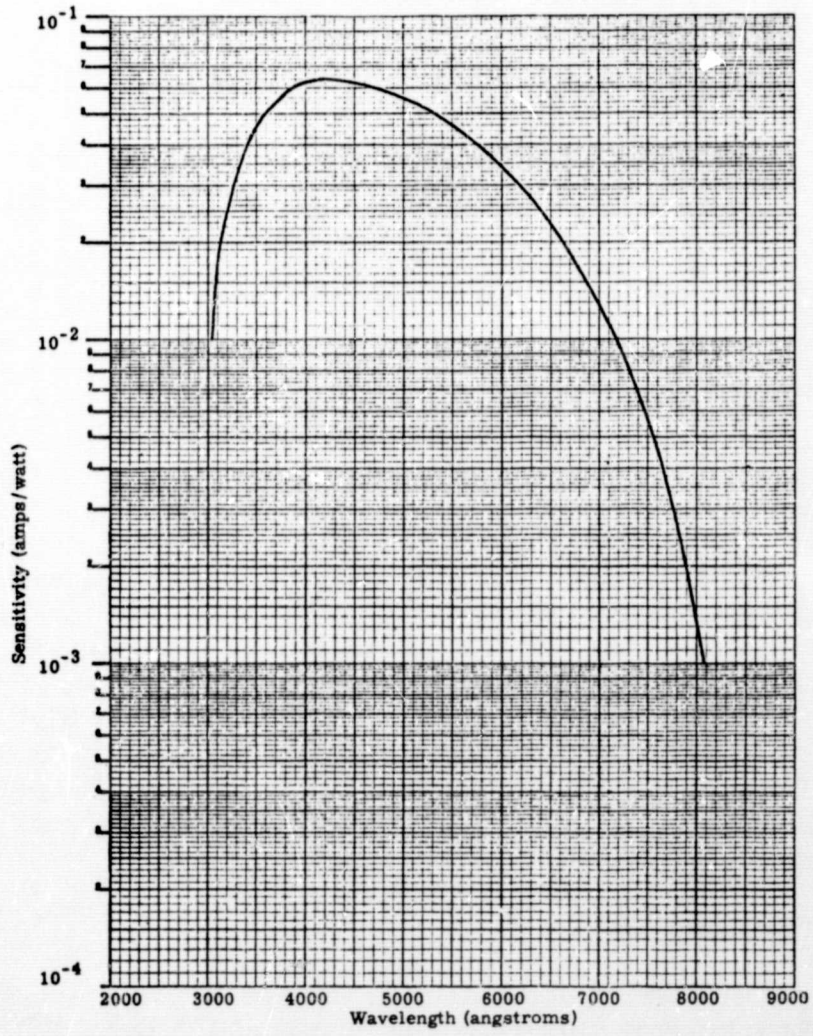

Figure V-1. Tyical Absolute Spectral Response Characteristics of Photoemissive Devices, S-20 Curve (Ref. V-2).

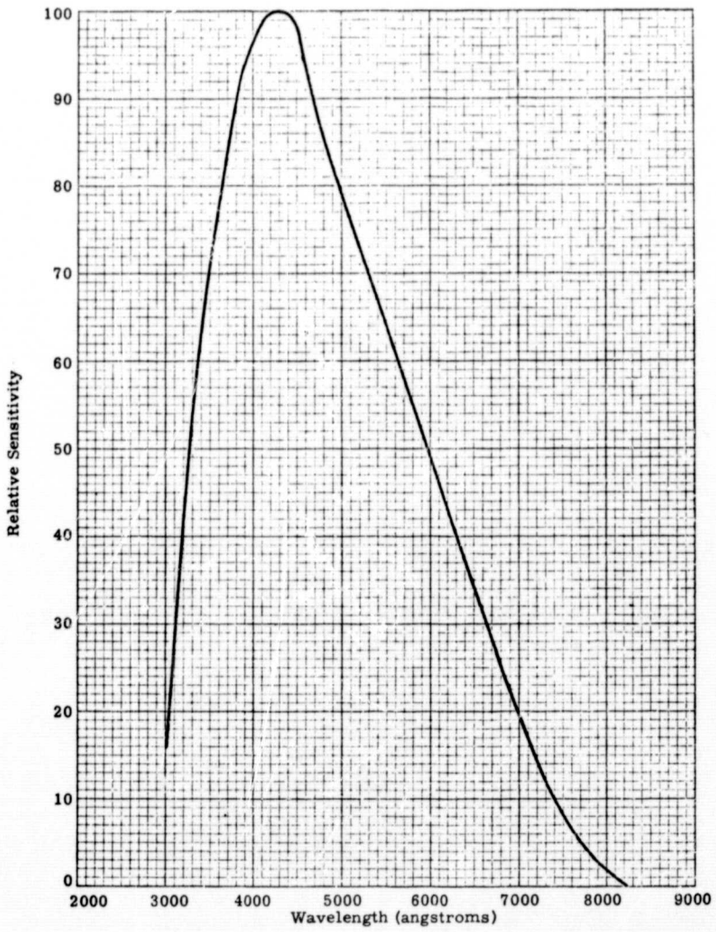

Figure V-2. Spectral Response Curve S-20 for RCA Phototubes (Ref. V-3).

3. SOLAR SPECTRUM

The major contributor to the problem as far as light scattering from the plume into the tracker is concerned is the sun. Analysis of this behavior requires the solar spectrum. This is given in Figure V-5, which gives the energy normal to the sun outside the atmosphere (1 au). The flux is expressed as watts per square centimeter per angstrom. To get total flux, one would integrate with respect to wavelength (λ). Integration from $\lambda = 0$ to ∞ gives a total flux of 0.1377 w/cm^2 (1377 w/m^2, 128.0 w/ft^2). (The tabulated data range to 70,000 Å, with 0.14 percent of the energy in the range $70000 < \lambda < \infty$. The Figure V-5 data are plotted using 50 Å increments for $2220 < \lambda < 6000$ and with 100 Å increments for $6000 < \lambda < 9000$. The data apply to the mean solar distance. They will be about 3.4 percent higher at the winter solstice in December and 3.4 percent smaller at the summer solstice in July. The data are estimated by the reference to be accurate to within ±2 percent.

4. SPECTRAL TERMINOLOGY.

At this point, we will deviate for the reader who is not familiar with spectra. Wavelengths commonly are given in microns (μ, 10^{-6} m or 10^{-4} cm) and angstroms (Å, 10^{-8} cm). Many times, wave numbers are used:

$$\tilde{\nu} = \frac{1}{\lambda}$$

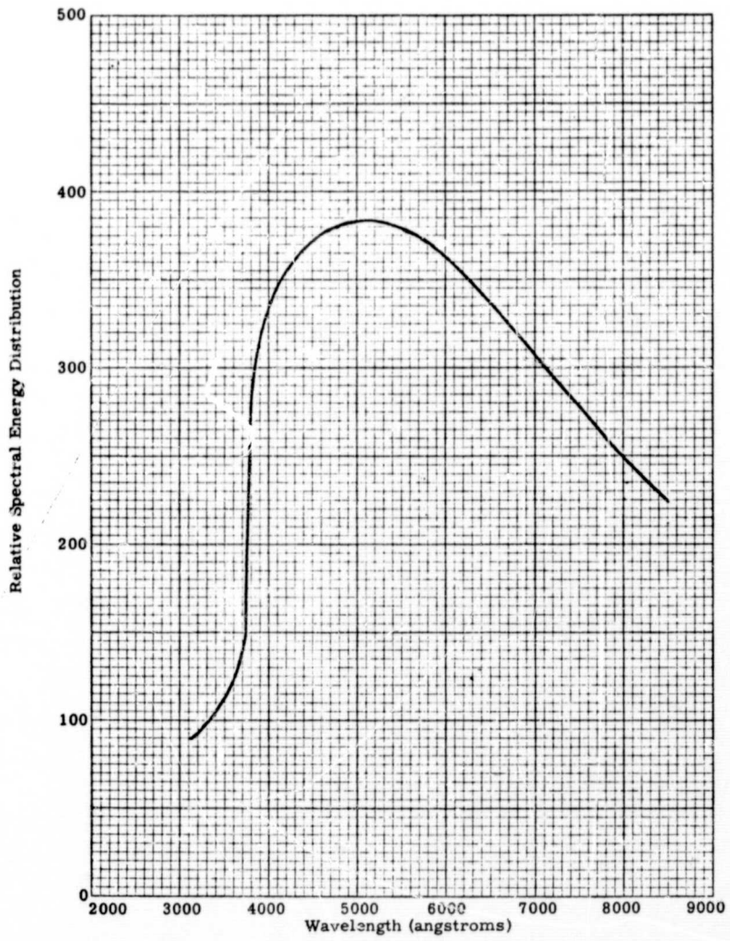

Figure V-3. Relative Spectral Energy Distribution for Alpha Ursa Minoris (Polaris) (Ref. V-4).

where:

$\tilde{\nu}$ = wave number (usually cm^{-1})

λ = wavelength

This should be interpreted as the number of waves per centimeter, or simply waves/cm. Frequencies are seldom used because of the size of the number (c/λ where c is the velocity of light). Wavelengths in air and vacua are different ($\sim$ one part in 3000). We will neglect the difference. Wave numbers occasionally are given in Kaysers (as in Table V-2). This is simply cm^{-1}. Frequency, ν, is related to the wave number by:

$$\nu = c\,\tilde{\nu}$$

where ν typically has units of sec^{-1} (waves per second). Energy is a common term. It may be related by:

$$E = h\,\nu$$

where

h = Boltzmann constant

$= 6.625 \times 10^{-27}$ erg sec

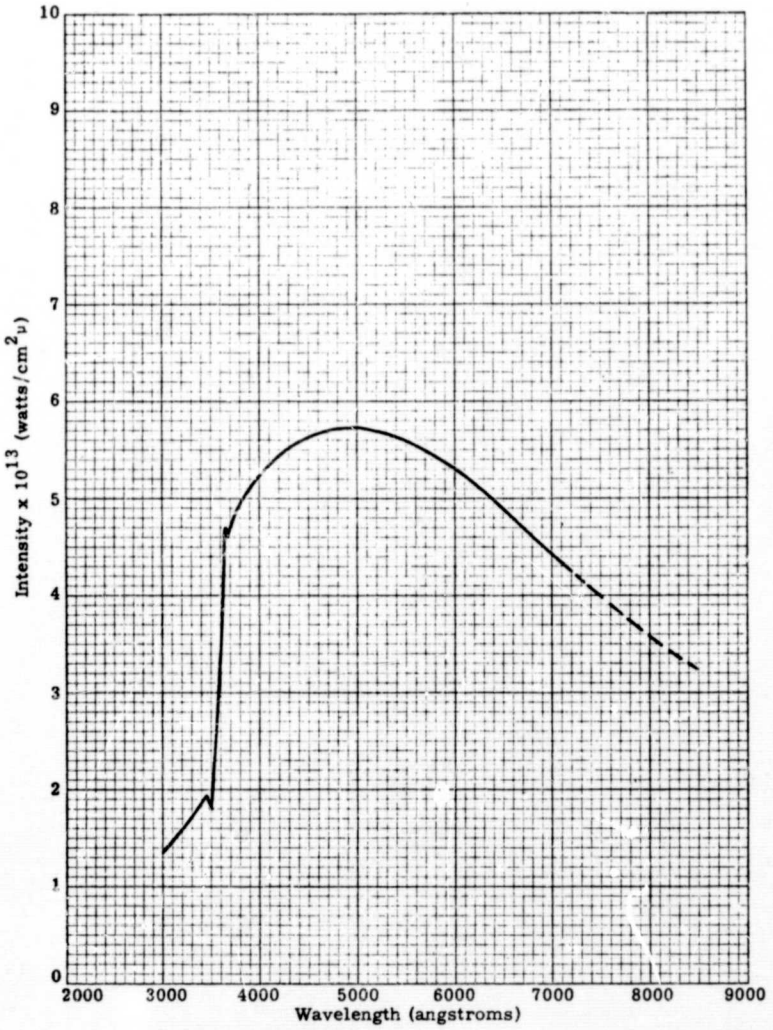

Figure V-4. Polaris Spectral Energy Distribution (Ref. V-4).

Inserting appropriate constants gives:

$\tilde{\nu}$ = 8066 E cm^{-1} (E in ev)

λ = 12398/E Å (E in ev)

The Rydberg constant many times appears. This is R = 109, 700 cm^{-1}. (It varies in the fourth significant figure for different atoms. The difference is, for our purposes, negligible.) This corresponds to the first state of the hydrogen atom (ν = 109, 678 cm^{-1}; E = energy = 217.3 × 10^{-13} ergs, = 13.58 ev).

We are dealing with an atom. (The spectrum of an atom is considerably less complicated than that of a molecule.) Cesium is a rather heavy atom with a relatively complex spectrum*, but most of this complexity is outside the range of response of the sensor. Therefore, it is of no concern to us. We need concentrate only in the range 3000 Å ≤ λ ≤ 8200 Å, as shown in Figure V-1. This brackets the visible light range. The states of

*Connerade (Ref. V-7) reported over 158 transitions of neutral cesium in the 600-9 ,0 Å region due to excitation from the $5p^6$ shell. This prompted the statement "The CsI absorption spectrum is the most complex we have encountered in our investigations."

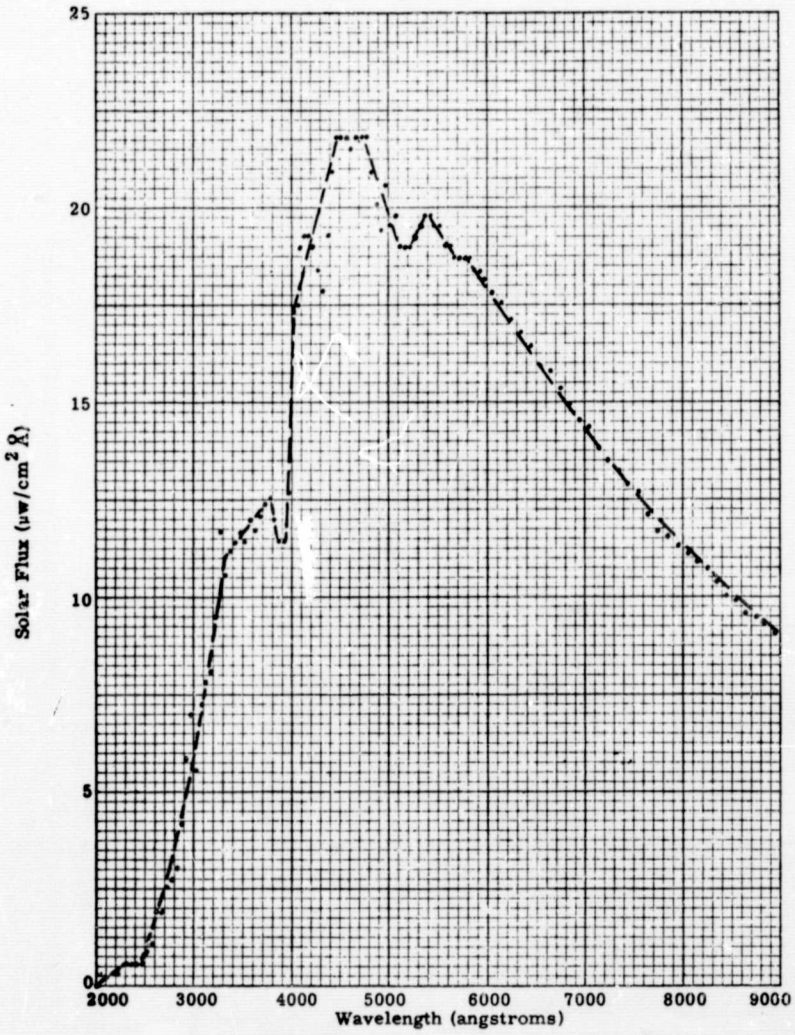

Figure V-5. Solar Spectral Irradiance (Ref. V-6).

excitation in which the radiation involved falls in the visible, near-infrared, or ultraviolet regions of the spectrum (our range of interest) involves only the outermost, valence, electrons (Ref. V-9). These are the electrons involved in ionization as well.

5. CESIUM SPECTRAL BEHAVIOR.

The reaction:

$$Cs \longrightarrow Cs^{+} + e^{-} \text{ (gas)}$$

has an ionization potential of 3.894 ev (Rev. V-8). This is a direct indication of the type of spectral behavior we may expect with energy.

If a high energy is required to ionize an atom, we would also expect that a high energy is required tc excite it from the ground state. Similarly, if an atom is easily ionized, it is easily excited. Neutral cesium (referred to as Cs I) has a low ionization potential.

The ionizatien potential of CS II (Cs^{+}) is 25.1 ev and that of Cs III (Cs^{++}) is about 34.6 ev. Obviously, considerably more energy is required to raise an electron in an ion from the ground state to a level required for ejection. Similarly, more energy will be required to raise it to the level of the first spectral line. This is an immediate indication that absorption due to ionized cesium may be negligible. (As shown in Table VI-1, excited state lifetimes are extremely short. We may assume ground state conditions exist.)

Table V-1
Cesium Spectra (Ref. V-10)

Principal Series		Sharp Series	
λ (ångstrom)	ev from Ground State	λ (ångstrom)	ev from Ground State
8943.46	1.386	14694.8	2.299
8521.12	1.455	13588.1	
4593.16	2.699	7944.11	3.016
4555.26	2.721	7609.13	
3888.65	3.188	6586.94	3.337
3876.39	3.198	6354.98	
3617.41	3.427	6034.6	3.509
3611.52	3.433	5839.11	
3480.13	3.562	5085	3.893
3476.88	3.566	4945	
3184.2	3.893		
Diffuse Series		**Fundamental Series**	
λ (ångstrom)	ev from Ground State	λ (ångstrom)	ev from Ground State
36127	1.798	10124.7	3.034
34892	1.810	10120.0	
30100		10025.1	
9208.4	2.801	8079.02	3.344
9172.23		8078.92	
8761.35	2.807	8015.71	
6983.37	3.230	7279.95	3.513
6973.17	3.233	7279.89	
6723.18		7228.53	
6217.27	3.449	5952	3.893
6212.87	3.450	5917	3.893
6010.33			
5085	3.893		
4945	3.893		

The various series of Cs I are summarized in Table V-1. Note that the first line of the principal series corresponds to about one-third the energy required for ionization. (This is the brightest series in the spectrum.) All of the series converge as they approach the ionization energy.

Considerably more level detail is provided by Moore (Ref. V-11). She has compiled spectra which, for CsI, show 73 levels for the principal series (transitions to the ground state). The applicable portion of her data is reproduced in Table V-2. Levels are given in the Kaysers (K). The ground state has a hyperfine structure as the ionization potential is approached (from 7 to $72p^2P^0$) with a separation of about 0.30 K.

Table V-2
CsI Energy Levels (Reproduced from Ref. V-11)

Config.	Desig.	J	Level	Interval
$5p^6(^1S)6s$	6s ^2S	0-1/2	0.00	
$5p^6(^1S)6p$	6p $^2P^o$	0-1/2	11178.24	554.11
		1-1/2	11732.35	
S)5d	5d ^2D	1-1/2	14499.490	97.59
		2-1/2	14597.08	
$5p^6(^1S)7s$	7s ^2S	0-1/2	18535.51	
$5p^6(^1S)7p$	7p $^2P^o$	0-1/2	21765.65	181.01
		1-1/2	21946.66	
$5p^6(^1S)6d$	6d ^2D	1-1/2	22588.89	42.94
		2-1/2	22631.83	
$5p^6(^1S)8s$	8s ^2S	0-1/2	24317.17	
$5p^6(^1S)4f$	4f $^2F^o$	3-1/2	24472.287	-0.176
		2-1/2	24472.463	
$5p^6(^1S)8p$	8p $^2P^o$	0-1/2	25709.14	82.64
		1-1/2	25791.78	
$5p^5(^1S)7d$	7d ^2D	1-1/2	26047.86	20.97
		2-1/2	26068.83	
$5p^6(^1S)9s$	9s ^2S	0-1/2	26910.68	
$5p^6(^1S)5f$	5f $^2F^o$	3-1/2	26971.415	-0.147
		2-1/2	26971.562	
$5p^6(^1S)5g$	5g ^2G	3-1/2, 4-1/2	27010	
$5p^6(^1S)9p$	9p $^2P^o$	0-1/2	27637.29	44.67
		1-1/2	27681.96	
$5p^6(^1S)8d$	8d ^2D	1-1/2	27811.25	11.69
		2-1/2	27822.94	
$5p^6(^1S)10s$	10s ^2S	0-1/2	28300.28	
$5p^6(^1S)6f$	6f $^2F^o$	3-1/2	28329.660	-0.102
		2-1/2	28329.762	
$5p^6(^1S)6g$	6g ^2G	3-1/2, 4-1/2	28347	
$5p^6(^1S)6h$	6h $^2H^o$	4-1/2, 5-1/2	28356	
$5p^6(^1S)10p$	10p $^2P^o$	0-1/2	28727.09	26.84
		1-1/2	28753.93	
$5p^6(^1S)9d$	9d ^2D	1-1/2	28828.90	7.16
		2-1/2	28836.06	
$5p^6(^1S)11s$	11s ^2S	0-1/2	29130	
$5p^5(^1S)7f$	7f $^2F^o$	3-1/2	29148.156	-0.069
		2-1/2	29148.225	
$5p^6(^1S)11p$	11p $^2P^o$	0-1/2	29403.68	17.42
		1-1/2	29421.10	
$5p^5(^1S)10d$	10d ^2D	1-1/2	29468.54	4.68
		2-1/2	29473.22	
$5p^6(^1S)12s$	12s ^2S	0-1/2	29686	
$5p^6(^1S)8f$	8f $^2F^o$	3-1/2	29678.983	-0.044
		2-1/2	29678.979	
$5p^6(^1S)12p$	12p $^2P^o$	0-1/2	29852.85	11.87
		1-1/2	29864.72	
$5p^6(^1S)12p$	11d ^2D	1-1/2	29896.64	3.25
		2-1/2	29899.89	
$5p^6(^1S)9f$	9f $^2F^o$	3-1/2	30042.515	-0.025
		2-1/2	30042.540	
$5p^6(^1S)13p$	13p $^2P^o$	0-1/2	30166.00	8.51
		1-1/2	30174.51	
$5p^6(^1S)12d$	12d ^2D	1-1/2	30197.02	2.33
		2-1/2	30199.35	
$5p^6(^1S)10f$	10f $^2F^o$	3-1/2	30302.383	-0.007
		2-1/2	30302.390	
$5p^6(^1S)14p$	14p $^2P^o$	0-1/2	30393.16	6.33
		1-1/2	30399.49	
$5p^6(^1S)13d$	13d ^2D	1-1/2	30416.06	1.70
		2-1/2	30417.76	
$5p^6(^1S)11f$	11f $^2F^o$	3-1/2, 2-1/2	30494.59	
$5p^6(^1S)15p$	15p $^2P^o$	0-1/2	30563.27	4.71
		1-1/2	30567.98	
$5p^6(^1S)14d$	14d ^2D	1-1/2	30580.46	1.33
		2-1/2	30581.79	
$5p^6(^1S)12f$	12f $^2F^o$	3-1/2, 2-1/2	30640.93	
$5p^6(^1S)16p$	16p $^2P^o$	0-1/2	30693.76	3.76
		1-1/2	30697.52	
$5p^6(^1S)15d$	15d ^2D	1-1/2	30707.11	0.85
		2-1/2	30707.96	
$5p^6(^1S)17p$	17p $^2P^o$	0-1/2	30796.20	2.95
		1-1/2	30799.15	
$5p^6(^1S)16d$	16d ^2D	1-1/2	30806.59	0.6
		2-1/2	30807.2	
$5p^6(^1S)18p$	18p $^2P^o$	0-1/2	30878.07	2.34
		1-1/2	30880.41	
$5p^6(^1S)17d$	17d ^2D	1-1/2, 2-1/2	30886.7	
$5p^6(^1S)19p$	19p $^2P^o$	0-1/2	30944.49	1.94
		1-1/2	30946.43	
$5p^6(^1S)18d$	18d ^2D	1-1/2, 2-1/2	30951.5	
$5p^6(^1S)20p$	20p $^2P^o$	0-1/2	30999.15	1.59
		1-1/2	31000.74	
$5p^6(^1S)19d$	19d ^2D	1-1/2, 2-1/2	31005.0	
$5p^6(^1S)21p$	21p $^2P^o$	0-1/2	31044.63	1.37
		1-1/2	31046.00	
$5p^6(^1S)20d$	20d ^2D	1-1/2, 2-1/2	31049.5	
$5p^6(^1S)22p$	22p $^2P^o$	0-1/2, 1-1/2	31084.08	
$5p^6(^1S)21d$	21d ^2D	1-1/2, 2-1/2	31086.7	
$5p^6(^1S)23p$	23p $^2P^o$	0-1/2, 1-1/2	31116.40	
$5p^6(^1S)24p$	24p $^2P^o$	0-1/2, 1-1/2	31144.13	
$5p^6(^1S)25p$	25p $^2P^o$	0-1/2, 1-1/2	31168.04	

Table V-2 (continued)

Config.	Desig.	J	Level	Interval	Config.	Desig.	J	Level	Interval
$5p^5(^1S)26p$	26p $^2P^\circ$	0-1/2, 1-1/2	31188.87		$5p^6(^1S)55p$	55p $^2P^\circ$	0-1/2, 1-1/2	31365.23	
$5p^6(^1S)27p$	27p $^2P^\circ$	0-1/2, 1-1/2	31207.07		$5p^6(^1S)56p$	56p $^2P^\circ$	0-1/2, 1-1/2	31366.78	
$5p^6(^1S)28p$	28p $^2P^\circ$	0-1/2, 1-1/2	31223.09		$5p^6(^1S)57p$	57p $^2P^\circ$	0-1/2, 1-1/2	31368.31	
$5p^6(^1S)29p$	29p $^2P^\circ$	0-1/2, 1-1/2	31237.24		$5p^6(^1S)58p$	58p $^2P^\circ$	0-1/2, 1-1/2	31369.69	
$5p^6(^1S)30p$	30p $^2P^\circ$	0-1/2, 1-1/2	31249.81		$5p^6(^1S)59p$	59p $^2P^\circ$	0-1/2, 1-1/2	31370.96	
$5p^6(^1S)31p$	31p $^2P^\circ$	0-1/2, 1-1/2	31261.05		$5p^6(^1S)60p$	60p $^2P^\circ$	0-1/2, 1-1/2	31372.26	
$5p^6(^1S)32p$	32p $^2P^\circ$	0-1/2, 1-1/2	31271.13		$5p^6(^1S)61p$	61p $^2P^\circ$	0-1/2, 1-1/2	31373.43	
$5p^6(^1S)33p$	33p $^2P^\circ$	0-1/2, 1-1/2	31280.17		$5p^6(^1S)62p$	62p $^2P^\circ$	0-1/2, 1-1/2	31374.56	
$5p^6(^1S)34p$	34p $^2P^\circ$	0-1/2, 1-1/2	31288.36		$5p^6(^1S)63p$	63p $^2P^\circ$	0-1/2, 1-1/2	31375.62	
$5p^6(^1S)35p$	35p $^2P^\circ$	0-1/2, 1-1/2	31295.76		$5p^6(^1S)64p$	64p $^2P^\circ$	0-1/2, 1-1/2	31376.62	
$5p^6(^1S)36p$	36p $^2P^\circ$	0-1/2, 1-1/2	31302.51		$5p^6(^1S)65p$	65p $^2P^\circ$	0-1/2, 1-1/2	31377.59	
$5p^6(^1S)37p$	37p $^2P^\circ$	0-1/2, 1-1/2	31308.61		$5p^6(^1S)66p$	66p $^2P^\circ$	0-1/2, 1-1/2	31378.56	
$5p^6(^1S)38p$	38p $^2P^\circ$	0-1/2, 1-1/2	31314.21		$5p^6(^1S)67p$	67p $^2P^\circ$	0-1/2, 1-1/2	31379.46	
$5p^6(^1S)39p$	39p $^2P^\circ$	0-1/2, 1-1/2	31319.39		$5p^6(^1S)68p$	68p $^2P^\circ$	0-1/2, 1-1/2	31380.29	
$5p^6(^1S)40p$	40p $^2P^\circ$	0-1/2, 1-1/2	31324.11		$5p^6(^1S)69p$	69p $^2P^\circ$	0-1/2, 1-1/2	31381.08	
$5p^6(^1S)41p$	41p $^2P^\circ$	0-1/2, 1-1/2	31328.47		$5p^6(^1S)70p$	70p $^2P^\circ$	0-1/2, 1-1/2	31381.87	
$5p^6(^1S)42p$	42p $^2P^\circ$	0-1/2, 1-1/2	31332.47		$5p^6(^1S)71p$	71p $^2P^\circ$	0-1/2, 1-1/2	31382.67	
$5p^6(^1S)43p$	43p $^2P^\circ$	0-1/2, 1-1/2	31336.19		$5p^6(^1S)72p$	72p $^2P^\circ$	0-1/2, 1-1/2	31383.28	
$5p^6(^1S)44p$	44p $^2P^\circ$	0-1/2, 1-1/2	31339.67		$5p^6(^1S)73p$	73p $^2P^\circ$	0-1/2, 1-1/2	31383.65	
$5p^6(^1S)45p$	45p $^2P^\circ$	0-1/2, 1-1/2	31342.84		----------				
$5p^6(^1S)46p$	46p $^2P^\circ$	0-1/2, 1-1/2	31345.80				----------	31406.71	
$5p^6(^1S)47p$	47p $^2P^\circ$	0-1/2, 1-1/2	31348.58						
$5p^6(^1S)48p$	48p $^2P^\circ$	0-1/2, 1-1/2	31351.18						
$5p^6(^1S)49p$	49p $^2P^\circ$	0-1/2, 1-1/2	31353.57						
$5p^6(^1S)50p$	50p $^2P^\circ$	0-1/2, 1-1/2	31355.85						
$5p^6(^1S)51p$	51p $^2P^\circ$	0-1/2, 1-1/2	31357.96						
$5p^6(^1S)52p$	52p $^2P^\circ$	0-1/2, 1-1/2	31359.95						
$5p^6(^1S)53p$	53p $^2P^\circ$	0-1/2, 1-1/2	31361.80						
$5p^6(^1S)54p$	54p $^2P^\circ$	0-1/2, 1-1/2	31363.60						

Moore gives the first level of Cs II as 107392 K (ground level is 0 K). This corresponds to a very high energy of 13.3 ev, roughly eight times the energy of the first line in Cs I. The wavelength corresponding to this energy is 930 Å, completely outside the range of response of the tracker.

Multiply ionized cesium probably does not occur, or occurs in a very small amount, in the thruster exhaust. According to Moore, little is know about Cs III. The ionization potential has been determined by extrapolation of the behavior. Most of the levels have not been identified. There is one odd set line at 13884 K (7200 Å) and the next line occurs at 127, 786 K (782 Å). We assume Cs III may be neglected in this analysis.

6. ABSORPTION

The spectral information we reproduced in the previous section enables us to calculate emission and absorption behavior (with certain restrictions). Before undertaking this calculation, we believe it wise to discuss some of the background theory.

If one applies classical theory, one finds that the frequencies emitted by an atom are identical to the atom's natural frequencies. One would assume that if photons of these frequencies are intercepted by the atom, the atom would be excited, and those photons could be absorbed. Stated differently, the absorption spectrum and emission spectrum would be the same. In some cases, this is observed experimentally. In other cases, it is not. Some atoms are completely transparent to photons which it emits in copious quantities when excited.

The explanation is straightforward. If we were exciting an atom by electron bombardment, the only requirement would be that the electron energy equal or exceed the energy required to displace an orbital electron to a different energy level. Excitation by absorption is different. It takes place only when the incoming photon energy is almost precisely the same as that required to move the electron from one level to another. Immediately, we conclude that the atom (or more properly, the gas composed of many atoms) will be completely transparent to photons whose energies do not coincide with the orbital electron transition differences.

Next, we must consider the original state of the atom. An excited atom will emit photons by movements of orbital electrons from one level to a lower level. Each jump will correspond to a particular wavelength. It is quite possible to excite an atom from the ground state to a higher level state, and then have several photons emitted as the atom decays back to the ground stage by an orbital electron jumping from level to level. In the initial process of excitation, we might absorb one photon. In the decay process, where several photons might be emitted, we would see a different response or spectrum. To absorb a photon of an energy corresponding to a particular spectral line, we first require that the atom be at the level corresponding to the lower level of the quantum jump. In the case of exhaust from the cesium thruster, we assume the neutral atoms are in the ground state. This assumption is justified, as we discuss elsewhere in this report, by the extremely short lifetimes of the excited states.* This means that absorption will only occur for transitions involving the ground state. Such transitions are indicated in Table V-2 by a J of 0 1/2.

The spectral line wavelengths are given to a great many significant figures. This implies that we absorb only photons which have an exceedingly narrow (and perhaps mathematically non-existent) range. Examination of Figures V-3 and V-5 shows continuum behavior. Absorption of mathematical lines from these spectra implies absorption of zero energy. In reality, this does not occur because of the phenomenon known as line broadening.

A number of things contribute to line broadening. Most line broadening is due to interaction of the excited atom with its surroundings during or following the decay process. Inherent in the emission process is the effect of the finite time the excited atom exists. The probability an atom lives in the excited state decreases exponentially

---

*Our calculations and recommended work may change this initial reaction.

with time. To measure the system energy with high precision, one must utilize a means of measurement which does not limit the time interval during which the measurement is obtained. If we measure characteristics for a short time, an indeterminancy is introduced. The shorter the time, the greater the uncertainty. An analytical analysis of the effect shows that the profile of a spectral line due to finite lifetime of the excited atom is a curve with the width inversely proportional to the decay time. This may be expressed by (Ref. V-9):

$$d\,I = I\,(E)\,d\,E = \frac{I_0\,\Gamma\,h^{-1}\,d\,E}{\Gamma^2/4 + (E - E_0)^2/h^2} \qquad \text{(V-1)}$$

where:

I = intensity of light with quantum energy between E and E + dE

Γ = reciprocal of mean life of the excited state

E_0 = average photon energy

I_0 = total rate of emission of energy in the transition

h = Planck's constant

$= 6.5817 \times 10^{-16}$ ev sec

$= 1.05443 \times 10^{-27}$ erg sec

Richtmyer (Ref. V-12) gives a simpler approximation for transitions involving the ground state:

$$\Delta = \frac{\lambda^2}{2\,\pi\,c\,\tau} \qquad \text{(V-2)}$$

where:

c = speed of light

τ = mean life of level

or, if two excited levels are involved:

$$\Delta = \frac{\lambda^2}{2\,\pi\,c}\left(\frac{1}{\tau_1} + \frac{1}{\tau_2}\right) \qquad \text{(V-3)}$$

This type effect is, as we mentioned, inherent in the process and will occur regardless of the surroundings.

The observed spectral line frequency may be changed from that emitted relative to the atom due to the motion of the radiating atom. This is called the Doppler effect. The

line apparent frequency increases if motion is toward the observer and decreases if motion is away from the observer. The actual frequency emitted corresponds to the observed frequency only when there is no velocity component in the direction of the observer. Normally, atoms in a gas will be moving with a Maxwellian type of velocity distribution. Consequently, the observed spectral line emitted by such a gas will be comprised of a range of frequencies. Since the velocity distribution broadens with increasing temperature, the observed range of frequencies also will broaden with temperature. This may be described by (Ref. V-12):

$$\Delta = 0.72 \times 10^{-6} \lambda \sqrt{\frac{T}{M}} \qquad \text{(V-4)}$$

where:

Δ = width of line, wavelength units

λ = wavelength

T = absolute temperature, °K

M = atomic weight.

Effects on the spectrum due to nonuniform external forces have been neglected. This is probably a good assumption for cases such as electrical and magnetic fields (The Stark and Zeeman effects, respectively*). Such fields would have to be much stronger than exist here to cause a perturbation in the reported results.

In our case, the atoms of cesium are moving outward in an increasingly rarefied manner. The probability of collision is extremely low, and the Doppler effect, as such, probably will not be seen or will be negligible.

Pressure also has an effect. Collisions are more frequent at higher pressures and this, via an intereffect with the light wave causes broadening as pressure increases. In our case, the situation is so rarefied that the pressure effect does not exist.

Several treatments of broadening have been presented in the literature. Gregory (Ref. V-13) presented a relatively easily understood treatment. He started by defining the intensity of absorption A_ν as the energy absorbed per unit cross section in unit time by a slab of thickness x:

$$A_\nu = i_0 (1 - e^{-\alpha_\nu x}) \qquad \text{(V-5)}$$

where:

α_ν = absorption coefficient

i = intensity

*These effects may cause splitting of certain spectral lines into several components. The cause is a modification of the quantum states of the atom. An excellent discussion of this field is given in Richtmyer (Ref. V-12).

and

$$\alpha_\nu = - \frac{d}{d x} \ell n \, (i_\nu) \tag{V-6}$$

when

$$\alpha_\nu \, x << 1, \; A_\nu \approx i_0 \, \alpha_\nu \, x$$

The intensity distribution of a broadened absorption line is defined to be proportional to the absorption coefficient:

$$I \, (\nu) \, \alpha \, \alpha_\nu \tag{V-7}$$

For $\alpha_\nu \, x << 1$, it is convenient to normalize $I(\nu)$:

$$\int_0^\infty I \, (\nu) \, d \, \nu = 1 \tag{V-8}$$

When I_ν is symmetric about $\nu = \nu_0$ at which frequency $I(\nu)$ is a maximum, then a convenient characteristic of the absorption line, $\Delta \nu_{1/2}$, the "half breadth, is defined:

$$I \left(\nu_0 \pm \frac{1}{2} \Delta \nu_{1/2} \right) = \frac{1}{2} I \, (\nu_0) \tag{V-9}$$

When $I(\nu)$ is not symmetric, the house of cards collapses.

The Einstein coefficient of absorption, B_{ij}, is connected to α_ν by:

$$B_{ij} = \frac{c}{h \, \nu_{ij} \, N} \int_{\substack{\text{over} \\ \text{line}}} \alpha_\nu \, d \, \Delta \nu \tag{V-10}$$

where:

c = velocity of light

h = Planck's constant

ν_{ij} = frequency

N = number of atoms per unit volume

The f-value is defined by:

$$f_{ji} = B_{ij} \, m \, h \, \nu_{ij} / \pi \, e^2 \tag{V-11}$$

where:

m = electron mass

e = electron charge, esu

These last two equations let us find the constant of proportionality.

Narrow lines are obtained for pressures below 10^{-2} mm. Fortunately for us, the symmetry is better at low pressures also. Gregory assumed the following distribution:

$$\alpha x = -\ln\left(\frac{i}{i_0}\right) = \frac{K x/2\pi}{(\Delta\nu)^2 + (\nu/2)^2} \qquad \text{(V-12)}$$

where:

$$K = \pi e^2 N f/m c$$

$$x = \text{tube length, cm} \qquad \text{(V-13)}$$

Further:

$$\int_{-\infty}^{+\infty} \left(1 - \frac{i}{i_0}\right) d\Delta\lambda = \text{constant} = A \qquad \text{(V-14)}$$

Substitution and integration gives:

$$C = 3.46 \times 10^{18} A^2 \qquad \text{(V-15)}$$

where:

$$C = \lambda_0^4 e^2 f x \gamma/2 m c^3 \ln(10) \qquad \text{(V-16)}$$

Knowledge of f and A lets us find γ. The $^2P_{3/2}$ and $^2P_{1/2}$ lines for cesium have f values of 0.66 and 0.32. Hence:

$$10^{40} C_1 = 0.707 N x \gamma_1 \qquad \text{(V-17)}$$

$$10^{40} C_2 = 0.416 N x \gamma_2 \qquad \text{(V-18)}$$

where subscript 1 refers to $^2P_{3/2}$ and 2 to $^2P_{1/2}$. Gregory concluded that $10^7\gamma_1/N = 1.45$, $10^7\gamma_2/N = 0.84$, and $\gamma_1/\gamma_2 = 1.8$ based upon his and other data.

Pollock has studied the effect further. He investigated the half-width at the half-height of the absorption curve as a function of atom density. His data covered the range from roughly 10^{15} atoms/cm^3 to beyond 10^{17} atoms/cm^3. The half-width plotted as a straight line on log-log paper against the density. The line slope was equal to one. He stated that the absorption data were similar to those of Gregory's with respect to the linear dependence of absorption width on atomic density. However, he found absolute values an order of magnitude greater than reported by Gregory. (Gregory's work was

reported in 1942; Pollock's in 1965.) Pollock states that his work has been corroborated by two other independent investigators. (He references two private communications.) He believes the error in Gregory's device was due to determination of the cesium pressure. Pollock's absorption coefficient widths are reproduced in Table V-3. The deviation from straight line behavior is greatest in the lower ranges, and the last two experimental widths lie above the line. Pollock determined the half-widths be plotting:

$$\ell n \left(\frac{I_0}{I}\right) = \alpha \ell_0 \qquad \text{(V-19)}$$

versus wavelength. All curves appear symmetrical (as Gregory assumed for his treatment) and peak at about $\ell n\ (I_0/I) = 1.66$, $\lambda = 8521$ Å. He used a 0.0762 cm path length (ℓ_0). He concludes that, in the pressure range from 0.2 to 10 torr:

$$\gamma k = 10^{-22}\ \text{cm}^3 \qquad \text{(V-20)}$$

where:

γ = absorption half-width

k = photon-atom absorption cross section

Several other terms are in the literature which are interrelated to the terms we have presented. Aller (Ref. V-15), in his summary treatment, introduces the Einstein coefficient of spontaneous emission, $A_{nn'}$, in the equation:

Table V-3
Resonance Absorption Coefficient Widths
For $6\ S_0 \longrightarrow 6^2P_{3/2}$ (Ref. V-14)

atoms/cm^3	Full-width at half-height, Å
1.39×10^{15}	4
2.17×10^{15}	3.5
4.06×10^{15}	4.5
1.39×10^{16}	14
2.02×10^{16}	15
3.37×10^{16}	29
4.74×10^{16}	48
5.72×10^{16}	67
6.29×10^{16}	74.5
6.66×10^{16}	73
1.055×10^{17}	111.5
1.33×10^{17}	130.25

$$N'_\nu = N_n A_{nn'} \tag{V-21}$$

where:

N'_ν = number of quanta of frequency $\nu(nn')$ emitted per unit volume per unit time

N_n = number of atoms per unit volume at level n

and the spontaneous decay is from n to n'. If radiation of frequency $\nu(nn')$ strikes atoms in level n, the atoms can be triggered into decaying with the emission of photons $\nu(nn')$. When this occurs, the total number of downward transitions becomes:

$$N'_\nu = N_n (A_{nn'} + B_{nn'} I_{\nu(nn')}) \tag{V-22}$$

where:

$B_{nn'}$ = coefficient of induced emission or negative absorption

$I_{\nu(nn')}$ = photon intensity, ergs/cm^2.

The interesting aspect of this behavior is the directionality. The induced photon emission is in the direction of the quantum responsible for the triggering. Hence, if we had a high population in excited states, the process we are going to follow might not be the correct one. Fortunately, we need consider only the ground state, and the multiplying process may be neglected.

Directly applicable to the absorption process is the effect predicted by B. If atoms of a lower level n' are exposed to photons of frequency ν (nn') at an intensity I_ν (nn'), the number of upward transitions per unit volume per unit time is:

$$N'_\nu = N_{n'} I_{\nu(nn')} B_{n'n} \tag{V-23}$$

Note that $B_{nn'} \neq B_{n'n}$, but they may be easily related. Aller substituted for $I_{\nu(nn')}$ the Planckian function for intensity*:

$$I_\nu = \frac{2h\nu^3}{c^2} \frac{1}{e^{h\nu/kT} - 1} \tag{V-24}$$

---

*This intensity is not the usual one with which the reader may be familiar. The units are:

$$I \equiv \frac{(\text{erg sec})(\text{sec})^{-3}}{(\text{cm/sec})^2} \equiv \text{erg/cm}^2$$

This is perhaps more properly termed an intensity distribution function. The true intensity over a frequency range $d\nu$ is $Id\nu$ erg/cm^2-sec. The units of B immediately follow as cm^2/erg-sec.

The following relationships may be shown to hold between them:

$$\tilde{\omega}_n B_{nn'} = \tilde{\omega}_{n'} B_{n'n} \tag{V-25}$$

$$\frac{\tilde{\omega}_n}{\tilde{\omega}_{n'}} A_{nn'} = B_{n'n} \frac{2 h \nu^3}{c^2} \tag{V-26}$$

Here $\tilde{\omega}_n$ is the statistical weight of level n. If its inner quantum number is J,

$$\tilde{\omega}_n = 2 J + 1 \tag{V-27}$$

The quantum-mechanical damping constant for pure radiation damping $\Gamma_{nn'}$, may be expressed in terms of the Einstein coefficients:

$$\Gamma_{nn'} = \Gamma_n + \Gamma_{n'} \tag{V-28}$$

where:

$$\Gamma_n = \sum_{n'} A_{nn'} (1 - e^{-h\nu/kT})^{-1} + \sum_{n''} A_{n''n} \frac{\tilde{\omega}_{n''}}{\tilde{\omega}_n} (e^{h\nu/kT} - 1)^{-1} \tag{V-29}$$

The first summation is taken over all levels n' lower than n: the second over all levels n'' above level n. If the intensity of the radiation is not large:

$$\Gamma_n = \sum_{n'} A_{nn'} \tag{V-30}$$

One may show that the Einstein A value is related to the f value by:

$$A_{nn'} = \frac{8 \pi^2 e^2 \nu^2}{mc^3} \frac{\tilde{\omega}_{n'}}{\tilde{\omega}_n} f_{nn'} \tag{V-31}$$

The energy levels involved may be characterized by their configurations (denoted as γ) and the quantum numbers L, S, and J. Thus the transition between two levels may be indicated as:

$$(\gamma\, LSJ) \longrightarrow (\gamma'\, L'\, S'\, J')$$

If the transition is a "permitted" one, i.e., of the electric-dipole type, the parity of the configuration must change in accordance with the Laporte rule, L can go to L or L ± 1, and J to J or J ± 1 except that J = 0 to J = 0 is excluded. If the atom is in good LS coupling, S cannot change.

In addition to f values and Einstein coefficients, it is useful to introduce the "line strength," a quantity which is symmetrical in the upper and lower levels:

$$f(\alpha' J'; \alpha J) = \frac{8\pi^2 m c}{3 h e^2} \frac{1}{\tilde{\omega}' \lambda} S(\alpha' J'; \alpha J) \qquad \text{(V-32)}$$

where the primes denote the lower level. The expressions for the strengths do not explicitly involve the wavelengths or frequencies of the emitted radiation, whereas the Einstein coefficients and f's do. This means that if we are concerned with multiplets or configuration arrays in which the lines fall at different wavelengths, we may obtain the relative strengths quickly from appropriate tables or formulas (at least for atoms in good LS coupling) whereas the relative f or A values require that the wavelength of each line be included.

The line strengths may be expressed in terms of the dipole moments for the transition involved between the individual Zeeman states:

$$S(\alpha' J'; \alpha J) = \sum_{M, M'} |\langle \alpha' J' M' | P | \alpha J M \rangle|^2 \qquad \text{(V-33)}$$

where M' and M denote the magnetic quantum numbers for the lower and upper states, respectively.

Like the f or A value, the strength of a line is an atomic constant. The intensity, however, depends on the physical excitation conditions. The relative, as well as the absolute, intensities of the lines in a given spectrum will vary in a more or less complicated fashion with change of excitation conditions. A knowledge of the relative intensities of the lines in a spectrum is of little help in obtaining empirical line strengths unless something is known about the mode of excitation.

In addition to the absorption oscillator strengths, an emission oscillator strength is defined as:

$$f_{nn'2} = \frac{\tilde{\omega}_{n'}}{\tilde{\omega}_n} f_{n'n} \qquad \text{(V-34)}$$

Although it is necessary to use the emission oscillator strengths in problems such as the application of sum rules, ordinarily it is better to employ conventional Ladenbrug f values.

If the wavelength is expressed in angstrom units (10^{-8} cm) and S in atomic units ($a_0^2 e^2$, where a_0 is the radius of the first Bohr orbit), Equation (V-32) becomes:

$$f(\alpha' J'; \alpha J) = \frac{304}{\tilde{\omega}' \lambda} S(\alpha' J'; \alpha J) \qquad \text{(V-35)}$$

and the corresponding expression for the Einstein A is:

$$A(\alpha J;\ \alpha' J') = \frac{2.02 \times 10^{18}}{\tilde{\omega} \lambda^3} \quad S(\alpha J;\ \alpha' J') \tag{V-36}$$

The strength S may be expressed as the product of three factors:

$$S(\alpha J;\ \alpha' J') = \mathcal{S}(\mathfrak{M})\ \mathcal{S}(\mathfrak{L})\ \sigma(\alpha';\ \alpha)^2 \tag{V-37}$$

where:

$\mathcal{S}(\mathfrak{M})$ = absolute strength of the whole multiplet

$\mathcal{S}(\mathfrak{L})$ = strength of the line divided by the sum of the strengths of the lines of that particular multiplet

$$\sigma(\alpha';\ \alpha) = \frac{1}{\sqrt{4\ell^2 - 1}} \int_0^\infty R(\alpha')\ R(\alpha)\ r^3\ d\ r \tag{V-38}$$

Here $R(\alpha')$ and $R(\alpha)$ are, respectively, the radial quantum wave functions for the lower and upper states of the transition. These wave functions are normalized and orthogonal in the usual ways:

$$\int_0^\infty R^2(\alpha)\ r^2\ d\ r = \int R^2(\alpha')\ r^2\ d\ r = 1 \tag{V-39}$$

$$\int_0^\infty R(\alpha)\ R(\alpha')\ r^2\ d\ r = 0 \tag{V-40}$$

Here ℓ is the greater of the two azimuthal quantum numbers involved in the wave functions $R(\alpha)$ and $R(\alpha')$.

The transition α LSJ - α'L'S'J' gives rise to a single spectral line.

The transitions from all the levels of one term (common αLS) to all the levels of another term (common α'L'S') comprise a multiplet.

All the transitions from the totality of terms based on a single parent (polyad) to another polyad compose a supermultiplet.

Finally, all the transitions from one configuration to another configuration make up a transition array.

Corliss (Ref. V-17) has compiled A and f values for Cs I, which we have reproduced in Table V-4. Stone (Ref. V-18) provides a more complete listing based upon calculations and a comparison with the available experimental data. His data for transitions involving the 6 $S_{1/2}$ ground state are reproduced in Table V-5. (The listed wave lengths are taken from Moore (Ref. V-11).) The data for transitions between excited states are given in Table V-6 (A is the initial state and B the final state of the transition). We will use

Table V-4
Cs I Behavior (Reproduced from Ref. V-17)

Wavelength A	Spectrum	Energy Levels K	gA 10^8/sec	gf	Log gf
4555.36	Cs I	0 - 21947	1.4	0.42	-0.37
4593.18	Cs I	0 - 21766	0.65	0.21	-0.69
5663.80	Cs I	11178 - 28829	0.88	0.43	-0.37
5844.70	Cs I	11732 - 28836	0.76	0.39	-0.41
6010.33	Cs I	11178 - 27811	1.9	1.0	0.01
6034.09	Cs I	11732 - 28300	0.38	0.21	-0.68
6212.87	Cs I	11732 - 27823	2.9	1.7	0.23
6217.27	Cs I	11732 - 27811	0.19	0.11	-0.95
6354.98	Cs I	11178 - 26911	0.48	0.29	-0.53
6586.51	Cs I	11732 - 26911	0.60	0.39	-0.41
6723.28	Cs I	11178 - 26048	3.2	2.2	0.34
6973.29	Cs I	11732 - 26069	3.3	2.4	0.39
6983.49	Cs I	11732 - 26048	0.58	0.42	-0.37
7609.01	Cs I	11178 - 24317	0.44	0.39	-0.41
8015.71	Cs I	14500 - 26971	1.5	1.4	0.16
8079.02	Cs I	14597 - 26971	2.0	2.0	0.29
8521.10	Cs I	0 - 11732	1.3	1.4	0.15
8761.38	Cs I	11178 - 22589	4.3	5.0	0.70
8943.50	Cs I	0 - 11178	0.48	0.57	-0.24

Table V-5
Principal Series Cs Oscillator Strengths

Initial State	f	λ, μm
6 $P_{1/2}$	0.394	0.8943
6 $P_{3/2}$	0.814	0.8521
7 $P_{1/2}$	0.284×10^{-2}	0.4593
7 $P_{3/2}$	0.174×10^{-1}	0.4555
8 $P_{1/2}$	0.317×10^{-3}	0.3888
8 $P_{3/2}$	0.349×10^{-2}	0.3876
9 $P_{1/2}$	0.725×10^{-4}	0.3618
9 $P_{3/2}$	0.125×10^{-2}	0.3612
10 $P_{1/2}$	0.289×10^{-4}	0.3481
10 $P_{3/2}$	0.620×10^{-3}	0.3478
11 $P_{1/2}$	0.124×10^{-4}	0.3401
11 $P_{3/2}$	0.356×10^{-3}	0.3399
12 $P_{1/2}$	0.620×10^{-5}	0.3350
12 $P_{3/2}$	0.208×10^{-3}	0.3348

Table V-6
Cesium Oscillator Strengths (Reproduced from Ref. V-18)*

Transition (A,B)	f(A,B)	Transition (A,B)	f(A,B)	Transition (A,B)	f(A,B)
$7S_{1/2}$, $6P_{3/2}$	0.208	$11S_{1/2}$, $7P_{3/2}$	0.00455	$11P_{3/2}$, $5D_{3/2}$	0.01842
$7S_{1/2}$, $6P_{1/2}$	0.171	$11S_{1/2}$, $7P_{1/2}$	0.09501	$5D_{3/2}$, $6P_{1/2}$	0.2509
$8S_{1/2}$, $6P_{3/2}$	0.0204	$12S_{1/2}$, $7P_{3/2}$	0.00259	$6D_{3/2}$, $6P_{3/2}$	0.3322
$8S_{1/2}$, $6P_{1/2}$	0.0202	$12S_{1/2}$, $7P_{1/2}$	0.00287	$6D_{3/2}$, $6P_{3/2}$	0.0397
$9S_{1/2}$, $6P_{3/2}$	0.00687	$13S_{1/2}$, $7P_{3/2}$	0.001643	$6D_{3/2}$, $6P_{1/2}$	0.2980
$9S_{1/2}$, $6P_{1/2}$	0.00702	$13S_{1/2}$, $7P_{1/2}$	0.001829	$7D_{3/2}$, $6P_{3/2}$	0.0951
$10S_{1/2}$, $6P_{3/2}$	0.00299	$14S_{1/2}$, $7P_{3/2}$	0.001128	$7D_{3/2}$, $6P_{3/2}$	0.0110
$10S_{1/2}$, $6P_{1/2}$	0.00326	$14S_{1/2}$, $7P_{1/2}$	0.001257	$7D_{3/2}$, $6P_{1/2}$	0.0927
$11S_{1/2}$, $6P_{3/2}$	0.00186			$8D_{3/2}$, $6P_{3/2}$	0.0418
$11S_{1/2}$, $6P_{1/2}$	0.00193	$7P_{3/2}$, $7S_{1/2}$	1.115	$8D_{3/2}$, $6P_{3/2}$	0.0048
$12S_{1/2}$, $6P_{3/2}$	0.00117	$7P_{1/2}$, $7S_{1/2}$	0.556	$8D_{3/2}$, $6P_{1/2}$	0.0419
$12S_{1/2}$, $6P_{1/2}$	0.00122	$8P_{3/2}$, $7S_{1/2}$	0.02558	$9D_{3/2}$, $6P_{3/2}$	0.0223
$13S_{1/2}$, $6P_{3/2}$	0.00078	$8P_{1/2}$, $7S_{1/2}$	0.00516	$9D_{3/2}$, $6P_{3/2}$	0.0025
$13S_{1/2}$, $6P_{1/2}$	0.00082	$9P_{3/2}$, $7S_{1/2}$	0.00502	$9D_{3/2}$, $6P_{1/2}$	0.0228
$14S_{1/2}$, $6P_{3/2}$	0.00056	$9P_{1/2}$, $7S_{1/2}$	0.00062	$10D_{3/2}$, $6P_{3/2}$	0.0135
$14S_{1/2}$, $6P_{1/2}$	0.00059	$10P_{3/2}$, $7S_{1/2}$	0.00187	$10D_{3/2}$, $6P_{3/2}$	0.0015
		$10P_{1/2}$, $7S_{1/2}$	0.00017	$10D_{3/2}$, $6P_{1/2}$	0.0139
$8S_{1/2}$, $7P_{3/2}$	0.333	$11P_{3/2}$, $7S_{1/2}$	0.000911	$11D_{3/2}$, $6P_{3/2}$	0.0088
$8S_{1/2}$, $7P_{1/2}$	0.297	$11P_{1/2}$, $7S_{1/2}$	0.000062	$11D_{3/2}$, $6P_{3/2}$	0.0010
$9S_{1/2}$, $7P_{3/2}$	0.0256	$12P_{3/2}$, $7S_{1/2}$	0.000486	$11D_{3/2}$, $6P_{1/2}$	0.0092
$9S_{1/2}$, $7P_{1/2}$	0.0305	$12P_{1/2}$, $7S_{1/2}$	0.000027		
$10S_{1/2}$, $7P_{3/2}$	0.00842			$6D_{3/2}$, $7P_{3/2}$	0.309
$10S_{3/2}$, $7P_{1/2}$	0.00964	$5D_{3/2}$, $6P_{3/2}$	0.2042	$6D_{3/2}$, $7P_{3/2}$	0.032
$7D_{3/2}$, $7P_{3/2}$	0.282	$5D_{3/2}$, $6P_{3/2}$	0.0211	$6D_{3/2}$, $7P_{1/2}$	0.327
$7D_{3/2}$, $7P_{3/2}$	0.034	$7P_{1/2}$, $5D_{3/2}$	0.6516	4F, $5D_{3/2}$	0.3244
$7D_{3/2}$, $7P_{1/2}$	0.237	$7P_{3/2}$, $5D_{3/2}$	0.208	4F, $5D_{3/2}$	0.3022
$8D_{3/2}$, $7P_{3/2}$	0.089	$7P_{3/2}$, $5D_{3/2}$	1.536	5F, $5D_{3/2}$	0.1272
$8D_{3/2}$, $7P_{3/2}$	0.0105	$8P_{1/2}$, $5D_{3/2}$	0.0915	5F, $5D_{3/2}$	0.1215
$8D_{3/2}$, $7P_{1/2}$	0.0822	$8P_{3/2}$, $5D_{1/2}$	0.0299	6F, $5D_{3/2}$	0.0650
$9D_{3/2}$, $7P_{3/2}$	0.0110	$8P_{3/2}$, $5D_{3/2}$	0.2188	6F, $5D_{3/2}$	0.0627
$9D_{3/2}$, $7P_{3/2}$	0.0047	$9P_{1/2}$, $5D_{3/2}$	0.0609	7F, $5D_{3/2}$	0.0683
$9D_{3/2}$, $7P_{1/2}$	0.0391	$9P_{3/2}$, $5D_{3/2}$	0.0809	7F, $5D_{1/2}$	0.0378
$10D_{1/2}$, $7P_{3/2}$	0.0228	$9P_{3/2}$, $5D_{3/2}$	0.0733	8F, $5D_{3/2}$	0.0241
$10D_{3/2}$, $7P_{3/2}$	0.0026	$10P_{1/2}$, $5D_{3/2}$	0.0146	8F, $5D_{3/2}$	0.0235
$10D_{3/2}$, $7P_{1/2}$	0.0221	$10P_{3/2}$, $5D_{3/2}$	0.004	9F, $5D_{3/2}$	0.0161
$11D_{3/2}$, $7P_{3/2}$	0.0112	$10P_{3/2}$, $5D_{3/2}$	0.0335	9F, $5D_{3/2}$	0.0160
$11D_{3/2}$, $7P_{3/2}$	0.0016	$11P_{1/2}$, $5D_{3/2}$	0.00708	10F, $5D_{3/2}$	0.0445
$11D_{3/2}$, $7P_{1/2}$	0.0139	$11P_{3/2}$, $5D_{3/2}$	0.00248	10F, $5D_{3/2}$	0.0114

*Errata indicate errors in this table. The n $P_{1/2}$, 5 $D_{3/2}$ entries should be multiplied by 2.5×10^{-2}; and the n $P_{3/2}$, 5 $D_{3/2}$ and n $P_{3/2}$, 5 $D_{5/2}$ entries should be multiplied by 10^{-2} (Ref. V-19).

Stone's data because it is more complete (Lancashire (Ref. V-20) also used his data with Moore's wavelengths).

To apply these data, we rewrite Equation (V-26):

$$B_{n'n} = \frac{\tilde{\omega}_n}{\tilde{\omega}_{n'}} \frac{c^2}{2 h \nu^3} A_{nn'} \qquad \text{(V-41)}$$

Next substitute Equation (V-31):

$$B_{n'n} = \frac{4\pi^2 e^2}{h m c \nu} f_{nn'} \qquad \text{(V-42)}$$

Substitution into Equation (V-23) gives:

$$N_{\nu'} = N'_n I_{\nu(nn')} \frac{4\pi^2 e^2}{h m c \nu} f_{nn'} \qquad \text{(V-43)}$$

which shows the photon absorption rate to be directly proportional to the number of atoms per unit volume.

Note that $\nu = c/\lambda$, so that Equation (V-43) can be rewritten:

$$N'_\nu = N'_n I_{\nu(nn')} \frac{4\pi^2 e^2 \lambda}{h m c^2} f_{nn'} \qquad \text{(V-44)}$$

This equation, coupled with the geometric considerations, makes it possible to compute plume absorption effects.

As we approach the ionization limit, the lines become closer together and, as the limit is passed, a continuous absorption phenomenon results. McDaniel (Ref. V-21) presents the curve shown in Figure V-6.

Ditchburn (Ref. V-22) shows the data presented in Figure V-7. He also states that the value for the absorption cross section at the series limit for cesium is given as $22 \pm 1 \times 10^{-20}$ cm^2 and as $23 \pm 2 \times 10^{-20}$ cm^2 by two different investigators.

The molecular absorption coefficient is estimated to be in the vicinity of 5×10^{-17} cm^2. Since we have few, if any, molecules, this higher value should cause no problems.

7. IONIZATION AND RECOMBINATION

The behavior for photoionization is treated in much the same manner as photon absorption without ionization. Following McDaniel (Ref. V-21), we recall:

$$I = I_0 e^{-\mu x} \qquad \text{(V-45)}$$

where:

I = final intensity

I_0 = initial intensity

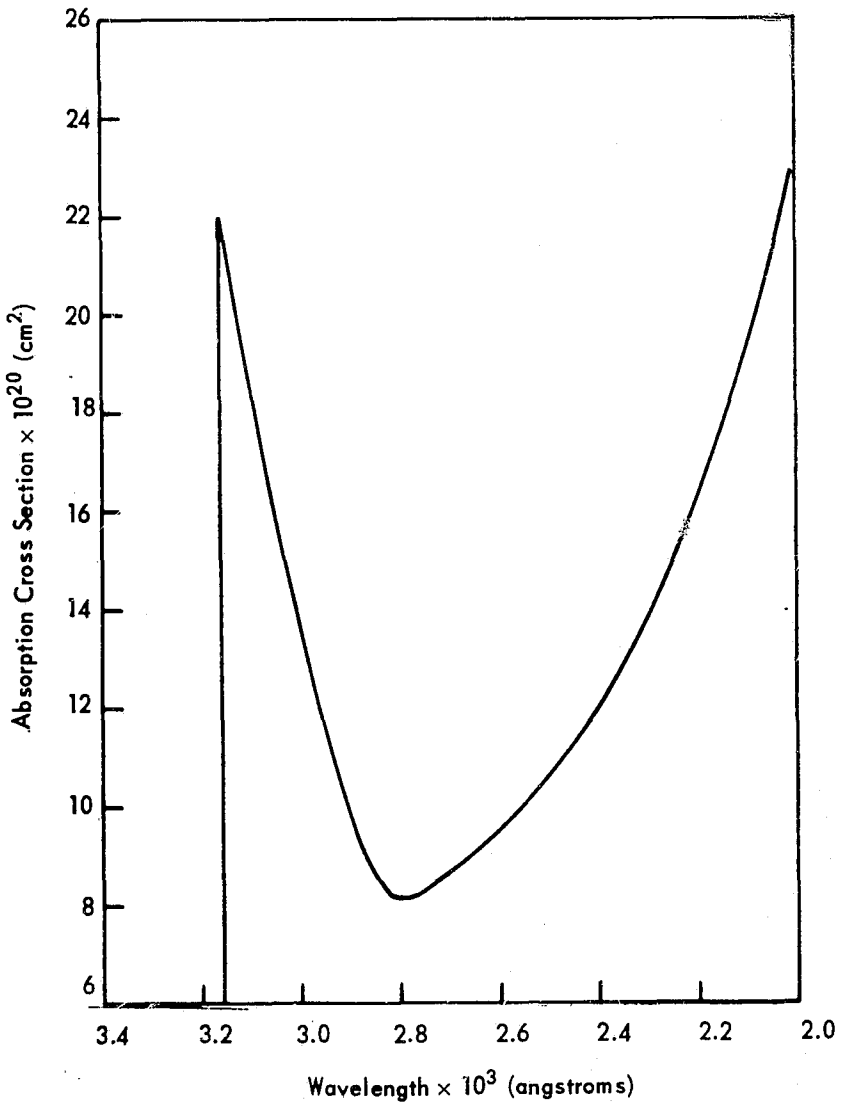

Figure V-6. Absorption Cross Section (Ref. V-21).

μ = absorption coefficient, cm^{-1}

x = gas thickness, cm

Also:

$$\mu = q_p N \tag{V-46}$$

where:

q_p = microscopic photoabsorption cross section

N = number density of the gas

For the absorption equation to hold, we require that the radiation be nearly monochromatic so that there is no change in effective absorption with position and μ must be independent of gas temperature and pressure. The second condition is satisfied if changes in p and T do not significantly change the gas composition. (For example, by molecular association or dissociation.)

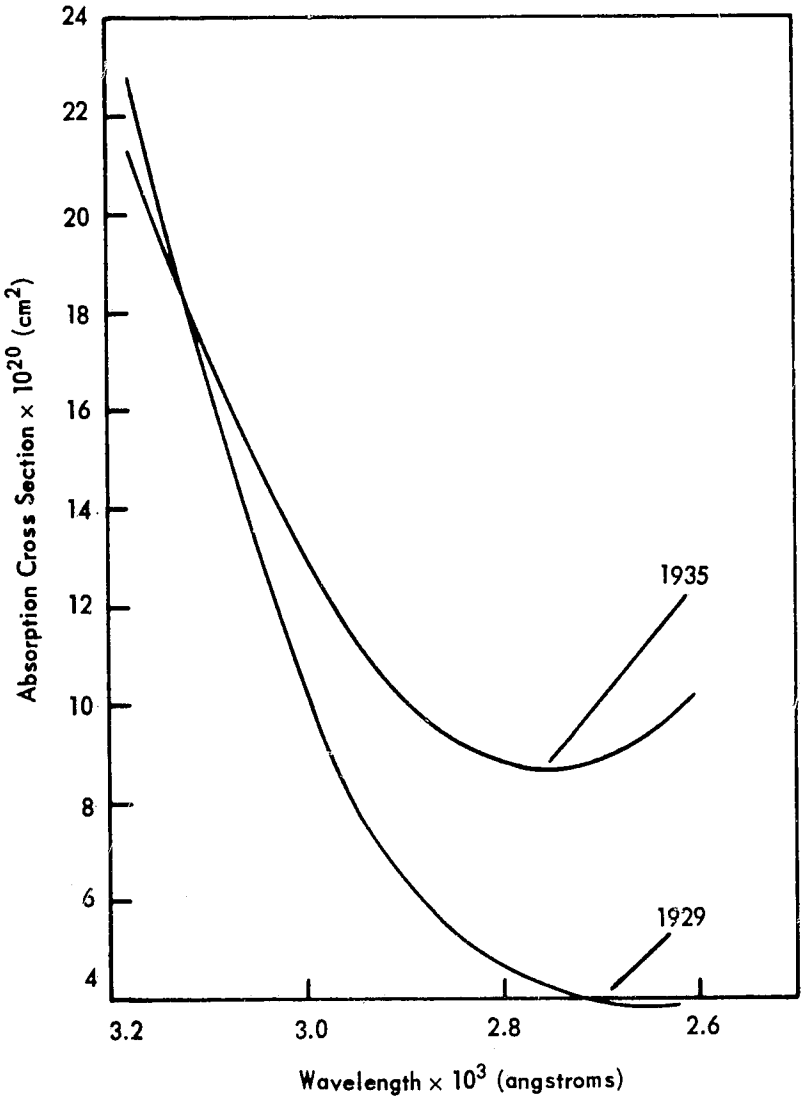

Figure V-7. Absorption Cross Section (Ref. V-22).

Photoionization cross sections may be related to the cross section for capture of an electron by:

$$\frac{q_c(v)}{q_p(\lambda)} = \frac{\Omega_i\, e}{2\,\Omega_f\, m\, c^2}\,\frac{V_p^2}{300\, V_e} \qquad \text{(V-47)}$$

where:

q_c = radiative capture cross section (for electron capture)

v = electron velocity

Ω_i = initial state statistical weight

Ω_f = final state statistical weight

e = electronic charge

m = electronic mass

V_p = potential (volts) corresponding to the energy of the incident photon

V_e = potential (volts) corresponding to the energy of the ejected electron.

From quantum mechanics:

$$h\nu = \frac{h\,c}{\lambda} = \frac{e\,(V_i + V_e)}{300} = \frac{e\,V_p}{300} \qquad \text{(V-48)}$$

where:

ν = incident radiation frequency

λ_i = incident radiation wavelength

V_i = ionization potential of the neutral structure

The photoabsorption cross sections for atomic systems are essentially equal to the cross sections for photoionization. (This is not true for molecular systems because a multiplicity of absorption mechanisms is available.) Interestingly, an appreciable amount of molecular absorption may occur in vapors that are predominantly monatomic, such as the alkalis. The molecular absorption cross sections are high enough that the cross sections may not be ignored.

The alkali vapors can be ionized by ultraviolet photons. The relationship describing this behavior is:

$$h\nu_i = h\frac{c}{\lambda_i} = e\,V_i \qquad \text{(V-49)}$$

where:

ν_i = threshold frequency

λ_i = wavelength for ejection of the least tightly bound electron

V_i = first ionization potential

h = Planck's constant

c = velocity of light in a vacuum

Further:

$$\lambda_i = \frac{12398}{V_i} \qquad \text{(V-50)}$$

where λ_i is given in angstroms and V_i is in volts. Ionization at wavelengths longer than the threshold value can occur in a two step process involving an atom (or molecule) that has already been excited. Wavelengths shorter than λ_i are required to eject electrons other than the one with the smallest binding energy in the atom.

For hydrogen-like structures, we may compute cross sections from the equation:

$$q_p\,(\nu,\,n) = \frac{g\,(32\,\pi^2\,e^6\,R\,Z^4)}{(3^{3/2}\,h^3\,\nu^3\,n^5)} \qquad \text{(V-51)}$$

where:

R = Rydberg constant

N = principal quantum number of the initial state

g = factor (see Ditchburn and Opik).

Marmo (Ref. V-23) and Ditchburn (Ref. V-24) provide additional information. According to Marmo, the probability of photoionization of a cesium atom in the upper atmosphere is 6.5×10^{-4} per atom per second.*

Recombination is described by:

$$R = \alpha n^+ n^- \qquad \text{(V-52)}$$

where:

R = number of recombination events per unit time and volume

n = number density of each of the charge carriers

α = recombination coefficient (cgs units of cm /sec)

The recombination coefficient can be related to the recombination cross section by:

$$\alpha = \int_0^\infty v_0 \, q_r \, (v_0) \, f \, (v_0) \, d \, v_0 \qquad \text{(V-53)}$$

where:

$f (v_0) d v_0$ = fraction of encounters between positive and negative particles in which the relative velocity lies between v_0 and $v_0 + dv_0$.

For most cases, α can be approximated by:

$$\bar{\alpha} = \bar{v}_0 \, q_r \, (\bar{v}_0) \qquad \text{(V-54)}$$

where $\bar{v}_0$ is the mean value of v_0.

Radiative recombination behaves according to:

$$X^+ + e \longrightarrow X^* + h \nu \qquad \text{(V-55)}$$

For thermal electrons (~300K) radiative recombination coefficients are in the range of 10^{-11} to 10^{-12} cm^3/sec for various positive ions.

---

*Cross section times intensity.

Bates (Ref. V-26) has studied electron-ion recombination for optically thin plasmas. He wrote the equation:

$$\gamma = \alpha - S \, X \, n\,(1)/n\,(c) \tag{V-56}$$

where:

γ = effective two body rate coefficient or collisional-radiative decay coefficient

α = collisional-radiative recombination coefficient

S = collisonal-radiative ionization coefficient

$X = n(c)/n(N^+)$

n (1) = number density of atoms or ions in the first level

n (c) = number density of free electrons

$n\,(N^+)$ = number density of singly charged ions

He neglects electronic transitions due to atom-atom, atom-ion and ion-ion collisions. He further supposed all radiation escapes without absorption. Further:

$$\frac{\gamma}{X} = \dot{n}\,(1)/n\,(c)^2 \tag{V-57}$$

where:

$\dot{n}\,(1)$ = rate of disappearance of free charges

$$n_S\,(1) = \alpha\, n\,(c)/X\,S \tag{V-58}$$

$$\dot{n}\,(1) = \gamma\, n\,(c)\; n\,(N^+) = -\dot{n}\,(N^+) \tag{V-59}$$

Some of his tables provide data for a modified hydrogen atom which serves as a crude model of an alkali atom with excitation potential 1.9 eV and ionization potential 3.4 eV. (This is close to cesium.) Three of his tables are reproduced in Tables V-7 and V-8.

Marmo (Ref. V-23) points out a serious discrepancy between theoretical and experimental determinations of electron-ion recombination rates. For example, values for cesium are reported as follows:

Electron Temperature, °K	Pressure mmHg	Recombination Coefficient, cm^3/in-sec
1300	$1\text{-}10 \times 10^{-2}$	3.6×10^{-10}
1200	$1\text{-}10 \times 10^{-2}$	3.4×10^{-10}
1400	0.32×0.68	3.5×10^{-7} 1.21×10^{-6}

Table V-7
Quantities α and S for the Collisional-Radiative Decay Coefficients
(Reproduced from Reference V-26)

n(c) (cm^{-3}) \ T(°K)	250	500	1000	2000	4000	8000
Collisional-Radiative Recombination Coefficient, α ($cm^3 S^{-1}$)						
limit n(c) → 0	3.8^{-12}	2.4^{-12}	1.5^{-12}	9.0^{-13}	5.4^{-13}	3.1^{-13}
10^8	7.8^{-11}	1.2^{-11}	3.2^{-12}	1.3^{-12}	6.4^{-13}	3.3^{-13}
10^9	3.3^{-10}	3.3^{-11}	6.0^{-12}	1.8^{-12}	7.5^{-13}	3.6^{-13}
10^{10}	2.8^{-9}	1.5^{-10}	1.6^{-11}	3.1^{-12}	9.8^{-13}	4.1^{-13}
10^{11}	2.7^{-8}	1.0^{-9}	6.1^{-11}	7.1^{-12}	1.6^{-12}	5.1^{-13}
10^{12}	2.6^{-7}	9.0^{-9}	3.6^{-10}	2.4^{-11}	3.2^{-12}	7.4^{-13}
10^{13}	2.6^{-6}	8.8^{-8}	3.0^{-9}	1.2^{-10}	9.3^{-12}	1.3^{-12}
10^{14}	2.6^{-5}	8.8^{-7}	2.9^{-8}	9.4^{-10}	4.0^{-11}	3.2^{-12}
10^{15}	–	8.8^{-6}	2.9^{-7}	8.5^{-9}	2.5^{-10}	1.6^{-11}
10^{16}	–	–	2.9^{-6}	8.4^{-8}	2.3^{-9}	1.4^{-10}
limit n(c) → ∞	2.6^{-19} n(c)	8.8^{-21} n(c)	2.9^{-22} n(c)	8.4^{-24} n(c)	2.3^{-25} n(c)	1.4^{-26} n(c)
Collisional-Radiative Ionization Coefficient S ($cm^3 S^{-1}$)						
limit n(c) → 0	–	–	1.1^{-25}	7.7^{-17}	2.7^{-12}	6.6^{-10}
10^8	–	–	2.6^{-25}	1.3^{-16}	3.6^{-12}	7.8^{-10}
10^9	–	–	5.2^{-25}	1.9^{-16}	4.4^{-12}	9.0^{-10}
10^{10}	–	–	1.6^{-24}	3.6^{-16}	6.6^{-12}	1.1^{-9}
10^{11}	–	–	8.4^{-24}	1.1^{-15}	1.3^{-11}	1.8^{-9}
10^{12}	–	–	8.8^{-23}	6.3^{-15}	4.6^{-11}	4.2^{-9}
10^{13}	–	–	1.5^{-21}	6.9^{-14}	2.8^{-10}	1.6^{-8}
10^{14}	–	–	1.4^{-20}	4.9^{-13}	1.1^{-9}	3.6^{-8}
10^{15}	–	–	3.4^{-20}	1.0^{-12}	1.7^{-9}	4.3^{-8}
10^{16}	–	–	3.8^{-20}	1.2^{-12}	1.8^{-9}	4.3^{-8}
limit n(c) → ∞	–	–	3.9^{-20}	1.2^{-12}	1.8^{-9}	4.3^{-8}
S + L	–	–	1.8^{-16}	1.1^{-11}	2.8^{-9}	5.0^{-8}

The indices give the power of 10 by which the entries in the α and S columns and the S + L row must be multiplied.

He concludes other processes besides radiative recombination are taking place.

The collision frequency between electrons and neutrals in the gas phase is given by (Ref. V-25):

$$\nu = \left(\frac{8\ k\ T_e}{\pi\ m}\right)^{1/2} \sum n_i\ Q_i \qquad \text{(V-60)}$$

Table V-8
Number Density of Normal Alkali Atoms in Steady State $n_S(1)$ and in Saha Equilibrium $n_E(1)$ cm^{-3} (with X = 1) (Reproduced from Reference V-26)

n(c) (cm^{-3}) \ T(°K)	1000	2000	4000	8000
	number densities $n_S(1)$			
limit n(c) → 0	1.4^{13} n(c)	1.2^{4} n(c)	2.0^{-1} n(c)	4.7^{-4} n(c)
10^8	1.2^{21}	1.0^{12}	1.8^{7}	4.3^{4}
10^9	1.1^{22}	9.9^{12}	1.7^{8}	4.0^{5}
10^{10}	9.7^{22}	8.6^{13}	1.5^{9}	3.6^{6}
10^{11}	7.2^{23}	6.6^{14}	1.2^{10}	2.9^{7}
10^{12}	4.1^{24}	3.9^{15}	6.9^{10}	1.8^{8}
10^{13}	2.0^{25}	1.8^{16}	3.3^{11}	8.5^{8}
10^{14}	2.0^{26}	1.9^{17}	3.5^{12}	8.9^{9}
10^{15}	8.5^{27}	8.1^{18}	1.5^{14}	3.8^{11}
10^{16}	7.5^{20}	7.1^{20}	1.3^{16}	3.3^{13}
$n_S(1)$ in limit n(c) → ∞ $n_E(1)$ for all n(c)	7.3^{-3} $n(c)^3$	7.0^{-12} $n(c)^2$	1.3^{-16} $n(c)^2$	3.2^{-19} $n(c)^2$

The indices give the power of 10 by which the entries in the columns for the number densities of normal atoms must be multiplied.

where:

ν = collision frequency, sec^{-1}

k = Boltzmann constant, 1.38×10^{-16} erg/°K

T_e = electron temperature, °K

m_e = electron mass

n_i = number of atoms of specie i per cm^2

Q_i = collision cross section of specie i, cm^3

Elastic electron-atom collisions are important only in high pressure plasma (Ref. V-27). Inelastic electron-atom collisions are important in both low and high pressure nonequilibrium plasmas.

Nygaard (Ref. V-28) presents cross section data for electron-impact ionization. First, we write the electron mean free path as:

$$\Lambda = (n\,\sigma)^{-1} \qquad \text{(V-61)}$$

where:

n = cesium density, atoms/cm^3

σ = cross section, cm^2

The slope of the 6s cross section curve is 2.7 Å^2/eV from $\sigma = 0$ to ~ 7 Å^2. It reaches a maximum of about 9.5 Å^2 at ~ 15 eV and the total cross section curve never exceeds this value (to the reported limit of the study at 100 eV).

Another equation which can be used to compute the rate of ion production in a gas column due to electron impacts is:

$$\nu_i = n\, n_a\, d\, K_I \exp\left(-\frac{V_I}{k\, T_e}\right) \qquad \text{(V-62)}$$

where:

n = electron (gas) density

n_a = atom density

d = gas column depth

K_I = factor which includes differential ionization cross section of the gas averaged over all excited states (and other quantities which are weakly dependent on n, T_e, and T_E if recombination is negligible

V_I = ionization potential of unexcited atom if all excited atoms and their resonance photons are rapidly lost from the plasma (when excited atoms and their resonance radiation are preferentially trapped in the plasma, V_I becomes the excitation energy for the limiting step leading to ionization.)

k = Boltzmann constant

T_e = electron (gas) temperature

T_E = emitter temperature.

The total effective emission current from the neutralizer (emitter) is:

$$J_s = J_S + J_i \qquad \text{(V-63)}$$

where:

J_s = total current

J_S = Schottky enhanced emission current

J_i = positive ion current from the ions

$$J_S = J_s' \exp\left(4.4E^{1/2}/T_E\right) \qquad \text{(V-64)}$$

where:

E = field strength, volts/cm

T_E = is in °K

J_s' = zero field electron emission current density.

The zero electrical field electron emission current density is:

$$J_s' = A\, T_E^2 \exp\left(-\Phi_E / k\, T_E\right) \qquad \text{(V-65)}$$

where:

A = Richardson constant

T_E = emitter temperature

Φ_E = emitter work function

k = Boltzmann constant

which can be applied to predict these characteristics.

Additional information in these general areas can be obtained from Hansen (Ref. V-29) and Dayton (Ref. V-30).

Rasor (Ref. V-31) has postulated a negative cesium ion, which he believes to be "a perfectly legitimate species of cesium." It has an electron affinity (energy required to remove the attached electron) estimated to be between 0.1 and 0.8 ev. The generation rate of such an ion should be given by a form of the Saha-Langmuir equation:

$$\frac{\nu_j}{\mu} = \left[1 + 2 \exp\left(\frac{\Phi - V_j}{k\, T}\right)\right]^{-1} \qquad \text{(V-66)}$$

where:

ν_j = negative ion emission rate

μ = cesium atom arrival rate

Φ = surface work function

V_j = electron affinity

k = Boltzmann constant

T = emitter temperature.

The work function of bulk cesium generally is taken as 1.8 ev. He concludes that negative cesium ion emission from beam-forming negative electrodes in ion propulsion engines could cause severe sputtering of the positive ion source. We have not studied this possible phenomenon further.

8. REFERENCES

V-1. "Proposal for Applications Technology Satellite F & G, Phase D," Book 1: Technical, Volume IC, Controls, SD Proposal N-21630, General Electric, McDonnell Douglas, and Hughes, 17 September 1969, pp. 4-121.

V-2. "Typical Absolute Spectral Response Characteristics of Photoemissive Devices," Sheet of Curves (not otherwise identified), ITT Industrial Laboratories, Fort Wayne, Indiana.

V-3. Unknown Reference, pp. 184-185.

V-4. Cleavinger, Richard L., Richard L. Gutshall, and C. Allen Morgan, "Final Report for Polaris Star Tracker Breadboard Model," No Number, Ball Brothers Research Corp., 23 May 1967 - 1 August 1968.

V-5. Hunter, R., and R. Bartlett, Personal Communication, GSFC, 17 April 1970.

V-6. Johnson, F. S., "The Solar Constant," Journal Meteorology 11(6), December 1954, pp. 431-439.

V-7. Connerade, J. P., "Absorption Spectrum of Cs I in the Vacuum Ultra-Violet," N69-35759, ESRIN Internal Note No. 37, May 1969 (Submitted to the Astrophysical Journal).

V-8. Franklin, J. L., et al., Ionization Potentials, Appearance Potentials, and Heats of Formation of Gaseous Positive Ions, NSRDS-NBS26, Department of Commerce, June 1969.

V-9. Leighton, Robert B., Principles of Modern Physics, McGraw Hill, 1959.

V-10. Nottingham, Wayne B., Proceedings of the IEEE, December 1963, pp. 1771-1772.

V-11. Moore, Charlotte, E., Atomic Energy Levels, Vol. III, NBS Circular 467, 1 May 1958.

V-12. Richtmyer, F. K., E. H. Kennard, and T. Lauritsen, Introduction to Modern Physics, McGraw Hill, 1955.

V-13. Gregory, Chris, "Resonance Broadening of Caesium," Physical Review, Vol. 61, 1 and 15 April 1942, pp. 465-469.

V-14. Pollock, D. H., and A. O. Jensen, "Absorption of Resonance Radiation and Formation of Molecular Ions in Cesium Vapor," Journal of Applied Physics, Vol. 36, No. 10, October 1965, pp. 3184-3192.

V-15. Aller, Lawrence, "Atomic Line Strengths," Chapter 3, Part 7, Reference II-16, pp. 7-54 - 7-65.

V-16. Condon, E. V., and Hugh Odishaw (Editors), Handbook of Physics, Second Edition, McGraw-Hill, 1967.

V-17. Corliss, Charles H., and William R. Bozman, "Experimental Transition Probabilities for Spectral Lines of Seventy Elements," NBS Monograph 53, 20 July 1962.

V-18. Stone, Philip M., "Cesium Oscillator Strengths," Physical Review, Vol. 127, No. 4, 15 August 1962, pp. 1151-1156.

V-19. Physical Review, Vol. 135, No. 7AB, 28 September 1964, p. 2.

V-20. Lancashire, Richard B., "Refractive Index - Particle Density Correlation for Non-equilibrium Cesium Plasmas Probed by a Multifrequency Helium-Neon Laser," NASA-TN-D-5328 (N69-30622), July 1969.

V-21. McDaniel, Earl W., Collision Phenomena in Ionized Gases, Wiley, 1964.

V-22. Ditchburn, R. W., P. J. Jutsum, and G. V. Mars, "The Continuous Absorption of Light in Alkali-Metal Vapours," Royal Society of London, Proceedings, Series A, 219, 1953, pp. 89-101.

V-23. Marmo, F. F., J. Pressman, and L. M. Aschenbrand, "Artificial Electron Clouds - II," Planetary and Space Science, Vol. 1, 1959, pp. 291-305.

V-24. Ditchburn, R. W., and U Opik, "Photoionization Processes," Atomic and Molecular Processes, (Edited by D. R. Bates), Academic Press, 1962.

V-25. Smoot, L. Douglas, and Donald L. Underwood, "Prediction of Microwave Attenuation Characteristics of Rocket Exhausts," Journal of Spacecraft and Rockets, Vol. 3, No. 3, March 1966, pp. 302-309.

V-26. Bates, D. R., et al., "Recombination Between Electrons and Atomic Ions, I - Optically Thin Plasmas," Proc. Roy. Soc. (London) Series A., Vol. 267, No. 1330, 22 May 1962, pp. 297-312.

V-27. Dugan, John V., "VIII - Plasma Chemistry and Ion-Molecule Interactions," contained in Plasmas and Magnetic Fields in Propulsion and Power Research, NASA SP-226, Proceedings of NASA-Lewis Research Center Conference, 16 October 1969.

V-28. Nygaard, Kaare J., "Electron-Impact Ionization Cross Section in Cesium," Journal of Chemical Physics, Vol. 49, 1 September 1968, pp. 1995 - 2002.

V-29. Hansen, L. K., "Cross Section of the Electron-Induced 6s-6p Transition in Cesium," Communications, 1963 (?), pp. 254-255.

V-30. Dayton, James A., "Survey of Electron-Cesium Collision Probabilities: Momentum Transfer Collisions," NASA-TM-X-1897, October 1969.

V-31. Rasor, N. S., "Practical Aspects of Fundamental Research in Therminionic Conversion," NSR-1-1, AD 699944, Final Technical Report, Contract NOOO14-69-C-0279, 1 March 1969 to 1 September 1969.

APPENDIX VI

PLUME BEHAVIOR CALCULATIONS

1. FLOW RATE

Specific impulse of the one millipound thruster is 2400 seconds (Ref. VI-1). The flow rate immediately is 0.001 lbs/2400 sec = 4.17×10^{-7} lbs/sec. This is composed of 10 percent neutrals and 90 percent ions (Ref. VI-1). Hence:

$$W_i + W_n = 4.17 \times 10^{-7}$$

$$\frac{W_n}{W_n + W_i} = 0.10$$

where:

W = weight flow rate

i refers to ionized portion

n refers to neutral portion.

Immediately:

$W_i = 3.76 \times 10^{-7}$ lbs/sec

$W_n = 4.17 \times 10^{-8}$ lbs/sec

2. NEUTRAL BEHAVIOR

2.1 Neutralizer Startup and Run Rates

The neutralizer is placed into operation before the thruster is started. The assumed cesium is 100 mg/start at a rate of 90 mg/hr. The steady state flow rate is 20 mg/hr. Emission is 100 percent neutrals (Ref. VI-1). By implication, the start time is:

$$\frac{100 \text{ mg}}{90 \text{ mg/hr}} = 1.11 \text{ hrs}$$

In engineering units, the flow rate at startup is:

$$\left(\frac{90 \text{ mg}}{\text{hr}}\right)\left(\frac{\text{gm}}{10^3 \text{ mg}}\right)\left(\frac{1\text{b}}{454 \text{ gms}}\right)\left(\frac{\text{hr}}{3600 \text{ sec}}\right)$$

$$= 5.51 \times 10^{-8} \text{ lbs/sec}$$

The steady state flow rate is:

$$5.51 \times 10^{-8} \left(\frac{20}{90}\right) = 1.226 \times 10^{-8} \text{ lbs/sec}$$

2.2 Neutrals from the Accelerator

The neutral atomic cesium flow density from the engine is 4.17×10^{-8} lbs/sec. The atomic weight of cesium is 132.9. The neutral cesium atom emission rate therefore is:

$$\left(\frac{4.17 \times 10^{-8} \text{ lbs}}{\text{sec}}\right)\left(\frac{454 \text{ gms}}{\text{lb}}\right)\left(\frac{\text{mole}}{132.9 \text{ gms}}\right)\left(\frac{6.03 \times 10^{23} \text{ atoms}}{\text{mole}}\right)$$

$$= 8.16 \times 10^{16} \text{ atoms/sec}$$

Mean velocity is given by Reference VI-2:

$$\bar{v} = \sqrt{\frac{8\,k\,T}{\pi\,m}}$$

where:

k = Boltzmann constant = 1.380×10^{-16} erg/°K

T = temperature, °K

m = atom mass = 2.20×10^{-22} gms/atom.

Neutral cesium leaving the engine has a thermal energy corresponding to 500° F (533°K). The mean neutral velocity due to its thermal energy is:

$$\bar{v} = \left(\frac{(8)\,(1.380)\,(10^{-16})\,(533)}{(\pi)\,(2.20)\,(10^{-22})}\right)^{1/2} = 2.91 \times 10^{4} \text{ cm/sec}$$

This will represent the neutral cesium velocity for those atoms that do not interact with anything after leaving the thruster.

The thruster opening has a 3.5 inch diameter (Ref. VI-3). Cross sectional area consequently is $(\pi)\,(1.75)^2\,(2.54)^2 = 61.2$ cm^2. As a rough approximation, the velocity normal to the plane of the opening will be 2.91×10^4 cm/sec. The neutral flux is $8.16 \times 10^{16}/61.2 = 1.33 \times 10^{15}$ atoms/cm^2-sec. Density under these conditions is $1.33 \times 10^{15}/2.91 \times 10^4 = 4.59 \times 10^{10}$ atoms/cm^3. The density at one atmosphere (STP) would be $6.02 \times 10^{23}/22400 = 2.69 \times 10^{19}$ atoms/cm^3. If the atoms were in an equilibrium situation, neutral exhaust partial pressure would be about $4.59 \times 10^{10}/2.69 \times 10^{19} \approx 10^{-9}$ atm. This is a rarefied flow situation.

3. STARTRACKER INTERACTIONS WITH NEUTRALS

3.1 Introduction

We have shown that, for practical purposes, the tracker will not see the primary exhaust beam (see Appendix IV), and even if it did, there would be no interaction. Hence, we may confine the interaction study to the effect of neutrals. For the time being, we consider only the neutrals that originate within the thruster, as opposed to those introduced via the neutralizer.

There are two possible interaction effects:

(1) Absorption

(2) Scattering

In the former, photons originating at the star are attenuated by the beam. In the latter, photons from other sources interact with the beam and are scattered into the tracker. We will treat this first and then cover the absorption calculations.

3.2 Sunlight Interaction Assumptions

The tracker sees a relatively broad expanse of exhaust plume as well as the star (as perturbed by the plume). This plume can act as a source of extraneous light. Sunlight, as well as light from the earth and moon, can interact with the plume and enter the tracker. Since the sun's light is by far the strongest source of such light, we will limit the study to the effect of the sun.

A comprehensive, accurate treatment of this phenomenon would be, to say the least, difficult. Fortunately, we can bypass this with some simplifying assumptions. These should be sufficient to enable us to understand the magnitude of the problem. Five basic assumptions are involved:

(1) Any sunlight absorbed by the beam is immediately reemitted.

(2) Reemission is an isotropic process.

(3) The reemitted light will have the same wavelength as the absorbed light.

(4) The intensity of the sun is not affected by the beam.

(5) Any reemitted light is unaffected by the beam.

The first assumption appears very reasonable. We have found no evidence of long life excited states of the cesium atom. Table VI-1 presents the decay coefficients (sec^{-1}), A_{UL}, for spontaneous decay from level U to L. Decay rate is given by:

$$\frac{d N_U}{d t} = - N_U \sum_{L<U} A_{UL}$$

where:

N_U = number of atoms at level U

t = time

Since all decay coefficients are large, and most are in the range of 16^6 sec^{-1}, we see that the lifetimes are quite short. However, as we will see later, excitation rates are high.

The second assumption neglects such effects as bending, reflection, etc. We merely assume that what does not pass through the beam has an equal probability of going in any direction from the point of absorption. This should introduce little error. In many cases, the third assumption is justified. If an electron is energized by dropping from the

Table VI-1
Radiative Decay Coefficients* (Reproduced Directly from Ref. VI-4)

L	U	A_{UL}	L	U	A_{UL}	L	U	A_{UL}	L	U	A_{UL}	L	U	A_{UL}
6S	6P	3.57 (7)	6P	7S	1.92 (7)	6P	5D	8.48 (5)	5D	7P	9.85 (5)	5D	4F	1.48 (7)
	7P	2.17 (6)		8S	6.66 (6)		6D	1.70 (7)		8P	3.27 (5)		5F	9.17 (6)
	8P	5.61 (5)		9S	3.27 (6)		7D	8.56 (6)		9P	1.51 (5)		6F	5.79 (6)
	9P	2.25 (5)		10S	1.73 (6)		8D	4.76 (6)		10P	8.01 (4)		7F	3.84 (6)
	10P	1.19 (5)		11S	1.16 (6)		9D	2.89 (6)		11P	4.88 (4)		8F	2.60 (6)
	11P	7.08 (4)		12S	7.82 (5)		10D	1.88 (6)		12P	3.23 (4)		9F	1.86 (6)
	12P	4.24 (4)		13S	5.40 (5)		11D	1.30 (6)						
7S	7P	4.17 (6)	7P	8S	3.80 (6)	7P	6D	7.14 (4)	6D	8P	6.74 (5)	6D	4F	1.50 (6)
	8P	3.58 (5)		9S	1.37 (6)		7D	2.01 (6)		9P	2.91 (5)		5F	7.03 (5)
	9P	1.05 (5)		10S	7.27 (5)		8D	1.32 (6)		10P	1.53 (5)		6F	6.38 (5)
	10P	4.73 (4)		11S	4.94 (5)		9D	8.41 (5)		11P	9.31 (4)		7F	5.12 (5)
	11P	2.56 (4)		12S	3.25 (5)		10D	5.60 (5)		12P	6.05 (4)		8F	3.90 (5)
	12P	1.46 (4)		13S	2.27 (5)		11D	3.90 (5)					9F	2.94 (5)
8S	8P	9.96 (5)	8P	9S	1.36 (6)	8P	7D	1.64 (4)	7D	9P	3.23 (5)	7D	5F	5.13 (5)
	9P	1.11 (5)		10S	4.57 (5)		8D	4.70 (5)		10P	1.56 (5)		6F	1.88 (4)
	10P	3.87 (4)		11S	2.90 (5)		9D	3.45 (5)		11P	9.00 (4)		7F	6.33 (4)
	11P	1.87 (4)		12S	1.88 (5)		10D	2.40 (5)		12P	5.78 (4)		8F	7.24 (4)
	12P	1.02 (4)		13S	1.28 (5)		11D	1.72 (5)					9F	6.44 (4)
9S	9P	3.23 (5)	9P	10S	5.05 (5)	9P	8D	5.16 (3)	8D	10P	1.57 (5)	8D	6F	2.05 (5)
	10P	4.38 (4)		11S	2.09 (5)		9D	1.45 (5)		11P	8.27 (4)		7F	6.01 (0)
	11P	1.73 (4)		12S	1.26 (5)		10D	1.18 (5)		12P	5.20 (4)		8F	1.72 (4)
	12P	8.55 (3)		13S	8.36 (4)		11D	9.07 (4)					9F	2.40 (4)
10S	10P	1.21 (5)	10P	11S	2.04 (5)	10P	9D	2.09 (3)	9D	11P	8.31 (4)	9D	7F	9.23 (4)
	11P	2.97 (4)		12S	9.68 (4)		10D	5.69 (4)		12P	4.70 (4)		8F	1.60 (3)
	12P	1.40 (4)		13S	6.08 (4)		11D	4.83 (4)					9F	4.73 (3)
11S	11P	6.30 (4)												
	12P	1.05 (4)												
4F	7D	3.56 (5)	4F	5G	4.68 (6)	5G	6F	2.33 (4)	5G	6H	1.65 (6)			
	8D	1.22 (5)		6G	1.46 (6)		7F	5.64 (3)		7H	5.08 (5)			
	9D	6.07 (4)		7G	6.79 (5)		8F	2.35 (3)		8H	2.34 (5)			
	10D	3.59 (4)		8G	3.81 (5)		9F	1.40 (3)		9H	1.30 (5)			
	11D	2.34 (4)		9G	2.39 (5)									
5F	8D	2.13 (5)	5F	5G	5.19 (1)	6G	7F	1.72 (4)	6G	7H	5.31 (5)			
	9D	8.36 (4)		6G	1.23 (6)		8F	5.06 (3)		8H	2.57 (5)			
	10D	4.04 (4)		7G	5.85 (5)		9F	2.86 (3)		9H	1.45 (5)			
	11D	2.41 (4)		8G	3.31 (5)									
				9G	2.08 (5)									
6F	9D	1.13 (5)	6F	6G	4.56 (1)	7G	8F	7.80 (3)	7G	8H	2.07 (5)			
	10D	5.24 (4)		7G	3.62 (5)		9F	4.26 (3)		9H	1.24 (5)			
	11D	2.48 (4)		8G	2.41 (5)									
				9G	1.53 (5)									
7F	10D	6.16 (4)	7F	7G	2.75 (1)									
	11D	2.83 (4)		8G	2.44 (5)									
				9G	1.10 (5)									
6H	7G	3.34 (3)	6H	7I	7.38 (5)	7I	8H	1.18 (3)	7I	8J	4.26 (5)			
	8G	1.30 (3)		8I	2.17 (5)		9H	4.39 (2)		9J	1.03 (5)			
	9G	6.48 (2)		9I	9.65 (4)									
7H	8G	3.82 (3)	7H	8I	2.78 (5)									
	9G	1.74 (3)		9I	1.31 (5)									

*The number in parenthesis is the power of ten by which the figures are multiplied.

energized state to the preenergized state, the same photon energy (wavelength) will result. In some cases, this may not occur. The effect should not be too serious. It will be minimized by the treatment that utilizes total energy scattered into the tracker. (Of course, this does not take into account the tracker sensitivity change with wavelength.) The effect can be calculated by determining production rate of each of the levels and computing resulting decay effects using the Table VI-1 coefficients. (We have not performed the calculations.)

The fourth and fifth assumptions are, at first glance, excellent. We are dealing with a very rarefied beam in the field of view of the tracker. The probability of photon interaction would appear to be very low. Unfortunately, the lines absorb strongly and make these assumptions poor ones close to the thruster. They are, however, sufficient to scope the interaction problem.

3.3 Sunlight Absorption

By definition, the change in intensity dI resulting from passage through a distance of material du is:

$$dI = -I \alpha du \qquad \text{(VI-1)}$$

where:

α = absorption coefficient

We may write α as (see Appendix V):

$$\alpha = C \rho \qquad \text{(VI-2)}$$

where:

C = a constant

ρ = atom density, atoms/unit volume

Therefore:

$$dI = -CI \rho du \qquad \text{(VI-3)}$$

If we normalize this by dividing by I_0, we obtain:

$$\frac{dI}{I_0} = -\frac{CI \rho du}{I_0} \qquad \text{(VI-4)}$$

But $-dI/I_0$ (with a constant I_0) is the probability of an absorption in traversing a distance du. The probability of absorption per unit length is:

$$P_a = -\frac{dI}{I_0 du} = C \rho \qquad \text{(VI-5)}$$

where, since $I \approx I_0$, we have cancelled the terms. Now we may evaluate Equation IV-72. First substitute for P_a :

$$I = \int_{y'=0}^{\infty} \int_{x'=y' \tan \alpha_1'}^{y' \tan \alpha_2'} \int_{z'=y' \tan \beta_1'}^{y' \tan \beta_2'} \frac{A_\ell \, y' \, C \, \rho \, I_0 \, dx' \, dy' \, dz'}{4 \pi (x'^2 + y'^2 + z'^2)^{3/2}} \tag{VI-6}$$

The density is given by:

$$\rho = \frac{\rho_0 \, A^2 \, (s_3 + s_4 \, y)}{(s_5 + s_6 \, y + s_7 \, y^2)^{3/2}} \tag{IV-36}$$

Substituting this, we find:

$$I = \frac{A_\ell \, C \, I_0 \, \rho_0 \, A^2}{4 \pi} \int_{y'=0}^{\infty} \int_{x'=y' \tan \alpha_1'}^{y' \tan \alpha_2'} \int_{z'=y' \tan \beta_1'}^{y' \tan \beta_2'} \tag{VI-7}$$

$$\left\{ \frac{y' \, (s_3 + s_4 \, y) \, dx' \, dy' \, dz'}{(s_5 + s_6 \, y + s_7 \, y^2)^{3/2} \, (x'^2 + y'^2 + z'^2)^{3/2}} \right\}$$

All of the terms may be evaluated readily in numeric form. (We haven't tried to integrate this mess in closed form.) The general approach is to write the equation as:

$$I = C' \sum_{i=1}^{I} \sum_{j=1}^{J} \sum_{k=1}^{K} f \left[x_j' + \frac{\Delta x_j'}{2}, \; y_i' + \frac{\Delta y_i'}{2}, \; z_k' + \frac{\Delta z_k'}{2} \right] \Delta z_k' \, \Delta x_j' \, \Delta y_i' \tag{VI-8}$$

where f is the function within the integral portion of Equation (VI-7) and C' represents all terms in front of the integral. This solution has been coded for solution on a digital computer and has been investigated parametrically by varying α, β, I, J, K, and $\Delta y_i'$ to obtain both sufficient accuracy and the effect of changing α and β. The results are shown in Table VI-2.

Clearly, the value at $\alpha = -0.0698$ (radians), $\beta = -0.262$ represents the worst case. (The + α and β values are beyond the range of interest but we did not change them since these zones are not as great a problem.) Hence, to evaluate the worst case, we rewrite Equation (VI-8) as:

$$I = 6.68 \times 10^{-6} \, C'$$

or, using Equation (VI-7):

$$I = 6.68 \times 10^{-6} \, \frac{A_\ell \, C \, I_0 \, \rho_0 \, A^2}{4 \pi} \tag{VI-9}$$

Table VI-2
Solution to Equation VI-8*

α_1	β_1	I/C', in^{-1}
0	0	5.96×10^{-6}
-0.0698	-0.262	6.68×10^{-6}
-0.0698	0.262	4.99×10^{-6}
0.0698	-0.262	5.98×10^{-6}
0.0698	0.262	4.64×10^{-6}

We know that:

$$\rho_0 = (4.59)(10^{10})(16.40)$$

$$= 7.55 \times 10^{11} \text{ atoms/in}^3$$

$$A = 1.75 \text{ in.}$$

Therefore:**

$$I = \frac{(6.68)\ (10^{-6})\ (7.55)\ (10^{11})\ (1.75)^2}{4\pi} C A_\ell I_0 \qquad \text{(VI-10)}$$

$$= 1.227 \times 10^6\ C A_\ell I_0$$

3.4 Line Width

The line width is given by:

$$\Delta = \frac{\lambda^2}{2\pi c \tau} \qquad \text{(V-2)}$$

where:

λ = wavelength

c = speed of light

τ = mean life

*Obtained by using $a\Delta y'$ proportional to y':

$$\sum_{i=1}^{I} \Delta y_i = 1.06 \times 10^6;$$

Δy_1 = 1 in., I = J = K = 14.

**1.227×10^6 in^{-2}

We do not have a detailed mean life listing, but we do have decay coefficients (Table VI-1) and oscillator strengths (Table V-5). Since the latter are more detailed, we will use them to compute decay coefficients and hence mean life. We have:

$$A_{nn'} = \frac{8\pi^2 e^2 \nu^2}{m c^3} \frac{\tilde{\omega}_{n'}}{\tilde{\omega}_n} f_{nn'} \qquad \text{(V-31)}$$

$$\tilde{\omega}_n = 2j + 1 \qquad \text{(V-27)}$$

Noting that $\nu = c/\lambda$, we obtain:

$$A_{nn'} = \frac{8\pi^2 e^2}{m c \lambda^2} \frac{2j' + 1}{2j + 1} f_{nn'} \qquad \text{(VI-11)}$$

which lets us compute the decay coefficient from λ and f.

Mean life is simply $1/A_{nn'}$. Therefore Equation (V-2) is:

$$\Delta = \frac{4\pi e^2}{m c^2} \frac{2j' + 1}{2j + 1} f_{nn'} \qquad \text{(VI-12)}$$

The following values (cgs) are applicable:

$e = 4.80 \times 10^{-10}$ esu (stat coulomb)*

$m = 9.11 \times 10^{-28}$ gm

$c = 2.99 \times 10^{10}$ cm/sec

Therefore:

$$\frac{4\pi e^2}{m c^2} = 3.55 \times 10^{-12} \text{ cm}$$

and:

$$\Delta = 3.55 \times 10^{-12} \frac{2j' + 1}{2j + 1} f_{nn'} \qquad \text{(VI-13)}$$

For the $P_{1/2}$ and $P_{3/2}$ initial states, respectively:

$$\frac{2j' + 1}{2j + 1} = 1 \qquad \frac{2j' + 1}{2j + 1} = 1/2$$

*The units of e (or ϵ, depending upon the reference) can introduce an understanding problem. Electrostatic force is described by $F = kq_1 q_2/r^2$ where k = constant, q = charge, r = distance. In the cgs system, k = 1. If $q_1 = q_2 = e$, we find $e^2 = Fr^2 \equiv$ dyne $cm^2 \equiv$ esu^2.

The line widths follow immediately from Table V-4. Comparison of mean lines from Equation (VI-11) and Table VI-1 is also of interest. The constant part of Equation (VI-11) is:

$$\frac{8\pi^2 e^2}{m c} = 0.667 \text{ cm}^2/\text{sec}$$

so that:

$$A_{nn'} = \frac{0.667}{\lambda^2} \frac{2j' + 1}{2j + 1} f_{nn'} \qquad \text{(VI-14)}$$

These data are summarized in Table VI-3. We see that the line widths are extremely small. Agreement of the decay constants appears reasonable, but we do not have a direct comparison because the Table VI-1 data do not differentiate between the doublet lines. (Disagreement of f values is drastic, and differences of a factor of 500 have been found between various investigators. Agreement to the accuracy we appear to have found is gratifying.)

Table V-3 provides additional information we can use for a comparison. This gives the width for the $6P_{3/2}$ transition. This fits an equation of the form:

$$\log N = A + B \log \Delta \qquad \text{(VI-15)}$$

Table VI-3
Cesium Line Widths and Decay Constants

Initial State	Line Width, cm	Decay Constant, sec^{-1}	
		Eq. VI-14	Table VI-1
$6P_{1/2}$	1.400×10^{-12}	3.29×10^{7}	3.57×10^{7}
$6P_{3/2}$	1.445×10^{-12}	3.74×10^{7}	
$7P_{1/2}$	1.009×10^{-14}	9.00×10^{5}	2.17×10^{6}
$7P_{3/2}$	3.09×10^{-14}	2.79×10^{6}	
$8P_{1/2}$	1.127×10^{-15}	1.363×10^{5}	5.61×10^{5}
$8P_{3/2}$	6.20×10^{-15}	7.72×10^{5}	
$9P_{1/2}$	2.58×10^{-16}	3.69×10^{4}	2.25×10^{5}
$9P_{3/2}$	2.22×10^{-15}	3.20×10^{5}	
$10P_{1/2}$	1.027×10^{-16}	1.590×10^{4}	1.19×10^{5}
$10P_{3/2}$	1.101×10^{-15}	1.707×10^{5}	
$11P_{1/2}$	4.40×10^{-17}	7.15×10^{4}	7.08×10^{4}
$11P_{3/2}$	6.32×10^{-16}	1.028×10^{5}	
$12P_{1/2}$	2.20×10^{-17}	3.79×10^{4}	4.24×10^{4}
$12P_{3/2}$	3.70×10^{-16}	6.17×10^{4}	

With $N = 4.06 \times 10^{15}$, $\Delta = 4.5$ Å; with $N = 1.055 \times 10^{17}$, $\Delta = 111.5$ Å. This gives:

$$\log \Delta = \log N - 14.96 \tag{VI-16}$$

At $N = 5 \times 10^{10}$ atoms/cm^3 (nozzle exit density), we obtain:

$$\left.\begin{aligned} \Delta &= 5.5 \times 10^{-5} \text{ Å} \\ &= 5.5 \times 10^{-13} \text{ cm} \end{aligned}\right\} \tag{VI-17}$$

Table VI-3 shows 1.4×10^{-12} cm for no influence between atoms. The experimental data extrapolate quite well, lending additional credence to the Table VI-3 calculations. Our line widths appear reasonable.

3.5 Sunlight Interaction Calculation

We have written the absorption coefficient as:

$$\alpha = C \rho \tag{VI-2}$$

where the absorption rate is given by the equation:

$$\frac{d I_{\nu (nn')}}{d u} d \nu (n n') = - I_{\nu (nn')} \alpha d \nu (n n') \tag{VI-18}$$

where $I_{\nu (nn')}$ $d\nu(nn')$ is the intensity over the interval $d\nu(nn')$, ergs/cm^2-sec.

But $-dI_\nu (nn')/du \, d\nu(nn')$ is the volumetric absorption rate (ergs/cm^3-sec). We have an expression for the volumetric absorption rate (photons/cm^3-sec):

$$N'_\nu = N'_n I_{\nu (nn')} \frac{4 \pi^2 e^2 \lambda}{h m c^2} f_{nn'} \tag{V-44}$$

The absorption rate on an energy basis is:

$$- \frac{d I_{\nu (nn')}}{d u} d \nu (n n') = N'_\nu h \nu \tag{VI-19}$$

But the density, indicated by ρ , is the same as N'_n , the number of absorbers per unit volume:

$$\rho = N'_n \tag{VI-20}$$

We may combine Equations (V-44), (VI-18), (VI-19), (VI-20), and (VI-2) to find:

$$C = \frac{1}{\Delta \nu\,(n\,n')} \frac{4\pi^2 e^2}{m c} f_{nn'} \tag{VI-21}$$

where we have substituted $\Delta \nu$ for $d \nu$ with the intention of using average values over a finite difference.

Next substitute into Equation (VI-10):

$$I = 1.227 \times 10^6 \frac{4\pi^2 e^2}{m c \Delta \nu\,(n\,n')} f_{nn'} A_\ell I_0 \tag{VI-22}$$

But the units on the constant are in^{-2}. Hence, we convert:

$$(1.227 \times 10^6\ in^{-2})\ (2.54\ cm/in)^{-2} = 1.900 \times 10^5\ cm^{-2}$$

and substitute into Equation (VI-22) to obtain consistent units:

$$I = 1.900 \times 10^5 \frac{4\pi^2 e^2}{m c \Delta \nu\,(n\,n')} f_{nn'} A_\ell I_0 \tag{VI-23}$$

Since $\nu = c/\lambda$:

$$|d \nu| = c/\lambda^2\, d\lambda \tag{VI-24}$$

$$|\Delta \nu| = \frac{c}{\lambda^2} \Delta \lambda \tag{VI-25}$$

The line width is $\Delta \lambda$. Equation (VI-23) is now:

$$I = 1.900 \times 10^5 \frac{4\pi^2 e^2 \lambda^2}{m c^2 \Delta \lambda} f_{nn'} A_\ell I_0 \tag{VI-26}$$

But the line width is given by:

$$\Delta \lambda = \frac{4\pi e^2}{m c^2} \frac{2j' + 1}{2j + 1} f_{nn'} \tag{VI-12}$$

Thus:

$$I = 5.97 \times 10^5 \lambda^2 \left(\frac{2j + 1}{2j' + 1}\right) A_\ell I_0 \tag{VI-27}$$

Or:

$$\frac{I}{A_\ell I_0} = 5.97 \times 10^5 \lambda^2 \left(\frac{2j + 1}{2j' + 1}\right) \tag{VI-28}$$

Table VI-4
Sunlight Interaction

$\lambda \times 10^4$, cm	Energy Ratio Seen By Tracker	
	Per Unit Wavelength	Per Line*
0.8943	4.76×10^{-3}	6.68×10^{-15}
0.8521	2.17	1.25×10^{-14}
0.4593	1.260	1.27×10^{-17}
0.4555	0.619	7.64×10^{-17}
0.3888	0.900	1.02×10^{-18}
0.3876	0.449	1.11×10^{-17}
0.3618	0.780	2.01×10^{-19}
0.3612	0.389	3.30×10^{-18}
0.3481	0.721	7.41×10^{-20}
0.3478	0.360	1.59×10^{-18}
0.3401	0.687	3.04×10^{-20}
0.3399	0.345	8.71×10^{-19}
0.3350	0.669	1.48×10^{-20}
0.3348	0.332	4.95×10^{-19}

*Solar intensity, flux, or what have you must be given in units of per cm of wavelength to be consistent with this column.

The behavior of this function is shown in the second column of Table VI-4. The function is the ratio of the energy seen by the tracker to the solar energy for each line.

The plume is transparent except for the lines (provided we are not in the continuous absorption region). The energy available to be intercepted by the plume is $I_0 \Delta \lambda$ if I_0 is the sunlight intensity distribution function as given in Figure V-5. If we substitute this energy in place of the unit wavelength value in Equation (VI-26) we find:

$$\frac{I}{A_\ell I_0} = 1.900 \times 10^5 \frac{4 \pi^2 e^2 \lambda^2}{m c^2} f_{nn'} \qquad \text{(VI-29)}$$

where the meaning of I now should be taken as ergs/sec (or its equivalent) for each total line instead of per unit wavelength. This can be rewritten:

$$\frac{I}{A_\ell I_0} = 2.12 \times 10^{-6} \lambda^2 f_{nn'} \qquad \text{(VI-30)}$$

This behavior also is shown in Table VI-4 (the last column). The wavelength unit corresponding to these numbers is centimeters.

The solar flux distribution function as a function of wavelength is given in Figure V-5. These values multiplied by the energy ratio per line from Table VI-4 give the flux seen by the tracker. This flux, multiplied by the relative sensitivity of the sensor (Figure V-2) gives the relative response of the sensor to the reflected sunlight. The results are summarized in Table VI-5. Note the cutoff of the two strongest lines. A sensor that included these lines would see significantly more solar energy.

The intensity distribution function for Polaris radiation is given in Figure V-4. This curve, multiplied by the curve of response (Figure V-2) gives relative response to Polaris as a function of wavelength. The integral of this function with respect to wavelength is the total relative response to Polaris. This value is 1.31×10^{-11} (based upon a Polaris flux of watts/cm^2).

The total relative response due to reflected sunlight is obtained by adding the last column of Table VI-5. There results a relative response of 2.01×10^{-5} based upon a solar flux of μwatts/cm^2, or 2.01×10^{-11} based upon a solar flux of watts/cm^2. The sunlight reflected from the plume provides a greater sensor response that Polaris!!!

This does not make sense unless the plume reacts relatively strongly when exposed to sunlight. To check this behavior, we note that Figure V-5 provides a solar flux of 21.8 μ w/cm^2 Å at the 4593 Å line. This is equivalent to:

$$21.8 \times 10^{-6} \times 10^{8} \times 10^{7} = 2.18 \times 10^{10} \text{ erg/cm}^3 - \text{sec}$$

Table VI-5
Solar Flux Seen By Tracker

$\lambda \times 10^4$, cm	Solar Flux μw/cm^2 - Å**	Sensor Relative Sensitivity	Sensor Relative Response*
0.8943	9.1	0	0
0.8521	10.2	0	0
0.4593	21.8	94.8	2.75×10^{-6}
0.4555	21.8	96.0	1.60×10^{-5}
0.3888	11.4	93.6	1.09×10^{-7}
0.3876	11.4	93.6	1.19×10^{-6}
0.3618	12.1	79.0	1.92×10^{-8}
0.3612	12.1	79.0	3.15×10^{-7}
0.3481	11.5	70.0	5.96×10^{-9}
0.3478	11.5	70.0	1.28×10^{-7}
0.3401	11.3	63.6	2.19×10^{-9}
0.3399	11.3	63.6	6.26×10^{-8}
0.3350	11.2	58.8	9.74×10^{-9}
0.3348	11.2	58.8	3.26×10^{-8}

*Based upon an intensity of μ w/cm^2.

**Converted to μw/cm^2 cm to obtain last column. See footnote in Table VI-3.

Since $\Delta\lambda = 10^{-14}$ cm:

$$I\,\Delta\nu = (2.18 \times 10^{10})\,(10^{-14}) = 2.18 \times 10^{-4}\ \text{erg/cm}^2 - \text{sec}$$

But:

$$\Delta\nu = \frac{c}{\lambda^2}\,\Delta\lambda$$

$$\frac{(2.99)\,(10^{10})\,(10^{-14})}{(4.59)^2\,(10^{-10})} = 1.422 \times 10^{5}\ \text{sec}^{-1}$$

so that:

$$I = \frac{2.18 \times 10^{-4}}{1.422 \times 10^{5}} = 1.531 \times 10^{-9}\ \text{erg/cm}^2$$

But:

$$B_{n'n} = \frac{\tilde{\omega}_{n'}}{\tilde{\omega}_n} = \frac{c^2\,A_{nn'}}{2\,h\,\nu^3}$$

and:

$$A_{nn'} = \frac{8\,\pi^2\,e^2\,\nu^2}{m\,c^3}\ \frac{\tilde{\omega}_{n'}}{\tilde{\omega}_n}\ f_{nn'}$$

$$B_{n'n} = \frac{4\,\pi^2\,e^2\,\lambda}{h\,m\,c^2} f_{nn'}$$

$$= 2.19 \times 10^{8}\ \text{cm}^2/\text{erg-sec}$$

Now:

Reaction Rate = NIB

$$= (4.6)(10^{10})(1.531)(10^{-9})(2.19)(10^{8})$$

$$= 1.54 \times 10^{10}\ \text{photons/cm}^3\text{-sec}$$

This represents an energy of:

$$\frac{(1.54)\,(10^{10})\,(6.63)\,(10^{-27})\,(2.99)\,(10^{10})}{(4.59)\,(10^{-5})}$$

$$= 6.65 \times 10^{-2}\ \text{ergs/cm}^3\text{-sec}$$

Or:

$$(6.65)\ (10^{-2})\ (10^{-7}) = 6.65 \times 10^{-9}\ \text{w/cm}^3$$

which obviously is wrong. This is more energy than entered the "cube" of gas. But we assumed a constant intensity. This answer shows that the assumption, at this density, is a poor one. The plume, at the exit nozzle density, is almost totally black to the solar flux in the vicinity of 4593 A.

A similar conclusion will follow for the other lines, although these are less intense and therefore their "blackness" will be less.

In any event, sunlight interaction appears to be a serious potential problem.

3.6 Polaris Energy Absorption Due to Cesium Lines

The line widths of cesium are very narrow and, excluding the first two principal lines, which are outside the sensor response range, total to 5.31×10^{-14} cm. The most sensitive range of sensor spectral response is from about 3600 Å to 6000Å, a range of 2400 Å or 2.4×10^{-5} cm. If the lines are totally black to light from Polaris, the fraction of energy absorbed which affects the sensor response will be about:

$$\frac{5.31 \times 10^{-14}}{2.4 \times 10^{-5}} \approx 2 \times 10^{-9}$$

The sensor response to light from Polaris is unaffected by absorption due to the cesium lines.

3.7 Polaris Energy Absorption in the Cesium Continuum Region

The cross section at the series limit is about 20×10^{-20} cm^2. We have shown that the number of cesium atoms seen by the tracker is less than 10^{12} atoms/cm^2. If these atoms are assumed to occupy one cm^3 of space, the ratio of exiting to incident photons is:

$$\frac{I_e}{I_0} = e^{-\sigma N}$$

where:

σ = cross section

N = atom density

(note that it makes no difference what length ℓ we choose for this calculation; $N\ell$ remains constant because the total number of atoms has been determined.) Hence:

$$\frac{I_e}{I_0} = e^{-(20)\ (10)^{-20}\ (10^{12})}$$

$$= e^{-2 \times 10^{-7}}$$

$$\approx 1 - 2 \times 10^{-7} \approx 1$$

The continuum region has no measurable effect upon light from Polaris.

4. REFERENCES

VI-1. Hunter, R., and R. Bartlett, Personal Communication, GSFC, April 17, 1970.

VI-2. Lee, John F., Francis W. Sears, and Donald L. Turcotte, Statistical Thermodynamics, Addison-Wesley, 1963.

VI-3. Bartlett, R., Personal Communication, GSFC, April 21, 1970.

VI-4. Norcross, D. W., and P. M. Stone, "Recombination, Radiative Energy Loss, and Level Populations in Non-equilibrium Cesium Discharges," J. Quant. Spectrosc. Radiat. Transfer., Vol. 8, pp. 655-684.

APPENDIX VII

TEFLON THRUSTER DATA AND EXPERIENCE

1. THRUSTER CONFIGURATION

The thruster used in the LES-6 spacecraft is shown schematically in Figure VII-1. The thruster consists of a spring loaded propellant rod, a retaining shoulder, an igniter plug, a housing, an exhaust cone or nozzle, electrodes (not shown, but located to impress a voltage differential across the end of the Teflon propellant rod), and suitable electronics. Excellent photographs of the thruster are shown in References VII-1, 2, and 3. Reference VII-3 is particularly good since it also shows the LES-6 satellite with attached thrusters.

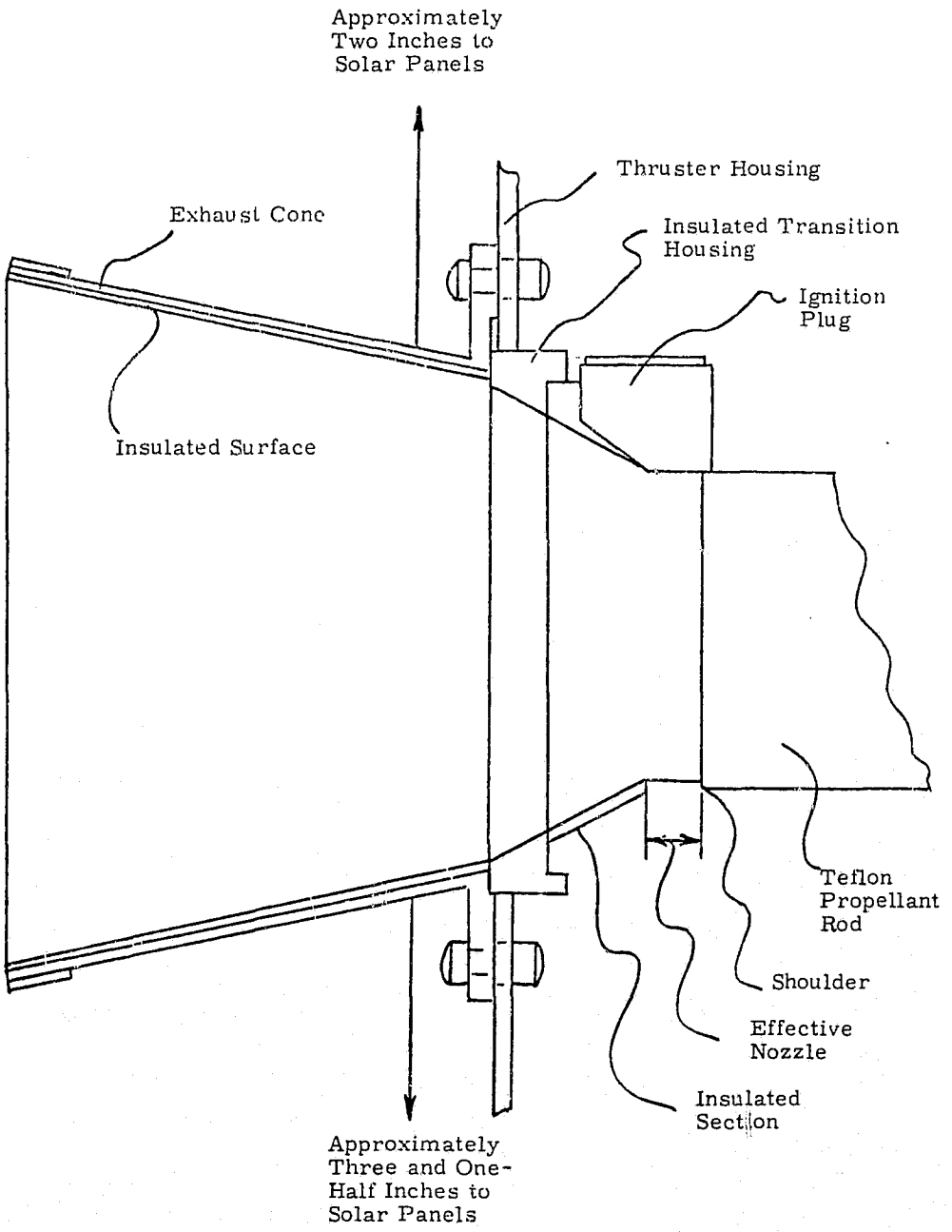

Figure VII-1. LES-6 Thruster Sketch (Ref. VII-4).

Operation is remarkably straightforward. First, the energy storage capacitor is charged to its operating voltage. This voltage also appears across the interelectrode spacing (one electrode is located at the shoulder shown in Figure VII-1, and the other at the igniter plug). Then the igniter plug is "fired" to initiate a micro-discharge in the interelectrode spacing. This depolymerizes a small portion of Teflon and ionizes part of the ablated portion. The voltage difference accelerates the ionized portion, causing further depolymerization and ionization until a microdischarge results which "closes" the circuit and allows the energy storage capacitor to discharge across the electrodes. This main discharge depolymerizes surface layers of the Teflon which become ionized and are ejected through the thruster nozzle by the electrical forces. The Teflon also depolymerizes behind the fuel retaining shoulder. A Negator spring is provided at the end of the Teflon rod to move propellant into the region depleted by the discharge. The ablated layer, typically, is of the order of Angstroms thick (per discharge).

2. TEFLON COMPOSITION, PROPERTIES, AND CHARACTERISTICS

2.1 Introduction

Two different classes of material have been referred to as Teflon in respect to use as a fuel in thrusters. One is the true Teflon produced by Dupont. The other is a mixture of various molecular weight chlorofluorocarbons. The true Teflon is used by Fairchild Hiller in their Teflon thruster. The chlorofluorocarbon has been referred to by LaRocca of General Electric as a possibility for a Teflon thruster. Most of the experimental work that has been reported involves the Dupont product. In this appendix, we will cover Dupont's Teflon in some detail. Then we will present what information we have obtained on the chlorofluorocarbons.

2.2 Teflon

Teflon was first discovered by Plunkett in the 1930's. Its discovery was completely accidental, and resulted from an attempt to extract tetrafluoroethylene gas from a pressure cylinder. When no gas could be removed, Dr. Plunkett examined the cylinder and found it filled with a dense white deposit (Ref. VII-5).

Teflon's unique properties caused Rudner (Ref. VII-7) to comment "at the time of this writing, no known material is as chemically inert and has the temperature capabilities of the fluorocarbons." The material has a crystalline structure at normal temperatures, but becomes an amorphous transparent gel when heated above 620°F. In this form, it will not flow to any extent. Only limited deformation can be tolerated prior to fracturing the gel. Its temperature capabilities are clearly indicated in Table VII-1, which shows virtually no change in weight at significant temperature levels (for an organic).

As would be expected from these data, the vapor pressure is extremely low, with values of 5×10^{-18} millimeters of mercury at 27°C and 5×10^{-12} at 100°C (Ref. VII-4). Sperati (Ref. VII-8) reports the polymer to be insoluble in all common solvents and highly resistant to chemical attack. It has an extremely low dielectric loss, high dielectric strength, and unique nonadhesion and antifrictional properties.

2.2.1 Teflon Production.* Teflon is produced by the polymerization of tetrafluoroethylene according to:

$$n\,C_2F_4 \longrightarrow (C_2F_4)_n + 41.12\ \text{kcal/mole}$$

*Portions of this and the following subsection are abstracted from Reference VII-8.

Table VII-1
Weight Loss of Teflon at
Various Temperatures (Ref. VII-7)

Temperature °F	Weight Loss %/hr
400	0.0002 (1)
500	0.0002 (1)
600	0.0002 (1)
680	0.001 (2)
734	0.006 (2)
788	0.09 (2)

(1) Granular molding powder
(2) Molded sheet

The monomer is a colorless, odorless gas which boils -76.3°C (one atmosphere pressure) and freezes at -142.5°C.

2.2.2 Properties. There are several kinds of polytetrafluoroethylene. One is a granular polymer which consists of spongy, white particles with a median size of roughly 600 microns. A second kind of polymer, a colloidal aqueous dispersion, exists in the form of dense spheres with about a 0.2 micron diameter. The primary dispersion particles have little, if any, porous structure.

Regardless of kind, polytetrafluoroethylene appears to be an entirely linear polymer. Its density at room temperature is about 2.0 and 2.3 gms/cm^3 for the amorphous and crystalline portions, respectively. In most polymerization reactions, the solid polymer is formed directly from the monomer. The polymer has a density between 2.28 and 2.295 gms/cm^3. This corresponds to a degree of crystallinity of between 93 and 98 percent.

The virgin polymer is exceedingly pure. According to Dupont (Ref. VII-9), the total impurities are in the one to two parts per million range; so low that they are beyond the range of the instruments normally available for analysis. Sperati concludes that each molecule of polytetrafluoroethylene contains two sulfonic or carboxyl end groups depending on the type of polymerization initiator used. Apparently, with the exception of these end groups and very small quantities of other material, virgin Teflon consists entirely of carbon and fluorine.

Teflon appears to vary in molecular weight, a phenomenon to be expected for polymeric material. Several values have been reported, including a range 142,000 to 534,000 on specially prepared low molecular weight polytetrafluoroethylenes, and 389,000 to 8,900,000 for polymers of industrial interest.

Bro (Ref. VII-10) provided a warning for our application. Teflon, as originally produced by Dupont, is extremely pure and for practical purposes we need not consider impurities. However, it is exceedingly important that virgin polymer be used. This is expensive, and scrap Teflon is commonly saved for reuse. Such Teflon, despite all precautions, becomes contaminated and the contaminant cannot be removed during reprocessing. Therefore, all of the conclusions in this report are applicable to virgin Teflon. Use of any other material, or introduction of impurities into the Teflon during processing, could negate our conclusions because of a change in the contaminant level.

2.2.3 Chemical Behavior. Our investigations quickly established that, within certain limits, no one knows precisely what is coming off a Teflon thruster. (We will say more of this later.) Consequently, to obtain an understanding of Teflon behavior, we have compiled its chemical characteristics under normal circumstances and have included as well several investigations of short-term behavior which may be enlightening.

Dr. Bro (Ref. VII-10) provided a number of known reactions. Basic polymer decomposition takes place according to:

$(CF_2)_n \longrightarrow CF_2:$

(Teflon) (a radical)

This process may be considered as an unzipping of the chain. Lower molecular weight polymer also may come off, but if hot enough this would decompose.

The radical then reacts according to:

$CF_2: \longrightarrow CF_2 = CF_2$

(the monomer)

$\longrightarrow CF_3$

$\xrightarrow{>960°C} CF_4 + C$

The products may react further to give:

$CF_2 = CF_2 \xrightarrow[\text{surface}]{\text{cold}} (CF_2)_n$

$CF_3 \longrightarrow CF = CF_2$

The $(CF_2)_n$ is the Teflon-type polymer. Its molecular weight will be a function of conditions, and may or may not be similar to Teflons. The $CF = CF_2$ (hexafluoropropylene) and the CF_4 (carbon tetrafluoride) are inert. Hence, under ordinary conditions, decomposition of Teflon results in inert materials which can deposit on other surfaces. In one case, the $CF_2 = CF_2$, presence of a surface will enhance the reaction. Since the materials are inert, once deposited they will stay.

Other reactions also occur. In the presence of H_2 or H_2O one obtains:

$CF_2: \longrightarrow CO\ F_2$

and in air:

$CF_2: \longrightarrow CO\ F_2 + HF + CO_2$

The $CO\ F_2$ (carbonyl fluoride) will hydrolyze immediately if H_2O is present.

According to Sperati (Ref. VII-8), the vacuum pyrolysis of thin samples follows first-order kinetics with monomer as the major decomposition product in the temperature range from 360°C to 510°C. The rate constant is independent of molecular weight and polymer type. It is charactized by an activation enthalpy of 83.0 kilocalories/mole and a frequency factor of 3×10^{19} $sec.^{-1}$. In thicker samples, the vacuum pyrolysis is controlled by monomer diffusion.

The presence of monomer or other gaseous pyrolysis products will affect the behavior. The most probable mechanism for vacuum pyrolysis appears to be random chain cleavage, propagation with a short kinetic chain length, and termination by disproportionation. Presence of monomer in equilibrium with a chain radical increases from 4.8×10^{-3} mm Hg at 327°C to 7.6 mm at 510°C. One atmosphere of tetrafluoroethylene would be in equilibrium with a chain radical at 712°C.

When polytetrafluoroethylene is exposed to ionizing radiation in the presence of oxygen, it degrades. No crosslinking behavior is found. Apparently, much of the degradation can be avoided if there is no oxygen. The irradiation appears to involve the breaking of carbon-fluorine bonds producing secondary radicals. In a vacuum, these radicals may combine to form crosslinks. However, they are quite reactive toward other substances. Therefore, with oxygen, one obtains chain cleavage and further degradation with monomer as the primary product.

Settlage (Ref. VII-11) has reported on the behavior of Teflon at elevated temperatures. He adds a few further comments on the decomposition. For example, gaseous products of pyrolysis are 94 to 97 percent tetrofluoroethylene with small amounts of fluorocarbons such as carbon tetrafluoride, hexafluoropropylene, and octafluorocyclobutane. (The author also gives various rate equations and Teflon properties.) Settlage conducted experiments in which specimens were placed in a solar furnace. Flux densities from 300 to 1100 watts/cm^2 were obtained. The disks which were thus irradiated were always smooth and showed no pits or cracks. Very small amounts of carbon were observed. He also exposed Teflon specimens to a plasma torch. Apparently, a slab of Teflon will not exceed 640°C, regardless of the heating rate. Above this temperature, only pyrolysis products are present. The maximum surface temperature under heating conditions appears to be in the vicinity of 700°C. The zone of partially decomposed material has a thickness of less than 0.2 mm. No evidence of degradation was observed in interior portions of samples.

Mathias (Ref. VII-12) reports upon decomposition in a microwave-excited glow discharge. The principle products obtained in helium (no oxygen) were C_2F_4, CF_4, C_2F_6, C_3F_6, C_3F_8, C, and polymer. With oxygen, COF_2, CF_4, C_2F_4, C_2F_6, C_3F_6, C_3F_8, CO, and CO_2 were obtained. The evidence, according to the authors, supports a mechanism involving CF_2 radical reactions. Their proposed reactions (which they in part support with other references – and which we in part quote) involved an initial step of free-radical formation via random chain cleavage:

$$(CF_2)_n \longrightarrow R_1CF_2 \cdot + R_2CF_2 \cdot .$$

This is followed by depropagation which occurs via CF_2 radical elimination:

$$R_1CF_2 \cdot \longrightarrow R_1 \cdot + CF_2$$

$$R_2CF_2 \cdot \longrightarrow R_2 \cdot + CF_2$$

The CF_2 radicals are produced in large concentrations and the following reactions occur:

$$CF_2 + CF_2 \longrightarrow C_2F_4$$

$$e^- + CF_2 \longrightarrow CF^+ + F + 2e^-$$

$$e^- + C_2F_4 \longrightarrow C_2F_4^+ + 2e^-$$

$$CF_2 \longrightarrow CF^+ + F^-$$

Another probable reaction is the free-radical reaction:

$$CF_2 \longrightarrow CF + F$$

The presence of carbon can be explained by the reaction:

$$2CF \longrightarrow CF_2 + C$$

The compounds CF_4, C_2F_6, and C_3F_8 were prominent reaction products found in the reported experiments. The major gaseous product is C_2F_4; the major ionized species are $C_2F_4^+$ and CF^+. The individual compounds produced are summarized in Table VII-2.

Table VII-2

Reaction Products from the Glow Discharge Decomposition of PTFE (Data Are Reported as Mole Percent) (Ref. VII-12)

	He	He + O_2	O_2	O_2
O_2		0.31	0.22	0.85
CO		1.77	0.64	3.97
CF_4	0.37	1.23	0.97	1.96
C_2F_6	6.43	11.22	9.24	16.10
CO_2		3.32	5.99	12.10
C_2F_4	85.22	70.60	72.22	52.62
C_3F_8	2.08	4.62	5.10	5.39
C_3F_6	5.90	6.93	5.62	7.01

Column 1 gives the average mole fractions determined from six experiments in which only helium was used as the carrier gas. Good reproducibility was obtained. Columns 2, 3, and 4 give the yield data for experiments in which helium plus oxygen or just oxygen was used as the carrier gas.

The C_3F_6 compound found in this work was hexafluoropropene and not the cyclic hexafluoropropane which has been reported from thermal degradation studies.

The highest molecular weight gaseous product found was C_3F_8. No higher C_4 fluorocarbons were detected by either the vpc or mass spectrograph.

Brandkamp (Ref. VII-13) subjected Teflon to laser irradiation to determine if the extremely fast heating rate produced any unusual changes in the solid or solidified melt. He used a Q-switched ruby laser that emitted a 6943 Å pulse of $\sim 45 \times 10^{-9}$ sec duration with an average fluence of 3×10^8 w/cm^2. He observed char formation in small globules below the surface. These were tentatively attributed to localized heating at small, highly absorbant impurity points dispersed within the Teflon. He could find no evidence of surface char formation. To check further, he fired the laser through a glass plate located next to the Teflon surface. Microscopic examination of the plate revealed only translucent Teflon particles; there was no char on the plate. He also checked with E. I. duPont de Nemours & Company (May 21, 1969). They reported no knowledge of a Teflon char being observed or reported.

Allen (Ref. VII-9) suggested the particles might be carbon, produced according to:

$$C_2F_4 \xrightarrow[\sim 1500^\circ F]{\sim 750^\circ C} C + CF_4$$

whereas the more usual reactions are:

$$C_2F_4 \xrightarrow[\sim 1200^\circ C]{\sim 600^\circ C} C_2F_4 + C_3F_6 + \text{higher mol. wt. products and}$$

$$C_2F_4 \xrightarrow{< 621^\circ F} (C_2F_4)_n$$

where:

$n \approx 3 \times 10^6$.

Brown (Ref. VII-14) compared several materials on the basis of outgassing rate and showed Teflon to have the lowest value (others were polystyrol, plexiglas, pertinax, several Epoxy-828 materials, and Epoxy-815). The principal gases given off were reported to be N_2, CO, CO_2, and O_2. Outgassing rate was about 3×10^{-8} torr liter/sec-cm^2 after 20 or 30 hours. Clearly, there are no decomposition products at room temperature and only adsorbed, and perhaps absorbed, gases are evident.

There were no literature references concerning Teflon under the conditions expected in a Teflon thruster. In our conversations with duPont (Refs. VII-9 and 10), we found they had no knowledge of Teflon response under pulse heating conditions of the type we are studying. (In fact, we ended up giving them some information from references they were not aware of.) Allen (Ref. VII-9) felt most of the evaporation products would be monomer since this is what happened in most cases. He pointed out that the transition from the homopolymer to the monomer occurs at 621°F. He added that gas generation occurs at 1200°F. Bro (Ref. VII-10) pointed out that the degree to which each of the various chemical reactions would be satisfied depends on the conditions of pressure, temperature, and so forth. He felt that in a Teflon thruster we probably would see all of the constituents to various degrees. He expected that some carbon may be formed, but with proper geometries would be blown out of the thruster and never seen. He would expect deposits with improper geometries. He also would anticipate a waxy deposit of Teflon on any surfaces which are exposed to the beam because the monomer reacts upon such surfaces. He further felt that the CF_2 would be blown out of the thruster and never "seen" as such. Tetrafluorethylene may or may not come out of the thruster. The hexaflouropropylene may decompose and then go out the nozzle, or may be ejected prior to change. He felt the waxy deposits which might be formed would be very transparent to infrared radiation. There are absorption peaks at 4.24 microns, at about 8 microns, and at about 10.7 microns. We also were warned that in working with these materials, one should be very careful of the monomer. Given sufficient temperature and agitation, it can explode violently. In all probability, a sufficient concentration of monomer for our application never would be formed.

This background of material lends insight into some of the observations. Brandkamp (Ref. VII-13) observed char formation and deposition of Teflon particles on a glass plate. He did not explain either reaction, and indeed in the case of carbon attempted to find an explanation and could not. The equations we have obtained from several investigators clearly provide a process where carbon formation not only is possible, but appears probable. The expected quantities would be low. Since most investigators feel the major product of Teflon decomposition is a monomer, Brandkamp's observation of a translucent deposit on a glass plate immediately appears to be Teflon which has polymerized on the surface. Guman's (Ref. VII-4, as well as others) observations of a deposit on a mirror and on bell jar surfaces similarly is partially explained. Bro's comment on hydralyzation

immediately can explain a change in deposit appearance when a material that has been coated in a vacuum chamber is removed and exposed to the air.

Several conclusions immediately follow for the Teflon thruster. Anything placed in the exhaust beam probably will be coated with Teflon as well as with undetermined reaction products from the Teflon and undetermined gaseous materials which may have been either entrained or reacted with beam constituents. The beam, because of the free radicals (at least in the initial portion) will be highly reactive chemically near to the thruster. Further away (of the order of one or two feet), we suspect most of the reactive components have already reacted.

A second conclusion involves the behavior of a beam or portion of a beam impacting upon a surface. Our suspicion is that two processes occur. In one, major constituents recombine and polymerize on the surface, forming a relatively dense coating. In the other process, reflection from the surface occurs in probably a roughly specular manner. We would anticipate a diffuse reflection as being of minimum consequence because of the polymerization reactions which take place. Probably, if the molecule is going to stick for a moment or two, which would be required for diffuse reflection, then it will stay there for a long time because of the chemical behavior which results in a very low vapor pressure polymer being formed.

Finally, any deposit which forms upon a surface is going to remain there for practical purposes forever. No reasonable amount of heating, such as has been proposed for low temperature radiators, would remove the deposit. One would have to heat the surface above the depolymerization temperature of Teflon in order to clean it. As a consequence, we strongly recommend that low temperature radiators and Teflon thrusters be located so that the possibility of interaction is exceedingly small.

2.3 Chlorofluorocarbons

LaRocca (Ref. VII-15) has recorded a somewhat different propulsion scheme utilizing a so-called liquid Teflon. LaRocca refers to the fuel as a perfluorocarbon wax which, even as a solid, feeds by capillary action. According to his report, losses of this liquid-like material due to evaporation are very low. He reports values of 1 milligram per week for an area of 12.7 cm^2 at 10^{-6} millimeters mercury and 20°C. He also proposes covering vents in the fuel container with a porous liner so that a fraction of a torr pressure is maintained within the container. If such a scheme is required, one would suspect the effective outgassing rate could introduce a problem. We have not investigated this effect, but would recommend doing so if LaRocca's approach is followed.

He refers to a high thrust mode which might be used during acquisition or station change. In this case, the thruster barrel might reach the melting point of the wax (120 to 200°F). LaRocca states this would transform the wax to a viscous oil (1000 to 2000 centipoises) which has a very high surface tension. We would be concerned in this area about evaporation rate. Again, we have not investigated the effect.

LaRocca reports that these materials have high thermal stability and are chemically inert. He adds that chemically, they differ from Teflon because of the presence of the carbon-chlorine bond.

In testing with these materials, he refers to a deposit formation and states "while not as good as that observed with Teflon (zero deposit), was negligible." Since we know that Teflon, in a long term test, produces significant deposit upon surfaces directly in the beam, we may surmise that the "liquid Teflon" approach will cause more of a deposit problem.

We visited with LaRocca (Ref. VII-16) to obtain more recent information on the wax-like fuel. He referred us to several JPL contract reports given as references in his paper (Ref. VII-15). When questioned further, he described limited spectroscopic studies they have conducted of thruster exhaust plumes. Unfortunately, he felt the results were inconclusive, and concluded they know very little concerning the molecular and atomic components.

They have placed a target in the exhaust plume at a distance of several inches, and observed a sharp shadow-graph. The exhaust cone semi-angle was about 15°. About 98 to 99 percent of the condensable material appears to be included within the cone. (La-Rocca emphasized that these were rough semi-qualitative numbers. They do not have good quantitative information.) They have observed no condensate outside of this angle, but emphasized they have not conducted tests to hunt for it in a comprehensive manner. Further, they have not placed low temperature surfaces in the vicinity of the exhaust plume.

Extrapolation of limited test data to expected spacecraft conditions leads to a tentative conclusion that motor operation should not affect spacecraft potentials by more than a fraction of a volt.

The "wax-like" substance referred to in LaRocca's paper is a "halocarbon" produced by the Halocarbon Corporation. This is basically a carbon-hydrogen-fluorine compound with one included chlorine atom. The Halocarbon Corporation could not identify the specific material LaRocca was using (Ref. VII-17). (Their files indicated material sent to LaRocca, but did not permit identification.) In general, the halocarbons are polymers built up on a basic carbon-three fluorine-chlorine structure. Normal thermal decomposition occurs at about 300 to 400°C, with the polymer breaking down by carbon-carbon cleavage to volatile chlorofluorocarbons. At ordinary temperatures, no solids are formed, nor is there any carbon. As a result, there is no residue. If the product is mixed with fluorine and subjected to an electric spark, carbon and CF_4 can be formed. In this respect, the material behaves similarly to Teflon (our comment). One also can get a range of molecular weight polymers in the product, depending upon the intensity of the spark and its duration. The latter affects the time available for reaction.

Ehrenfield said he could envision a fine mist of wax being blown out of the vicinity of a spark under certain conditions. This apparently has not been observed by LaRocca, and indeed if it were, would be reason for a redesign. When questioned concerning molecular weight, Ehrenfield said the basic product was a mixture of various molecular weight chlorofluorocarbons. Other than the polymer, impurities are less than about one part per million. To his knowledge, quantitative determination of impurities had not been obtained. We asked about the vapor pressure. He identified one product by number (1425) which is a heavy oil. This has a vapor pressure of 5 microns at 140°F. Vapor pressures of the waxes are in the tenths to hundredths of a micron range.

LaRocca indicated that General Electric has done limited work with duPont with a Teflon-like material which was liquid under the proper conditions. If more information is required in this respect, we should follow up on Reference VII-18. Reference was also made to a powdered Teflon embedded in a suitable material to provide flow characteristics. Apparently, General Electric has done only limited work in this area.

2.4 Comparison of Teflon and Chlorofluorocarbon

In many respects, the exhaust plume behavior of the General Electric and Fairchild-Hiller concepts appears similar. Exhaust plume angles and quantitative distribution, based on preliminary information, appear similar. We know somewhat more about the solid Teflon, both the basic material and the thruster, than concerning the wax-like fuel.

Our suspicion is that the General Electric approach is somewhat more susceptible to contamination due to outgassing than is the Fairchild-Hiller approach. Application of the former would require additional work with the literature, with General Electric, and with the Halocarbon and duPont Companies (depending on the manufacturer of the material) to determine the characteristics required to prove an outgassing or evaporation problem would not exist.

3. EXHAUST PLUME CHARACTERISTICS

3.1 Overall Plume Behavior

At present, no one knows precisely how a Teflon thruster works, but the MIT Lincoln Laboratory is attempting to find out (Ref. VII-19). Although they have not been specifically searching for exhaust characteristics with respect to contamination effects, they have been studying the plume to learn how the thruster operates. Some of the material coming off is ionized and travels in straight lines at high velocities. When they place a target in the beam path, they find sharply defined shadows on the target. This is an indication of a free molecular flow regime with few, if any, interactions.

Guman (Ref. VII-2) reports similar shadow effects. He has repeatedly observed that an object placed in the exhaust beam will shade any region downstream. A slight diffraction pattern appears to be formed by the edges of the interspersed object on a downstream plane. He further comments that a true gaseous efflux would tend to expand around the interspersed object and fill any void spaces in the exhaust. This is characteristics of the behavior of a flux of particles as opposed to a gaseous cloud.

Similar behavior is reported by General Electric. LaRocca (Ref. VII-16) discussed placement of a target in the exhaust plume at a distance of several inches. He found a sharp shadowgraph. He reports an exhaust cone semi-angle of about 15 degrees, and he estimates between 98 and 99 percent of the condensable material to be within this cone. However, he cautions that this is a qualitative number, and does not represent reliable information. General Electric personnel have not observed neutral condensate outside of the 15° angle. Again, LaRocca cautioned us. They have not conducted extended tests in an attempt to find neutral condensate. Further, the limited tests they have conducted do not involve low temperature surfaces in the vicinity of the exhaust plume.

LaRocca also mentioned that General Electric has conducted only limited spectroscopic studies of Teflon thruster exhaust plumes. The results have been inconclusive. Basically, they know very little concerning the molecular, ionic, and atomic components.

Guman (Ref. VII-4) substantiated McClellan's and LaRocca's comments in regard to the LES-6 thruster work and Fairchild-Hiller Corporation experience. Their laboratory testing shows that most of the mass is ejected along the plume axis. Guman feels that the Prandtl-Meyer expansion characteristic can be assumed for the ejected mass for purposes of establishing an exhaust limit surface. He feels that instrumentation technology is not sufficiently advanced that we can determine behavior of Teflon thruster exhaust plumes. The entire thrusting event covers only microseconds, and there is not time for the instrumentation to react to the transient-spacial plume behavior. Limited observations have been conducted of light characteristics. These show about a ten to one difference between the highest velocities in the plume (the ions) and the mass averaged velocity that is obtained from specific impulse characteristics.

In effect, there is only limited information available which will describe a Teflon thruster exhaust plume. Consequently, we will only be able to estimate quantitative effects and characteristics. Nevertheless, these estimates should be sufficient to identify potential trouble areas and to indicate how they can be avoided.

3.2 Chemical Composition

The best information we have obtained which covers Teflon thruster exhaust composition was originated by the MIT Lincoln Laboratory. Vondra (Ref. VII-20) discussed a spectroscopic examination of Teflon thruster exhaust. Carbon, fluorine, and iron were identified. Both neutral and charged species have been observed. Specifically, they have found, in addition to unidentified molecular species, the materials: C, F, C^{+}, C^{++}, C^{+3}, F^{-}, F^{--}, F^{-3}, Fe, Fe^{+}, Fe^{++}. The iron is believed to originate from the stainless steel electrodes and from the spark plug. One would suspect that other stainless steel components also would be present. The amounts of iron and other components related to the stainless steel are small because electrode erosion is not a problem. Quantitative information has not been obtained, nor have all components been identified.

Murphy (Refs. VII-21 and VII-22) has conducted several analyses of exhaust deposits. Some of these data were obtained on Fairchild-Hiller furnished samples, whereas other information resulted from analysis of crud buildup in various vacuum chambers. Typical are results from bell jar testing. A brown coating was observed within bell jars that would peel off and deposit on the base. This coating, as were all such coatings, was removed from the vacuum and shipped to an independent concern for analyses. Unfortunately, this permits further reactions which may mask the original coating composition. We know that such reactions do occur. For example, Guman (Ref. VII-4) commented that when he used a mirror to observe the exhaust plume and placed the mirror in the plume, that it was coated by a deposit. When the mirror was removed from the vacuum chamber, the deposit color would change in about 20 to 25 minutes, and some of the deposit would flake off of the mirror. The reaction implications are obvious.

Murphy (Ref. VII-12) was careful to point out additional problems as well. In effect, he considers that the exhaust acts as an excellent gettering material. The deposit which results is a conglomerate of junk (for want of a better word) that is well tied up in the Teflon deposit. The exhaust plume is a very active reagent and the exhaust constituents appear to combine with anything which they contact close to the nozzle. With these introductory remarks, we will consider some of Murphy's results.

Reference VII-23 discusses analysis of a char sample obtained from Dr. Guman at Fairchild-Hiller (May 14, 1968). This resulted from a vacuum chamber run of about 8×10^6 cycles. Magnification (100X) showed regularly dispersed metal speckles (10-25 μ). Analysis showed:

	Percentage				
	Carbon	Fluorine	Nitrogen	Hydrogen	Ash
Initial Analytical Results	30.45	53.63	1.98	0.95	–
	31.30	51.27	3.68	0.50	–
	31.77	–	0.88	1.13	9.59
Average:	31.17	52.45	2.18	0.86	
Corrected Results	35	57	2.4	0.95	
Theoretical Results (Teflon)	24	76			
Char contains		57/76 × 100 = 75% Teflon origin			

In discussing results, Murphy indicated that the literature seemed to prefer the "breakdown products of Teflon to be multiples of CF_2 and C_2F_4. Free fluorine is unlikely because the average bond energy of the carbon (C) to fluorine (F) atom is quite high. A few of the average bond energies pertinent to this case are listed. Bear in mind that this energy is an average to break all the bonds of a particular structure.

Chemical Bond Energies (k cal/mole)

C-C	83.1	C-N	69.7
C-H	87.3	C-O	84.0
O-H	110.6	C-F	105
N-H	93.4	C-C1	78.5

"In our 'initial analytical results' we got 31.17 percent carbon, 52.45 percent fluorine, etc., based on a char that had a 10 percent inorganic residue ash. This was determined lastly. Therefore, this elemental analysis was based on a 90 percent organic char and we, therefore, can correct the 'initial analytical results' to 35 percent carbon and 57 percent fluorine. With a theoretical composition of Teflon (C_2F_4) as 24 percent carbon and 76 percent fluorine, then the Teflon residue is 75 percent. The fluorine only requires 19 percent of the 35 percent (remainder 16 percent) carbon found to satisfy its Teflon nature.

"The remaining 25 percent is probably from the back streaming of the organic diffusion pump oil. The nitrogen found is probably from the air when the vacuum is released. If it were from the epoxy polyamide, there should be an equal amount of hydrogen. Interestingly, if one takes 25 percent of a polyamide segment, one gets:

18.5 percent carbon	1.25 percent oxygen
2.7 percent hydrogen	2.7 percent nitrogen

This is almost what we have left over. The molecular weight minimum of an epoxy polyamide monomer is 1300. This has a fantastically low vapor pressure."

An emission spectroanalysis of the same sample was conducted. This yielded:

Iron, Silicon } Over 10 percent

Magnesium - faint trace
Molybdenum - faint trace
Aluminum - trace

Chromium - trace

Manganese - faint trace

Nickel - medium

The Fe, Cr, Ni, and Mn indicate erosion of the stainless steel (17-7 PH) electrode of the spark plug. In the absence of silicone oil, the Mikroy Grade 1100 glass mica insulation of the spark plug was suspected.

Murphy concluded that the char is principally from Teflon and the erosion products of the spark plug. The remainder of the carbon is from the back streaming of the diffusion pump oil.

In another report (Ref. VII-24) Murphy reports on a four foot diameter vacuum chamber test. This test, conducted during April 1968, involved a pre-prototype thruster

with its throat approximately two feet from the monopole of an antenna. Most of the resulting thin brown deposit which was formed was well bonded to an aluminum surface. However, on some shiny aluminum areas, light fluffy films of material had lifted and were readily removable. Murphy estimated the film thickness to be about 10,000 Å. Analysis of the film sample showed 53.31 percent carbon, 3.57 percent hydrogen, 1.41 percent nitrogen, and 14.59 percent fluorine. These results are quite different from the previously reported results. An additional spectrographic analysis showed about 0.1 percent by weight of silicone. Since the carbon to fluorine ratio of pure Teflon is 24 percent carbon to 76 percent fluorine, the data indicate that only about 20 percent of the deposit is Teflon. Murphy concluded that the contribution from the silicone diffusion pump oil was minimal since only 0.1 percent silicone was found. He then added that spark erosion from the porcelain insulator could have contributed to the silicone in addition. The remaining material appeared to have been captured by the thruster which acted like a vacuum cleaner toward the outgassing material.

Adherent material from the same test run was obtained by scraping and an indicating spectrum was obtained:

Absorption Wave Length, Microns	Comments
3.0	Amine groups - possibly from the hardener of the epoxy resin.
3.4	Methyl groups -Teflon has none.
5.75-6	Amide and carboxyl groups - typical organic structure missing in Teflon.
8-9	This is an intense region of absorption for Teflon also.

"There was no significant absorption at 4.2 μ. Teflon has one. Very crudely, therefore, my guesstimate is that our deposit on the ground plain antenna is only about 20-25 percent from Teflon and the rest from outgassing organic materials. Pure identification would probably be always difficult due to the variety of interpolymerizations possible from the free radicals of the ionized materials."

In another analysis (Ref. VII-25), a sample was obtained from Fairchild-Hiller following qualification engineering testing of the LES-6. The sample came from a mirror located about 24 inches from the nozzle. Slightly less than 850,000 pulses of the Teflon thruster were involved. Analysis showed 53.87 percent carbon, 1.16 percent hydrogen, 0.28 percent nitrogen and 31.29 percent fluorine. The apparent film Teflon content is about 41 percent.

Murphy indicates that the high carbon content may have resulted from polymerization of something else besides Teflon in the plasma jet. He suspects items such as a non-silicon diffusion pump oil and outgassed vapors from organic materials such as conformal coatings, pottings, or O-rings. Loss of free fluorine to the vacuum is considered unlikely because it is too reactive and has a high bond strength (C-F).

"We believe this deposit is extremely complex since we are unable to obtain any clear infra red spectrum from the deposit. We have tried both direct transmission through an IR transparent NaCl window as well as on an internal reflection Ge crystal. Normally, we can see the faintest deposit of any standard complicated organic compound.

"A qualitative emission spectroanalysis yielded the following:

Si major	Al
Ti	Mg
Cu	Vd
Fe	

These are probably from an eroding spark plug unless the mirror cited by F/H was a primary mirror or they scrapped the deposit vigorously and/or some SiO_2 was removed."

Another sample, collected from a Lucite substrate (no Si), gave the following mass spectrometer results:

Fluorine - major

Oxygen - major

Na, Si - 1-10 percent atomic

Fe, Cl = 0.1 - 1 percent

Ca, K = 0.3 - 3 percent

Cr, Zn, Al, Ni = 0.01 - 0.1 percent

Cu, Co = 0.001 - 0.01 percent

Oxygen as a major constituent is surprising. There are several possibilities:

(a) Poor vacuum

(b) Captured volatiles had a number of functional groups (epoxy , carbonyl- from most resins)

(c) The film reacted with oxygen on exposure to air

"None of these possibilities are convincing." Murphy concluded, as in the previous memos, "that this plasma phenomenon is "pulling" all nearby volatiles into its energy center and polymerizing an extremely complex, solid dark brown deposit."

Several conclusions regarding plume chemical composition appear reasonable:

(1) The plume consists of a large number of ionic and neutral species.

(2) The plume is composed of individual carbon and fluorine atoms, and probably about every imaginable combination of these atoms. Molecular weights range from those of the individual atoms (or ions) up to the molecular weight of individual Teflon polymer molecules.

(3) The plume is highly reactive near the nozzle.

(4) At distances reasonably far removed from the nozzle, the plume will contain, in addition, any other atoms or molecules which may have been "in the way."

(5) Plume contaminants originating from the thruster will consist of electrode materials, atoms and ions from any insulating ceramics, and any outgassing constituents originating within the thruster. These will all be minor. There will be virtually no contamination originating from the Teflon fuel.

3.3 Material Distribution in the Plume

Distribution of material within the Teflon thruster plume is relatively unknown. McCellan (Ref. VII-19) indicated that a few crude tests had been conducted. At this stage in the technology, the statement gives us a proper perspective for interpreting the remainder of this section.

McCellan mentioned that, as a result of their tests, they had found nothing which would indicate an angle with the plume centerline of anywhere near 180°. He felt that the maximum turning angle probably was less than 90°. He cautioned, however, that these conclusions were based upon analysis of room temperature targets. The Lincoln Laboratory is putting together a sophisticated vacuum system that will permit more accurate studies. This sytem will eliminate the oil back-diffusion problem that has been common to many of the previous studies. It will utilize a liquid nitrogen target, operating at 77°K, which should trap most of the material which initially sticks to it. This is an interesting selection because in the SMS we are considering a 70°K target.

On a quantitative basis, only preliminary numbers are available. Vondra (Ref. VII-20) indicates that the total included angle for most of the material is 20°. The ions may be represented by a Gaussian curve with a 1/e value at 13° from the symmetry line. Vondra feels that a very small flux at 180° might be reasonable. We did not discuss the possibility of how this would occur. In any event, MIT has measured at angles as far as 40° from the centerline and received positive electrical currents. (They detect via a Faraday cup to obtain the ion flux.) Vondra also emphasized that, although the Laboratory has built a neutral particle detector and is planning to study both neutral velocities and directions, they have not done this yet. They have not tried the instrument and, if it fails, they have several other ideas for investigating neutral behavior. This would postpone availability of further information.

Guman (Refs. VII-2 and 3) has reported on exhaust beam observations. In these observations, a calibrated RCA-1P42 vacuum photo tube and a high speed Tektronix voltage probe were used to examine luminous discharge and discharge voltage variation. The phototube was positioned to look along the thrust axis directly into the thruster nozzle. The voltage probe provided discharge voltage wave form. The thruster that was tested had been operated at the 22 micropound thrust level for an extensive time. The results showed that the capacitor (which powers the thruster) was discharged in about 2.2 microseconds. The plasma persisted for slightly over 10 microseconds with a peak light intensity at 1.45 microseconds. Obviously, the thruster generates extremely short plasma bursts. Photographs of the exhaust showed that the column of highest luminosity underwent only a minor expansion. It did not subsist for any great distance downstream of the thruster nozzle exhaust plane.

Vondra (Ref. VII-1) provides additional information on the thruster installed on the LES-6 satellite. He states that each current pulse ablates about 10^{-8} kilograms of Teflon (6×10^{16} molecules of C_2F_4). This is exhausted at an average velocity of 3000 m/sec. He also reports on Langmuir probe measurements of electron density and temperature, K- and microwave interferometer measurements of density and collision frequency, spectroscopic analysis of ion species, and results of Faraday cup measurement of ion velocity. Overall published conclusions are that the ion velocities are about 35,000 meters per second, from which one immediately finds that the gas is only partially ionized. The remaining neutral gas appears to be gas dynamically pushed off of the Teflon face.

The reported electron densities are reproduced in Figure VII-2. Estimated electron temperature an inch from the Teflon surface was about 20 ev (2×10^5 °K) at four microseconds after initial discharge. The authors are careful to point out that the accuracy is not as good as they would have liked. They also observed spectral lines of Ciii and Fiii.

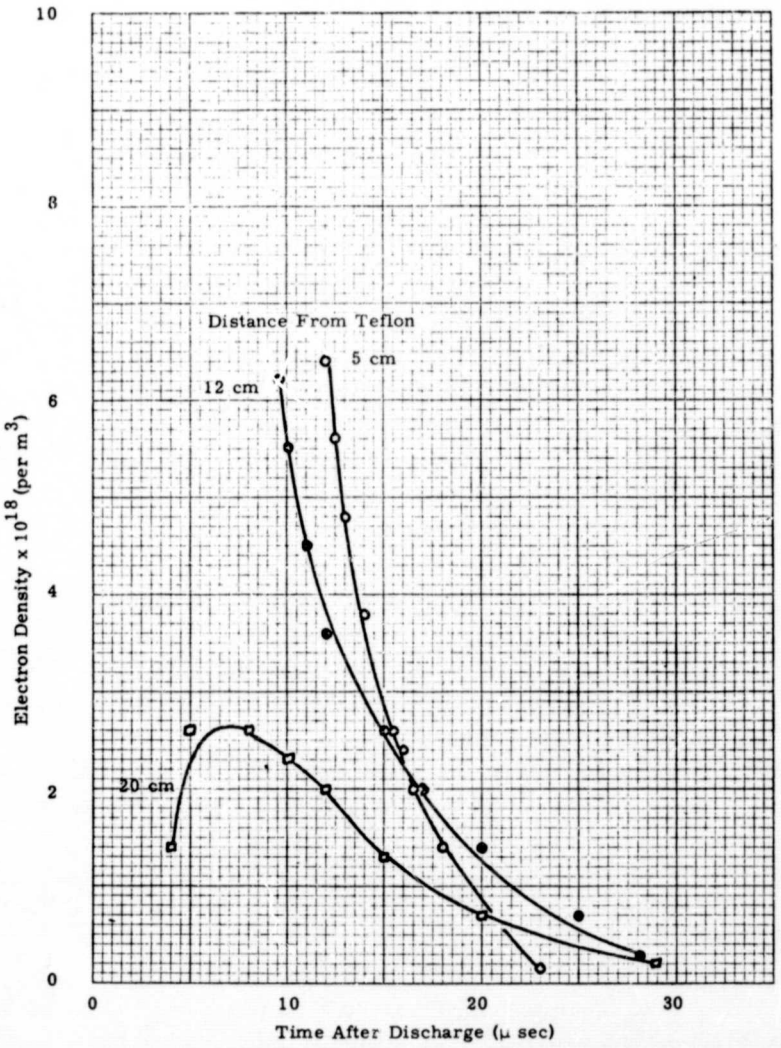

Figure VII-2. Electron Density (Approximate Reproduction From Ref. VII-1).

The authors conclude by stating that the data can be explained if one assumes 3/40 of the gas is ionized and accelerated during the current pulse, with the remaining neutrals oozing off the hot Teflon following that. The ions are considered to free stream away without any neutral collisions, while the neutrals that follow have negligible velocity because the neutral pressure is small. They point out, however, that it is also possible that all of the gas is ablated during the current pulse, but is only partially ionized. If this were the case, then neutral-ion collisions would be more likely. We cannot determine which situation exists until further experiments have been conducted on neutral behavior.

The authors also point out that some estimates are possible on neutral characteristics. They state there are 3.6×10^{17} neutrals per pulse, and they assume a neutral temperature of about 10,000 °K (one electron volt).

3.4 Ion Behavior

Vondra (Ref. VII-20) suggests representing the thruster ion distribution by a Gaussian curve with a 1/e value at 10°*. The equation for a Gaussian distribution is:

---

*He later suggested 13°. We will present the 10° results as an indication of behavior.

$$F(x) = e^{-x^2/2} \tag{VII-1}$$

where x is the independent variable. This may be written as:

$$F(\theta) = e^{-\beta^2\theta^2/2} \tag{VII-2}$$

where:

β = a parameter

θ = angle from the plume centerline, deg.

At 10°, $F(\theta) = 1/e$. Hence:

$$1/e = e^{-50\beta^2} \tag{VII-3}$$

$$\beta^2 = 1/50 \tag{VII-4}$$

and:

$$F(\theta) = e^{-\theta^2/100} \tag{VII-5}$$

The behavior of this function is shown in Figure VII-3 and Table VII-3.

Now consider the opening to the thruster as a mathematical point, P, and "look" a distance R from this point in all directions. All of the exhaust ions must pass through the surface of a sphere of radius R. Therefore, if N_0 is the number of ions produced per thruster pulse, then:

$$N_0 = \int_{\Phi=0}^{2\pi} \int_{\theta=0}^{180°} \alpha\, e^{-\theta^2/100}\, R^2 \sin\theta\, d\theta\, d\Phi \tag{VII-6}$$

where α is a normalizing factor. This becomes:

$$N_0 = 2\pi\alpha R^2 \int_{\theta=0}^{180°} e^{-\theta^2/100} \sin\theta\, d\theta \tag{VII-7}$$

Without the sin θ term, this is simply an error function. With it the function is not immediately recognizable. Therefore, we have plotted the function exp (- $\theta^2/100$) sin θ as a function of θ and obtained the area under the curve, which is 0.853 deg. Hence:

$$\alpha = \frac{N_0}{5.42\ R^2} \qquad \text{(VII-8)}$$

The ion flux is:

$$N = \alpha F(\theta) \qquad \text{(VII-9)}$$

where N is ions per unit area per pulse. Or:

$$\frac{N}{N_0} = \frac{e^{-\theta^2/100}}{5.42\ R^2} \qquad \text{(VII-10)}$$

This behavior is shown in Figure VII-4 and Table VII-4.

3.5 Neutral Behavior

In the previous section, we showed a highly preferential ion distribution, with very little spreading of the ion beam. (Recognize that this is based upon preliminary data and

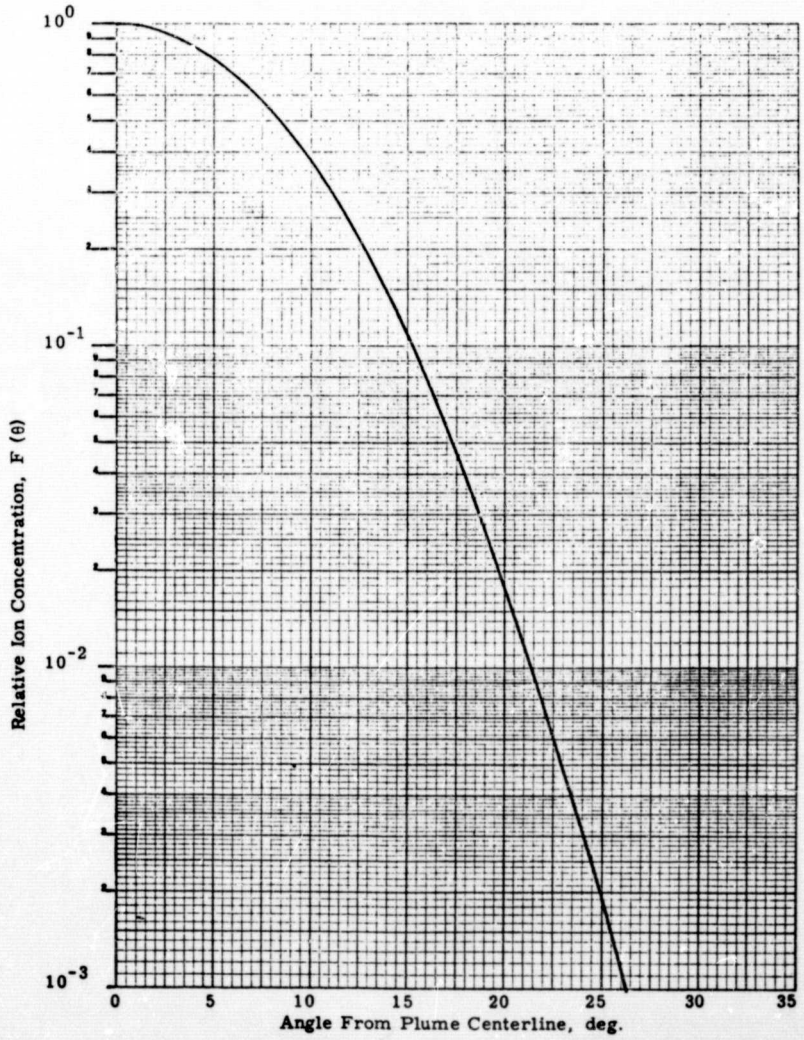

Figure VII-3. Relative Teflon Ion Concentration in the Exhaust Plume.

Table VII-3
Relative Teflon Ion Concentration in the Exhaust Plume

Angle From Plume Centerline, deg	Relative Ion Concentration
0	1
10	3.68×10^{-1}
20	1.83×10^{-2}
30	1.23×10^{-4}
40	1.13×10^{-7}
50	1.39×10^{-11}
60	2.32×10^{-16}
70	5.24×10^{-22}
80	1.60×10^{-28}
90	6.64×10^{-36}

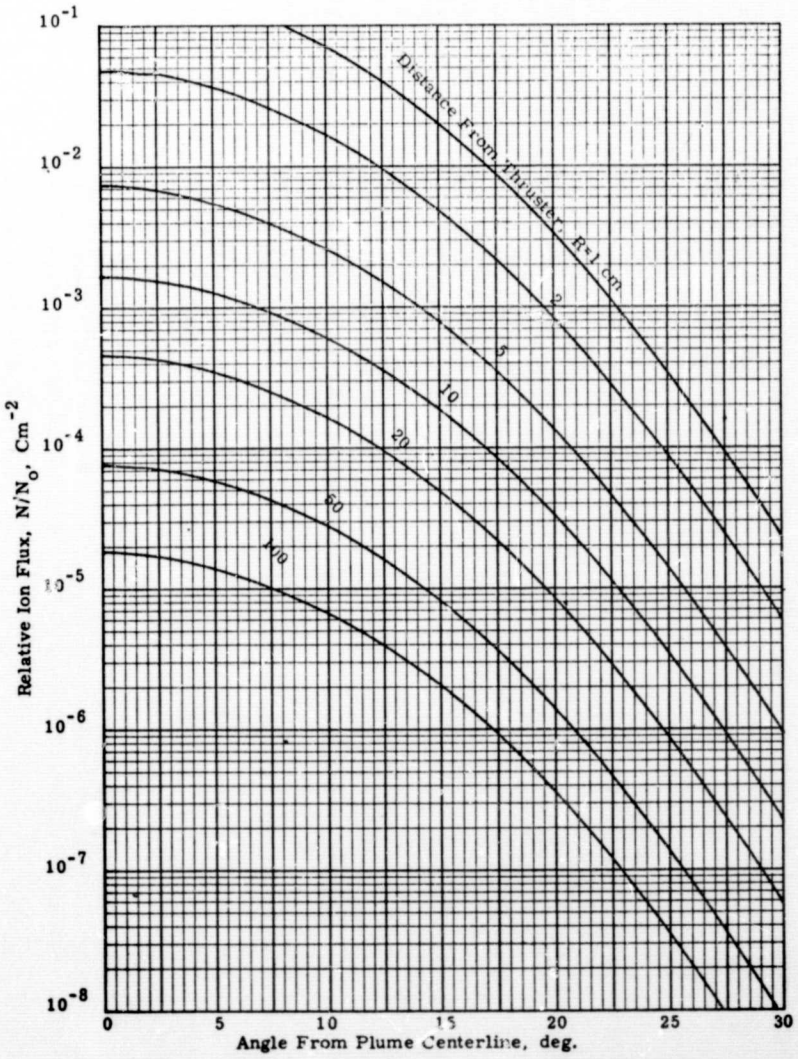

Figure VII-4. Relative Ion Flux, N/N_0.

an unpublished distribution function which was later modified.) If this distribution is correct, then we suspect there are few elastic ion-atom collisions. Such collisions would tend to spread the beam. This behavior supports the premise that the ions are discharged from the nozzle first, followed by the neutral atoms that are "oozing" off the Teflon surface. A later conversation (Ref. VII-6) adds further support to this behavior. Guman's experience has been that the high velocity particles appear within nanoseconds followed by slower and slower particles as time increases, with thermal energy particles appearing toward the end of the pulse. (Remember, the entire pulse is completed within microseconds.)

This behavior is very important. It renders charge exchange reactions unimportant since the daughters of the exchange will have the same properties as the parents. Thus, a mechanism that was an important effect for a cesium thruster becomes unimportant for a Teflon thruster.

Overall pulse characteristics are presented by Vondra (Ref. VII-1). The electron density measurements, as shown typically in Figure VII-2, indicate that the pulse event is over in less than about 30 microseconds as far as electrons are concerned.

Almost all tests of Teflon thrusters, regardless of conditions, have resulted in a propellant weight emission of between 10^{-7} and 10^{-8} pounds/pulse. (See Ref. VII-2 for tabulated data.) Flight prototype testing of the LES-6 thruster provided an impulse of 5.36 μlb sec/discharge with a specific impulse of 308 seconds (Ref. VII-3). The propellant used is $(5.36)(10^{-6})/308 = 1.74 \times 10^{-8}$ lbs/discharge. Vondra (Ref. VII-1), in a later report, presents a 312 second specific impulse and a 7 μlb sec total impulse. We will use the latter values since we also want to utilize some of his other data. The propellant for these conditions is $(7)(10^{-6})/312 = 2.24 \times 10^{-8}$ lbs/discharge (1.02×10^{-8} kg/discharge, consistent with Vondra's reported 10^{-8}).

If we assume the plume is characterized by C_2F_4 molecules (as assumed in Ref. VII-1), then the average molecular weight of the exhaust products is M = (2)(12) + (4)(19) = 100 gms/mole. The mass of a molecule immediately follows:

$$m = \frac{100 \text{ gms}}{\text{mole}} \quad \frac{\text{mole}}{6.02 \times 10^{23} \text{ molecules}}$$

$$= 1.66 \times 10^{-22} \text{ gms/molecule}$$

The number of molecules per pulse is:

$$N = \frac{2.24 \times 10^{-8} \text{ lbs}}{\text{pulse}} \quad \frac{454 \text{ gms}}{\text{lb}} \quad \frac{\text{molecule}}{1.66 \times 10^{-22} \text{ gms}}$$

$$= 6.11 \times 10^{16} \text{ molecules/pulse}$$

The effective exhaust velocity is:

$$v = I_{sp} g$$

Table VII-4
Relative Ion Flux, N/N_o

Angle θ, deg.	Distance From Thruster, R, Cm						
	1	2	5	10	20	50	100
	Relative Ion Flux*, N/N , Cm^{-2}						
0	(1)1.84	(2)4.60	(3)7.36	(3)1.84	(4)4.60	(5)7.36	(5)1.84
2.5	(1)1.73	(2)4.32	(3)6.92	(3)1.73	(4)4.32	(5)6.92	(5)1.73
5	(1)1.44	(2)3.60	(3)5.76	(3)1.44	(4)3.60	(5)5.76	(5)1.44
10	(2)6.92	(2)1.73	(3)2.77	(4)6.92	(4)1.73	(5)2.77	(6)6.92
15	(2)1.99	(3)4.98	(4)7.96	(4)1.99	(5)4.98	(6)7.96	(6)1.99
20	(3)3.27	(4)8.18	(4)1.31	(5)3.27	(6)8.18	(6)1.31	(7)3.27
25	(4)3.51	(5)8.78	(5)1.40	(6)3.51	(7)8.78	(7)1.40	(8)3.51
30	(5)2.27	(6)5.68	(7)9.08	(7)2.27	(8)5.68	(9)9.08	(9)2.27
40	(8)2.08	(9)5.20	(10)8.32	(10)2.08	(10)5.20	(12)8.32	(12)2.08
50	(12)2.56	(13)6.40	(13)1.02	(14)2.56	(15)6.40	(15)1.02	(16)2.56
60	(17)4.28	(17)1.07	(18)1.71	(19)4.28	(19)1.07	(20)1.71	(21)4.28
70	(23)9.67	(23)2.42	(24)3.87	(25)9.67	(25)2.42	(26)3.87	(27)9.67
80	(29)2.95	(30)7.38	(30)1.18	(31)2.95	(32)7.38	(32)1.18	(33)2.95
90	(36)1.23	(37)3.08	(38)4.92	(38)1.23	(39)3.08	(40)4.92	(40)1.23

*( ) indicates negative value of 10; 3 means $\times 10^{-3}$.

where:

I_{sp} = specific impulse

g = acceleration of gravity

Hence:

$$v = (312 \text{ sec})\ (980 \text{ cm/sec}^2)$$

$$= 3.06 \times 10^5 \text{ cm/sec}$$

The mean velocity is (Ref. VII-27):

$$\bar{v} = \sqrt{\frac{8kT}{\pi m}}$$

where:

k = Boltzmann constant

$= 1.38 \times 10^{-16}$ erg/°K molecule

T = temperature, °K

This can be rewritten as:

$$T = \frac{\pi m\, v^2}{8k}$$

so that:

$$T = \frac{(\pi)\ (1.66)\ (10^{-22})\ (3.06)^2\ (10^{10})}{(8)\ (1.38)\ (10^{-16})} = 44{,}200°K$$

which is the mean temperature of all of the material.

Vondra (Ref. VII-1) reports ion velocities of 35,000 m/sec (3.5×10^6 cm/sec), a decade higher than the previously calculated mean velocity. He also has determined typical electron temperatures to be about 20 ev (2×10^5 °K) an inch from the surface at 4 μ sec. (He carefully points out that the "accuracy of our results is not as good as we would like. . ."). These data are inconsistent with using one mean temperature to represent all of the material.

Vondra assumed 3/40 of the gas was ionized and accelerated during the current pulse and the remaining neutrals came off the hot Teflon after the pulse. Following this statement, we note that gas formation occurs at 850°C (1123°K), under normal heating conditions. The mean velocity corresponding to this temperature is:

$$\bar{v} = \left[\frac{(8)\ (1.38)\ (10^{-16})\ (1123)}{(\pi)\ (1.66)\ (10^{-22})}\right]^{1/2} = 44{,}700 \text{ cm/sec}$$

The mass released per pulse is:

$$m = m_i + m_u$$

where:

m = mass per pulse

m_i = mass ionized per pulse

m_u = mass un-ionized per pulse

A momentum balance provides:

$$m\,\overline{v} = m_i\,\overline{v_i} + m_u\,\overline{v_u}$$

Substituting for m_u:

$$\frac{m_i}{m} = \frac{\overline{v} - \overline{v}_u}{\overline{v}_i - \overline{v}_u} = \frac{(3.06)\,(10^5) - (4.47)\,(10^4)}{(3.5)\,(10^6) - (4.47)\,(10^4)} = 0.0756$$

which is in close agreement with Vondra's 3/40 (=0.0750). Substituting into the mass balance equation provides:

$$m = 0.0756\,m + m_u$$

Since:

$m = 1.02 \times 10^{-8}$ kg/discharge:

$m_i = (0.0756)\,(1.02)\,(10^{-8})$

$= 7.71 \times 10^{-10}$ kg/discharge

$m_u = 1.02 \times 10^{-8} - 0.08 \times 10^{-8}$

$= 9.4 \times 10^{-9}$ kg/discharge

Conversion of these masses to number of atoms and neutrals is a problem. The number of molecules per pulse on a C_2F_4 basis is 6.11×10^{16}. But this is not necessarily a real number. Vondra, in Reference VII-1, also reported 3.6×10^{17} neutrals, obtained by assuming everything was broken down to atomic species (Ref. VII-28). Our numbers provide:

$(6.11)\,(10^{16})\,(6)\,(1 - 0.0756) = 3.39 \times 10^{17}$ neutral atoms/pulse.

The spectral analyses show about half the exhaust to be single atoms or ionized single atoms. The remainder could be molecular. However, about one fourth has not been identified (Ref. VII-28). We conclude the following:

(1) About 7-1/2 percent of the exhaust is ionized.

(2) Roughly 3×10^{16} ions per pulse are produced.

(3) Most of the thrust is due to the ionic species.

(4) About 10^{17} to 3×10^{17} neutrals per pulse are produced.

(5) Neutral velocities probably are in the temperature range from ~850°C (Teflon outgassing temperature) to 10,000°K (a rough guess used in Ref. VII-1).

Now we are in a position to approximate the exhaust plume behavior with respect to neutrals. Somewhat arbitrarily, we will assume 2×10^{17} neutrals per pulse. Taking Vondra's guess of 10,000°K and one cubic centimeter (Ref. VII-1), the pressure at the Teflon surface becomes:

$$(1 \text{ atm}) \left(\frac{10{,}000}{273}\right)\left(\frac{2 \times 10^{17}}{6.02 \times 10^{23}}\right)\left(\frac{22{,}400}{1}\right) = 0.272 \text{ atm}$$

provided an ideal gas representation is correct. At 1123°K, the pressure would be:

$$(0.272) \left(\frac{1123}{10{,}000}\right) = 0.0306 \text{ atm}$$

We will use a pressure of 0.2 atm for estimation purposes. The effective temperature is (0.2/0.272) (10,000) = 7350°K.

According to a simple model of the kinetic behavior of gases, the specific heat ratio is (Ref. VII-29):

$$\gamma = \frac{n + 2}{n}$$

where:

n = number of degrees of freedom of the molecule.

Therefore, for a single atom, k = 3/2. The velocity of sound for an ideal gas is given by (Ref. VII-29):

$$u^* = \sqrt{\frac{2\gamma R T_0}{(\gamma + 1) M}}$$

where:

R = gas constant

M = molecular weight

T_0 = chamber temperature

The average molecular weight is:

$$M = \frac{(2)(12) + (4)(19)}{2 + 4} = 16.7$$

if the material is all atomic in nature. If it is about 1/3 C_2F_4 and the remainder atomic, then:

$$M = (2/3)\ (16.7) + (1/3)\ (100) = 44$$

Using this guess, the sonic velocity becomes (we've modified γ to account for about 2/3 atomic, 1/3 molecular):

$$c = \left[\frac{(2)\ (1.3)\ (1544)\ (7350)\ (1.8)\ (32.2)}{(2.3)\ (44)}\right]^{1/2} = 4100 \text{ ft/sec}$$

The LES-6 nozzle dimensions are 0.4 in × 1-1/8 inches, which gives a flow area of 0.450 in^2 (Ref. VII-26).

The flow rate through an opening of this size is:

$$\left(\frac{4100 \text{ ft}}{\text{sec}}\right)\ (0.450 \text{ in}^2)\ \left(\frac{12 \text{ in}}{\text{ft}}\right) = 22{,}200 \text{ in}^3/\text{sec}$$

$$\equiv 3.66 \times 10^5 \text{ cm}^3/\text{sec}$$

We are assuming about 2×10^{17} neutrals in one pulse. These occupy a volume of:

$$(2 \times 10^{17}) \left(\frac{22{,}400}{6.02 \times 10^{23}}\right) \left(\frac{1}{0.2}\right) \left(\frac{7350}{273}\right) = 1.0 \text{ cm}^3$$

(An interesting coincidence – this is precisely the volume of Vondra assumed.)

The time required for the passage of this volume is:

$$t = 1.0/3.66 \times 10^5 = 3 \times 10^{-6} \text{ sec}$$

This is in the ball park of the time we would expect to find. In reality, the material coming off later in the pulse probably will be cooler, resulting in a longer time for all of the exhaust to pass through the opening.

Now we may approximate exhausting into a vacuum. We first postulate that we may use the Prandtl-Meyer expansion characteristics to compute an exhaust limit surface (as suggested by Guman, Ref. VII-4). But, in using this approach, we must recognize that the Prandtl-Meyer expansion is limited to a perfect gas expanding under steady state conditions.

Shapiro (Ref. VII-29) states that the maximum turning angle for Prandtl-Meyer type flow is 130.5° when expanding from Mach one at the exit to zero pressure. (We will assume the nozzle is relatively ineffective as an expander and that supersonic flow is not obtained.) The area on a sphere with the origin at the nozzle exit that is affected by the exhaust is:

$$A = 2\pi rh$$

where:

r = sphere radius

h = height of spherical segment

This geometry may be represented by:

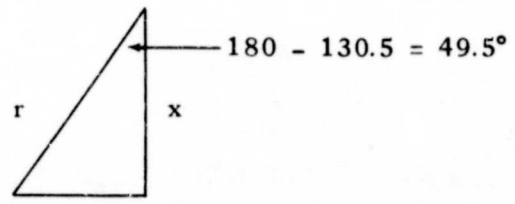

where:

$$h = 2r - x$$

Since x = r Cos (49.5°), × = 0.650 r, and we immediately find h = 1.350 r, A = (2) (π) (1.350) r^2 = 8.48 r^2.

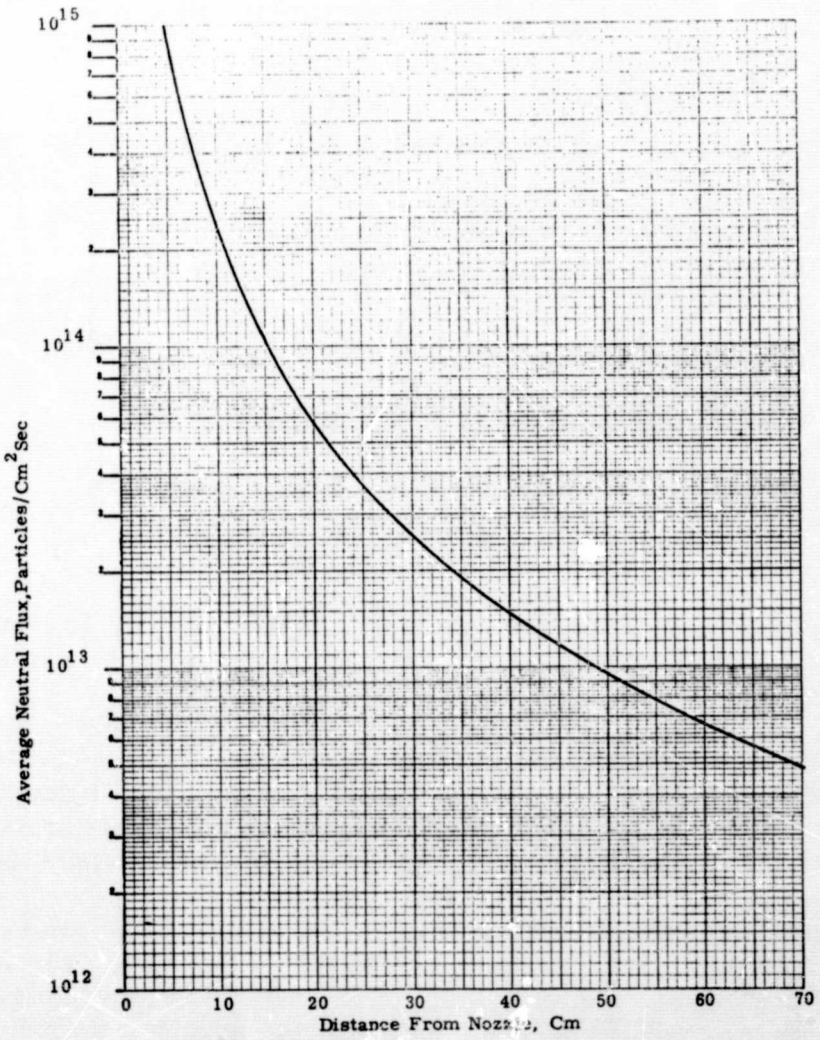

Figure VII-5. Average Neutral Flux.

Since we know the number of neutral molecules per pulse to be $\sim 2 \times 10^{17}$, we now may compute the average surface interception rate. This behavior is shown in Figure VII-5.

The fuel utilization rate is 10^{-5} gm/pulse or 10 gms/10^6 pulses. If the deposit is assumed to have Teflon's density, the volume is 10/2.29 = 4.37 cm^3 per million pulses. If all of this material is deposited, the build up is as shown in Figure VII-6. In referring to this curve, please remember it is based largely upon conjecture. It is intended only for scoping purposes and could easily be a decade or two (a factor of 10^1 or 10^2) in error.

3.6 Observed Behavior From Long Term Tests

We had the opportunity to observe several test chambers and thrusters at Fairchild-Hiller on March 31, 1970. Several of these observations lend additional insight into deposit behavior.

One thruster similar in size to the one which would be used for the SMS spacecraft is being life tested. After pulsing for the equivalent of about seven years use on SMS, a deposit buildup in the chamber is visible. A mirror, turned at roughly 45° to the plume, is used for observation. By looking in a side window of the vacuum chamber, one can

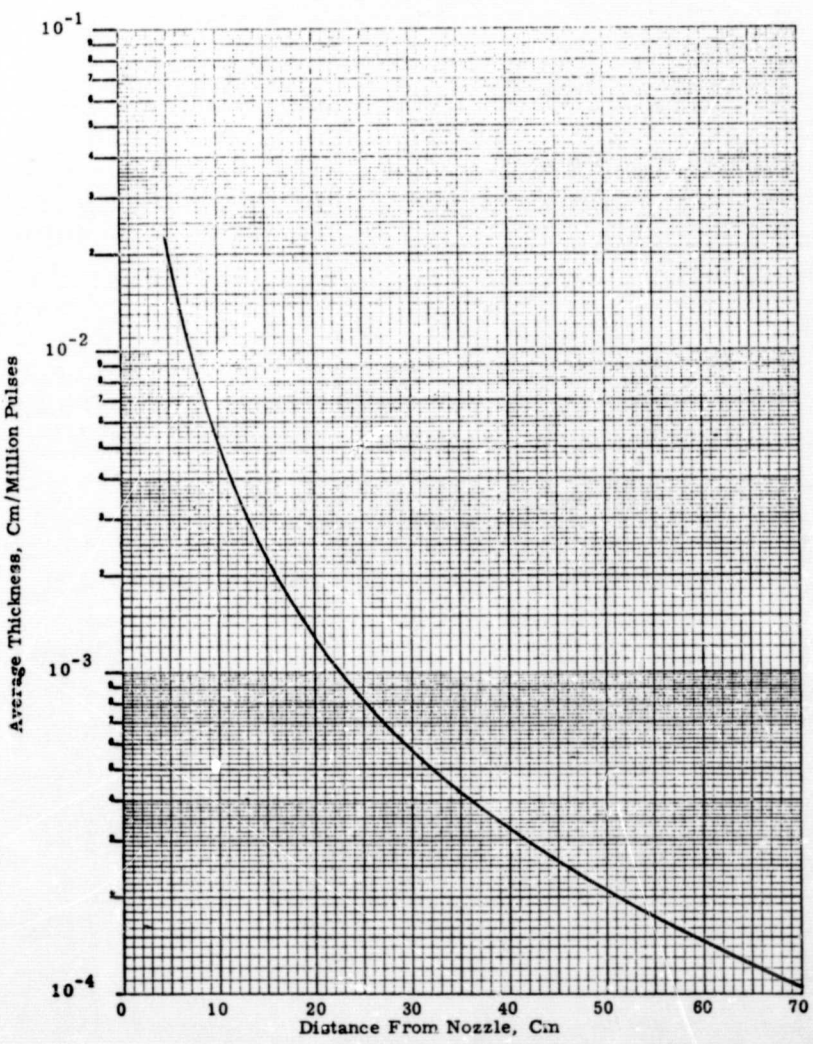

Figure VII-6. Neutral Build-Up Rate if All Emitted Neutrals Stick to a Surface.

look directly at the Teflon surface of the thruster. A visible deposit has been accumulated on the mirror, but it is not sufficient to significantly degrade the thruster appearance as seen by the casual observer. If past experience may be applied, the mirror surface will not have been degraded. According to Guman (Ref. VII-30) the mirror could probably be cleaned very simply. In the past, they have merely let the mirror be exposed to air for a half hour or so, after which most of the deposit flaked off. Simple cleaning with soap and water then would restore the mirror surface so that it could be reused.

Of significant interest is the behavior of the viewing windows. Several of these are located in the vacuum chamber so that the plume can be observed from the sides. One is located at about the nozzle exit plane, and another at about the plane of the viewing mirror. Neither of these windows appears to have a significant deposit (although they are not clean). Personnel conducting the tests could not recall when the windows had last been cleaned, and some of the "dirt" could have been there at the start of the test. In any event, clearly there has not been a large quantity of exhaust products deposited on the windows. To the casual observer, specular reflection with subsequent sticking of exhaust material does not appear significant. If this were the case, the viewing windows in the chamber probably would not be clean.

These tentative conclusions are based upon space chamber observations. The pressure in the chamber is significantly higher than will be the case in space. There exists the possibility that plume interactions with material in the chamber will change the plume characteristics. Thus, what may bounce off and eventually be pumped out of the system under test conditions may stick under space conditions. Further, sticking characteristics change with time. A clean surface can be expected to behave quite differently than one which has accumulated a significant deposit. A deposit consisting of trash which has been entrained by the exhaust beam during laboratory testing may be quite different in its behavior than a more pure deposit which might be obtained under space operation conditions.

Another interesting feature of the exhaust characteristics was observed. In testing in a bell jar, a deposit was initially formed, but then appeared to be eroded away (or otherwise removed) toward the center of the beam. We will not attempt to explain the reasons for this behavior.

4. REFERENCES

VII-1. Vondra, Robert, Keith Thomassen, and Albert Solbes, "Analysis of Solid Teflon Pulsed Plasma Thruster," AIAA Paper No. 70-179, AIAA 8th Aerospace Sciences Meeting, New York, New York, January 19-21, 1970.

VII-2. Guman, William J., "Pulsed Plasma Technology In Microthrusters," AFAPL-TR-68-132, Fairchild-Hiller Corporation, November 1968.

VII-3. Guman, William J. and David M. Nathanson, "Pulsed Plasma Microthruster Propulsion System for Synchronous Orbit Satellite," AIAA Paper No. 69-298, AIAA 7th Electric Propulsion Conference, Williamsburg, Virginia, March 3-5, 1969.

VII-4. Guman, Dr. William J., Personal Communication, Fairchild-Hiller Corporation, Farmingdale, New York, March 31, 1970.

VII-5. Park, Joseph D., "Recent Advances in Organic Fluorine Chemistry," Chapter IX of Ref. VII-6.

VII-6. Arm, David L. (editor), Vistas in Science, Thirteenth IFSOR Science Seminar, AD679198 (no date, received by DDC on December 17, 1968).

VII-7. Rudner, Merritt Allen, Fluorocarbons, Reinhold, 1958.

VII-8. Sperati, C. A., and H. W. Starkweather, Jr., "Fluorine-Containing Polymers. II. Polytetrafluorethylene," Advances in Polymer Science, 1961, pp. 465-495.

VII-9. duPont de Nemours, E. I. & Co., Personal Communication, David Allen (Washington, D.C. office) and Mr. Jordan (Baltimore, Maryland office), March 3, 1970.

VII-10. Bro, Dr. M. I., Personal Communication, E. I. duPont de Nemours & Co., Wilmington, Delaware (302-774-8364), March 4, 1970.

VII-11. Settlage, P. H., and J. C. Siegle, "Behavior of 'Teflon' Fluorocarbon Resins at Elevated Temperatures," Planetary and Space Science, 3, 1961, pp. 73-81.

VII-12. Mathias, Eckart, and Glenn H. Miller, "The Decomposition of Polytetrafluorethylene in a Glow Discharge," Journal of Physical Chemistry, Vol. 71, No. 8, July 1967, pp. 2671-2675.

VII-13. Brandkamp, W., A. DeCecco, and J. Hanson, "Laser-Induced Teflon Char," Journal of Spacecraft, Vol. 6, No. 9, September 1969, pp. 1087-1088.

VII-14. Brown, R. D., "Outgassing of Epoxy Resins in Vacuum," Vol. 17, No. 9 (date not given in reproduced paper; probably 1967).

VII-15. LaRocca, A. V., and G. S. Perkins, "Pulsed Plasma Micro-thruster Applications and Techniques," AIAA Paper No. 68-554, 4th Propulsion Joint Specialist Conference, Cleveland, Ohio, June 10-14, 1968.

VII-16. LaRocca, A. V., Personal Communication, General Electric Co., Valley Forge, Pennsylvania, 823-2287, March 4, 1970.

VII-17. Ehrenfield, Personal Communication, Halocarbon Corp., Hackensack, New Jersey, 201-343-8703, March 4, 1970.

VII-18. Lawson, E. I. duPont de Nemours & Co., Wilmington, Delaware, 302-774-5721.

VII-19. McClellan, Donald, Personal Communication, MIT Lincoln Laboratory, Cambridge, Massachusetts (Telephone No. 617-862-5500), March 5, 1970.

VII-20. Vondra, Dr. Robert, Personal Communication, MIT Lincoln Laboratory, Cambridge, Massachusetts, (Telephone No. 617-862-5500, ext. 7241), March 5 and 30, 1970.

VII-21. Murphy, Edward B., Personal Communication, MIT Lincoln Laboratory, Cambridge, Massachusetts, (Telephone No. 617-862-5500, ext. 5515 or 7745), March 5, 1970.

VII-22. Nathanson, David M., Personal Communication, MIT Lincoln Laboratory, Cambridge, Massachusetts (Telephone No. 617-862-5500, ext. 7241), March 5, 1970.

VII-23. Murphy, E. B., "Analysis of Char From Teflon Arc Thruster," Materials and Processing Memo #4E, MIT Lincoln Laboratory, June 6, 1968.

VII-24. Murphy, E. B., "RFI Teflon Vacuum Arc Thruster Vs. Ground Plain Antenna," MIT Lincoln Laboratory Memo, August 5, 1968.

VII-25. Murphy, Ed., "VAT Deposit-Fairchild Hiller Sample (Memo #4G)," MIT Lincoln Laboratory Memo, May 1, 1969.

VII-26. Guman, Dr. William J., March 24, 1970 (see Ref. VII-4).

VII-27. Lee, John F., Francis W. Sears, and Donald L. Turcotte, Statistical Thermodynamics, Addison-Wesley, 1963.

VII-28. Vondra, Dr. Robert, March 30, 1970 (see Ref. VII-20).

VII-29. Shapiro, Ascher H., The Dynamics and Thermodynamics of Compressible Fluid Flow, Ronald Press, 1953.

VII-30. Guman, Dr. William J., March 31, 1970 (see Ref. VII-4).

APPENDIX VIII

HYDRAZINE THRUSTER BACKGROUND

1. INTRODUCTION

For purposes of this study we have assumed a thruster based upon the catalytic decomposition of hydrazine. The catalyst used is Shell 405. This consists of an alumina vehicle containing iridium, the active ingredient. Cold hydrazine, under pressure, is forced through an injector within the thruster into the catalyst bed. This passes through the bed, decomposing during passage, and passes into a nozzle. Upon leaving the nozzle, it is ejected to space.

In a cold catalyst bed (approximately 70° F), hydrazine will begin to decompose in 10 to 100 milli-seconds. The reaction is strongly exothermic and will rapidly heat the bed, resulting in a rapidly increasing decomposition rate. The initial thruster effluent may contain a small portion of hydrazine, but for practical purposes after roughly 0.1 seconds no further hydrazine will be seen. Decomposition is complete, and the principle products of the catalytic decomposition are hydrogen and nitrogen. In the catalytic bed, a portion of these products will then undergo an endothermic reaction from ammonia. Once these three constituents leave the catalytic bed, the composition is chemically frozen.

Shell 405 catalyst loss has been discussed in the literature. Loss rates between 10 percent per minute and 0.05 percent per minute have been reported. Particle sizes have ranged between 1 and 500 microns. Hence, added to the hydrogen, nitrogen, and ammonia in the exhaust will be catalyst particles. These will be composed of an alumina vehicle containing iridium metal.

2. HYDRAZINE PROPERTIES

2.1 General

Hydrazine is a clear, oily liquid at room temperature with an ammonia-like odor. It boils at 236° F and melts at close to the freezing point of water. Vapor pressure and compatibility have been discussed in Appendix II.4.4 and II.6.3.

2.2 Purity

Hydrazine normally is purchased according to the specifications given in Table VIII-1. This is not particularly informative since the impurities are not specified and it is, in part, the impurities that could cause trouble.

Salvinski (Ref. VIII-2) has reported the analysis of propellant grade N_2H_4. In a sample taken from a test run (the previous handling was not documented) he found:

N_2H_4	98.8%
H_2O	0.5%
NH_3 + amines	0.7%
Density at 25° C	1.006 gm/ml
Particulate	0.5 mg/l
Non-volatile residue	5.0 mg/l

Table VIII-1
N_2H_4 Specifications (Ref. VIII-1)

Particulate Content	≤ 10.0 mg/l
N_2H_4 Assay	≥ 97.5% by wt.
Water soluble impurities	≤ 2.5% by wt.
Density @ 77°F	≤ 1.006 gm/cm^3
	≥ 1.002 gm/cm^3
Color when examined visually by transmitted light	colorless, homogeneous liquid

The following particle size distribution information was recorded:

Particle size, microns	No. of Particles/100 ml
10-25	201
25-50	52
50-75	10
75-100	0
100-250	3
>250	2

Dissolved metals were:

Item	ppm
Ni	nil
Cu	nil
Zn	2
Fe	2
Al	≤ 60 (min. det.)

The analysis of a "reference sample" (not otherwise identified) is presented in Table VIII-2.

2.3 Hydrazine Chemistry

Eberstein (Ref. VIII-3) reported that in high temperature gas phase reactions or in surface reactions, hydrazine was likely to be in the form:

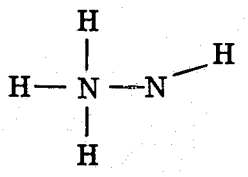

The initial step in decomposition of this form probably is:

$$N_2H_4 \longrightarrow NH_3 + :NH$$

At low temperatures and high hydrazine concentrations association is likely. Then the reaction:

$$(N_2H_4)_2 \longrightarrow N_2H_4 + 2NH_3$$

$$\downarrow$$

$$N_2 + H_2 + 2NH_3$$

may be postulated. Similar behavior may occur on a metal surface. In the presence of platinum black, the reaction proceeds according to:

$$2N_2H_4 \longrightarrow 2NH_3 + N_2 + H_2$$

Table VIII-2
N_2H_4 Reference Sample Analysis (Ref. VIII-2)

Item	Result
% N_2H_4	98.7%*
H_2O plus soluble impurities	0.4
Density at 77°F	1.006
Particulate	1.0 mg/l
NH_3 plus amines	0.9%*
Dissolved metals (ppm)	
Iron	3.5
Aluminum	≤20**
Nickel	4
Manganese	≤ 0.5**
Cobalt	≤ 2.0**
Chromium	≤ 1.0**
Copper	3
Zinc	3
Dissolved anions (ppm)	
Chloride	2.0
Sulfate	≤ 5**
Nitrate	***
Non-volatile residue	42 mg/l

*w/w
**Detection limit
***Could not be determined because of interference with an unknown contaminant.

In the presence of Raney nickel, a greater volume is obtained than indicated by this equation. Increasing the catalyst quantity increases the gas volume, until the volume approaches that required for the reaction:

$$3N_2H_4 \longrightarrow 2NH_3 + 2N_2 + 3H_2$$

Probably, in this reaction the molecule is broken up on the metal surface and then reacts to form products. In the gas phase or on a metal surface, it may decompose by simple N - N bond rupture:

$$N_2H_4 \longrightarrow 2NH_2$$

On a silica surface, the following reactions have been proposed:

$$3N_2H_4 \longrightarrow N_2 + 4NH_3$$

$$2N_2H_4 \longrightarrow H_2 + N_2 + 2NH_3$$

This is not postulated as proceeding by a free radical mechanism. Eberstein concludes that decomposition on silica appears to involve the dissociation of hydrazine molecules on the surface, whereas decomposition on metal surfaces appears to proceed by donations of electrons from N atoms in hydrazine to a partially filled d band in the metal. This is followed by rupture of the N-N bond and further surface reactions.*

Lucien (Ref. VIII-5) has studied N_2H_4 decomposition rates. He reported rates between 10^{-4} and 2 percent per hour, depending upon reaction conditions. Decompositions were characterized by an initial linear rate followed by an increased constant rate. Both rates varied with the initial NH_3 concentration, with pressure, and with temperature. Decomposition rate also is affected by presence of certain surfaces (especially metals and salts), pH, oxygen, and carbon dioxide. Ammonia retarded the decomposition rate, as one would expect from the reaction equations (but not to the degree found). The effect was greatest with NH_3 concentrations less than 2 percent. The additional effect was small at greater concentrations. Pressure retards decomposition and, of course, temperature enhances it. Rate varies from 10^{-4} %/hr. at 175°C to 1%/hr. at 250°C at ~ 400 lbs./in.^{2}.

The reported reactions are:

$$3N_2H_4 \longrightarrow 4NH_3 + N_2$$

Small quantities of H_2 are formed, probably by:

$$2NH_3 \longrightarrow N_2 + 3H_2$$

$$N_2H_4 \longrightarrow N_2 + 2H_2$$

*Eberstein mentions that Fresenius (Ref. VIII-4) has conducted spectroscopic studies of hydrazine. Any effort in this area may find the reference a useful one.

None of these species should cause troubles in the exhaust. Eberstein (Ref. VIII-6) reports the overall reaction order to be close to unity. The behavior for decomposition in a three inch duct (vapor phase) is given as:*

$$k = A\, e^{-E/RT}$$

where:

k = Arrhenius rate constant

A = Preexponential factor

= $10^{10.33}$ sec^{-1}

E = Activation energy

= 36.2 kcal/mole

R = Gas constant

T = Temperature

Table VIII-3
N_2H_4 Decomposition (Ref. VIII-6)

Reaction Type	Reaction	A cm^3/mole sec	E cal/mole
Initiation	$x + N_2H_4 \longrightarrow x + 2NH_2$	10^{19}	60,000
Propagation	$N_2H_4 + NH_2 \longrightarrow N_2H_3 + NH_3$	10^{13}	7,000
	$N_2H_3 + x \longrightarrow N_2 + H_2 + H + x$	10^{13}	20,000
	$H + N_2H_4 \longrightarrow NH_3 + NH_2$	10^{13}	7,000
Branching	$N_2H_3 + x \longrightarrow NH + NH_2 + x$	$10^{12.8}$	18,000
	$N_2H_4 + NH \longrightarrow NH_2 + N_2H_3$	10^{14}	10,000
Termination	$NH_2 + N_2H_3 \longrightarrow NH_3 + N_2 + H_2$		$k = 10^{12.5}$
	$N_2H_3 + N_2H_3 \longrightarrow 2NH_3 + N_2$		$k = 10^{12.3}$
	$N_2H_3 + H \longrightarrow N_2 + 2H_2$		$k = 10^{15}$
	$NH_2 + NH_2 \longrightarrow N_2H_4$		$k = 10^{13}$

This is considered as providing an empirical description of the overall behavior. The overall decomposition mechanism is not considered to be understood, but one that explains the behavior is shown in Table VIII-3.

---

*The Arrhenius expression is:

$$-\frac{dC}{dt} = k\, C^n$$

where:

C = Concentration

t = Time

n = Order

2.4 Hydrazine Photochemistry

Stief (Ref. VIII-7) has covered the photochemistry of N_2H_4 in the vacuum-ultraviolet. Photolysis of the vapor at 1236 Å gives a 3360 Å fluorescence which the author attributed to an $NH(A^3\pi \longrightarrow X^3\Sigma)$ transition. No emissions were found at 1470 Å. Formation of $N_2H_4^+$ is reported as probable at 1236 Å but not at 1470 Å. The photolysis reaction appears to be:

$$N_2H_4 + h\nu \longrightarrow N_2H_3 + H$$
$$H + N_2H_4 \longrightarrow H_2 + N_2H_3$$

Some hydrogen may be produced by:

$$N_2H_4 + h\nu \longrightarrow N_2H_2 + H_2$$

Decomposition and disproportionation also may occur by:

$$N_2H_3 \longrightarrow N_2H_2 + H$$
$$2N_2H_3 \longrightarrow N_2H_2 + N_2H_4$$
$$NH_2 + N_2H_3 \longrightarrow N_2H_2 + NH_3$$
$$N_2H_2 \longrightarrow N_2 + H_2$$
$$NH_3 + h\nu \longrightarrow NH_2 + H$$
$$2NH \longrightarrow N_2 + H_2$$

Ammonia may be formed at 1470 Å by:

$$NH_2 + N_2H_4 \longrightarrow NH_3 + N_2H_3$$
$$NH_2 + N_2H_3 \longrightarrow NH_3 + N_2H_2$$
$$N_2H_4 + h\nu \longrightarrow NH_3 + NH$$
$$2N_2H_3 \longrightarrow N_2 + 2NH_3$$

(The last reaction cannot be considered a major source of NH_3.) The importance of all of these reactions is that each product has a lower molecular weight than N_2H_4. Hence, one would expect the vapor pressure to be less and condensation of products would not be a problem if the parent N_2H_4 would not condense under identical circumstances.

2.5 Catalytic Decomposition

An equation that represents the overall hydrazine decomposition process in the catalyst bed is:

$$2N_2H_4 \longrightarrow 2NH_3 + N_2 + H_2$$

The first step in the catalyst bed is:

$$N_2H_4 \longrightarrow 4/3\ NH_3 + 1/3\ N_2$$

followed by a much slower endothermic decomposition:

$$NH_3 \longrightarrow 1/2\ N_2 + 3/2\ H_2$$

The first reaction, once initiated, generally goes to completion.

Combination of these reactions yields:

$$N_2H_4 \longrightarrow 4/3\ (1 - x)\ NH_3 + 1/3\ (1 + 2x)\ N_2 + 2xH_2$$

where x = fraction of originally formed NH_3 that is dissociated (Ref. VIII-8). Schreib (Ref. VIII-9) gives the same overall reaction and adds the heat generation rate as (1503-825x) Btu/lb M.

Since the only gases formed are NH_3, N_2, and H_2 and since the product temperature is less than 1800°F, all chemical reactions essentially cease at the exit of the catalyst bed. Subsequent gas flow can be considered frozen (from a chemical viewpoint) (Ref. VIII-8).

According to Price (Ref. VIII-10) hydrazine, in contact with Shell 405 catalyst, will begin to decompose in 10-100 msec when both substances are at a temperature no higher than 70°F. The reaction is self sustaining once initiated. He gives the same equations as the previous authors, but adds that the first reaction is controlled by transport

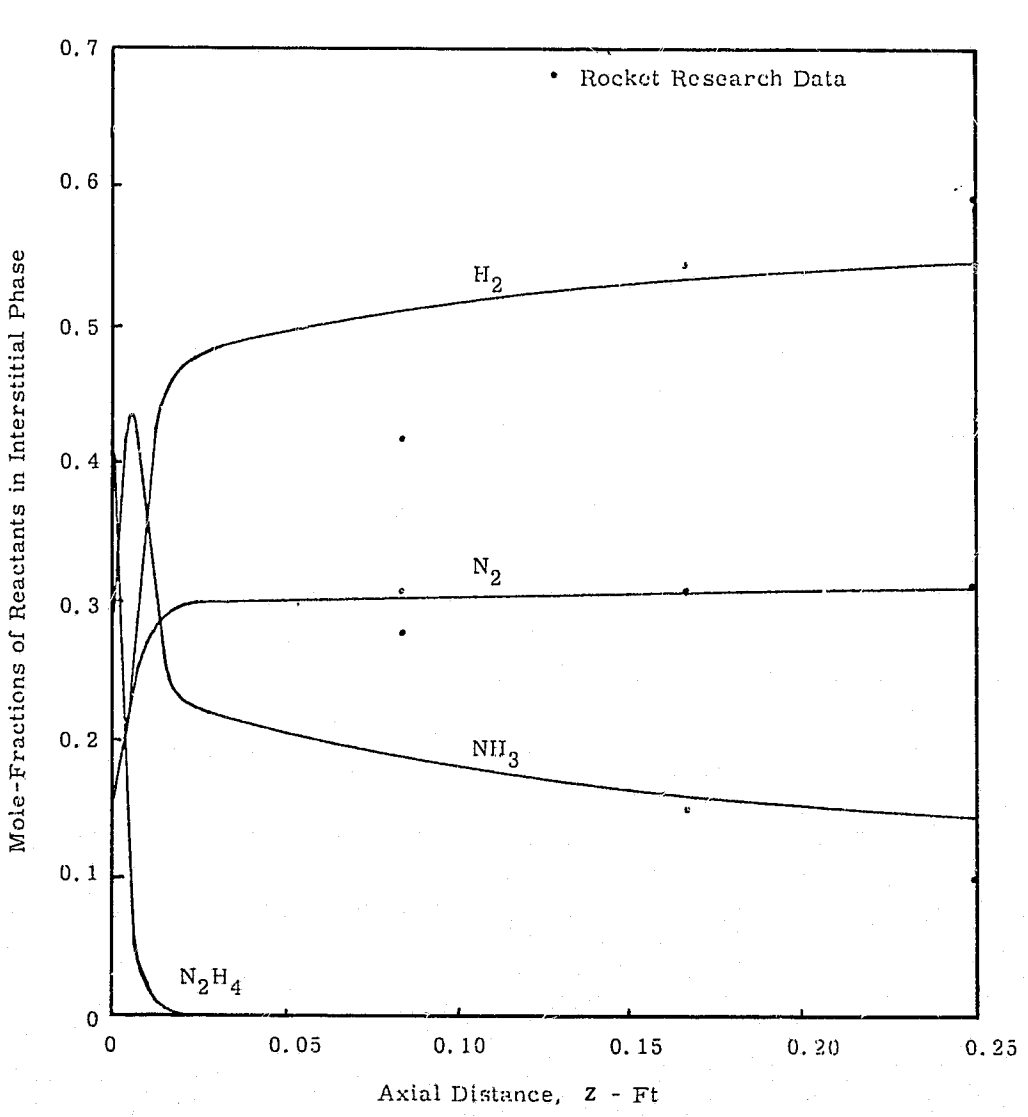

Figure VIII-1. Steady-State Axial Profiles of Mole-Fractions of Reactants (Ref. VIII-11).

processes; the second by kinetics (rate limited). Because of this, the exhaust composition and temperature can be controlled over wide limits by varying catalyst led length and hence residence time.

Kesten (Refs. VIII-11 through VIII-13) has reported behavior within the catalyst bed. Three of his curves, taken from Reference VIII-11, are reproduced in Figures VIII-1 through VIII-3. Figure VIII-1 shows the decomposition of N_2H_4 to be so complete that we cannot differentiate between the actual amount and zero. These are calculated lines with experimental date added. (Actual values were not given in this report. We may conclude that, in the steady state, the quantity of N_2H_4 escaping the thruster is very small. This is not necessarily the case in the transient, as shown in Figure VIII-2. The quantity of N_2H_4 at the end of the bed is small, but still readable. The transient behavior of the NH_3 is shown in Figure VIII-3.

Other catalysts than Shell 405 also are used such as H-7 or HA-3. These are predecessors of Shell 405. They do not provide as attractive a catalysis effect, but are more durable.

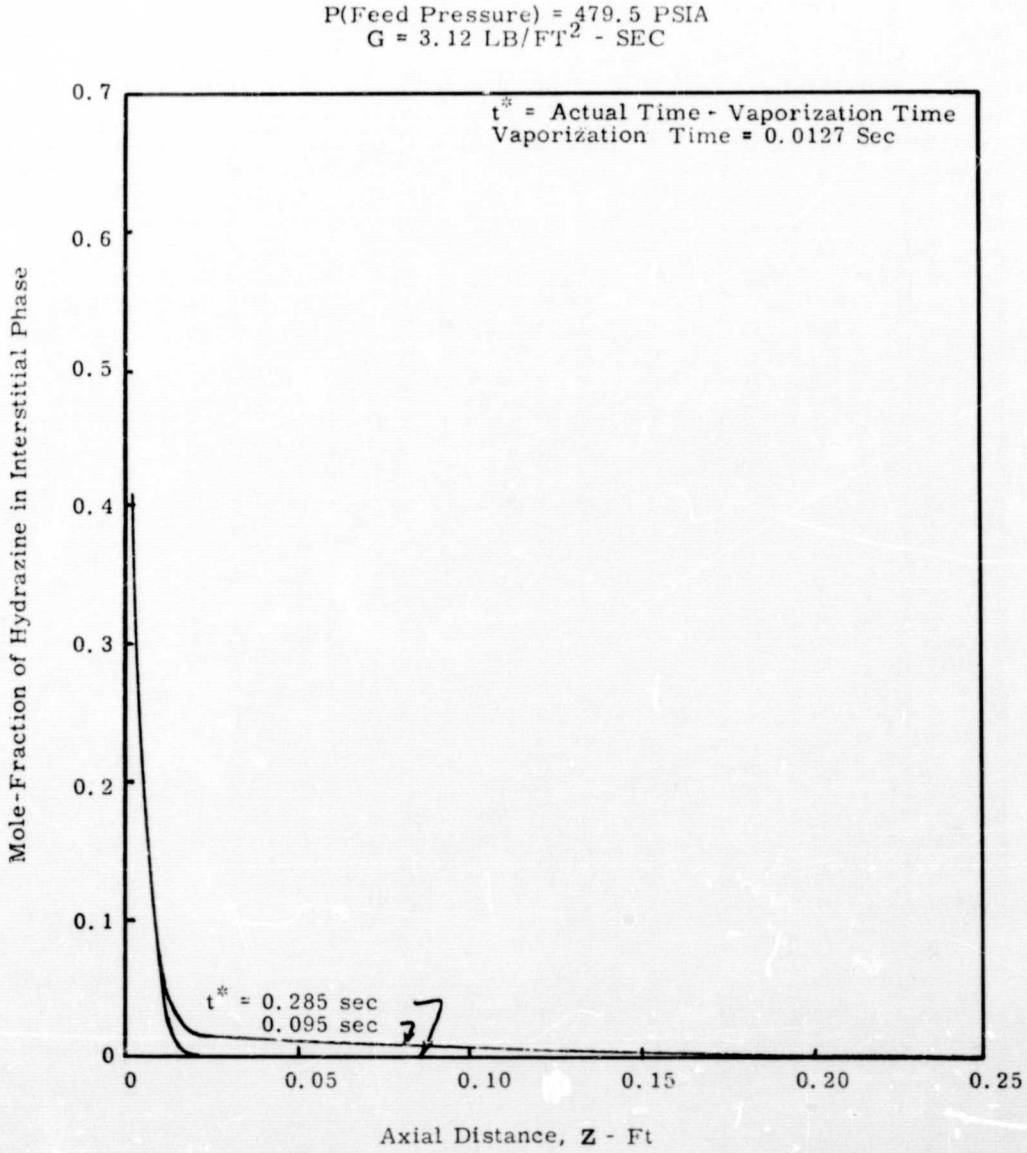

Figure VIII-2. Transitent Axial Profiles of Mole-Fraction of Hydrazine (Ref. VIII-11).

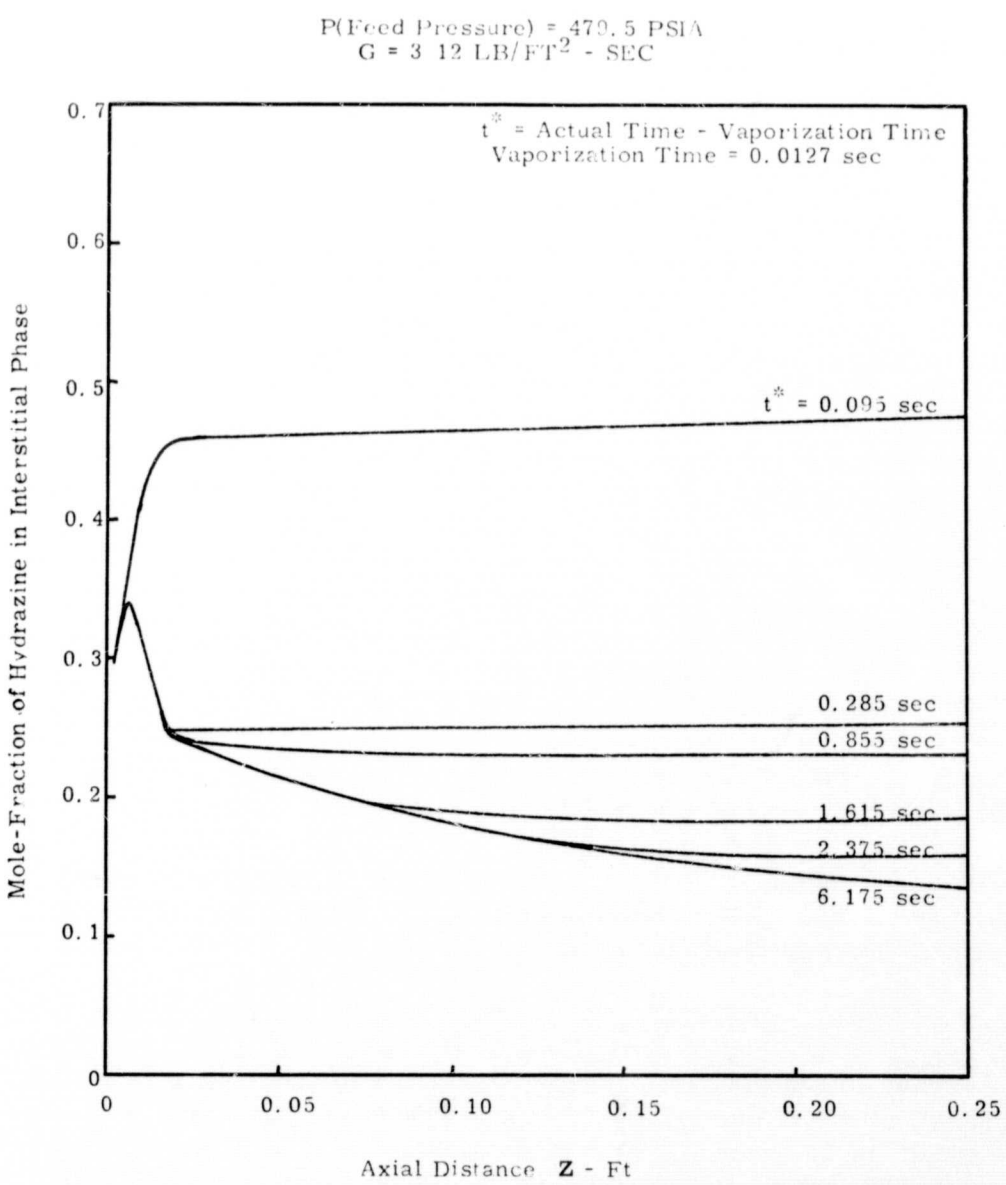

Figure VIII-3. Transient Axial Profiles of Mole-Fraction of Ammonia (Ref. VIII-11).

3. CATALYST LOSS

Shell 405 exhibits an apparent strength reduction at high temperatures, which may cause physical loss of catalyst from the motor. If this occurs, even in a small part, the exhaust plume will contain solid particles. This also will change the NH_3 dissociation rate and quantity (Ref. VIII-14).

Loss of catalyst also is mentioned by Sutherland (Ref. VIII-15). He adds that catalyst loss is a function of a number of variables, which we will not cover. Instances of activity changes and ignition delay also are referenced. No indications of exhaust products under these conditions are given.

Catalyst loss rates vary widely, depending upon the system. Loss rates of 10 percent/min. and 0.05 percent/min. have both been reported. Particle sizes in the range of 1 to 500 μm occurred in the 50 pounds thrust motors used on Mariner. (Ref. VIII-8.)

4. OTHER CATALYST EFFECTS

Shell 405 catalyst will adsorb significant quantities of gases which then are outgassed when exposed to a vacuum environment. (See Reference VIII-16 for detailed rate

information.) This will provide a source of contaminants to the spacecraft environment which will decrease with time in space and should be reduced considerably the first time the thruster is operated.

5. PHOTON ABSORPTION

Thin films of N_2H_4 absorb relatively strongly in the 2.5 - 20 μ region. Typical reported transmittances range from almost zero to ~80 percent in a reference sample and from 60 to ~95 in a specification grade sample. (Ref. VIII-2.) (Ref. VIII-7) used a photolysis cell cold trap to catch the N_2H_4 at -78°C. He checked the N_2H_4 removal by disappearance of the 3360 Å emission line when the trap was in operation. He stated that this trap did not remove the NH_3 because of its 30 torr vapor pressure at -78°C and as evidenced by the NH_3 3240 Å emission line. However, cooling the trap to -196°C did remove the NH_3 line. Finally, he states that no further emissions were found in the 2000 to 7000 Å range.

Considerable literature exists in this area, as evidenced by a number of entries in the Chemical Abstracts. Further data may be obtained by starting at this source.

6. EXHAUST EFFECTS

Few studies of exhaust effects were found in the literature, and none were found that were general or which covered low temperature surfaces.

NASA - Lewis is conducting some studies for Skylab that may provide useful information for our investigation. They may do some N_2H_4 work in the future (Ref. VIII-17). Results of these studies should be followed.

Massie (Ref. VIII-18) has studied the effects of a hydrazine thruster upon solar cells. He used a 25 pound thrust engine with Shell 405 catalyst and 2 × 2 cm, 10 ohm cm cells having 20 mil fused silica covers. Testing was accomplished in a high altitude chamber and consisted of cell exposure to 200 firings of 200 msec duration each. One group of cells was located five feet downstream of the nozzle and the other group was provided with a nine foot separation. Both groups were placed directly in the plume. Comparison of pre- and post-exposure electrical data showed no significant changes "as a result of plume impingement." Optical examination of the cells uncovered no apparent mechanical damage.

These tests were of a transient nature. Firings were spaced about 15 minutes apart and at no time during firing did a sample temperature rise more than 100°C. As a consequence, results should not be extrapolated to extended run times.

7. HYDRAZINE THRUSTER CHARACTERISTICS

7.1 Assumed Thruster

For study purposes we assumed two thrusters, one at 5 lbs thrust and one at 0.5 lbs (considerably larger than the other thruster types studied). Rocket Research characteristics were assumed as shown in Table VIII-4.

7.2 Five Pound Thruster Calculations

With an expansion ratio of 40 and a specific heat ratio of 1.28, Figure X-2 gives θ_∞ = 76° and M_e = 4.8. The bell nozzle exist angle is only defined to $0 < \theta_e < 15°$. The conservative angle is the larger one. For a semi-conservative angle of 10°, θ_∞ is 76 + 10 = 86°. At 15°, θ_∞ = 76 + 15 = 91°, a surface mounted nozzle might return a small quantity of exhaust. (These calculations could easily be off a degree or two.)

Table VIII-4
N_2H_4 Thruster Characteristics (Ref. VIII-19)

Rocket Research Five Pound (f) Engine			
Chamber Pressure P_c, psia	132	106	63
Thrust Coefficient C_F	1.761	1.754	1.729
Gas Molecular Weight	12.78	12.73	12.61
Chamber Temperature, T_c, °F	1632	1623	1597
Throat Diameter, inches	0.197		
Area Ratio	40/1		
Specific Impulse, sec	~ 230		
Heat Capacity Ratio, C_p/C_v	~ 1.28		
Nozzle Shape	(Bell, exit flow angle >0°, < 15°)		

Rocket Research 1/2 Pound (f) Engine		
Chamber Pressure, P_c, psia	200	100
Thrust, Pound (f)	0.50	0.25
Ammonia Dissociation	0.661	0.693
Throat Area, in^2	0.00143	
Area Ratio	100:1	
Nozzle Shape	Conical, 15° half angle	
Heat Capacity Ratio, C_p/C_v	~ 1.28	
Specific Impulse, sec	~225	

The parameter B, from Figure X-6, is 0.20, so that Eq. X-33 can be written as:

$$\rho = 0.20\ \rho_0 \left(\frac{d^*}{x}\right)^2 \qquad \text{(VIII-1)}$$

or

$$x = d^* \left(\frac{0.20\ \rho_0}{\rho}\right)^{1/2} \qquad \text{(VIII-2)}$$

with which we can predict distance along the centerline as a function of density ratio.

To obtain plume shape we substitute Equation (X-8) into (X-9) to find:

$$\rho u r^2 = \left(\frac{d \dot{m}}{d \psi}\right)_{\theta = 0} \exp \{- \delta^2 [1 - \cos \theta]^2\} \qquad \text{(VIII-3)}$$

which becomes:

$$\rho = \frac{1}{u r^2} \left(\frac{d \dot{m}}{d \psi}\right)_{\theta = 0} \exp \{- \delta^2 [1 - \cos \theta]^2\} \qquad \text{(VIII-4)}$$

At r = X which corresponds to $\theta = 0$, we know the ratio ρ_0 / ρ. Hence, we write:

$$\frac{\rho}{\rho_0} \left(\frac{\rho_0}{\rho_X}\right) = \exp \{- \delta^2 [1 - \cos \theta]^2\} \frac{X^2}{r^2} \qquad \text{(VIII-5)}$$

But:

$$r = \frac{x}{\cos \theta} \qquad \text{(VIII-6)}$$

and

$$\frac{\rho}{\rho_0} = \frac{X^2 \cos^2 \theta}{x^2} \exp \{- \delta^2 [1 - \cos \theta]^2\} \qquad \text{(VIII-7)}$$

from which:

$$x = X \cos \theta \sqrt{\frac{\rho_0 \rho_X}{\rho \rho_0}} \exp \left\{- \frac{\delta^2}{2} [1 - \cos \theta]^2\right\} \qquad \text{(VIII-8)}$$

Now we calculate for a constant $\rho / \rho_0 = \rho_X / \rho_0$ so that:

$$x = X \cos \theta \exp \left\{- \frac{\delta^2}{2} [1 - \cos \theta]^2\right\} \qquad \text{(VIII-9)}$$

To use this, we must find δ. Since we know M_e and δ, we can use:

$$\frac{V_e}{V_{max}} = M_e \left[\frac{\gamma - 1}{2} \left(1 + \frac{\gamma - 1}{2} M_e^2\right)^{-1}\right]^{1/2} \qquad \text{(X-38)}$$

and

$$\frac{C_F}{C_{F\,max}} = \frac{1}{2}(1 + \cos \theta_e) \frac{V_e}{V_{max}} [1 + (\nu M_e^2)^{-1}] \qquad \text{(X-39)}$$

Followed by:

$$\gamma = \left[\sqrt{\pi} \left(1 - \frac{C_F}{C_{F\,max}} \right) \right]^{-1} \tag{X-30}$$

Or:

$$\frac{V_e}{V_{max}} = 4.8 \left[\frac{0.28}{2} \left(1 + \frac{.28}{2} (4.8)^2 \right)^{-1} \right]^{1/2} \tag{VIII-10}$$
$$= 0.875$$

$$\frac{C_F}{C_{F\,max}} = \frac{1}{2} (1 + .965) (.875) \left[1 + \frac{1}{(1.28) (4.8)^2} \right] \tag{VIII-11}$$
$$= 0.889$$

$$\gamma = [\sqrt{\pi} (1 - 0.889)]^{-1} = 5.08 \tag{VIII-12}$$

Now we may compute plume shape, as shown in Fig. VIII-4. This presents isodensity curves for $\rho_0/\rho = 10^4, 10^5$, and 10^6 and indicates the maximum angle through which the exhaust effluent can turn. We may conclude that the quantity of exhaust returning to the spacecraft is very small. We have not attempted to provide a quantitative number because of the sensitive nature of the calculation to the nozzle exit angle and the approximate nature of the analysis.

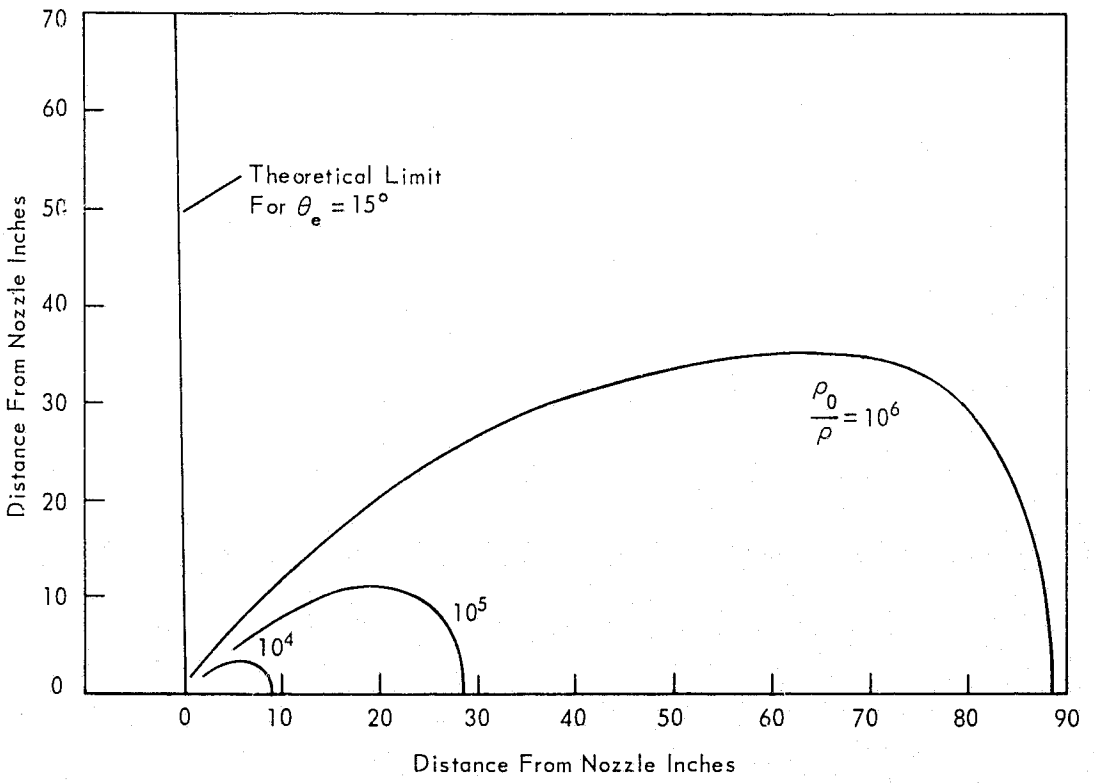

Figure VIII-4. Five Pound Thruster Exhaust Plume Density.

The thruster, when operating at 5 pounds thrust, is ejecting 5/230 = 0.0217 pounds/sec of gas. With an average molecular weight of 12.73 (see Table VIII-4), the number of molecules ejected is:

$$\frac{.0217 \text{ pounds}}{\text{sec}} \Big/ \frac{454 \text{ gms}}{\text{pounds}} \Big/ \frac{\text{mole}}{12.73 \text{ gms}} \Big/ \frac{6.02 \times 10^{23} \text{ molecules}}{\text{mole}}$$

$$= 4.65 \times 10^{23} \text{ molecules/sec}$$

For study purposes we will assume an approximate SMS spacecraft configuration. This is a right circular cylinder 40 in. high and 56 in. radius. Its area is 77,000 cm^2. The ejected molecules ratioed to the spacecraft area gives $4.65 \times 10^{23} / 77{,}000 = 6 \times 10^{18}$ molecules/cm^2 sec. Figure VIII-1 shows that the mole fraction of NH_3 in the exhaust is about 0.15. The number of ammonia molecules in the previous number is $(6 \times 10^{18})(.15) = 9 \times 10^{17}$ molecules/cm^2 sec. As shown in Appendix II.4.3., a 70°K radiator can accept 18^8 molecules of NH_3 per cm^2 sec with no accumulation. The threshold number is $10^8 / 9 \times 10^{17} \approx 10^{-10}$. If more than one ammonia molecule in ten billion in the exhaust is returned to the spacecraft, it will accumulate on the 70°K radiator. This is a very small number and indicates that a potential accumulation problem may exist. The plume calculations were based upon continuum theory which does not take individual particles into account. For a return factor of 10^{-10}, non-continuum behavior could be very important. Particle collision could conceivably occur in such a manner that this return rate would be achieved. Consequently, while we may conclude that the vast majority of the exhaust plume will initially behave as predicted by continuum theory, we should be very careful in extending these predictions into a regime where the behavior of the individual molecules become important.

For a 100°K radiator the evaporation rate of NH_3 is 5×10^{14} molecules/cm^2 sec. This would appear to be no problem for most geometric arrangements.

The vapor pressure of hydrazine is significantly lower than that of ammonia. At 70°K, we predict an evaporation rate of about 10^{-9} molecules per square centimeter second. Statistically, this number is meaningless. Practically, it means that no hydrazine will evaporate from a 70°K surface. Consequently, any hydrazine that makes its way to the radiator will remain on the radiator until its temperature is increased. We performed a rough calculation of how much hydrazine would be available to reach the radiator. The preliminary numbers indicated that ammonia normally would be a more serious consideration. However, we must caution that the hydrazine rates used are highly inaccurate and are based upon an analytical prediction. We would much prefer to see experimental data, which could drastically perturb our conclusion. In any event, heating the radiator would boil off both the hydrazine and the ammonia.

Hydrazine will contain about (.005)(32)/18 = .009 molecules of water per molecule of hydrazine. Hence, we eject (.009) $(4.65)(10^{23}) = 4.2 \times 10^{21}$ molecules/sec of water. Using the return factor of 10^{10} which we found "safe" for ammonia, we find a return of 4.2×10^{11} molecules/sec of water. With an overall area of 77000 cm^2, this is 5.5×10^6 molecules of water/cm^2 sec. On the average, this would not appear to be a serious problem if ammonia is not a problem.

7.3 Startup

Figure VIII-2 shows that at the end of roughly 0.1 sec the mole fraction of hydrazine in the exhaust is of the order of 0.005. Taking this value, the number of hydrazine molecules ejected in a transient is $(6 \times 10^{18})(.1)(.005) = 3 \times 10^{15}$ molecules/cm^2 of spacecraft surface. If we apply the same "return factor" that was marginal for ammonia, then the

number of hydrazine molecules reaching the radiator would be $3 \times 10^5/cm^2$ per start up (cold).

The density of solid hydrazine is 1.146 gm/cm^3 (Ref. VIII-21). One mole would occupy a volume of (32 gm)/(1.146 gm/cm^3) = 27.9 cm^3. The volume of one molecule is $27.9/6.02 \times 10^{23} = 4.63 \times 10^{-23}$ cm^3. Treating this as a cube, the side dimension is $(4.63 \times 10^{-23})^{1/3} = 3.59 \times 10^{-8}$ cm. One square centimeter one monolayer thick will contain $1/(3.59 \times 10^{-8})^2 = 7.75 \times 10^{14}$ molecules of hydrazine. A startup that deposits 3×10^5 molecules/cm^2 is not going to affect a surface that requires 7.75×10^{14} molecules/cm^2 for a one monolayer depth.

8. ADDITIONAL INFORMATION

Haws (Ref. VIII-20) provides several physical properties and a Mollier diagram. These data may be useful for some studies, but the lowest temperature covered is 0°C.

Audrith (Ref. VIII-21) presents considerable additional information in a number of categories. Additional chemical behavior is covered in Axworthy (Ref. VIII-22) and Takimoto (Ref. VIII-23). Catalytic bed behavior is covered by Kesten (Ref. VIII-24).

9. REFERENCES

VIII-1. "Military Specification, Propellant, Hydrazine," MIL-P-26536B, 13 March 1964.

VIII-2. Salvinski, R. J., "Investigation of the Formation and Behavior of Clogging Material In Earth and Space Storable Propellants," Interim Report, No. 08113-6016-R000, NASA CR-191569 (X69-16132), TRW Systems, Oct. 1968.

VIII-3. Eberstein, I. J., and I. Glassman, "Consideration of Hydrazine Decomposition," ARS Propellants, Combustion, and Liquid Rockets Conference, Columbus, Ohio, July 18-19, 1960. Contained in Liquid Rockets and Propellants, pp. 351-366.

VIII-4. Fresenius, W., and J. Karweil, "The Normal Oscillations and the Configuration of Hydrazine," Z. Physikal. Chem. Abt. B. Bd. 44, Heft I. pp. 5-12.

VIII-5. Lucien, Harold W., "Thermal Decomposition of Hydrazine," Journal of Chemical and Engineering Data, Vol. 6, No. 4, October 1961, pp. 584-586.

VIII-6. Eberstein, Igor J., "The Gas Phase Decomposition of Hydrazine Propellants," Technical Report 708, Department of Aerospace and Mechanical Sciences, Princeton University, AD607334, 1964.

VIII-7. Stief, L., J., V. J. DeCarlo, and R. J. Mataloni," Vacuum-Ultraviolet Photochemistry. VII. Photolysis of Hydrazine at 1236 and 1470 A," The Journal of Chemical Physics, Vol. 46, No. 2, 15 January 1967, pp. 592-598.

VIII-8. Price, T. W., and D. D. Evans, "The Status of Monopropellant Hydrazine Technology," Technical Report 32-1227, N68-16344, NASA-CR-92742, Jet Propulsion Laboratory, Feb. 15, 1968.

VIII-9. Schreib, R. R., T. K. Pugmire, and S. G. Chapin, "The Hybrid (Hydrazine) Resistojet," AIAA Paper 69-496, AIAA 5th Propulsion Joint Specialist Conference, June 9-13, 1969.

VIII-10. Price, T. W., "Hydrazine Monopropellant Provides 0.5-600 lb. Thrust," Space/Aeronautics, October 1969, pp. 70-72.

VIII-11. Kesten, Arthur S., "Analytical Study of Catalytic Reactors for Hydrazine Decomposition," UACRL F910461-12, N68-10633, NASA CR-89791, United Aircraft, May 1967.

VIII-12. Kesten, A. S., NASA-CR-80336, N67-12972, October 1966.

VIII-13. Kesten, A. S., NASA-CR-92988, N68-16663, January 1968.

VIII-14. "Spacecraft Attitude Control Gas Systems Analysis," NASA-CR-86661, N67-32369, Hughes, April 1967.

VIII-15. Sutherland, George S., et. al., "Monopropellant Hydrazine Reaction Control Systems - A Five Year Status Report," obtained from AIAA under A68-33429.

VIII-16. Carlson, Ronald A., Jack L. Blumenthal, and Robert J. Grassi, "Space Environment Operation of Experimental Hydrazine Reactors," Rpt. No. 4715. 3.68-27, N69-12432, TRW Systems, July 1968.

VIII-17. Mark, Dr. Herman, Personal Communication, NASA Lewis, 216-433-4000, ext. 201, June 4, 1970.

VIII-18. Massie, Lowell D., and Paul J. Martinkovic, "Attitude Control Rocket Exhaust Plume Effects On Solar Cells," A69-35678, 7th Photovoltaic Specialists Conference, Pasadena, California, November 19-21, 1968.

VIII-19. Yetman, A., Personal Communication, GSFC, 301-982-5021, May 19, 1970.

VIII-20. Haws, Jimmy L., and Darrel G. Harden, "Thermodynamic Properties of Hydrazine," Journal of Spacecraft and Rockets, Vol. 2, No. 6, Nov.-Dec. 1965, pp. 972-974.

VIII-21. Audrith, L. F., and B. A. Ogg, The Chemistry of Hydrazine, Wiley, 1951.

VIII-22. Axworthy, A. E., et al., "Research On Hydrazine Decomposition," AD826121, AD830860, and AD842500, Rocketdyne, January 1968, April 1968, and October 1968.

VIII-23. Takimoto, Hideyo H., and Genevieve C. Denault, "Hydrazine Compatibility with Ethylene-Propylene Elastomers," AD688486, Aerospace Corp., February 1969.

VIII-24. Kesten, Arthur S., "Turbulent Diffusion of Heat and Mass in Catalytic Reactors for Hydrazine Decomposition," Journal of Spacecraft and Rockets, Vol. 7, No. 1, January 1970, pp. 31-36.

APPENDIX IX

AMMONIA THRUSTER BACKGROUND DATA

1. SPACECRAFT CONFIGURATION

The spacecraft assumed for analysis purposes approximates the ATS-F. It consists of a cube connected to a parabolic antenna as shown in Figure IX-1. (Ref. IX-1). The cube is four feet on each edge with 12 thrusters located around the equator. The antenna is placed 14 feet from the cube upper surface and is 30 feet in diameter. The center of gravity is located 2-1/2 feet above the top of the cube. Four station keeping thrusters are located in the plane of the center of gravity.

The thrusters located on the cube have about a 60 to 1 to 100 to 1 expansion ratio. Throat diameter is about 0.057 inches (Ref. IX-2). Nozzle total included angle is 60° (Refs. IX-1 and IX-3). In all cases the end of the nozzle is located about 2 in. outside of the cube. These thrusters are used for initial acquisition and for wheel dumping. The 50 millipound thrusters provide pitch and roll control; the 25 millipound provide for yaw. Maximum usage will occur shortly after launch, with anticipated behavior as follows (Ref. IX-4):

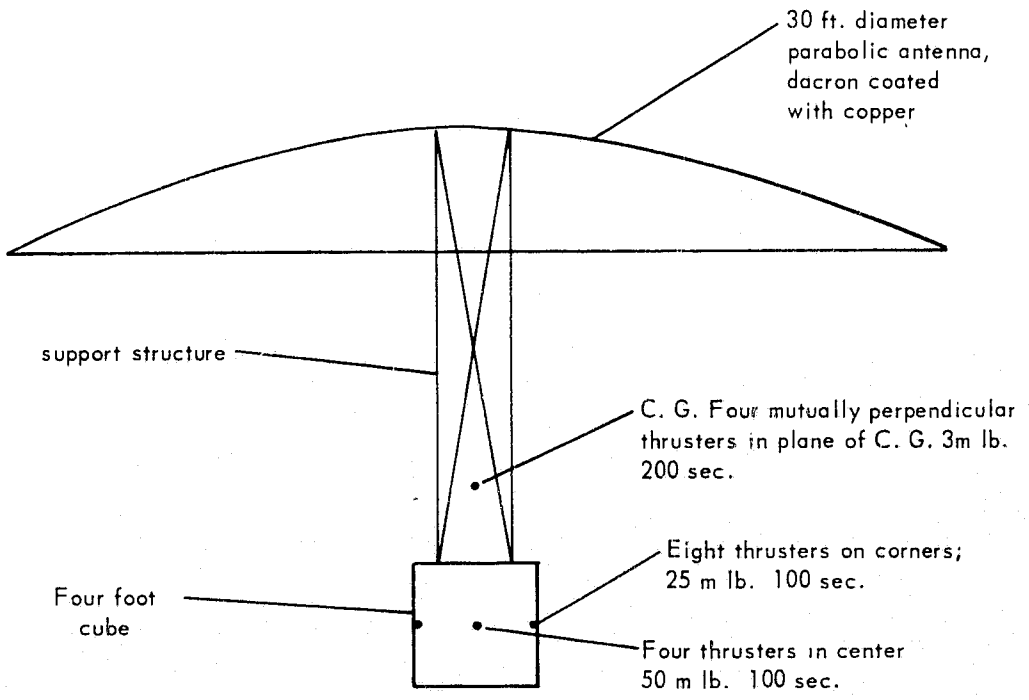

Figure IX-1. Assumed ATS Configuration.

Thrusting time, minutes (each firing)	Number of times fired	Control Provided
1.6	2	yaw
1.6	1	pitch
1.6	1	roll
~3.4	1	pitch
~3.4	1	roll

The first three items are anticipated to bring yaw under control; the last two bring pitch and roll under control. After these firings, the usage will be limited to wheel dumping.

The three millipound thrusters located in the center of gravity plane provide an orbit correction and station change capability. Operation time has not been specified, but long term (> several hours) is possible. Throat diameter of these is 0.012 inches and total included angle is 60° (Ref. IX-1).

Firing sequences also are of interest. The station keeping and wheel dump operations occur independently of each other. Wheel dump, roll, yaw, and pitch operations will never cause two thrusters located on the same plane of the "cube" to operate simultaneously but thrusters located on the same corner (but different planes) could be in operation at once.

The spacecraft also contains the same radiator we studied for the cesium thruster interaction (see Appendix III).

2. AMMONIA PROPERTIES

Most applicable NH_3 properties have been covered in previous sections. One area remains - purity. Flight certified NH_3, according to AVCO (Ref. IX-2), has the following impurity concentrations:

H_2O	<33 ppm
Oil	<2 ppm
Salt (borax, silicon)	<10 ppm

Page (Ref. IX-5) has reported on propellants used in resistojet life tests. These were of the highest purity obtainable at a reasonable cost. Hydrogen purity was 99.9996 percent. Major impurities reported were 0.8 ppm O_2 and 0.7 ppm H_2O. Ammonia purity was 99.99 percent minimum. Impurities were:

Non-Basic Gas in Vapor Phase	- 25 ppm maximum
Non-Basic Gas in Liquid Phase	- 10 ppm maximum
Water	- 33 ppm maximum
Oil (as soluble in petroleum ether)	- 2 ppm maximum

Knox (Ref. IX-6) states that propellant grade ammonia has a minimum purity of 99.5 weight percent (according to Military Specification JAN-A-162). Maximum water is 0.5 percent, with oil present to 5 ppm. He also states that the water probably will react to form ammonium hydrate.

The Reference IX-2 data, with the possible addition of the gases mentioned in Reference IX-5, probably represent the most accurate description.

3. RADIATOR CHARACTERISTICS AND REFLECTED AMMONIA

We analyzed the 100°K radiator in Appendix III and found that if the incoming molecules are traveling downward and arriving at an angle of 82° with respect to the plane of the opening, then the following result:

Flux Hitting Surface, Molecules/cm² sec	Surface
2.3×10^{12}	300°K, lower
1.14×10^{11}	300°K, upper
1.26×10^{11}	200°K, upper
2.39×10^{11}	200°K, lower

This portion of the results, although calculated for cesium, may be applied to ammonia. The mean flux on the 200°K surfaces is $(1.26 \times 10^{11} + 2.39 \times 10^{10})/2 = 7.5 \times 10^{10}$ molecules/cm² sec. For ammonia, these molecules will evaporate about as fast as they arrive.

The cold patch view factor to the 200°K side walls is 0.670 and to space is 1 - 0.670 = 0.330. Since the molecules are evaporating from the side walls as fast as they arrive, the cold patch will "see" a flux of $(7.5)(10^{10})(0.67) = 5.0 \times 10^{10}$ molecules/cm² sec on the basis of the 2.3×10^{12} rate at the lower 300°K surface. The reduction factor is $5.0 \times 10^{10}/2.3 \times 10^{12} = 0.022$.

Examination of the radiator geometry shows that we can increase the angle of 23° while only about doubling the reduction factor. For analysis purposes we will assume a factor of (0.022)(2) = 0.044. Therefore, since a 100°K surface may receive a flux of 5×10^{14} molecules/cm² sec, the lower surface may receive a flux of $5 \times 10^{14}/0.044 \approx 10^{17}$ molecules/cm² sec.

The exit area of the 3 m lb thruster is about 0.04 cm² and that of the 50 m lb thruster is about one cm². Hence, the exhaust fluxes during operation are $2.41 \times 10^{20}/0.04 = 6 \times 10^{21}$ and 8×10^{21} molecules/cm² sec, respectively. The flux at the exit is about the same.

The geometry does not allow the radiator opening to "see" the 3 m lb thruster, but it does see the antenna. If the antenna is assumed to be a solid structure, the mean flux will be roughly:

$$\frac{2.41 \times 10^{20} \text{ molecules}}{\text{sec}} \quad \frac{2}{4\pi (16)^2 (2.54)^2 (12)^2}$$

$$= 1.6 \times 10^{14} \text{ molecules/cm}^2 \text{ sec}$$

where we have assumed uniform spreading of the exhaust over one hemisphere at a 16 foot distance – a pessimistic assumption because of the plume and antenna shape. The antenna cannot return a greater flux than this to the spacecraft. We immediately conclude this reflection will not disturb the radiator operation.

The same assumption applied to one of the 50 m lb thrusters provides a flux to the antenna of:

$$(1.6)\ (10^{14})\ \frac{8 \times 10^{21}}{2.41 \times 10^{20}} = 5.3 \times 10^{15}\ \text{molecules/cm}^2\ \text{sec}$$

This still is significantly below what can hit the lower 300°K surface in the radiator, but is about a factor of ten above what could impinge upon the 100°K surface without accumulation. This would appear to still be safe if we allow for the geometry effects and provided a major perturbation does not result from the direct view from the exhaust to the radiator opening.

4. EXHAUST SHAPE

These thrusters have an expansion ratio of about 80. The specific heat ratio of NH_3 is about 1.3. Figure X-2 gives $\theta_\infty \approx 65°$ for these conditions with $\theta_e = 0$. Since θ_e for this nozzle is 30°, we find, by Equation (X-4), $\theta_\infty = 30 + 65 = 95°$. Approximately, then, the exhaust plume will affect one hemisphere. The density behavior along the plume axis is given by Equation (X-31). The parameter, B, for this equation for the thruster is obtained from Figure X-6 as 0.30. Hence:

$$\rho = 0.30\ \rho_0 \left(\frac{d^*}{x}\right)^2 \qquad \text{(IX-1)}$$

(Note the difference between this result and Equation (X-7) – about 50 percent which is about the type of error Sibulkin told us to expect.)

The 50 m lb thruster extends two inches from the spacecraft. The angle a line between the exit end of the nozzle and the edge of the cube portion makes with respect to the exhaust plume centerline is:

$$\Phi = 90 + \tan^{-1}\left(\frac{2}{24}\right) = 95° \qquad \text{(IX-2)}$$

The exhaust plume boundary barely intersects the spacecraft at the center of an edge, but will impinge slightly on the corners. The angle measured parallel to the surface at the edge is 5°. The angle at one foot from the thruster is:

$$\Phi' = \tan^{-1}\left(\frac{2}{12}\right) = 9.5° \qquad \text{(IX-3)}$$

This clearly shows that direct thruster effluent will not penetrate to the 200°K surface, but first must "bounce" off a 300°K surface.

We next rewrite the density relationship to obtain:

$$x = d^* \left(\frac{0.3\ \rho_0}{\rho}\right)^{1/2} \qquad \text{(IX-4)}$$

This immediately provides the following density ratios along the exhaust centerline:

	Distance, x (ft)	
$\frac{\rho_0}{\rho}$	3 m lb Thruster	50 m lb Thruster
10^5	0.17	0.82
10^6	0.55	2.68
10^7	1.73	8.20
10^8	5.50	26.8

To obtain plume shape we use:

$$x = X \cos\theta \exp\left\{-\frac{\delta^2}{2}\left[1 - \cos\theta\right]^2\right\} \qquad \text{(VIII-9)}$$

Next we determine δ. From Figure X-2, the exit Mach number is about 5.6. Applying Equation (X-35) gives:

$$u^* = \left[\frac{(2)\,(1.3)\,(2920)\,(1960)}{2.3}\right]^{1/2} = 2540 \text{ ft/sec} \qquad \text{(IX-5)}$$

for the 3 m lb thruster and:

$$u^* = \sqrt{\frac{530}{1960}}\ 2540 = 1320 \text{ ft/sec} \qquad \text{(IX-6)}$$

for the 50 m lb. Maximum velocities are $2540\ \sqrt{2.3/.3} = 7030$ and $1320\ \sqrt{2.3/0.3} = 3650$ ft/sec. Equation (X-39) now gives:

$$\frac{C_F}{C_{F_{max}}} = \frac{1}{2}\ \frac{1320}{3650}\ (1.866)\ \{1 + [(1.3)\,(5.6)^2]^{-1}\} = 0.345 \qquad \text{(IX-7)}$$

for both thrusters. Now Equation (X-30) gives:

$$\delta = [\sqrt{\pi}\ (1 - 0.345)]^{-1} = 0.861 \qquad \text{(IX-8)}$$

and, from Equation (X-45):

$$\left(\frac{d\dot{m}}{d\psi}\right)_{\theta=0} = \frac{0.861}{\pi^{3/2}}\ \dot{m} = 0.156\ \dot{m} \qquad \text{(IX-9)}$$

which gives values of 2.33×10^{-6} and 7.78×10^{-5} lbs/sec for this parameter.

Now we apply Equation (X-40) to obtain:

$$u = u^* \left(\frac{2}{2.3}\right)^{1/0.3}\ \frac{0.861}{(4)\ (0.3)\ \sqrt{\pi}} = 0.254\ u^* \qquad \text{(IX-10)}$$

from which u = 645 ft/sec and 334 ft/sec for the two thrusters. Next we compute values of x/X and θ which give a constant ρ/ρ_0 by Eq. VIII-9:

x/X	θ, deg.
1	0
.860	30
.750	40
.612	50
.456	60
.291	70
.135	80
.064	85

The characteristic curves resulting from these data are plotted in Figure IX-2. The curves are "fatter" than ordinarily expected because of the high expansion ratio as well as the expansion into a vacuum. The shape indicates that assuming a uniform flux on a hemispherical surface to represent the exhaust impingement is reasonable.

5. ABSORPTION

Interactions of the thruster exhaust with portions of the spacecraft will perturb the molecular density. An indication of the magnitude of this perturbation, on the average,

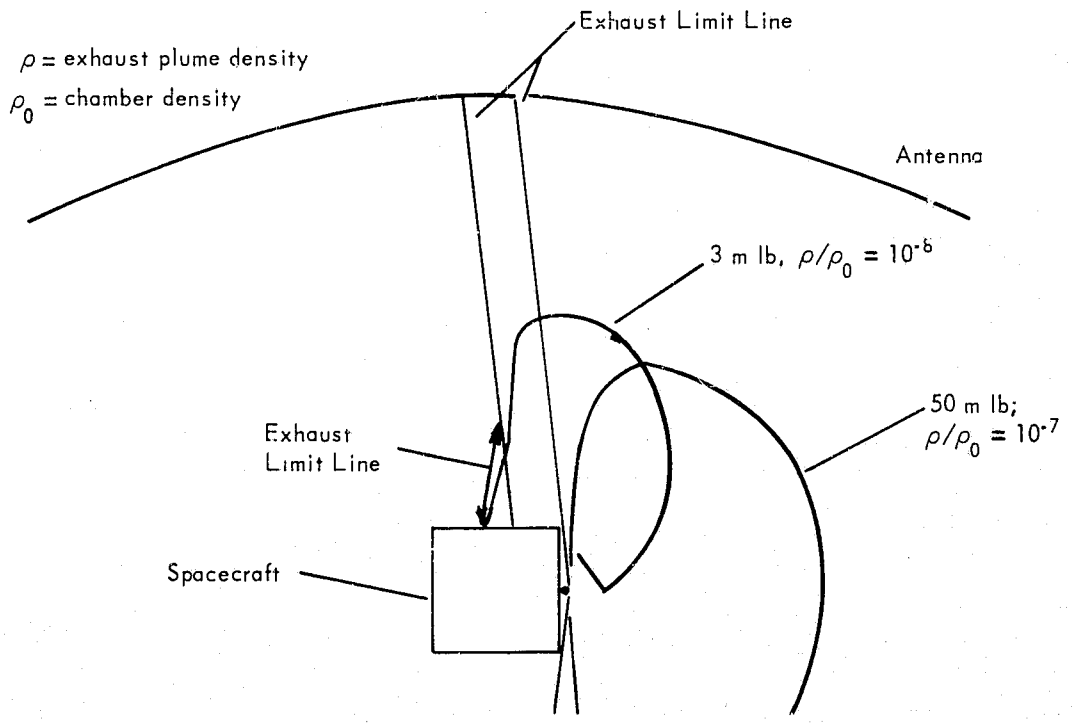

Figure IX-2. Exhaust Plume Shape.

will be of interest from an overall evaluation viewpoint. We will base the analysis upon the following assumptions:

1. Exhaust plume molecules that do not intersect the spacecraft will leave its vicinity quickly. These will not be of interest to this analysis.

2. Exhaust plume molecules which hit the spacecraft will be reemitted at a velocity determined by the spacecraft temperature.

3. Sufficient interaction with spacecraft structure will occur that the flux of collided molecules leaving the spacecraft vicinity is a function of distance from the spacecraft only.

The last assumption is not satisfied but the objective is to establish an order of magnitude density. The error will be acceptable.

Assumption two gives (Ref. IX-7, Equation 3-32)

$$\bar{v} = \sqrt{\frac{8\,k\,T}{\pi m}} \qquad \text{(IX-11)}$$

where:

$\bar{v}$ = average molecular velocity

k = Boltzmann constant

T = absolute temperature

m = molecular mass.

The time, t, required for a molecule to travel one unit length of distance is:

$$t = \frac{1}{\bar{v}} \qquad \text{(IX-12)}$$

If the number of molecules produced per unit time is $\dot{M}$, then the number per unit time passing through a spherical control surface is simply $\dot{M}$. The number of molecules in a volume of one unit time thickness in the vicinity of the control surface is also $\dot{M}$. The density at this location is:

$$\rho = \frac{\dot{M}}{V} = \frac{\dot{M}}{4\pi x^2\,\bar{v}} \qquad \text{(IX-13)}$$

where:

V = volume

x = radius of control surface (distance from spacecraft).

The total contaminant mass "seen" from the spacecraft per unit area is:

$$m' = \int_{x_0}^{\infty} m\rho\,dx \qquad \text{(IX-14)}$$

where:

x_0 = effective radius of the observer.

since we effectively see an infinite distance. Hence:

$$m' = \int_{x_0}^{\infty} \frac{m\dot{M}\,dx}{4\pi x^2 \bar{v}} = \frac{m\dot{M}}{4\pi x_0 \bar{v}} \tag{IX-15}$$

Fishburne (Ref. IX-8) has applied this approach to the absorption of solar radiation. His equation for absorption is:

$$\ln\left(\frac{I_0}{I}\right) = \frac{2.5 \times 10^4\, \alpha}{M'} \int_{x_0}^{\infty} \rho\, dx \tag{IX-16}$$

where:

I_0 = unperturbed intensity

I = intensity with absorption

M' = molecular weight, gms/mole

α = absorption coefficient

Substitution yields:

$$\ln\left(\frac{I_0}{I}\right) = \frac{2.5 \times 10^4\, \dot{M}\alpha}{4\pi \bar{v}\, x_0\, M'} \tag{IX-17}$$

Representative values of α for continuous absorption, such as occurs in photoionization and photodissociation, range below 3000 $atm^{-1}\ cm^{-1}$. Using this value, a mass release rate of 0.025 gm/sec of O_2, $\bar{v} = 6 \times 10^4$ cm/sec, and $x_0 = 300$ cm, Fishburne obtained $\ln (I_0/I) = 3 \times 10^{-4}$. This represents completely negligible absorption.

Atomic line and molecular band absorption is expected to cause the largest amount of absorption. Fishburne states that values of the absorption coefficient for a line may have a maximum value of 10^6. However, these lines occur at very isolated portions of the spectrum and should not affect the over-all level of the radiation.

The 3 m lb thruster to be used on ATS ejects 1.5×10^{-5} lbs/sec (0.0068 gms/sec). If we assume all of this ammonia is intercepted by the spacecraft and then re-evaporated and that the absorption coefficient is 3000, both of which are highly conservative, we obtain, for a spacecraft of $x_0 = 24$ cm:

$$\ln\left(\frac{I_0}{I}\right) = \frac{(3)\,(10^{-4})\,(.0068)\,(32)\,(300)}{(.025)\,(17)\,(24)} = 1.9 \times 10^{-3} \tag{IX-18}$$

The conclusion remains the same, absorption will not be a problem.

Fishburne also treated the case of a rocket plume where the exhaust gases were interposed between the observer and observed point. He analyzed the diffusion of exhaust gases in space by introducing two assumptions:

1. the expansion was treated as a moving free-molecular point source

2. the exit mass velocity was assumed hypersonic.

Following his approach, for a source emitting molecules hypersonically at a rate $\dot{N}(t)$, the density field $\dot{N}(r, \theta, t)$ is:

$$N(r, \theta, t) = \frac{\beta_0}{\pi r^2} u_0 \cos\theta \dot{N} \left(t - \frac{r}{u_0 \cos\theta}\right) e^{-u_0^2 \beta_0 \sin^2\theta} \qquad \text{(IX-19)}$$

and the velocity field is:

$$u(r, \theta, t) = u_0 \cos\theta \qquad \text{(IX-20)}$$

where:

r and θ = polar coordinates from the source

t = time since the start of firing

u_0 = exhaust velocity

β_0 = $1/2\ RT_0$

T_0 = assumed (free molecular) final static temperature after expansion of the exhaust

A square-wave pulse, corresponding to a finite firing time, Δt, of the rockets, is represented by:

$$\dot{N}(t) = \dot{N}_0 \{H(t) - H(t - \Delta t)\} \qquad \text{(IX-21)}$$

where:

$\dot{N}_0$ = constant value

$H(t)$ = Heaviside step function

Along the axis $\theta = 0$, the density field for such a pulse is:

$$N = \frac{\beta_0}{\pi r^2} u_0 \dot{N}_0 \left\{H\left(t - \frac{r}{u_0}\right) - H\left(t - \Delta t - \frac{r}{u_0}\right)\right\} \qquad \text{(IX-22)}$$

For an observation time, t, the attenuation factor, $\int \rho\ dx$, becomes:

$$\int_{r_2}^{r_1} \rho \, dx = \frac{M u_0 \dot{N}_0}{R T_0 \pi} \int_{r_2}^{r_1} \frac{1}{r^2} \, dr \qquad \text{(IX-23)}$$

where:

$r_2 = u_0 \ (t - \Delta t)$

M = molecular weight

$r_1 = u_0 t$

r represents the radial limits of the pulse at time t.

Integrating, we find:

$$\int_{r_2}^{r_1} \rho \, dx = \frac{M \dot{N}_0 \, \Delta t}{\pi R T_0 \, t^2} \qquad \text{(IX-24)}$$

for $t \gg \Delta t$.

Fishburne applied the results to a total pulse of 15 bursts of 13 milliseconds each and found $\int \rho \, dx \approx 7 \times 10^{-11}$ gm/cm² after 45 minutes with $T_0 = 0.005°K$ (estimated). (A higher T_0 would reduce the attenuation.) His results for the assumed exhaust composition are presented in Table IX-1.

For $\theta = 0$, Equations (IX-19) and (IX-21) may be rewritten for the steady state as

$$N(r) = \frac{\beta_0 u_0 \dot{N}_0}{\pi r^2} \qquad \text{(IX-25)}$$

Table IX-1
Exhaust Attenuation Effect (Ref. IX-8)

Species	Mole %	Max μ	$(I_o - I)/I_o$
H_2O	36	10^7 cm²/gm	0.02×10^{-2}
N_2	32	10^7	0.02
H_2	13	10^9	0.90
CO	9.6	10^7	0.007
CO_2	3.7	10^7	0.003
H	1.9	10^9	0.13
OH	1.6	10^9	0.11
NO	0.24	10^8	0.002
O_2	0.15	10^9	0.011
O	0.14	10^9	0.011

Or, eliminating β_0:

$$N(r) = \frac{u_0 \dot{N}_0}{2\pi R T_0 r^2} \tag{IX-26}$$

But:

$$R = k N_0'/M \tag{IX-27}$$

where:

k = Boltzmann Constant

N_0' = Avogadro number

Therefore:

$$N(r) = \frac{u_0 \dot{N}_0 M}{2\pi k N_0' T_0 r^2} \tag{IX-28}$$

Leighton (Ref. IX-9, p. 422) gives linear absorption as:

$$I(r) = I_0 e^{-\sigma_L r} \tag{IX-29}$$

where:

σ_L = linear absorption coefficient.

We may introduce the atomic absorption coefficient by:

$$\sigma_a = \frac{\sigma_L M}{\rho' N_0'} \tag{IX-30}$$

where:

ρ' = mass density

Equation (IX-29), on a differential basis, is:

$$\frac{dI(r)}{dr} = -\sigma_L I(r) \tag{IX-31}$$

Substituting Equation (IX-30) gives:

$$\frac{dI(r)}{dr} = -\frac{\sigma_a \rho' N_0' I(r)}{M} \tag{IX-32}$$

But:

$$\rho' = \frac{N(r)\,M}{N_0'} \tag{IX-33}$$

So that Equation (IX-32) becomes:

$$\frac{dI(r)}{dr} = -\sigma_a\, N(r)\, I(r) \tag{IX-34}$$

Now use Equation (IX-28) to obtain:

$$\frac{dI(r)}{dr} = -\frac{\sigma_a\, u_0\, \dot{N}_0\, I(r)\, M}{2\pi k N_0'\, T_0\, r^2} \tag{IX-35}$$

In consistent notation, Equation IX-11 may be rewritten as:

$$u_0 = \sqrt{\frac{8kT_0\, N_0'}{\pi M}} \tag{IX-36}$$

Or:

$$T_0 = \frac{\pi M u_0^2}{8\,k\,N_0'} \tag{IX-37}$$

Substitution gives us:

$$\frac{dI(r)}{dr} = -\frac{4\sigma_a\, \dot{N}_0}{\pi^2\, r^2\, u_0}\, I(r) \tag{IX-38}$$

Or:

$$\int_{I_0}^{I} \frac{dI(r)}{I(r)} = -\frac{4\sigma_a\, \dot{N}_0}{\pi^2\, u_0} \int_{r_0}^{\infty} \frac{dr}{r^2} \tag{IX-39}$$

$$\ln\left(\frac{I}{I_0}\right) = -\frac{4\sigma_a\, \dot{N}_0}{\pi^2\, u_0 r_0} \tag{IX-40}$$

Mass absorption coefficients given in Table IX-1 range from 10^7 to 10^9 cm^2/gm. Taking 10^9, we obtain:

$$\sigma_a = \frac{10^9\, M}{N_0'} \tag{IX-41}$$

so that:

$$\ln\left(\frac{I_0}{I}\right) = \frac{4 \times 10^9\, \dot{N}_0 M}{\pi^2\, u_0 N_0'\, r_0} \tag{IX-42}$$

The ideal "frozen" velocity of the 3 m lb. nozzle exit gas may be obtained from:

$$V_{max} = \sqrt{\frac{2\gamma RT_0}{\gamma - 1}} \tag{X-36}$$

The specific heat ratio of NH_3 is about 1.3 (Ref. IX-10). Hence, for $T_c = 1500°F$:

$$V_{max} = \left[\frac{(2)\ (1.3)\ (2920)\ (1960)}{0.3}\right]^{1/2}$$

$$= 7050 \text{ ft/sec} = 2.15 \times 10^5 \text{ cm/sec} \tag{IX-43}$$

where:

$$R = \left(\frac{1545 \text{ ft lbs}}{\text{mole}°R}\right)\left(\frac{32.2 \text{ ft}}{\text{sec}^2}\right)\left(\frac{\text{mole}}{17 \text{ lbs}}\right)$$

$$= 2920 \text{ ft}^2/\text{sec}^2 \ °R \tag{IX-44}$$

We select the following values:

$\dot{N}_0 = (.0068)(6.02)(10^{23})/17 = 2.41 \times 10^{20}$ atoms/sec

$u_0 = 2.15 \times 10^5$ cm/sec

$M = 17$ gms/mole

$N_0' = 6.02 \times 10^{23}$ molecules/mole

$r_0 = 24$ cm

Equation (IX-42) now provides:

$$\ln\left(\frac{I_0}{I}\right) = \frac{(4)\ (10^9)\ (2.41)\ (10^{20})\ (17)}{(\pi^2)\ (2.15)\ (10^5)\ (6.02)\ (10^{23})\ (24)}$$

$$= 0.534 \tag{IX-45}$$

Clearly, if we look directly down the center of the exhaust plume there will be some pertubation ($I_0/I = 1.71$). This is an unlikely situation which can be avoided by moving a short distance away from the plume. Calculation of this effect may be performed by considering the spacecraft geometry. We have not performed the analysis.

If desired, we could perform a more sophisticated analysis using the distribution equations developed in Appendix X.

6. SCATTERING

Kovar (Ref. IX-11) has investigated this problem for the Gemini, Apollo, and ATM (Apollo Spacecraft Mount) spacecraft. This reference considers the particle scattering

contribution to an apparent brightness by analyzing the column mass density of the material surrounding the spacecraft. They first assumed that a particle of radius r leaves the spacecraft in a radial direction at a rate dm/dt and a velocity v_0. The most effective removal mechanism is stated to be aerodynamic drag and this mechanism is unimportant. Consequently, the column mass density of material surrounding a spherical spacecraft is represented by:

$$M_s = \frac{1}{4\pi R_0 v_0} \left[\frac{dm}{dt}\right] \qquad \text{(IX-46)}$$

where the particles are assumed to be composed of ice. The authors have treated the ATM spacecraft by assuming a cylindrical geometry of radius R_0 and Length L. They then assumed the amount of material outgassed along the length was small in comparison to that outgassed at the cylindrical ends. With this assumption, the column mass density becomes:

$$M_s = \frac{1}{2\pi L v_0} \left(\frac{dm}{dt}\right)_{H_2O} \ln\left(\frac{R_1}{R_2}\right) \qquad \text{(IX-47)}$$

where:

R_1 = distance the column of material extends from the spacecraft.

The value of L is about 3000 centimeters. The value of R_0 for the ATM is the radius of the S-IVD stage. This is 300° centimeters. For the Gemini and Apollo spacecraft, the radius is 200 centimeters. The pertinent data and solution of the equations is given in Table IX-2.

Table IX-2
Spacecraft Parameters (Ref. IX-11)

Spacecraft	Altitude	dm/dt gm/sec	M_s (gm/cm^3)
Gemini 3	160	4.2×10^{-3}	1.5×10^{-12}
Gemini 11	300	1.4×10^{-2}	5.1×10^{-12}
Apollo	300	3×10^{-2}	1×10^{-11}
ATM	400-500	1×10^{-1}	1×10^{-10}

The Apollo and the ATM calculations are based upon estimated leak rates rather than experimental determination. The given leakage rates are total leaks rather than simply water. The estimated water vapor is about three percent of the Table IX-2 values. Considerable discussion is devoted to determining whether the water is all converted to particulate contamination or whether almost none of it is. (Various references differ.) Further, considerable discussion is devoted to the question of expulsion velocity. The assumptions which were made were that all of the water vapor was converted to ice particles and that the particle velocity away from the spacecraft was the speed of sound at the leakage orifice. With these assumptions, the authors calculated the last column of Table IX-2 which applies strictly to the ice particles. These data next are applied to determining the radiance of the debris cloud. The primary contribution is that of sunlight which is scattered by the ice particles. Also, there is scattering of the light by the spacecraft as well as scattering of earthlight. The authors did not attempt to calculate the spacecraft scattering effect because of inadequate data. They do however, treat the sun and earth effects. The radiance of the debris atmosphere can be described by:

$$\frac{B}{B'} \approx \Omega' \, \sigma(\epsilon) \, M_s \qquad \text{(IX-48)}$$

where:

B = debris cloud brightness

B′ = sun's mean surface brightness

$\sigma(\epsilon)$ = mass scattering function

Ω' = solid angle subtended by the sun at the spacecraft

The relative Mie scattering functions $\sigma'(\theta)$, for spherical particles having an index of refraction, m, of 1.30 were calculated. A particle size distribution $n(r) \propto r^{-k}$ with k = 3 was selected. (This distribution provides numerous small particles.) The value chosen for k lies between that normally selected for zodiacal particles and that used for aerosols. The range of particle radii was $0.2 < r < 10\mu$ (corresponding to a range in $\alpha = 2\pi r/\lambda$ of $2 \leq \alpha \leq 120$ for $\lambda = 5300$ A). For particles of size much smaller than 1μ, the scattering would approach Rayleigh scattering. Particles of size much larger than 10μ would tend to scatter as random individuals and would not contribute to the general background radiance. The total scattering function is related to the relative scattering function by:

$$\sigma(\theta) = 1.2 \times 10^2 \, \sigma'(\theta) = 1.2 \times 10^2 \int_2^{120} [i_1(\alpha, \theta) + i_2(\alpha, \theta)] \alpha^{-3} \, d\alpha. \qquad \text{(IX-49)}$$

Here i_1 and i_2 are the individual particle scattering functions. Selected values of $\sigma'(\theta)$ are presented in Table IX-3.

Table IX-3
Values of the Relative Scattering Function $\sigma'(\theta)$ for $\lambda = 5300$ Å, $n(r) \propto r^{-3}$, and $2 \leq \alpha \leq 120$ (Ref. IX-11)

θ	$\sigma'(\theta)$
1°	5.3×10^5
2°	2.2×10^5
4°	5.7×10^4
6°	2.6×10^4
10°	1.1×10^4
20°	3.7×10^3
40°	4.0×10^2
60°	6.0×10^1
80°	2.1×10^1
100°	7.8
120°	6.7
140°	7.8
160°	1.1×10^1
180°	3.4×10^1

To obtain the apparent brightness of the Earth at spacecraft altitudes (160 to 500 km), the earthlight observations of Danjon (Ref. IX-12) were used. For this altitude range the Earth will appear more luminous (than as seen at the Moon) by factors of 160 to 420, respectively. Thus, the Earth will appear brighter by D magnitudes at the spacecraft, and Danjon's relation becomes:

$$E - S \approx 10 - D + 1.30 \left(\frac{\tau}{100}\right) + 0.19 \left(\frac{\tau}{100}\right)^2 + 0.48 \left(\frac{\tau}{100}\right)^3 \qquad \text{(IX-50)}$$

where:

$E - S$ = brightness differences (in magnitudes) between the Earth and Sun

τ = phase angle of the spacecraft as seen from the center of the Earth.

The intensity of the scattered earthlight is given by:

$$\left(\frac{B}{B'}\right)_{EL} \approx \Omega'' \frac{B''}{B'} \sigma(\Phi) M_s \qquad \text{(IX-51)}$$

$$\log \left(\frac{B''}{B'}\right) = - 0.4 \ [E - S] \qquad \text{(IX-52)}$$

where:

EL = refers to earthlight

Φ = scattering angle

$= 180° - (\epsilon - \tau)$

The total radiance produced by the debris atmosphere is:

$$\left(\frac{B}{B'}\right)_{total} = \frac{B}{B'} + \left(\frac{B}{B'}\right)_{EL} \qquad \text{(IX-53)}$$

Reference IX-11 presents several figures showing the results of these calculations. The significant conclusions are daylight observations of dim light sources probably will not be feasible from Apollo and ATM. Calculated Gemini background brightness is roughly as reported by the astronauts. The background radiance of GT-3 is about 3×10^{-11} B', and that of GT-11 is about 10^{-10} B'. With these background values, stars fainter than about a magnitude 4.0 to 4.5 cannot be observed.

Now we roughly apply these results to the effect from the ammonia thruster. We will base the comparison on the spherical spacecraft model. Examination of Equation (IX-46) shows the column mass density to be inversely proportional to spacecraft radius and directly proportional to mass release rate. The brightness relationships in Equations IX-48 and IX-51 are directly related to the column mass density. Consequently, if we neglect all other variables, we may write:

$$R = \left[\frac{(6.8 \times 10^{-3}) \left(\frac{45}{10^6}\right)}{(4.2 \times 10^{-3}) (.03)}\right] \left(\frac{200}{24}\right) = 2 \times 10^{-3} \qquad \text{(IX-54)}$$

where the first term is the water (or other contaminant), the second is the spacecraft radius ratio, and R is the change in the debris brightness. The particulate contribution is based upon the 3 mlb thrust engine with all of the water, oil, and salt impurities but none of the NH_3 appearing as condensate (see Section IX-2). The ratio is based upon a comparison to the Gemini 3 spacecraft, which had the smallest leak rate. The perturbation due to scattering of sun and earthlight with these assumptions is roughly a factor of 1000 less with the ATS spacecraft than with the Gemini 3 spacecraft.

Of course, this comparison was based upon a uniform ejection of material from the spacecraft. The thruster does not operate in this manner but preferentially ejects material. If the material impinges totally upon the spacecraft and then is reemited, the comparison is roughly valid. If, on the other hand, we consider that we are "looking" down the exhaust plume, then it is more grossly in error because of two effects. In one case, the exhaust velocity from the thruster probably will be higher than assumed by the Gemini calculation, which makes the value of R in Equation IX-54 smaller than shown. Counterbalancing this is the preferential grouping of the exhaust plume into a smaller solid angle, which increases the ratio. The effects tend to balance although we have not evaluated them quantitatively.

We have not mentioned an additional effect which could occur. This is the effect of condensation in the thruster exhaust which forms droplets or particles of ammonia. This phenomenon has been studied extensively but is not fully understood. For example, Feder (Ref. IX-13) has reviewed the field of homogenous nucleation in the condensation process and has found a discrepancy of a factor of 10^{-18} in prediction of nucleation rates by the classical theory as compared to the steady state theory. Further, this reference casts doubt upon the correctness of the available experimental data. Courtney (Ref. IX-14) reaches a similar qualitative conclusion and further states ". . . the validity and usefulness of the various nucleation theories remain uncertain or at least quite arguable."

The processes are discussed further and in many instances specifically applied to various gas phenomena in References IX-15 through IX-24. We have not investigated this phenomenon, and such a lack of investigation is a weak point of this report.

Another weakness is lack of investigation of a molecular or atomic interaction. Most of the exhaust material is in a non-particulate form and hence neglected in the previous scattering investigation. The effect, although small, could be significant for sensitive instruments. Of course, similar behavior also would result with hydrazine thrusters.

6. ATMOSPHERIC DENSITY DETERMINATION

So far, we have found the perturbation due to the ammonia thrusters to be negligible. This is not necessarily the case if the spacecraft is attempting to determine ambient density. Typical densities are listed in Table IV-4.

To approximate the ammonia density in the vicinity of the spacecraft, we first assume all of the ammonia exhaust intersects the spacecraft where it is absorbed and reevaporated. (Of course, this is a conservative assumption). Next, we assume an effective spacecraft temperature of 300°K and calculate the velocity of particles at this temperature according to:

$$\bar{v} = \sqrt{\frac{8k\,T_0\,\dot{N}_0'}{\pi M}} \qquad \text{(IX-36)}$$

$$= \left[\frac{(18)\,(1.38)\,(10^{-16})\,(300)\,(6.02)\,(10^{23})}{(\pi)\,(17)}\right]^{1/2} \qquad \text{(IX-55)}$$

$$= 6.10 \times 10^4 \text{ cm/sec}$$

Table IX-4
Space Plasma Properties (Ref. IX-25)

Altitude (km)	Density Particles/cm^3		Temperature °K		Mean Mass (ions) (amu)
	Neutral	Charged	Neutral	Charged	
100	10^{13}	10^5	200	200 - 250	30
400	10^8	10^6	1400	1600 - 2800	20
1200	10^5	10^4	1400	2600 - 3000	10
3000	10^4	10^4 - 10^3	–	5000	2
2 R_E	–	10^3	–	10^5	~1
10 R_E	–	10^2	–	10^5	~1
1000 R_E	–	10	–	10^5	~1
(R_E = earth radius, 6380 km)					

Now we may obtain the particle density from

$$\rho = \frac{\dot{M}}{4\pi x^2 \bar{v}} \qquad \text{(IX-13)}$$

$$= \frac{(2.41)(10^{20})}{(4\pi)(6.10)(10^4)x^2} \qquad \text{(IX-56)}$$

$$= 3.14 \times 10^{14}/x^2$$

Typical densities obtained by this equation are:

Distance From Spacecraft Center, cm	Density, Particles/cm^3
24 (surface)	5×10^{11}
50	1×10^{11}
100	3×10^{10}
500	1×10^9

In comparing these numbers with the Table IX-4 data, we see that the particle density at roughly 100 centimeters is of the order of a factor of 10 higher than the density which could result from the ammonia thruster. The density at 400 centimeters is lower than that indicated for the thruster. However, because of the conservatism in calculating the thruster caused particle densities, we may only draw the conclusion that there might be an interference problem. Certainly, if such density measurements are to be performed aboard the spacecraft, then further analysis is indicated.

This comparison was done on the basis of the three millipound thrust engine. Operation of the other thrusters causes release of significantly greater quantities of material for short time periods. Such emissions would significantly perturb the ambient density for a short time. Since these thrusters are only subject to intermittent operation, the perturbation situation should clear rapidly.

7. OTHER EFFECTS

Few exhaust interaction problems were encounted in the hydrazine and ammonia studies. We studied a number of mechanisms in an attempt to find such reactions that have not been covered in this report. Several of these studies will be covered in this section.

7.1 Thermal Ionization

Consider a pure substance composed of molecules which we will designate by A. If this substance is heated it will begin to dissociate according to the chemical reaction equation:

$$A \longleftrightarrow B + C \tag{IX-57}$$

As the temperature increases, the dissociation shifts toward the right. At high enough temperatures the molecules become almost completely dissociated into atoms.

As temperature is increased further another reaction begins to occur:

$$B \longleftrightarrow B^{+} + e^{-} \tag{IX-58}$$

This equation represents the splitting of electrons from the neutral atoms with the formation of a charged ion and an electron. At higher temperatures further electrons can be split off to form doubly charged ions, etc. This process can be investigated by considering it as a chemical reaction which occurs according to:

$$\nu_1 A_1 \longleftrightarrow \nu_2 A_2 + \nu_3 A_3 \tag{IX-59}$$

where:

A = refers to substances involved in the reaction

ν = number of atoms or molecules of the respective substance

For a homogeneous phase under equilibrium conditions, we must have:

$$\nu_1 \mu_1 = \nu_2 \mu_2 + \nu_3 \mu_3 \tag{IX-60}$$

where:

μ = chemical potential.

For an ideal gas the chemical potential may be represented by (see, for example Reference IX-26):

$$\mu = RT\,(\Phi + \ln P + \ln x) \tag{IX-61}$$

where:

R = gas constant

T = temperature

Φ = function of temperature

P = pressure

x = mole fraction.

This may be substituted to yield:

$$\ln\left(\frac{x_2 x_3}{x_1} P^{\nu_2+\nu_3-\nu_1}\right) = -(\nu_2\Phi_2 + \nu_3\Phi_3 - \nu_1\Phi_1) \tag{IX-62}$$

The right hand side of this expression is a function of temperature only. It may be represented by a "constant," K, so that:

$$K = \frac{x_2 x_3}{x_1} P^{\nu_2+\nu_3-\nu_1} \tag{IX-63}$$

The term K is the equilibrium constant. Equation (IX-63) is called the law of mass action.

The variable Φ can be shown to be (Ref. IX-26):

$$\Phi = \frac{h_0}{RT} = \frac{1}{R}\int \frac{\int C_p\,dT}{T^2}\,dT - \frac{s_0}{R} \tag{IX-64}$$

where:

h = enthalpy

C_p = heat capacity at constant pressure

s = entropy

0 = refers to a reference value

Further:

$$C_p = \nu_2 C_{p2} + \nu_3 C_{p3} - \nu_1 C_{p1} \tag{IX-65}$$

$$\Delta H_0 = \nu_2 h_{02} + \nu_3 h_{03} - \nu_1 h_{01} \tag{IX-66}$$

$$\Delta S_0 = \nu_2 s_{02} + \nu_3 s_{03} - \nu_1 s_{01} \tag{IX-67}$$

From which we may obtain:

$$\ln K = -\frac{\Delta H_0}{RT} + \frac{1}{R}\int \frac{\int (\nu_2 C_{p2} + \nu_3 C_{p3} - \nu_1 C_{p1})\, dT}{T^2}\, dT + \frac{\Delta S_0}{R} \tag{IX-68}$$

which is called Nernst's equation: Now we consider the ionization reaction of a nitrogen atom:

$$N \longleftrightarrow N^+ + e^- \tag{IX-69}$$

We will treat this as a mixture of three ideal monatomic gases (following the approach of Saha as outlined in Reference IX-26). Since we have monatomic gases:

$$C_p = \frac{5R}{2} \tag{IX-70}$$

and:

$$\frac{1}{R}\int \frac{\int (\nu_2 C_{p2} + \nu_3 C_{p3} - \nu_1 C_{p1})\, dT}{T^2}\, dT = \frac{5}{2}\ln T \tag{IX-71}$$

Now, ΔH_0 is the energy required to ionize one mole of atoms. If the ionization potential is E (volts), then:

$$\Delta H_0 = \frac{E(\text{volts}) \times 1.59 \times 10^{-19} \frac{\text{coulomb}}{\text{electron}} \times 6.06 \times 10^{23} \frac{\text{electrons}}{\text{mole}}}{4.19 \frac{\text{joule}}{\text{cal}}} = 23{,}070E \text{ cal/mole.} \tag{IX-72}$$

If we also define a constant B by:

$$\ln B = \frac{\Delta S_0}{R} \tag{IX-73}$$

then, by substitution, we find:

$$\ln K = \frac{23070E}{RT} + \frac{5}{2}\ln(T) + \ln B \tag{IX-74}$$

Saha obtained B from a statistical thermodynamic treatment, which gave:

$$\log (K) = -\frac{23070E}{4.573T} + \frac{5}{2}\log (T) + \log\left(\frac{\omega_i\, \omega_e}{\omega_a}\right) - 6.491 \qquad \text{(IX-75)}$$

where:

T = °K

K = atm

ω = constant

The ω's refer to the ion, electron, and atom, as indicated by the subscript. These terms account for the degeneration of spin in the electrons and for degeneration of angular momentum in ions and neutral atoms (Ref. IX-27). The value of ω_e is 2. The other values can be $\omega_i = 1$, $\omega_a = 2$; or $\omega_i = 2$, $\omega_a = 1$. For N we use $\omega_a = 2$, $\omega_i = 1$. Hence,

$$\log (K) = -\frac{23070E}{4.573T} + \frac{5}{2}\log (T) - 6.491 \qquad \text{(IX-76)}$$

An alternate form that is sometimes useful is given by Reference IX-27:

$$\frac{x'^2}{1 - x'^2} = \frac{(\pi m)^{3/2}\,(2k)^{5/2}}{h^3}\,\frac{\omega_i}{\omega_a}\,\frac{T^{5/2}}{p}\,e^{W_0/RT} \qquad \text{(IX-77)}$$

where:

x′ = extent of reaction

m = mass of a gaseous atom

k = Boltzmann's constant

h = Planck's constant

W_0 = ionization potential per mole of atoms

and the mole ratios of the constituents are given by:

$$x_a = \frac{1 - x'}{1 + x'} \qquad \text{(IX-78)}$$

$$x_i = x_e = \frac{x'}{1 + x'} \qquad \text{(IX-79)}$$

The ionization potential is about 15 eV (Ref. IX-28). Hence, at 70°F (294°K) we find:

$$\log (K) = -\frac{(23070)\,(15)}{(4.573)\,(294)} + \frac{5}{2}\log (294) - 6.491 = -257 \qquad \text{(IX-80)}$$

and at 1500°F (1090°K):

$$\log (K) = - \frac{(23070)\,(15)}{(4.573)\,(1090)} + \frac{5}{2} \log (1090) - 6.491$$

$$= -68.4 \qquad \text{(IX-81)}$$

$$K\ @\ 70°F = 10^{-257} \quad K\ @\ 1500°F = 4 \times 10^{-69}$$

At one atm Equation IX-63 gives:

$$\frac{x_2 x_3}{x_1} = K \qquad \text{(IX-82)}$$

We know that:

$$x_2 = x_3 \qquad \text{(IX-83)}$$

$$x_1 + x_2 + x_3 = 1 \qquad \text{(IX-84)}$$

so that:

$$\frac{x_2^2}{1 - 2x_2} = K \qquad \text{(IX-85)}$$

$$x_2 = \frac{- 2K \pm \sqrt{4K^2 + 4K}}{2} \qquad \text{(IX-86)}$$

Since x_2 must be positive, we find:

$$x_2 = - K + \sqrt{K^2 + K} \qquad \text{(IX-87)}$$

At 70°F, we find:

$$x_2 = - 10^{-257} + \sqrt{10^{-514} + 10^{-257}} \approx 10^{-128} \qquad \text{(IX-88)}$$

At 1500°F:

$$x_2 = - 4 \times 10^{-69} + \sqrt{16 \times 10^{-8} + 4 \times 10^{-69}}$$

$$\approx 2 \times 10^{-34} \qquad \text{(IX-89)}$$

We conclude there is negligible ionization due to the reaction:

$$N \longleftrightarrow N^+ + e^- \qquad \text{(IX-90)}$$

at one atmosphere pressure. Examination of Equation (IX-63) shows that changing the pressure within reasonable limits (a few decades) will have no effect upon the conclusion.

A number of ionization reactions are possible, as shown in Table IX-5. The mathematical treatment we have presented may be strictly applied only to monoatomic processes, which restricts it to the first reaction. The heat capacity and degeneracy term differ for the remainder of the equations. A cursory look at the equations leads to a tentative conclusion that the degree of ionization may be changed drastically for these other processes - but not so drastically that we should change our conclusions. Hence, ionization should not occur to a sufficient degree that charged particles are produced which in turn react with the spacecraft to cause a problem with an ammonia thruster.

7.2 Charged Polymer Formation

Bentley (Ref. IX-29) has reported that charged polymers exist in some gases when they are under pressure. He reports the effect of pressure on CO_2 as shown in Figure IX-3. The behavior follows the equation:

$$I_2 = K_2 P^{2.85} \qquad \text{(IX-91)}$$

where:

$I_2 = (CO_2)_2^+$ ion intensity

K_2 = constant

P = pressure

Table IX-5
Ionization Reactions (Ref. IX-28)

Reaction	Ionization Potential (eV)
$N \longleftrightarrow N^+ + e^-$	15
$N_2 \longleftrightarrow N + N^+ + e^-$	24
$NH_3 \longleftrightarrow N^+ + H_2 + H + e^-$	23
$NH_3 \longleftrightarrow N^+ + 3H + e^-$	27
$N_2 \longleftrightarrow N_2^+ + e^-$	16
$N_2 \longleftrightarrow N_2^{+2} + 2\,e^-$	44
$NH \longleftrightarrow NH^+ + e^-$	13
$NH_3 \longleftrightarrow NH^+ + H_2 + e^-$	17
$NH_3 \longleftrightarrow NH^+ + 2H + e^-$	22
$NH_2 \longleftrightarrow NH_2^+ + e^-$	11
$NH_3 \longleftrightarrow NH_2^+ + H + e^-$	16
$NH_3 \longleftrightarrow NH_3^+ + e^-$	10
$NH_3 \longleftrightarrow NH_3^{+2} + 2\,e^-$	~35

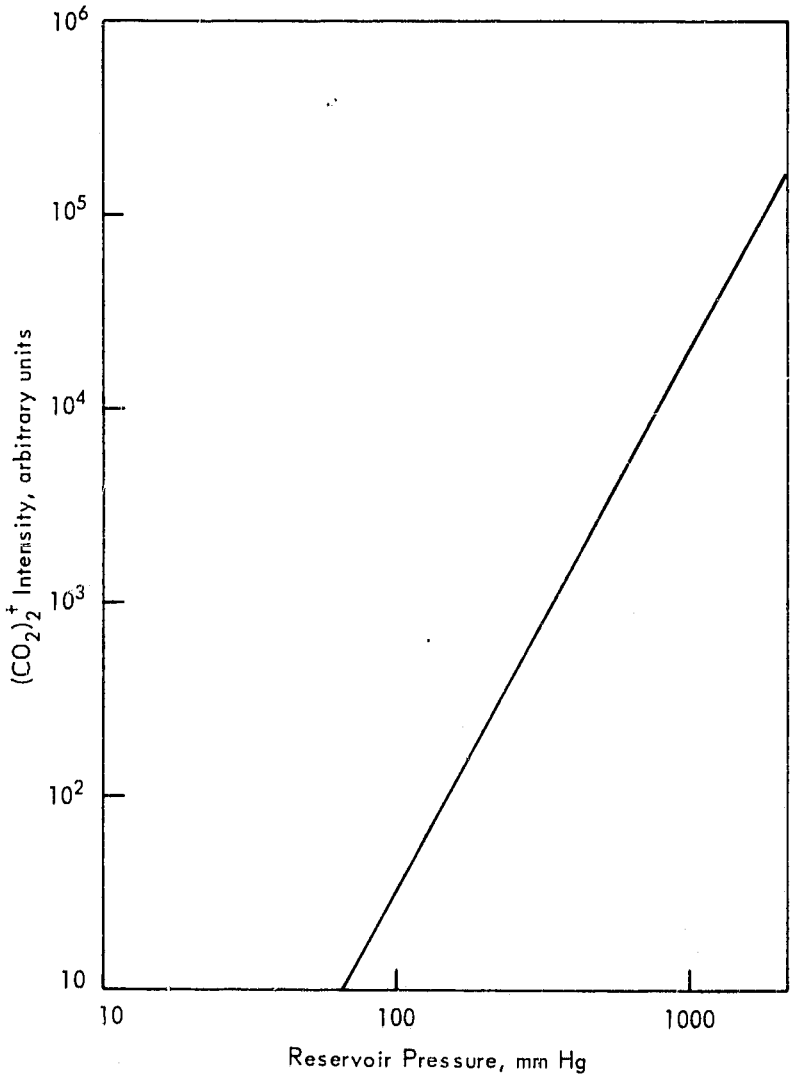

Figure IX-3. Variation of $(CO_2)_2^+$ Ion Intensity with Pressure.

He also reports for $(CO_2)_3^+$ and $(CO_2)_4^+$:

$$I_3 = K_3 P^{7.8} \tag{IX-92}$$

$$I_4 = K_4 P^{11} \tag{IX-93}$$

and states that the pressure variation is too rapid to permit measurement for the larger polymers. The overall measured ion intensities are shown in Figure IX-4.

The source of these polymers has not been positively identified nor has the effect of temperature been investigated. The author also suggests that investigation of other gases would be of interest.

This is the only report of this nature we have found in the literature (admittedly - our literature search is not complete - particularly with respect to this effect). The ratio of charged polymers to neutral atoms, particularly at the lower molecule sizes, is significant. The effect with increasing pressure also is pronounced. If this effect were real with NH_3, it could have a pronounced effect upon the spacecraft. We do not believe this is the case, nor are we completely convinced it would occur with CO_2 flowing through a nozzle. Reference IX-28 gives a few effects with NH_3 (see Table IX-5), but

there is little information regarding charged polymers. There is nothing of interest regarding $(CO_2)_n^+$ and we find it difficult to believe that Franklin (Ref. IX-28) would have missed Bentley's report (the former issued in 1969, the latter in 1961). Consequently, we tentatively conclude that either no substantiating quantitative information is available or the effect was unique to Bentley's apparatus. If a more complete study of nozzle effects is deemed advisable, we recommend a further investigation of this phenomenon.

7.3 Charge Generation

Charges can be produced under many circumstances, a few of which are:

1. Surface separation
2. Rise of gas bubbles
3. Liquid atomization
4. Breakup of a liquid stream by impact upon a dissimilar surface
5. Passage of a semiconducting liquid such a gasoline through a metallic pipe.

The phenomena have been recognized for many years, but the theory is not well developed. The situation is complicated by a lack of reproducibility. Molmud (Ref. IX-30)

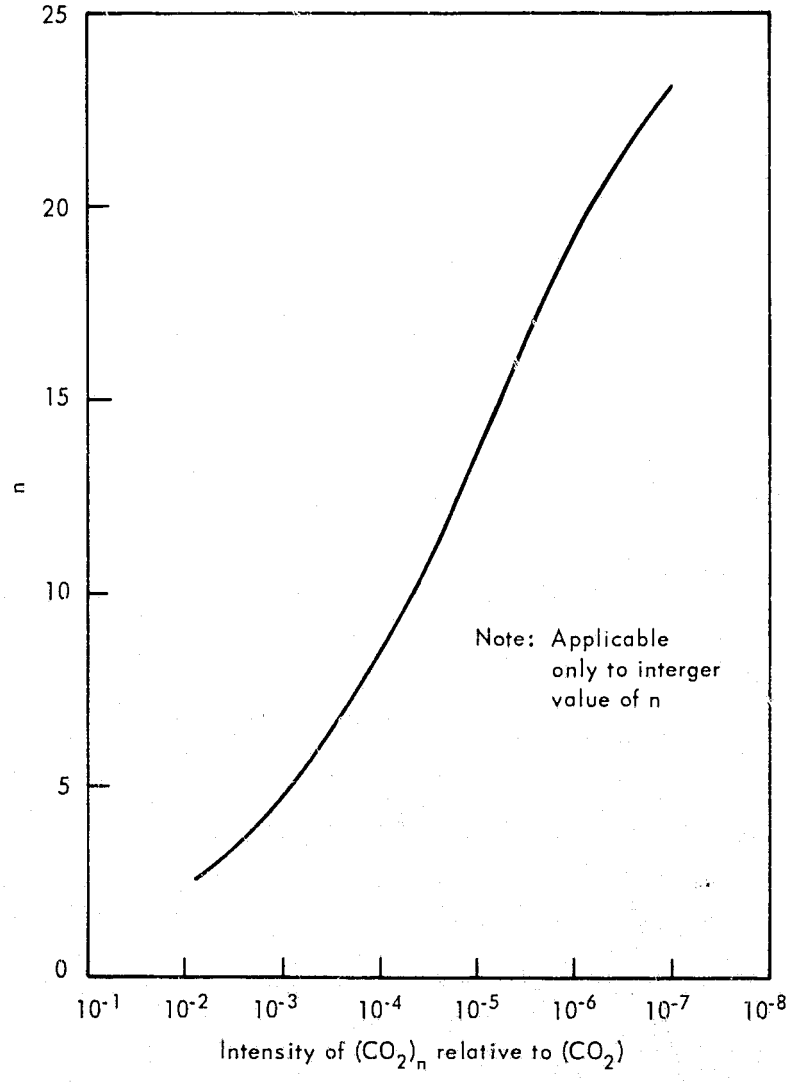

Figure IX-4. Ion Intensities for a Reservoir Pressure of 3800 mm Hg.

cites a study with hydrocarbons in which electrification occurs with fresh liquid, but the effect is diminished when the liquid is reused. Somehow, the liquid loses its ability to electrify.

Vance (Ref. IX-31) has investigated the situation further. He discusses in some depth the charging effects of jet engines, where there appears to be a relation to throttle setting, the water injection system, and time from take off. The maximum observed rate was about 800 μ amp. The qualitative theory ascribes the effect to plasma processes in the combustion chamber. A positive ion sheath is supposed to develop in the chamber and a portion of this is presumed to be expelled with the exhaust gases. This adequately explains the observed negative charge buildup in many observations. Unfortunately, positive charge buildup also is observed. Separate mechanisms are postulated to explain this. These include:

1. Combustion chamber and wall photoemission
2. Combustion chamber and wall thermionic emission
3. Triboelectric charging due to particle - wall collisions in the combustion chamber, fuel flow, and atomization.

Further mechanisms are proposed to supplement the negative charging:

1. Contact ionization
2. Triboelectric charging
3. Fuel flow

Most of these postulates do not stand up to a careful examination. For example, using Vance's data for typical conditions in a rocket motor:

Temperature	=	3000°K
Pressure	=	30 atm
Charge density	=	10^{12} charges/cm^3
Exhaust velocity	=	2000 m/sec
Atomic Number	=	28

and

$$\sigma_e = \frac{ne^2}{m\nu_e} \qquad \text{(IX-94)}$$

$$\sigma_i = \frac{ne^2}{M\nu_i} \qquad \text{(IX-95)}$$

where:

σ_e = electronic conductivity of combustion products
n = electron density
e = electron charge
m = electron mass
ν_e = electron-neutral collision frequency

σ_i = ionic conductivity

M = ion mass

ν_i = ion-neutral collision frequency,

and where we have assumed a neutral plasma (ion and electron densities equal and the ions are singly charged), then we obtain $\sigma_e = 8 \times 10^{-4}$ m ohm m, $\sigma_i = 9 \times 10^{-7}$ m ohm m. Vance states that the time constant for exponential decay of a charge in a conductive medium is $8.85 \times 10^{-12} / \sigma$ sec. Hence, we obtain an expected life of $8.85 \times 10^{-12} / 8 \times 10^{-4} = 10^{-8}$ sec. for electrons and $8.85 \times 10^{-12} / 9 \times 10^{-7} = 10^{-5}$ sec. for the positive ions. Exhaust velocities are a few mm/sec. Therefore, few exhaust particles can be swept out of the engine prior to neutralization. The conclusion is that all of the postulated charging mechanisms fall apart except the positive ion sheath approach - and this only accounts for negative charge build up.

Vance postulated that electron emission from the back of an engine nozzle could account for negative charge production. He performed a preliminary analysis to support the postulate. He also warned that the postulate neither proved nor disproved that triboelectric charging could be an effective positive charging mechanism. He further went into the effect of charged smoke particles and several other mechanisms which are not applicable to the ATS System.

Some work was reported for the Nike-Cajuns. The predicted vehicle potential due to exhaust emission was only 0.54 volts. This effect was extremely low insofar as charge distribution effect was concerned, and probably could not be determined easily because ionospheric effects would mask the low potential due to the small emission effect. Of direct application to the ATS satellites is the magnitude of the effect. The reported data are for a rocket engine operating at high temperatures where the charging should be much greater than for the ammonia thrusters we are investigating. Aronowitz (Ref. IX-32) studies the problem further by investigating vehicles in space. One of his conclusions is of direct concern since it potentially could have a large effect. In discussing the potential a space vehicle can achieve, Aronowitz states "The potential that this mechanism can generate is limited, since the residual negative charge left on the vehicle will attract the positive charge in the exhaust. . . In space this potential is small, an indication that no serious charging effects are produced by a rocket engine." Immediately, we see that Aronowitz has concluded that if charges are present, they will be rapidly neutralized by attracting positive ions to the spacecraft. This is precisely the effect we wish to investigate since it is a direct mechanism for transferring exhaust effluent back to the spacecraft and its experiments.

Analyses of the effect are based upon the presence of a stable space charge region called a sheath. This exists where the plasma contacts an electrode wall. The postulated reason for its existence is that the diffusion rate of electrons from the plasma to the wall is greater than the diffusion rate of positive ions. This results in a layer which is depleted of electrons and consequently has a net positive charge. This positive charge then is postulated as being carried out of the rocket in the exhaust. The key requirement for our investigation is the presence of an ionized plasma. If that does not exist, then the effect is not present. As we have seen, there were not a sufficient number of charges generated by the previously postulated mechanisms to be of concern for the low temperature exhaust. Even a 1500°F temperature, associated with the station keeping thrusters, is insufficient for a reasonable quantity of ion production.

Unfortunately, this approach fails to consider the static electricity effect of nonconductors which have been observed in some flows (for example, gasoline, as we previously mentioned). As near as we can tell, the lack of an adequate theoretical understanding of the phenomena will not permit a quantitative analysis. We may only conclude that the problem is not of sufficient magnitude to cause trouble. The conclusion is based

upon the lack of reported problems in this category in the literature. Unfortunately, such problems may exist but have not been recognized, and could perturb sensitive components. Therefore, this conclusion must be considered as a weak point in our presentation. Further investigation is desirable.

7.4 Charge Exchange

The charge exchange cross sections for several charged particles interacting with ammonia are shown in Figure IX-5. These cross sections are of the usual magnitude and require a substantial number of charged particles in order to create sufficient interactions to cause a problem. As we have seen, there is no source of a large number of particles. Further, there is no possibility of substantial cross section changes outside the range of Figure IX-5. The charge exchange cross section theoretically approaches zero. No drastic effects occur at the higher energies. We conclude that charge exchange is not a problem for ammonia thrusters.

7.5 Photochemical Charge Generation

Photochemical decomposition of ammonia has been reported by Bayes (Ref. IX-34). The photochemical decomposition of ammonia is started in the long wave-length absorption region between 2.200 A and 1650 A by the predissociation:

$$NH_3 + h\nu \rightarrow NH_2 + H \quad (\lambda < 2.200A) \qquad \text{(IX-96)}$$

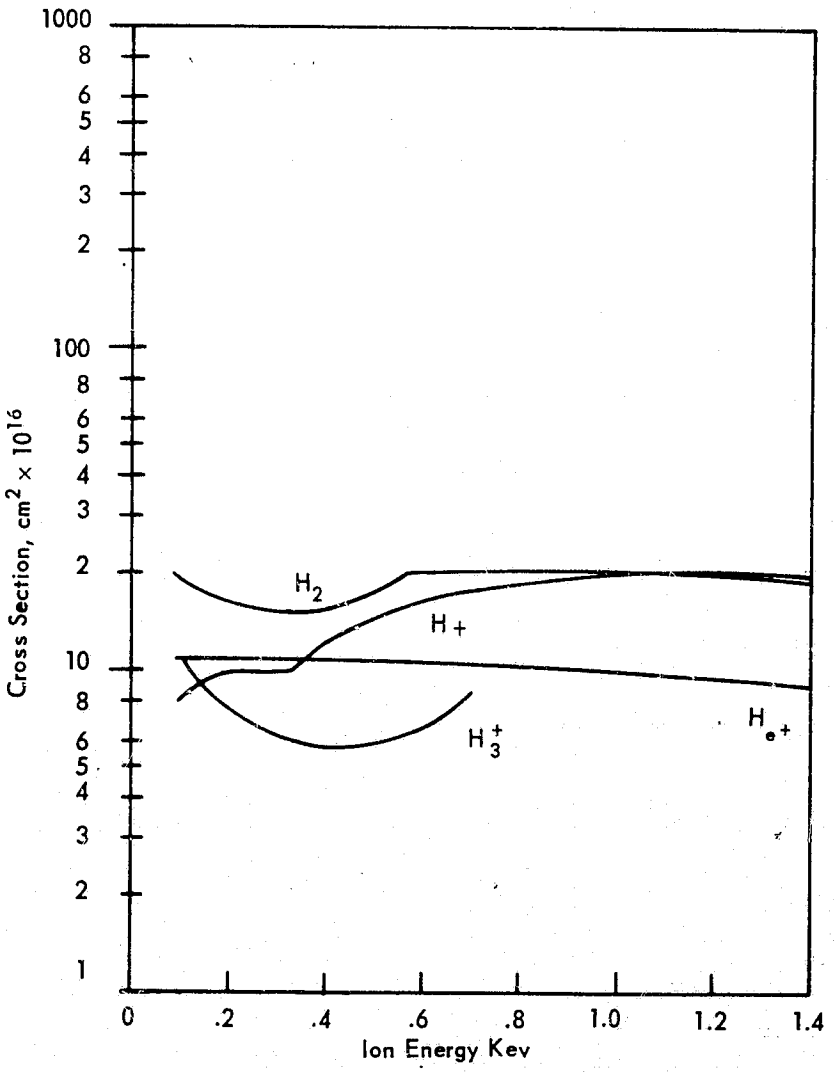

Figure IX-5. NH_3 Charge Exchange Cross Sections (Ref. IX-33).

At shorter wavelengths the NH_2 radical can be formed in an electronically excited state ($NH_2^{\equiv}$):

$$NH_3 + h\nu \rightarrow NH_2^{\equiv} + H \quad (\lambda < 1.630\text{Å}) \tag{IX-97}$$

Also reported is formation of the NH radical by:

$$NH_3 + h\nu \rightarrow NH + H_2 \quad (\lambda < 1.550\text{Å}) \tag{IX-98}$$

Below 1.225 Å until about 750 Å about 50% of the total absorption cross section is given by the ionization cross section:

$$NH_3 + h\nu \rightarrow NH_3^+ + e^- \quad (\lambda < 1.225\text{Å}) \tag{IX-99}$$

No quantitative data were given. However, because of the low density of ammonia in the exhaust plume, we consider it doubtful that significant reaction by these processes can take place in the plume. There may be a chance such processes could take place on the spacecraft surface, but most of these constituents probably exist on the surface in any event. Further, the quantity that could remain on most surfaces will be limited to one or two monolayers.

An interesting combination of ionization analysis with analysis of an exhaust distribution is presented by Yushchenkova (Ref. IX-35). This reference presented techniques whereby the kinetics of the processes could be investigated. We found no additional information which would lead us to change any of the previously reported conclusions, and consequently did not apply the analysis techniques.

8. MISCELLANEOUS CALCULATIONS

Specific impulse is related to flow rate by:

$$\dot{W} = F/I \tag{IX-100}$$

where:

$\dot{W}$ = propellant flow rate, lbs/sec

F = thrust, lbs.

I = specific impulse, sec

Thus, a 3 m lb thruster with a specific impulse of 200 sec requires $W = (3)(10^{-3})/200 = 1.5 \times 10^{-5}$ lbs/sec; a 50 mlb thruster with a specific impulse of 100 sec requires $(50)(10^{-3})/100 = 5 \times 10^{-4}$ lbs/sec.

The molecular weight of NH_3 is 17.0 gms/mole. Each pound of NH_3 contains:

$$(1\ \text{lb})\left(\frac{454\ \text{gms}}{\text{lb}}\right)\left(\frac{\text{mole}}{17\ \text{gms}}\right)\left(\frac{6.03 \times 10^{23}\ \text{molecules}}{\text{mole}}\right)$$

$$= 1.610 \times 10^{25}\ \text{molecules}$$

The 3 m lb thruster exhausts $(1.5 \times 10^{-5})(1.61 \times 10^{25}) = 2.41 \times 10^{20}$ molecules/sec. The 50 m lb uses $(5 \times 10^{-4})(1.61 \times 10^{25}) = 8.05 \times 10^{21}$ molecules/sec. The former may operate for extended periods, whereas the latter is limited, except at launch, to short pulses.

The evaporation rate of NH_3 molecules at 250°K is 5×10^{23} molecules/cm^2 sec. Clearly, NH_3 will not accumulate upon most spacecraft surfaces. The rate at 100°K is 5×10^{14} molecules/cm^2 sec. Given an unfavorable geometry NH_3 could accumulate at this temperature.

9. REFERENCES

IX-1. Sabelhaus, A., GSFC, personal communication, October 3, 1969.

IX-2. Suddeth, D., GSFC, personal communication, October 1, 1969.

IX-3. Ibid, September 11, 1969.

IX-4. Callens, R., GSFC, personal communication, September 2, 1969.

IX-5. Page, Russell, Carl R. Halback, Michael L. Ownby, and Robert A. Short, "Life Test of Six High Temperature Resistojets," AIAA 7th Electric Propulsion Conference, Paper No. 69-294, March 3-5, 1969.

IX-6. Knox, Bruce P., and Henry R. Eberle, "Propellant Performance Handbook, Volume IV, Part A, Fluorine/Ammonia," Bell Aerosystems, 8173-903008-Vol. 4, Part A, AD 802908, June 1964.

IX-7. Lee, John F., Francis W. Sears, and Donald L. Turcotte, Statistical Thermodynamics, Addison-Wesley, 1963.

IX-8. Fishburne, E. S., R. A. Oman, and J. W. Brook, "Estimated Effects of Gaseous Contaminants on Apollo Applications LM Spectroscopy, "Grumman Research, Dept. Memo. RM-361, N67-31135, April 1967.

IX-9. Leighton, Robert B., Principles of Modern Physics, McGraw Hill, 1959.

IX-10. Perry, John H. (Ed.) Chemical Engineers Handbook, McGraw Hill, 1950.

IX-11. Kovar, N. S., R. P. Kovar, and G. P. Bonner, "Light Scattering By Manned Spacecraft Atmospheres, "Planet. Space Science, Vol. 17, 1969, pp. 143-154.

IX-12. Danjon, A., The Earth as a Planet (Cp. 15 of a book edited by G. P. Kuiper), University of Chicago Press, 1954.

IX-13. Feder, J., J. P. Hirth, J. Lothe, K. C. Russell, and G. M. Pound, "Homogeneous Nucleation in Condensation," AIAA Heterogeneous Combustion Conference, Dec. 11-13, 1963.

IX-14. Courtney, Welby G., "Homogeneous Nucleation from Simple and Complex Systems," AIAA Heterogeneous Combustion Conference, Preprint 63-494, Dec. 11-13, 1963.

IX-15. Glenn, L. A., "Recondensation from a Particle-Vapor Source Flow into Vacuum," AIAA Journal, Vol. 7, No. 4, April, 1969, pp. 593-597.

IX-16. Friichtenicht, J. F., "Evaporation of High-Velocity Particles in Free-Molecule Flow," AIAA Journal, Vol. 7, No. 4, April, 1969, pp. 598-601.

IX-17. Lewis, D. W., "Mariner 69 Contamination" Interoffice Memorandum (not a published document) M69-2011 (SE) Jet Propulsion Laboratory, 23 November 1966.

IX-18. Wegener, Peter P., "Condensation Phenomena in Nozzles," Preprint 63-509, AIAA Heterogeneous Combustion Conference, Palm Beach, Florida, December 11-13, 1963.

IX-19. Wrobel, J. R., "Analysis of the Impingement of Condensed Rocket Exhaust Products upon Proximate Space Vehicles," Contained in The Fluid Dynamic Aspects of Space Flight, Vol. 2, AGARD ograph 87, AGARD-NATO Specialist Meeting Marseille, April 20-24, 1964, Gordon and Breach, 1966, (N68-28999) pp. 291-306.

IX-20. Griffin, James L., and Pauline M. Sherman, "Computer Analysis of Condensation in Highly Expanded Flows," AIAA Journal, Vol. 3, No. 10, October 1965, pp. 1813-1819.

IX-21. Jarvinen, Phillip O., and James Stark Draper, "Underexpanded Gas-Particle Jets," AIAA Journal, Vol. 5, No. 4, April 1967, pp. 824-825.

IX-22. Sutherland, George S., and Michael E. Maes, "A Review of Microrocket Technology: 10^{-6} to 1 lb Thrust," Journal of Spacecraft and Rockets, Vol. 3, No. 8, August 1966, pp. 1153-1165.

IX-23. Greer, H., and D. J. Griep, "Low Thrust Reaction Jet Performance," Aerospace Corporation, TDR-469(5230-33)-2, SSD-TR-65-122, AD470960, August 1965.

IX-24. "Spacecraft Attitude Control Gas System Analysis," SSD-70172R, Hughes Aircraft Company, N67-32369, April 1967.

IX-25. Samir, Uri, "Spacecraft/Space Plasma Interaction," Space Flight, Vol. 10, August 1968, pp. 285-288.

IX-26. Zemansky, Mark W., Heat and Thermodynamics, 4th edition, 1957.

IX-27. Lype, E. F., "Introduction to the Advanced Methods of Thermodynamics," R58AGT412, General Electric (Distribution Restricted to GE employees), June 1958.

IX-28. Franklin, J. L., J. G. Dillard, et al., Ionization Potentials, Appearance Potentials, and Heats of Formation of Gaseous Positive Ions, NSRDS-NBS 26, Department of Commerce, National Bureau of Standards, June 1969.

IX-29. Bentley, P. G., "Polymers of Carbon Dioxide," Nature, volume 190, No. 4774, April 29, 1961, pp. 432-433.

IX-30. Molmud, P., "Frictional Electricity in Missile Systems," ARS Journal, January 1959, pp. 73-75.

IX-31. Vance, E. F., and J. E. Nanevicz, "Rocket Motor Charging Experiments," AFCRL-66-497, Scientific Report 2, AD 638181, June 1966.

IX-32. Aronowitz, Leonard, "Electrostatic Potential generated by Rockets on Vehicles in Space," IEEE Transactions on Electromagnetic Compatibility, Volume EMC-10, No. 4, December 1968, pp. 341-346.

IX-33. Koopman, David W., "Charge Exchange in CH_4 and NH_3," J. Chem. Phys., Volume 49, pp. 5203-5205, December 1, 1968 (A69-17114).

IX-34. Bayes, K. D., K. H. Becker, and K. H. Welge, "Flash Photolyses of NH_3 in the Vacuum Ultraviolet," AF61(052)-381, Bonn University (West Germany), AD 664932.

IX-35. Yushchenkova, N. I., V. I. Nemchenko, and S. A. Lyzhnikov, "Influence of Kinetics of Elementary Processes on Ionization of Low-Temperature Plasma Jets with Various Laws of Distribution of Parameters in the Jets," Air Force Systems Command (translation), FTD-MT-65-548, AD644074.

PRECEDING PAGE BLANK NOT FILMED

APPENDIX X

EXHAUST PLUME ANALYSIS

A number of investigators are studying the effects of exhaust from a nozzle into a vacuum. These studies fall into two general categories:

(1) The method of characteristics - a numerical technique which provides excellent correlation with experimental data in the continuum region, but is time consuming and costly. A large digital computer is required and, frequently, several codes are used consecutively to obtain a solution.

(2) Approximate approaches - various techniques which, in part, avoid the complication of item one. A digital computer may or may not be required, depending upon the investigator and his assumptions.

The latter will be sufficient for our purposes. Further, we will avoid computerized approaches unless necessary to obtain a reasonable accuracy. This will make it easier to retain an "engineering feel" of the behavior.

Obviously, the highest exhaust densities are obtained near the nozzle. As the exhaust expands outward into the void surrounding a spacecraft, its density will decrease. As this occurs, the probability of interactions between molecules within the plume will become lower, finally approaching zero. As long as a large number of molecular interactions are taking place (per unit volume and time) the flow may be considered as continuum. When the interaction rate becomes negligibly small, free molecular flow will exist. The type of flow may be characterized by the Knudsen number (Ref. X-1).

$$K_n = \lambda / \ell \qquad \text{(X-1)}$$

where:

λ = mean free path (mean distance between collisions)

ℓ = characteristic or typical dimension.

The characteristic dimension is taken as the distance a molecule has traveled from the nozzle exit (Ref. X-2).

If no interactions are taking place within the exhaust plume, then nothing is changing the direction of travel of the molecule.

Hence, if the exhaust plume is viewed from a distance, all molecules appear to originate from a common source of point. This "radial flow" is illustrated in Figure X-1 (taken from Sibulkin, Reference X-3). For radial flow, we may write:

$$m' = \rho u \propto 1/r^2 \qquad \text{(X-2)}$$

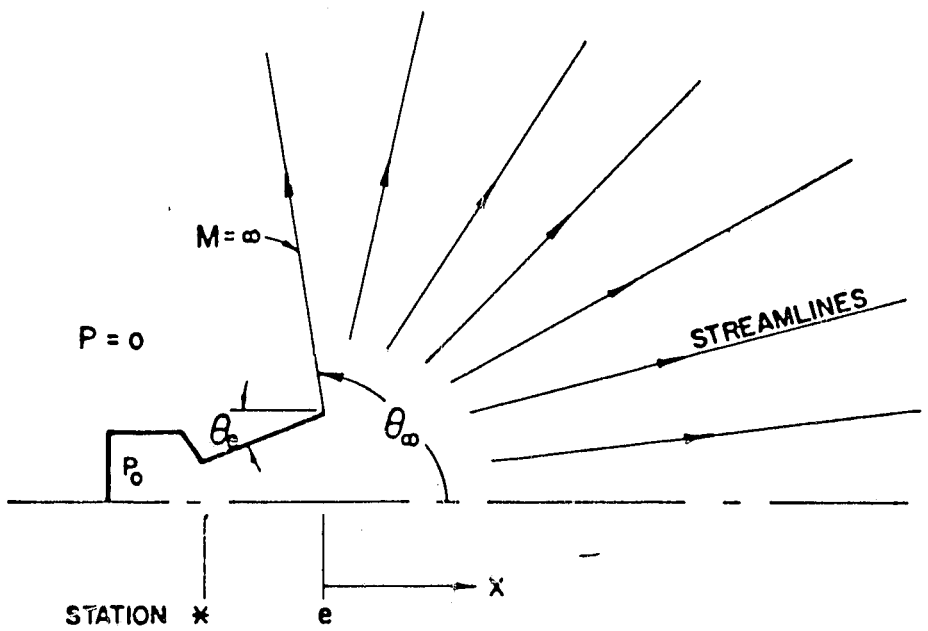

Figure X-1. Schematic of Nozzle Exhausting into a Vacuum (Ref. X-3).

where:

m' = mass flux

α = indicates proportionality

ρ = density

u = velocity (along a streamline)

r = distance from source point.

The velocity approaches a constant as the pressure approaches zero. Therefore, Sibulkin represents the axial density distribution by:

$$\frac{\rho}{\rho_0} = B\left(\frac{r}{d^*}\right)^{-2} \qquad \text{(X-3)}$$

where:

d^* = nozzle throat diameter

ρ_0 = chamber density

B = constant which depends upon the nozzle shape and gas properties.

Figure X-1 indicates a limiting streamline at θ_∞ along which the pressure, P, is zero and the Mach number, M, is infinite. This angle was calculated by Sibulkin using the Prandtl-Meyer equation. The results are shown in Figure X-2 which presents θ_∞ as a function of area ratio A_e/A^* (See figure X-1) for a specific heat ratio γ and a nozzle exit angle $\theta_e = 0$. Other values of θ_e may be investigated from:

$$\theta_\infty = (\theta_\infty)_{\theta=0} + \theta_e \qquad \text{(X-4)}$$

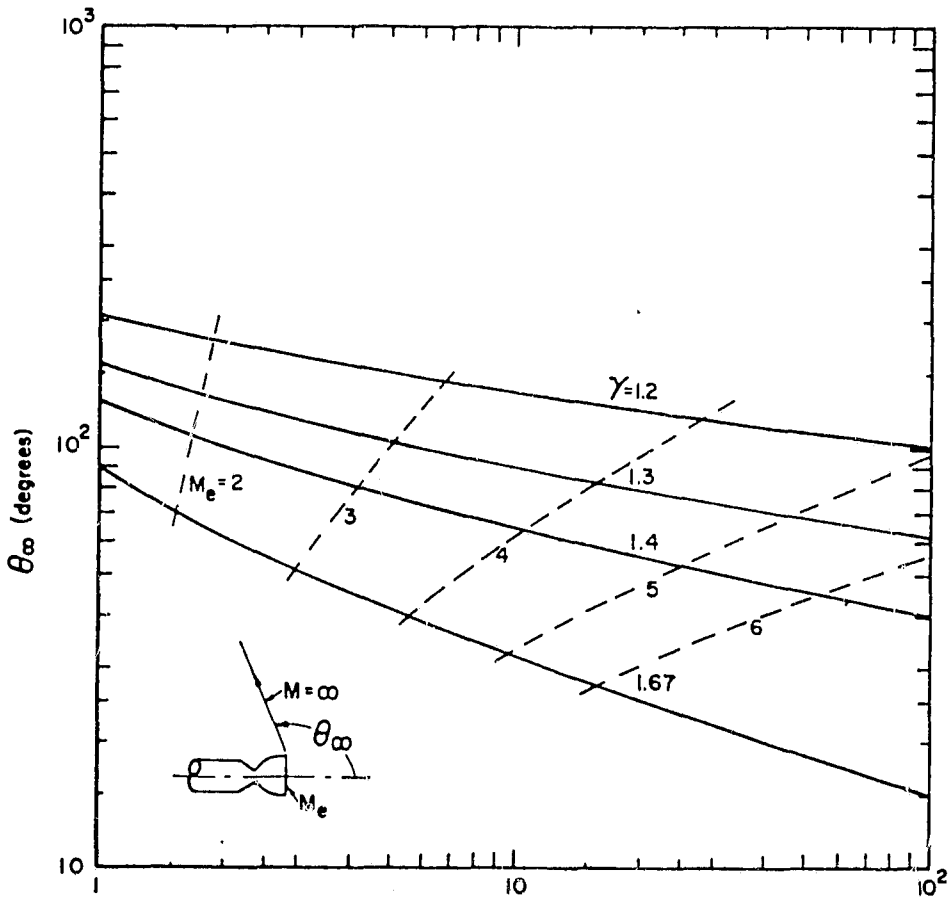

Figure X-2. Variation of the Limiting Streamline Angle θ_∞ with Area Ratio A_e/A^* (Ref. X-3).

The angle θ_∞ defines a cone of solid angle ψ_∞ according to:

$$\psi_\infty = 2\pi\,[1 - \cos(\theta_\infty)] \tag{X-5}$$

This cone contains all of the molecules which exit from the nozzle. Sibulkin postulated that B, therefore, could be represented by a function of ψ_∞ only. This postulation is shown in Figure X-3. The data points are method of characteristics solutions; the broken lines represent approximate solutions for $\theta_e = 0$ (Ref. X-4). The solid line is:

$$B = \frac{0.4\,\pi}{\psi_\infty} \tag{X-6}$$

which gives values of B which are good to within about a factor of 1.5.

Now we substitute Equations (X-6) and (X-5) into (X-3) to obtain:

$$\frac{\rho}{\rho_0} = 0.2\,\frac{(d^*/r)^2}{1 - \cos(\theta_\infty)} \tag{X-7}$$

Hence, as a first approximation of behavior, θ_∞ may be obtained from Figure X-2 and the density distribution calculated using Equation X-7.

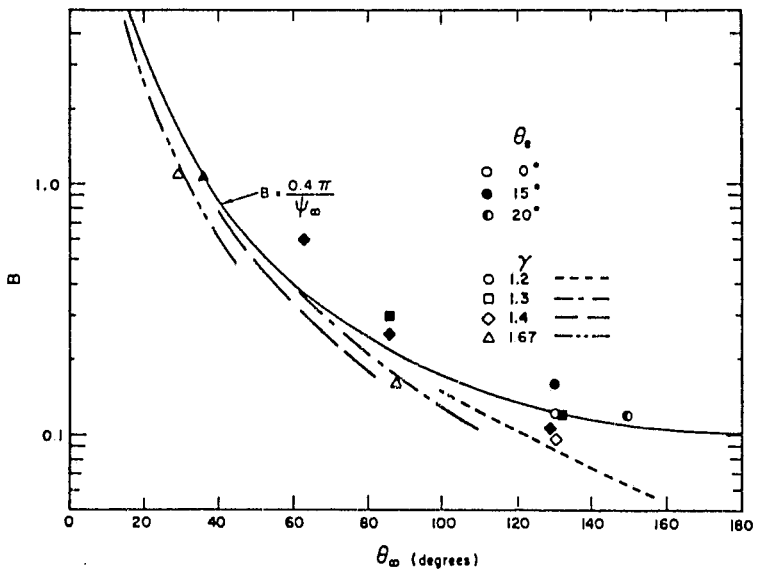

Figure X-3. Density Parameter B as a Function of θ_∞ (Ref. X-3).

Hill (Ref. X-5) made use of the behavior described in Equation (X-2) to write:

$$\frac{d\dot{m}}{d\psi} = \rho u r^2 = \text{a constant along a streamline} \tag{X-8}$$

where:

$\dot{m}$ = mass flow rate.

He further approximated the behavior of $d\dot{m}/d\psi$ by:

$$f(\theta) = \frac{d\dot{m}/d\psi}{(d\dot{m}/d\psi)_{\theta=0}} = \exp\{-\delta^2 [1 - \cos(\theta)]^2\} \tag{X-9}$$

where:

δ = plume shape or spreading parameter

The total mass flow rate is:

$$\dot{m} = \int_0^{\psi_\infty} \frac{d\dot{m}}{d\psi} d\psi \tag{X-10}$$

But

$$d\psi = 2\pi \sin\theta \, d\theta \tag{X-11}$$

and, from Equation (X-9):

$$\frac{d\dot{m}}{d\psi} = f(\theta) \left(\frac{d\dot{m}}{d\psi}\right)_{\theta=0} \tag{X-12}$$

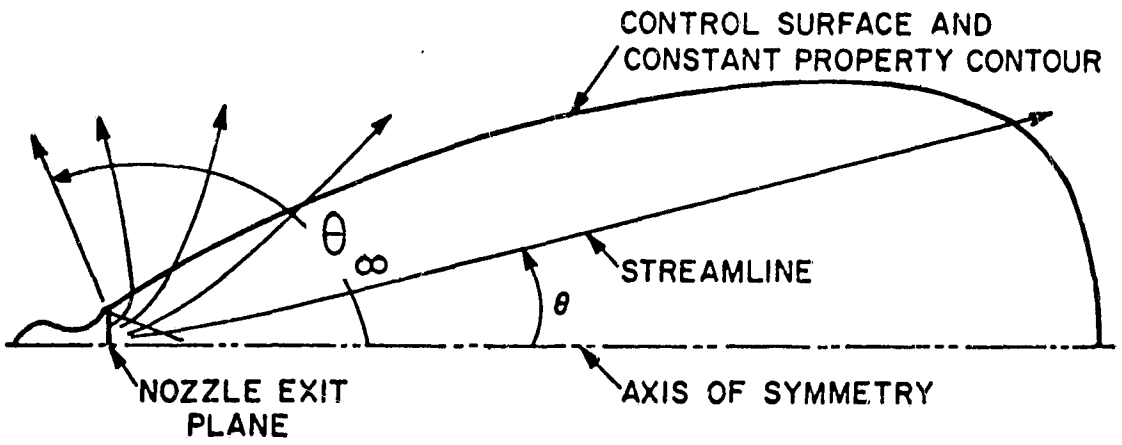

Figure X-4. Schematic Flow Pattern of a Nozzle Exhausting into a Vacuum (Ref. X-5).

so that Equation (X-10) can be written:

$$\dot{m} = 2\pi \left(\frac{d\dot{m}}{d\psi}\right)_{\theta=0} \int_0^{\theta_\infty} f(\theta) \sin\theta \, d\theta \qquad \text{(X-13)}$$

The thrust coefficient is defined by*:

$$C_F = \frac{F}{p_c A^*} \qquad \text{(X-14)}$$

where:

F = thrust

p_c = thruster chamber pressure

A^* = nozzle throat area

But thrust is:

$$F = \frac{\dot{m} V_j}{g} \qquad \text{(X-15)}$$

where:

V_j = effective exhaust velocity at exit

g = gravitation constant

and Equation (X-14) becomes:

$$C_F = \frac{\dot{m} V_j}{p_c g A^*} \qquad \text{(X-16)}$$

*See, for example, Reference X-6, page 432.

Calculation of the mass, as obtained by Equation (X-13) can be accomplished by any desired path. Correlation of the thrust and exhaust pattern is not as straightforward. Hill (Ref. X-5) established the constant density control surface shown in Figure X-4. With this restriction in mind, we relate u to V_j according to:

$$V_j = \frac{\int_0^{\psi_\infty} \frac{d\dot{m}}{d\psi} u \cos\theta \, d\psi}{\int_0^{\psi_\infty} \frac{d\dot{m}}{d\psi} d\psi} \tag{X-17}$$

Substituting Equations (X-11) and (X-12) gives:

$$V_j = \frac{\int_0^{\theta_\infty} f(\theta) \, u \cos\theta \sin\theta \, d\theta}{\int_0^{\theta_\infty} f(\theta) \sin\theta \, d\theta} \tag{X-18}$$

If we integrate along a control surface of constant u, we may write:

$$V_j = \frac{u \int_0^{\theta_\infty} f(\theta) \cos\theta \sin\theta \, d\theta}{\int_0^{\theta_\infty} f(\theta) \sin\theta \, d\theta} \tag{X-19}$$

Substituting Equation (X-13) results in:

$$V_j = \frac{2\pi u}{\dot{m}} \left(\frac{d\dot{m}}{d\psi}\right)_{\theta=0} \int_0^{\theta_\infty} f(\theta) \cos\theta \sin\theta \, d\theta \tag{X-20}$$

We now may write Equation (X-16) as:

$$C_F = \frac{2\pi u}{p_c g A^*} \left(\frac{d\dot{m}}{d\psi}\right)_{\theta=0} \int_0^{\theta_\infty} f(\theta) \cos\theta \sin\theta \, d\theta \tag{X-21}$$

The maximum value of C_F is obtained if all exhaust molecules leave at an angle $\theta = 0$ with a velocity $V_j = u$. Under this condition, Equation (X-16) is:

$$C_{F\,max} = \frac{\dot{m} u}{p_c g A^*} \tag{X-22}$$

$$C_{F\,max} = \frac{2\pi u \left(\frac{d\dot{m}}{d\psi}\right)_{\theta=0}}{p_c g A^*} \int_0^{\theta_\infty} f(\theta) \sin\theta \, d\theta \tag{X-23}$$

Now combine Equations (X-21) and (X-23):

$$\frac{C_F}{C_{F\,max}} = \frac{\int_0^{\theta_\infty} f(\theta) \sin\theta \cos\theta \, d\theta}{\int_0^{\theta_\infty} f(\theta) \sin\theta \, d\theta} \tag{X-24}$$

and substitute Equation (X-9):

$$\frac{C_F}{C_{F\,max}} = \frac{\int_0^{\theta_\infty} \exp\{-\delta^2 [1 - \cos(\theta)]^2\} \sin\theta \cos\theta \, d\theta}{\int_0^{\theta_\infty} \exp\{-\delta^2 [1 - \cos(\theta)]^2\} \sin\theta \, d\theta} \tag{X-25}$$

For convenience, define

$$\eta = 1 - \cos(\theta) \tag{X-26}$$

Hence:

$$\frac{C_F}{C_{F\,max}} = \frac{\int_0^{\eta_{max}} e^{-\delta^2\eta^2} (1 - \eta) \, d\eta}{\int_0^{\eta_{max}} e^{-\delta^2\eta^2} \, d\eta} \tag{X-27}$$

The number of molecules which leave the control surface for $\theta > \theta_\infty$ is zero. The mathematical model, described by Equation (X-9), provides a small fraction for $\theta > \theta_\infty$. If we assume this fraction to be negligible, then Equation (X-27) becomes:

$$\frac{C_F}{C_{F\,max}} = \frac{\int_0^{\infty} e^{-\delta^2\eta^2} (1 - \eta) \, d\eta}{\int_0^{\infty} e^{-\delta^2\eta^2} \, d\eta} \tag{X-28}$$

This may be integrated to yield (Ref. X-7):

$$\frac{C_F}{C_{F\,max}} = 1 - \frac{1}{\delta\sqrt{\pi}} \tag{X-29}$$

Or:

$$\delta = \left[\sqrt{\pi}\left(1 - \frac{C_F}{C_{F\,max}}\right)\right]^{-1} \tag{X-30}$$

Hence, δ may be computed from easily determined test data.

Hill's comparison of this technique to the method of characteristics and to Sibulkins' approximation is shown in Figures X-5 and X-6.

The Figure X-6 comparison is obtained by writing Equation (X-3):

$$B = \frac{\rho}{\rho_0}\left(\frac{x}{d^*}\right)^2 \tag{X-31}$$

for Sibulkin's approach. Hill compares this to:

$$B = \left(\frac{2}{\gamma+1}\right)^{\frac{1}{\gamma-1}} \frac{\delta}{4\sqrt{\pi}} \frac{u^*}{u} \tag{X-32}$$

which he states to be his approximation.

We now are in a position to perform limited calculations.

First use Figure X-6 to obtain B. Immediately, we may apply Equation (X-31) rewritten in the form:

$$\frac{\rho}{\rho_0} = B\left(\frac{d^*}{x}\right)^2 \tag{X-33}$$

which enables us to compute density ratio in the plume. Figure X-2 may be used to obtain θ_∞ for $\theta_e = 0$ and, if desired, to approximate the exit Mach number, M_e. The value of θ_∞ for $\theta_e \neq 0$ follows from Equation (X-4). An alternate approach is to calculate the Mach number by (Ref. X-11, p. 6):

$$\frac{A^*}{A_e} = \left(\frac{\gamma+1}{2}\right)^{\frac{\gamma+1}{2(\gamma-1)}} M_e \left[1 + \frac{\gamma-1}{2} M_e^2\right]^{-\frac{\gamma+1}{2(\gamma-1)}} \tag{X-34}$$

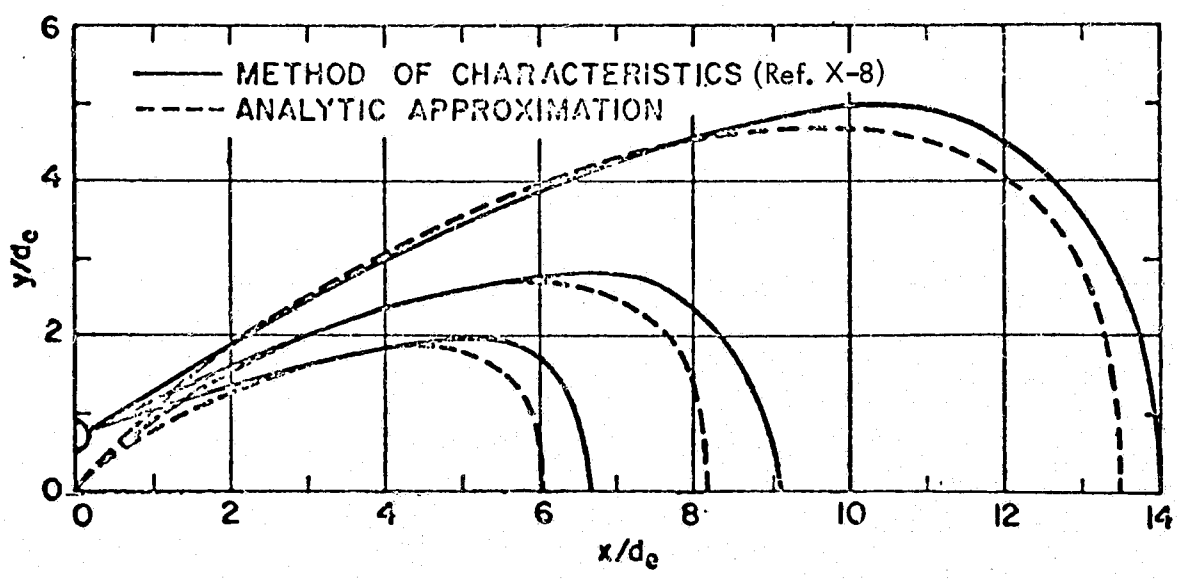

Figure X-5. Constant Density Contours for $A/A^* = 25$, $\gamma = 1.29$ (Ref. X-5).

We may compute the velocity at the throat by (Ref. X-10, p. 80):

$$u^* = \sqrt{\frac{2\gamma R T_0}{\gamma + 1}} \tag{X-35}$$

since we know T_0, the chamber temperature. Further (Ref. X-10, p. 79):

$$V_{max} = \sqrt{\frac{2\gamma R T_0}{\gamma - 1}} \tag{X-36}$$

Reference X-11 (p. 5) gives:

$$\left(\frac{V}{V_{max}}\right)^2 = \frac{\gamma - 1}{2} M^2 \left(1 + \frac{\gamma - 1}{2} M^2\right)^{-1} \tag{X-37}$$

which we may rewrite to obtain the exit velocity:

$$V_e = M_e V_{max} \left[\frac{\gamma - 1}{2} \left(1 + \frac{\gamma - 1}{2} M_e^2\right)^{-1}\right]^{1/2} \tag{X-38}$$

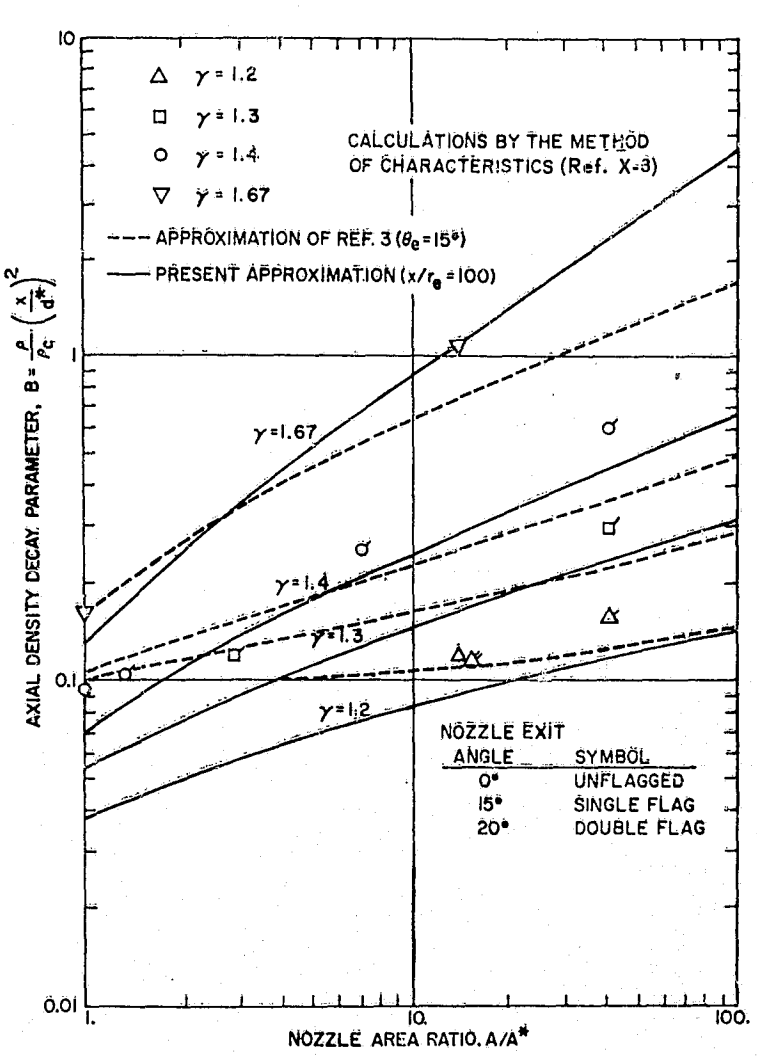

Figure X-6. Density Decay along Plume Axis (Ref. X-5).

Now we may use Brook's (Ref. X-9) relationship:

$$\frac{C_F}{C_{F\,max}} = \frac{1}{2}(1 + \cos\theta_e)\frac{V_e}{V_{max}}\left[1 + (\gamma M_e^2)^{-1}\right] \tag{X-39}$$

Next we compute δ from Equation (X-30). Then u is obtained by rewriting Equation (X-32):

$$u = u^* \left(\frac{2}{\gamma + 1}\right)^{\frac{1}{\gamma - 1}} \frac{\delta}{4B\sqrt{\pi}} \tag{X-40}$$

Substitute Equation (X-9) into (X-13):

$$\dot{m} = 2\pi \left(\frac{d\dot{m}}{d\psi}\right)_{\theta=0} \int_0^{\theta_\infty} \exp\left(-\delta^2\left[1 - \cos(\theta)\right]^2\right) \sin\theta\, d\theta \tag{X-41}$$

Next use Equation (X-26) to obtain:

$$\dot{m} = 2\pi \left(\frac{d\dot{m}}{d\psi}\right)_{\theta=0} \int_0^{\eta_{max}} e^{-\delta^2\eta^2} d\eta \tag{X-42}$$

Noting, as before, that the contribution between η_{max} and ∞ is small, we write:

$$\dot{m} = 2\pi \left(\frac{d\dot{m}}{d\psi}\right)_{\theta=0} \int_0^{\infty} e^{-\delta^2\eta^2} d\eta \tag{X-43}$$

$$= \frac{\pi}{\delta}\left(\frac{d\dot{m}}{d\psi}\right)_{\theta=0}\sqrt{\pi} \tag{X-44}$$

Or:

$$\left(\frac{d\dot{m}}{d\psi}\right)_{\theta=0} = \frac{\dot{m}\,\delta}{\pi^{3/2}} \tag{X-45}$$

which will provide $(d\dot{m}/d\psi)_{\theta=0}$ since $\dot{m}$ is known.

Next we rewrite Equation (X-20):

$$u = \frac{V_j\,\dot{m}}{2\pi\left(\frac{d\dot{m}}{d\psi}\right)_{\theta=0} \int_0^{\infty} f(\theta)\cos\theta\sin\theta\, d\theta}$$

With Equations (X-26) and (X-9) this becomes:

$$u = \frac{V_j\,\dot{m}}{2\pi\left(\frac{d\dot{m}}{d\psi}\right)_{\theta=0} \int_0^{\infty} e^{-\delta^2\eta^2}(1 - \eta)\, d\eta}$$

which becomes:

$$V_j = \frac{\pi u}{\dot{m}\ \delta^2} \left(\frac{d\ \dot{m}}{d\ \psi}\right)_{\theta=0} \dot{} \left[\delta \sqrt{\pi} - 1\right] \tag{X-46}$$

so that this parameter can be calculated.

Reference X-11 (p. 4) gives:

$$\frac{T}{T_t} = \left(1 + \frac{\gamma - 1}{2} M^2\right)^{-1} \tag{X-47}$$

where:

T_t = temperature under the conditions that would exist if the gas were brought to rest isentropically.

Applying this to the throat gives:

$$T^* = T_0 \left(1 + \frac{\gamma - 1}{2}\right)^{-1} \tag{X-48}$$

where T_t has been replaced by T_0 since the process is reversible and negligible flow rate is assumed in the chamber. The ideal gas law is:

$$p\ v = R\ T \tag{X-49}$$

where:

v = specific volume.

Or:

$$\frac{p}{\rho} = R\ T \tag{X-50}$$

which we can apply to the throat:

$$p^* = R\ T^*\ \rho^* \tag{X-51}$$

provided we know the density. The mass flow rate is simply described by:

$$\dot{m} = \rho\ u\ A \tag{X-52}$$

which may be used to compute density at the throat:

$$\rho^* = \frac{\dot{m}}{u^*\ A^*} \tag{X-53}$$

since all items on the right hand side of Equation (X-53) have been calculated. Now we may compute p* by Equation (X-51). Density and pressure in the chamber follow immediately by rewriting (Ref. X-11, p. 4):

$$\frac{p}{\rho_t} = \left(1 + \frac{\gamma - 1}{2} M^2\right)^{-\frac{1}{\gamma-1}} \tag{X-54}$$

$$\frac{\rho}{\rho_t} = \left(1 + \frac{\gamma - 1}{2} M^2\right)^{-\frac{1}{\gamma-1}} \tag{X-55}$$

to obtain:

$$p_0 = p^* \left(1 + \frac{\gamma - 1}{2}\right)^{\frac{1}{\gamma-1}} \tag{X-56}$$

$$\rho_0 = \rho^* \left(1 + \frac{\gamma - 1}{2}\right)^{\frac{1}{\gamma-1}} \tag{X-57}$$

The thrust coefficient now follows from Equation (X-14) written as:

$$C_F = \frac{F}{\rho_0 A^*} \tag{X-58}$$

These relations completely characterize the thruster and avoid the problem of an unknown chamber pressure. Instead, we have computed a pressure (and hence density) which is consistent with the remainder of the analysis.

Several cautions are necessary when we use this analysis:

1. We have assumed an idealized flow throughout the thruster. In practice, this will not be obtained and the isentropic assumptions in particular will be violated.

2. Continuum flow exists within the thruster but in the far field free molecular flow occurs. We have avoided a transition region in the analysis and any attempt to apply the analysis in the region will be grossly incorrect. Nevertheless, as a rough approximation, we will apply the analysis anyway - but must recognize the potential error involved.

3. Momentum and mass flux are not always conserved in the analysis - an obvious inconsistency.

A number of authors have extended these techniques further, while retaining some of the basic simplicity of the approximate approach. Brook (Ref. X-9) corrects for some of the problems, but, as he states, the technique is not entirely predictive because correlations of previous exact calculations or from an analysis of the axial density decay rate are required. Grier (Ref. X-2) has studied the problem in detail. Draper and Hill (Ref. X-12) consider the onset of rarefaction in an extension of their previous technique we have applied. References X-13-19 address this problem in various approaches. A wealth of more accurate computerized data also is available. Typical is that of Lockheed (Ref. X-20 among many others), Cassanova (Ref. X-21) and the extensive charts of Phillips (Ref. X-22).

REFERENCES

X-1. Rohsenow, W. M., Developments in Heat Transfer, The M.I.T. Press, 1964, p. 135.

X-2. Grier, Norman T., "Back Flow From Jet Plumes in Vacuum, "NASA-TN D-4978 (N69-14385), January 1969.

X-3. Sibulkin, M. and W. H. Gallaher, "Far-Field Approximation for a Nozzle Exhausting into a Vacuum," AIAA Journal, Volume 1, No. 6, June 1963, pp. 1452-1453.

X-4. Mirles, H., and J. F. Mullen, "Expansion of Gas Clouds and Hypersonic Jets Bounded by a Vacuum," AIAA Journal, Volume 1, No. 3, March 1963, pp. 596-602.

X-5. Hill, Jacques A. F., and James Stark Draper, "Analytical Approximation for the Flow from a Nozzle into a Vacuum," J. Spacecraft and Rockets Volume 3, No. 10, October 1966, pp. 1552-1554.

X-6. Zucrow, M. J., Aircraft and Missile Propulsion, Volume II, Wiley, 1964.

X-7. Grobner, Wolfgang, and Nikolaus Hofrieter, Integraltafel Zweiter Teil Bestimmte Integrale, Springer-Verlag, 1958.

X-8. Altshuler, S., M. M. Moe, and P. Molund, "The Electromagnetics of the Rocket Exhaust," STL, GM-TR-0165-00397, June 15, 1958 (Reference not consulted, included for completeness of report).

X-9. Brook, John W., "Far Field Approximation for a Nozzle Exhausting into a Vacuum," J. Spacecraft and Rockets, Volume 6, No. 5, May 1969, pp. 626-628.

X-10. Shapiro, Ascher H., The Dynamics and Thermodynamics of Compressible Fluid Flow, Volume 1, Ronald Press, 1953.

X-11. "Equations, Tables, and Charts for Compressible Flow," Report 1135, Ames Research Staff, NACA, 1953.

X-12. Draper, James Stark, and Jacques A. F. Hill, "Rarefaction in Underexpanded Flows," AIAA Journal, Volume 7, No. 7, July 1969, pp. 1400-1401.

X-13. Grier, Norman T., "Back Flow of Jet Plumes in Vacuum," NASA TM X-52468, N68-29919, paper presented at 6 International Symposium on Rarefied Gas Dynamics, Cambridge, Massachusetts July 22-26, 1968.

X-14. Patterson, Gordonn, "A Synthetic View of the Mechanics of Rarefied Gases," AIAA Journal Volume 3, No. 4, pp. 577-590, April, 1965.

X-15. Milligan, Mancil W., "Nozzle Characteristics in the Transition Regime between Continuum and Free Molecular Flow," AIAA Journal, Volume 2, No. 6, June 1964, pp. 1088-1092.

X-16. Freeman, N. C., "Solution of the Boltzmann Equation for Expanding Flows," AIAA Journal, Volume 5, No. 9, September, 1967, pp. 1696-1700.

X-17. Grundy, R. E., and D. R. Thomas, "Unsteady Spherically Symmetric Expansion of a Fixed mass of Gas into Vacuum," AIAA Journal, Volume 7, No. 5, May 1969, pp. 967-969.

X-18. Edwards, R. H., and H. K. Cheng, "Steady Expansion of a Gas into a Vacuum," AIAA Journal, Volume 4, No. 3, March, 1966, pp. 558-561.

X-19. Fisher, Sams, and Eldon L. Knuth, "Properties of Low-Density Free Jets Measured using Molecular-Beam Techniques," AIAA Journal, Volume 7, No. 6, June 1969, pp. 1174-1177.

X-20. Albini, Frank A., "Approximation Computation of Under-Expanded Jet Structure," AIAA Journal, Volume 3, No. 8, August, 1965, pp. 1535-1537.

X-21. Ratliff, Blackladge, Butler, and Kooker, "Analysis of Heating Rates and Forces on Bodies Subject to Rocket Exhaust Fume Impingement. Lockheed Missiles and Space Company, HREC-1150-1, N69 18037, March, 1968.

X-22. Cassonova, R. A., and W. B. Stephenson, "Expansion of a Jet into Near Vacuum," Arnold Engineering Development Center, AEDC-TR-65-151, AD469041, August, 1965.

X-23. Phillips, William W., and Ross A. Fiddler, "Thrust Coefficient and Thrust Deflection Angles on ATC," Boeing Company, AD686763, March, 1968.